

BULLETIN OF RUSSIAN STATE MEDICAL UNIVERSITY

BIOMEDICAL JOURNAL OF PIROGOV RUSSIAN NATIONAL
RESEARCH MEDICAL UNIVERSITY

EDITOR-IN-CHIEF Denis Rebrikov, DSc, professor

DEPUTY EDITOR-IN-CHIEF Alexander Oettinger, DSc, professor

EDITORS Valentina Geidebrekht, Nadezda Tikhomirova

TECHNICAL EDITOR Nina Tyurina

TRANSLATORS Ekaterina Tretiyakova, Vyacheslav Vityuk

DESIGN AND LAYOUT Marina Doronina

EDITORIAL BOARD

Averin VI, DSc, professor (Minsk, Belarus)

Alipov NN, DSc, professor (Moscow, Russia)

Belousov VV, DSc, professor (Moscow, Russia)

Bogomilskiy MR, corr. member of RAS, DSc, professor (Moscow, Russia)

Bozhenko VK, DSc, CSc, professor (Moscow, Russia)

Bylova NA, CSc, docent (Moscow, Russia)

Gainetdinov RR, CSc (Saint-Petersburg, Russia)

Gendlin GYe, DSc, professor (Moscow, Russia)

Ginter EK, member of RAS, DSc (Moscow, Russia)

Gorbacheva LR, DSc, professor (Moscow, Russia)

Gordeev IG, DSc, professor (Moscow, Russia)

Gudkov AV, PhD, DSc (Buffalo, USA)

Gulyaeva NV, DSc, professor (Moscow, Russia)

Gusev EI, member of RAS, DSc, professor (Moscow, Russia)

Danilenko VN, DSc, professor (Moscow, Russia)

Zarubina TV, DSc, professor (Moscow, Russia)

Zatevakhin II, member of RAS, DSc, professor (Moscow, Russia)

Kagan VE, professor (Pittsburgh, USA)

Kzyshkowska YuG, DSc, professor (Heidelberg, Germany)

Kobrinikii BA, DSc, professor (Moscow, Russia)

Kozlov AV, MD PhD, (Vienna, Austria)

Kotelevtsev YuV, CSc (Moscow, Russia)

Lebedev MA, PhD (Darem, USA)

Manturova NE, DSc (Moscow, Russia)

Milushkina OYu, DSc, professor (Moscow, Russia)

Mitupov ZB, DSc, professor (Moscow, Russia)

Moshkovskii SA, DSc, professor (Moscow, Russia)

Munblit DB, MSc, PhD (London, Great Britain)

Negrebetsky VV, DSc, professor (Moscow, Russia)

Novikov AA, DSc (Moscow, Russia)

Pivovarov YuP, member of RAS, DSc, professor (Moscow, Russia)

Platonova AG, DSc (Kiev, Ukraine)

Polunina NV, corr. member of RAS, DSc, professor (Moscow, Russia)

Poryadin GV, corr. member of RAS, DSc, professor (Moscow, Russia)

Razumovskii AYU, corr. member of RAS, DSc, professor (Moscow, Russia)

Rebrova OYu, DSc (Moscow, Russia)

Rudoy AS, DSc, professor (Minsk, Belarus)

Rylova AK, DSc, professor (Moscow, Russia)

Savelieva GM, member of RAS, DSc, professor (Moscow, Russia)

Semiglazov VF, corr. member of RAS, DSc, professor (Saint-Petersburg, Russia)

Skoblina NA, DSc, professor (Moscow, Russia)

Slavyanskaya TA, DSc, professor (Moscow, Russia)

Smirnov VM, DSc, professor (Moscow, Russia)

Spallone A, DSc, professor (Rome, Italy)

Starodubov VI, member of RAS, DSc, professor (Moscow, Russia)

Stepanov VA, corr. member of RAS, DSc, professor (Tomsk, Russia)

Suchkov SV, DSc, professor (Moscow, Russia)

Takhchidi KhP, member of RAS, DSc, professor (Moscow, Russia)

Trufanov GE, DSc, professor (Saint-Petersburg, Russia)

Favorova OO, DSc, professor (Moscow, Russia)

Filipenko ML, CSc, leading researcher (Novosibirsk, Russia)

Khazipov RN, DSc (Marsel, France)

Chundukova MA, DSc, professor (Moscow, Russia)

Shimanovskii NL, corr. member of RAS, DSc, professor (Moscow, Russia)

Shishkina LN, DSc, senior researcher (Novosibirsk, Russia)

Yakubovskaya RI, DSc, professor (Moscow, Russia)

SUBMISSION <http://vestnikrgmu.ru/login?lang=en>

CORRESPONDENCE editor@vestnikrgmu.ru

COLLABORATION manager@vestnikrgmu.ru

ADDRESS ul. Ostrovityanova, d. 1, Moscow, Russia, 117997

Indexed in Scopus. CiteScore 2018: 0.20

Scopus[®]

Indexed in WoS. JCR 2018: 0.21

WEB OF SCIENCE[™]

Five-year h-index is 6

Google
scholar

Indexed in RSCI. IF 2018: 0.321

**НАУЧНАЯ ЭЛЕКТРОННАЯ
БИБЛИОТЕКА
LIBRARY.RU**

Listed in HAC 31.01.2020 (№ 507)



**ВЫСШАЯ
АТТЕСТАЦИОННАЯ
КОМИССИЯ (ВАК)**

Open access to archive

CYBERLENINKA

Issue DOI: 10.24075/brsmu.2020-05

The mass media registration certificate no. 012769 issued on July 29, 1994

Founder and publisher is Pirogov Russian National Research Medical University (Moscow, Russia)

The journal is distributed under the terms of Creative Commons Attribution 4.0 International License www.creativecommons.org



Approved for print 31.10.2020
Circulation: 100 copies. Printed by Print.Formula
www.print-formula.ru

ВЕСТНИК РОССИЙСКОГО ГОСУДАРСТВЕННОГО МЕДИЦИНСКОГО УНИВЕРСИТЕТА

НАУЧНЫЙ МЕДИЦИНСКИЙ ЖУРНАЛ РНИМУ ИМ. Н. И. ПИРОГОВА

ГЛАВНЫЙ РЕДАКТОР Денис Ребриков, д. б. н., профессор

ЗАМЕСТИТЕЛЬ ГЛАВНОГО РЕДАКТОРА Александр Эттингер, д. м. н., профессор

РЕДАКТОРЫ Валентина Гейдебрехт, Надежда Тихомирова

ТЕХНИЧЕСКИЙ РЕДАКТОР Нина Тюрина

ПЕРЕВОДЧИКИ Екатерина Третьякова, Вячеслав Виток

ДИЗАЙН И ВЕРСТКА Марины Дорониной

РЕДАКЦИОННАЯ КОЛЛЕГИЯ

В. И. Аверин, д. м. н., профессор (Минск, Белоруссия)
Н. Н. Алипов, д. м. н., профессор (Москва, Россия)
В. В. Белоусов, д. б. н., профессор (Москва, Россия)
М. Р. Богомилский, член-корр. РАН, д. м. н., профессор (Москва, Россия)
В. К. Боженко, д. м. н., к. б. н., профессор (Москва, Россия)
Н. А. Былова, к. м. н., доцент (Москва, Россия)
Р. Р. Гайнетдинов, к. м. н. (Санкт-Петербург, Россия)
Г. Е. Гендлин, д. м. н., профессор (Москва, Россия)
Е. К. Гинтер, академик РАН, д. б. н. (Москва, Россия)
Л. Р. Горбачева, д. б. н., профессор (Москва, Россия)
И. Г. Гордеев, д. м. н., профессор (Москва, Россия)
А. В. Гудков, PhD, DSc (Буффало, США)
Н. В. Гуляева, д. б. н., профессор (Москва, Россия)
Е. И. Гусев, академик РАН, д. м. н., профессор (Москва, Россия)
В. Н. Даниленко, д. б. н., профессор (Москва, Россия)
Т. В. Зарубина, д. м. н., профессор (Москва, Россия)
И. И. Затевахин, академик РАН, д. м. н., профессор (Москва, Россия)
В. Е. Каган, профессор (Питтсбург, США)
Ю. Г. Кжышковска, д. б. н., профессор (Гейдельберг, Германия)
Б. А. Кобринский, д. м. н., профессор (Москва, Россия)
А. В. Козлов, MD PhD (Вена, Австрия)
Ю. В. Котелевцев, к. х. н. (Москва, Россия)
М. А. Лебедев, PhD (Дарем, США)
Н. Е. Мантурова, д. м. н. (Москва, Россия)
О. Ю. Милушкина, д. м. н., доцент (Москва, Россия)
З. Б. Митупов, д. м. н., профессор (Москва, Россия)
С. А. Мошковский, д. б. н., профессор (Москва, Россия)
Д. Б. Мунблит, MSc, PhD (Лондон, Великобритания)

В. В. Негребецкий, д. х. н., профессор (Москва, Россия)
А. А. Новиков, д. б. н. (Москва, Россия)
Ю. П. Пивоваров, д. м. н., академик РАН, профессор (Москва, Россия)
А. Г. Платонова, д. м. н. (Киев, Украина)
Н. В. Полунина, член-корр. РАН, д. м. н., профессор (Москва, Россия)
Г. В. Порядин, член-корр. РАН, д. м. н., профессор (Москва, Россия)
А. Ю. Разумовский, член-корр., профессор (Москва, Россия)
О. Ю. Реброва, д. м. н. (Москва, Россия)
А. С. Рудой, д. м. н., профессор (Минск, Белоруссия)
А. К. Рылова, д. м. н., профессор (Москва, Россия)
Г. М. Савельева, академик РАН, д. м. н., профессор (Москва, Россия)
В. Ф. Семглазов, член-корр. РАН, д. м. н., профессор (Санкт-Петербург, Россия)
Н. А. Скоблина, д. м. н., профессор (Москва, Россия)
Т. А. Славянская, д. м. н., профессор (Москва, Россия)
В. М. Смирнов, д. б. н., профессор (Москва, Россия)
А. Спаллоне, д. м. н., профессор (Рим, Италия)
В. И. Стародубов, академик РАН, д. м. н., профессор (Москва, Россия)
В. А. Степанов, член-корр. РАН, д. б. н., профессор (Томск, Россия)
С. В. Сучков, д. м. н., профессор (Москва, Россия)
Х.П.Тахчиди, академик РАН, д. м. н., профессор (Москва, Россия)
Г. Е. Труфанов, д. м. н., профессор (Санкт-Петербург, Россия)
О. О. Фаворова, д. б. н., профессор (Москва, Россия)
М. Л. Филипенко, к. б. н. (Новосибирск, Россия)
Р. Н. Хазипов, д. м. н. (Марсель, Франция)
М. А. Чундокова, д. м. н., профессор (Москва, Россия)
Н. Л. Шимановский, член-корр. РАН, д. м. н., профессор (Москва, Россия)
Л. Н. Шишкина, д. б. н. (Новосибирск, Россия)
Р. И. Якубовская, д. б. н., профессор (Москва, Россия)

ПОДАЧА РУКОПИСЕЙ <http://vestnikrgmu.ru/login>

ПЕРЕПИСКА С РЕДАКЦИЕЙ editor@vestnikrgmu.ru

СОТРУДНИЧЕСТВО manager@vestnikrgmu.ru

АДРЕС РЕДАКЦИИ ул. Островитянова, д. 1, г. Москва, 117997

Журнал включен в Scopus. CiteScore 2018: 0,20

Журнал включен в WoS. JCR 2018: 0,21

Индекс Хирша (h²) журнала по оценке Google Scholar: 6

Scopus®

WEB OF SCIENCE™

Google
scholar

Журнал включен в РИНЦ. IF 2018: 0,321

Журнал включен в Перечень 31.01.2020 (№ 507)

Здесь находится открытый архив журнала

НАУЧНАЯ ЭЛЕКТРОННАЯ
БИБЛИОТЕКА
LIBRARY.RU



ВЫСШАЯ
АТТЕСТАЦИОННАЯ
КОМИССИЯ (ВАК)

CYBERLENINKA

DOI выпуска: 10.24075/vrgmu.2020-05

Свидетельство о регистрации средства массовой информации № 012769 от 29 июля 1994 г.

Учредитель и издатель — Российский национальный исследовательский медицинский университет имени Н. И. Пирогова (Москва, Россия)

Журнал распространяется по лицензии Creative Commons Attribution 4.0 International www.creativecommons.org



Подписано в печать 31.10.2020

Тираж 100 экз. Отпечатано в типографии Print.Formula
www.print-formula.ru

REVIEW	5
<hr/>	
Antiviral system of innate immunity: COVID-19 pathogenesis and treatment Kazimirskii AN, Salmasi JM, Poryadin GV	
Антивирусная система врожденного иммунитета: патогенез и лечение COVID-19 А. Н. Казимирский, Ж. М. Салмаси, Г. В. Порядин	
ORIGINAL RESEARCH	14
<hr/>	
New anti-mesothelin single-domain antibodies and cell models for developing targeted breast cancer therapy Kravchenko YuE, Chumakov SP, Frolova EI	
Новые однодоменные антитела к мезотелину и клеточные модели для разработки таргетной терапии рака молочной железы Ю. Е. Кравченко, С. П. Чумаков, Е. И. Фролова	
ORIGINAL RESEARCH	22
<hr/>	
Immunohistochemical expression of Nanog protein in prostate cancer cells of distinct Grade Groups Kudryavtsev GYu, Kudryavtseva LV, Mikhaleva LM, Kudryavtseva YaYu, Solovyeva NA, Osipov VA, Babichenko II	
Иммуногистохимическая экспрессия белка Nanog в клетках рака предстательной железы различных прогностических групп Г. Ю. Кудрявцев, Л. В. Кудрявцева, Л. М. Михалева, Я. Ю. Кудрявцева, Н. А. Соловьева, В. А. Осипов, И. И. Бабиченко	
ORIGINAL RESEARCH	29
<hr/>	
Prospective pharmacological effects of psoralen photooxidation products and their cycloadducts with aminothiols: chemoinformatic analysis Skarga VV, Zadorozhny AD, Shilov BV, Nevezhin EV, Negrebetsky VV, Maslov MA, Lagunin AA, Malakhov MV	
Потенциальные фармакологические эффекты продуктов фотоокисления псоралена и их циклоаддуктов с аминотиолами: хемоинформационный анализ В. В. Скарга, А. Д. Задорожный, Б. В. Шилов, Е. В. Невежин, В. В. Негребецкий, М. А. Маслов, А. А. Лагунин, М. В. Малахов	
ORIGINAL RESEARCH	37
<hr/>	
Effect of neuromodulation on neurotrophic factors in patients with chronic disorders of consciousness Iazeva EG, Legostaeva LA, Bakulin IS, Poydasheva AG, Abaimov DA, Suponeva NA, Shabalina AA, Ryabinkina YV, Piradov MA	
Влияние курса нейромодуляции на профиль нейротрофических факторов у пациентов с хроническими нарушениями сознания Е. Г. Язева, Л. А. Легостаева, И. С. Бакулин, А. Г. Пойдашева, Д. А. Абаймов, Н. А. Супонева, А. А. Шабалина, Ю. В. Рябинкина, М. А. Пирадов	
ORIGINAL RESEARCH	44
<hr/>	
Effect of robot-assisted gait training on biomechanics of ankle joint in patients with post-stroke hemiparesis Klochov AS, Zimin AA, Khizhnikova AE, Suponeva NA, Piradov MA	
Влияние роботизированных тренировок на биомеханику голеностопного сустава у пациентов с постинсультным парезом А. С. Клочков, А. А. Зимин, А. Е. Хижникова, Н. А. Супонева, М. А. Пирадов	
ORIGINAL RESEARCH	54
<hr/>	
Taxonomic dysbiosis of gut microbiota and serum biomarkers reflect severity of central nervous system injury Chernevskaya EA, Meglei AYU, Buyakova IV, Kovaleva NYu, Gorshkov KM, ZakharchenkoVE, Beloborodova NV	
Таксономический дисбиоз микробиоты и сывороточные биомаркеры как отражение тяжести поражения центральной нервной системы Е. А. Черневская, А. Ю. Меглей, И. В. Буйкова, Н. Ю. Ковалева, К. М. Горшков, В. Е. Захарченко, Н. В. Белобородова	
ORIGINAL RESEARCH	62
<hr/>	
Semen microbiota: cluster analysis of real-time PCR data Voroshilina ES, Zornikov DL, Ivanov AV, Pochernikov DG, Panacheva EA	
Микробиота эякулята: кластерный анализ результатов, полученных при исследовании методом ПЦР-РВ Е. С. Ворошилина, Д. Л. Зорников, А. В. Иванов, Д. Г. Почерников, Е. А. Паначева	
ORIGINAL RESEARCH	70
<hr/>	
EEG sensorimotor rhythms in children with autism spectrum disorders Kaida AI, Eismont EV, Mikhailova AA, Pavlenko VB	
Сенсомоторные ритмы ЭЭГ у детей с расстройствами аутистического спектра А. И. Кайда, Е. В. Эйсмонт, А. А. Михайлова, В. Б. Павленко	
ORIGINAL RESEARCH	77
<hr/>	
Telomerized fibroblasts as a candidate 3D <i>in vitro</i> model of pathological hypertrophic scars Shadrin VS, Kozhin PM, Shoshina OO, Luzgina NG, Rusanov AL	
Теломеризованные фибробласты как потенциальный объект для 3D-моделирования патологических гипертрофических рубцов <i>in vitro</i> В. С. Шадрин, П. М. Кожин, О. О. Шошина, Н. Г. Лузгина, А. Л. Русанов	

ORIGINAL RESEARCH	85
<hr/>	
Clinical significance of the musculus gluteus minimus in total hip arthroplasty Yegiazaryan KA, Sirotin IV, Chizhikova IO, Lazishvili GD, Ratiev AP, But-Gusaim AB	
Клиническое значение малой ягодичной мышцы при эндопротезировании тазобедренного сустава К. А. Егиазарян, И. В. Сиротин, И. О. Чижикова, Г. Д. Лазишвили, А. П. Ратьев, А. Б. Бут-Гусаим	
CLINICAL CASE	90
<hr/>	
Retinal laser photocoagulation in management of Eales' disease Takhchidi KhP, Takhchidi EKh, Kasminina TA, Tebina EP, Mokrunova MV	
Применение лазерной коагуляции сетчатки при болезни Илза Х. П. Тахчиди, Е. Х. Тахчиди, Т. А. Касмынина, Е. П. Тебина, М. В. Мокрунова	
CLINICAL CASE	97
<hr/>	
Staged approach to treatment of combined hamartoma of the retina and retinal pigment epithelium Takhchidi KhP, Takhchidi NKh, Kasminina TA, Tebina EP	
Поэтапный подход в лечении комбинированной гамартомы сетчатки и ретиального пигментного эпителия Х. П. Тахчиди, Н. Х. Тахчиди, Т. А. Касмынина, Е. П. Тебина	
CLINICAL CASE	102
<hr/>	
Difficulties in differential diagnosis of cutaneous manifestations in patients with coronavirus infection Tairova RT, Gaydina TA, Dvornikov AS, Tazartukova AD, Lyang OV	
Сложности дифференциальной диагностики кожных проявлений при коронавирусной инфекции Р. Т. Таирова, Т. А. Гайдина, А. С. Дворников, А. Д. Тазартукова, О. В. Лянг	
ORIGINAL RESEARCH	108
<hr/>	
Efficacy of smartphone-compatible optical instrument for assessing melanocytic nevi for malignancy Gaydina TA, Dvornikova EG	
Эффективность использования оптической системы смартфона для оценки злокачественности меланокитарных невусов Т. А. Гайдина, Е. Г. Дворникова	
ERRATUM	113
<hr/>	
Erratum to Hypoxia enhances transcytosis in intestinal enterocytes Maltseva DV, Shkurnikov MYu, Nersisyan SA, Nikulin SV, Kurnosov AA, Raigorodskaya MP, Osipyants AI, Tonevitsky EA Published in Bulletin of RSMU (july–august 2020, 60–66).	
Исправление к статье Гипоксия усиливает трансцитоз в энтероцитах кишечника Д. В. Мальцева, М. Ю. Шкурников, С. А. Нерсисян, С. В. Никулин, А. А. Курносов, М. П. Райгородская, А. И. Осипьянц, Е. А. Тоневицкий Опубликована в журнале Вестник РГМУ (июль–август 2020, с. 63–69).	

ANTIVIRAL SYSTEM OF INNATE IMMUNITY: COVID-19 PATHOGENESIS AND TREATMENT

Kazimirskii AN , Salmasi JM, Poryadin GV

Pirogov Russian National Research Medical University, Moscow, Russia

Antiviral system of innate immunity includes two main components: the mitochondrial antiviral sensor — the mitochondrial outer membrane protein and peripheral blood neutrophils capable of forming neutrophilic extracellular traps. Depending on the activation pathway of the mitochondrial antiviral sensor (MAVS), two possible variants of cells death, apoptosis or cellular degeneration with necrotic changes, develop during cell infection with an RNA-containing virus. The development of virus-induced apoptosis of infected cells causes the formation of neutrophilic extracellular traps, the secretion of inflammatory cytokines, ROS generation, tissue damage, hemocoagulation and the development of an acute inflammatory process with the development of COVID-19 pneumonia. Violation of the prion-like reaction of MAVS in response to viral infection of the cell triggers an alternative pathway for activating autophagy. Cells under conditions of prolonged activation of autophagy experience necrotic changes and are eliminated from the organism by monocytes/macrophages that secrete anti-inflammatory cytokines. This type of reaction of the antiviral system of innate immunity corresponds to the asymptomatic course of the disease. From the most significant aspects of the pathogenesis of the coronavirus infection COVID-19 given, recommendations for the prophylactic treatment of this dangerous disease follow. The proposed treatment can significantly decrease the severity of COVID-19 disease and reduce mortality.

Keywords: innate immunity, antiviral system, mitochondrial antiviral signaling protein, MAVS, neutrophilic extracellular traps, COVID-19 treatment

Author contribution: the authors contributed equally to all aspects of the article.

✉ **Correspondence should be addressed:** Alexander N. Kazimirskii
Ostrovityanova, 1, Moscow, 117437; alnica10@mail.ru

Received: 31.08.2020 **Accepted:** 13.09.2020 **Published online:** 21.09.2020

DOI: 10.24075/brsmu.2020.054

АНТИВИРУСНАЯ СИСТЕМА ВРОЖДЕННОГО ИММУНИТЕТА: ПАТОГЕНЕЗ И ЛЕЧЕНИЕ COVID-19

А. Н. Казимирский , Ж. М. Салмаси, Г. В. Порядин

Российский национальный исследовательский медицинский университет имени Н. И. Пирогова, Москва, Россия

В обзоре представлена концепция антивирусной системы врожденного иммунитета и описаны главные структурные компоненты этой системы в организме человека, действующей против РНК-содержащих вирусов. Антивирусная система врожденного иммунитета включает в себя два главных компонента: митохондриальный антивирусный сенсор (MAVS) — белок наружной мембраны митохондрий и нейтрофилы периферической крови, способные формировать нейтрофильные экстраклеточные ловушки. В зависимости от пути активации MAVS при инфицировании клетки РНК-содержащим вирусом развиваются два возможных варианта ее гибели — апоптоз или дегенерация клеток с некротическими изменениями. Развитие вирус-индуцированного апоптоза инфицированных клеток вызывает формирование нейтрофильных экстраклеточных ловушек, секрецию воспалительных цитокинов, генерацию АФК, тканевое повреждение, гемокоагуляцию и возникновение острого воспалительного процесса с развитием COVID-19-пневмонии. Нарушение прионоподобной реакции MAVS в ответ на вирусное инфицирование клетки запускает альтернативный путь активации аутофагии. Клетки в условиях продолжительной активации аутофагии испытывают дегенеративные изменения и элиминируются из организма моноцитами/макрофагами, которые секретируют противовоспалительные цитокины. Такой тип реакции антивирусной системы врожденного иммунитета соответствует бессимптомному течению заболевания. Из приведенных наиболее существенных сторон патогенеза коронавирусной инфекции COVID-19 вытекают рекомендации по профилактическому лечению этого опасного заболевания. Предлагаемое лечение позволит значительно ослабить тяжесть заболевания Covid-19 и снизить летальность.

Ключевые слова: врожденный иммунитет, антивирусная система, митохондриальный антивирусный сигнальный белок, MAVS, нейтрофильные экстраклеточные ловушки, лечение COVID-19

Вклад авторов: равнозначный

✉ **Для корреспонденции:** Александр Николаевич Казимирский
ул. Островитянова, д. 1, г. Москва, 117437, alnica10@mail.ru

Статья получена: 31.08.2020 **Статья принята к печати:** 13.09.2020 **Опубликована онлайн:** 21.09.2020

DOI: 10.24075/vrgmu.2020.054

In the past 20 years, eight new deadly viruses have been discovered that threaten humans, which actualized the search for components of the organism's antiviral system. Several studies have shown that the antiviral system of the human organism is associated with innate immunity and it activates immediately when the virus enters into the human cells, so it can be called the antiviral system of innate immunity.

The existence of the antiviral system of innate immunity is recognized by some researchers, but both the components of this system and its functioning are still unclear. At the same time, the accumulated experimental material allows us to identify the main parts of this system and create a model of its functioning. In no case do we claim to fully cover this issue, but we suppose that the antiviral system of innate immunity has

two main components: the mitochondrial antiviral sensor — the outer membrane protein of mitochondrion and neutrophils that can form neutrophilic extracellular traps.

Mitochondrial antiviral sensor

Mitochondrial antiviral sensor (mitochondrial antiviral signaling protein, MAVS) — a surface protein of the outer mitochondrial membrane with prion-like activity has the ability to change conformation when interacting with viral RNA. Viral infection triggers the formation of aggregates of mitochondrial antiviral signaling protein (MAVS), which actively stimulates immune signaling [1]. The antiviral effect of this protein depends on the speed of its renewal. The weakening of the immune response

and increased intracellular infection is due to the inhibition of ubiquitin ligase, which is responsible for the accelerated renewal of MAVS [2]. Mutations in MAVS that disrupt its prion-like activity also completely cancel its ability to transmit immune activation signals in mammalian cells. The results of some studies show that prion-like polymerization is a conservative mechanism of signal transmission of activation of innate immunity even in the development of inflammation [3, 4]. The importance of mitochondrial antiviral signaling protein (MAVS) has been demonstrated in the infection of wild-type mice with Ebola virus (EBOV). MAVS controlled EBOV replication through IFN α expression, impaired inflammatory responses in the spleen, and prevented liver cell death. MAVS (-/-) mice developed severe inflammation, viral replication, and decreased IFN-I synthesis [5]. The threat, associated with Zika virus epidemics (ZIKV) and its association with serious complications, confirms the need for a better understanding of ZIKV pathogenic mechanisms. Examining RNA sequencing in the blood of patients infected with ZIKV, it was found that programs of transcriptional antiviral interferon-stimulated genes and innate immune sensors in patients infected with ZIKV remained inactive compared to those in healthy donors. In infected patients, ZIKV was able to suppress the induction of IFN-I, and the viral protein ZIKV NS4A bound MAVS and thereby interrupted the interaction of RIG-I/MAVS reducing the synthesis of INF-I [6]. Some extracellular pathogens can activate intracellular defense mechanisms against viral infections. Pneumolysin (Ply), the main virulence factor of *Streptococcus pneumoniae*, is able to initiate oxidative damage to mitochondria, which causes the release of mitochondrial DNA, which mediates the expression of IFN β in macrophages. In response to pneumolysin, macrophages express IFN β using an interferon gene stimulator STING (stimulator of interferon genes) [7]. The activation of the main intracellular adapter proteins of the antiviral defense MAVS and STING consists in their phosphorylation with the participation of certain (serine-threonine) protein kinases (IKK and/or TBK1) when pathogens enter the cell [8]. An intracellular signal of cell infection is an unusual noncanonical cyclic dinucleotide 2'3'-cGAMP (cGAMP) [9]. The organism of higher mammals and humans synthesizes the cyclic guanyl-adenyl dinucleotide 2'3'-cGAMP capable of activating the main intracellular adapter antiviral defense proteins MAVS and STING under the influence of the enzyme cGAMP synthase. The formation of 2'3'-cGAMP is catalyzed by cGAMP synthase (cGAS) when a cytosolic double-stranded DNA is detected and functions as an endogenous inducer of innate immunity by directly binding and activating an adapter protein, an interferon gene stimulator (STING). This cyclic 2'3'-cGAMP dinucleotide stimulates the secretion of interferon- β (IFN β), a major defense signaling pathway that is independent of activation of innate immunity receptors (toll-like receptors, TLRs) [10]. The Vaccinia virus in human cells induces the synthesis of specific nucleases called poxins capable of catalyzing the cleavage of the 3'-5' bond, converting the cyclic 2',3'-cGAMP into a linear Gp[2'-5']Ap[3'] dinucleotide. Linear guanyl-adenyl dinucleotide loses its ability to activate the interferon gene stimulator (STING), while the antiviral mechanisms do not work. The results demonstrate the mechanism by which viruses avoid innate immunity [11].

In the recognition of intracellular pathogens and the production of interferons I, (IFN-I), the most important role belongs to dendritic cells and macrophages [12]. When mice were infected with respiratory syncytial virus (RSV), which is the most common cause of respiratory infections in infants and young children, alveolar macrophages were identified as

the main source of IFN-I [13]. Infection of genetically modified Myd88/Trif/Mavs (-/-) mice in which signaling was impaired by all TLR, RLR (RIG-I, MDA5, LGP2) and IL-1R, as well as other cytokine receptors, such as IL18 receptor showed that in such RSV-infected animals, the early production of pro-inflammatory mediators was completely absent. However, RSV-specific CD8⁺ T-lymphocytes were observed in lung tissue and airways. RSV-infected Myd88/Trif/Mavs (-/-) mice with disabled innate immunity overcame the infection, but showed higher viral load, severe and prolonged inflammation, and weight loss. These data demonstrate both a certain level of redundancy in the organism's immune defense and the fact that the involvement of cytotoxic T-lymphocytes in the response is provided by cells of the infected tissue itself producing IFN γ [14]. In the experimental model of Toxoplasmosis (*Toxoplasma gondii*), the presence of a non-lymphoid source of IFN γ was determined in genetically modified mice with the absence of all lymphoid cells due to deficiencies of recombinant activating genes 2 and IL-2R γ , which also produced IFN γ in response to a simple parasite. Flow cytometry and morphological studies showed that in this experimental model, the sources of IFN γ are neutrophils, not NK cells and not CD8⁺ T lymphocytes [15, 16]. Intracellular pathogens also induce accelerated formation of IFN γ . Moreover, viral infection does not increase the expression of innate immunity receptors (TLRs) in plasmacytoid dendritic cells. Mice infected with the lymphocytic choriomeningitis virus developed strong TLR-independent production of interferon I (IFN-I) using RNA helicase and with the participation of mitochondrial antiviral signaling protein (MAVS) [17].

MAVS induces apoptosis

MAVS (IPS-1, VISA or Cardif) is important for protecting the host organism against viral infection not only by inducing interferons-I (IFN-I), but it also causes apoptosis of infected cells regardless of its function in initiating production IFN-I. Moreover, MAVS (-/-) fibroblasts are resistant to apoptosis caused by the Sendai virus. Functional screening shows that severe acute respiratory syndrome coronavirus (SARS-CoV) protein (NSP15) inhibits MAVS-induced apoptosis and this is a method of coronavirus immune evasion [18]. In MAVS-deficient cells, caspase-8 and -3 activation are reduced. After infection with the RNA virus, MAVS induces type I antiviral response and recruits caspase-8 in mitochondria to ensure activation of caspase-3 and apoptosis of infected cells [19]. African swine fever virus increases MAVS expression in alveolar macrophages. MAVS expression was enhanced by intracellular reactive oxygen species (ROS). In addition, MAVS increased the induction of antiviral and proinflammatory cytokines and apoptosis of infected cells and inhibited virus replication [20].

In mice with MAVS deficiency, hepatitis A virus causes histological signs of liver damage, leukocyte infiltration, and the release of liver enzymes into the blood [21]. The miR-33/33* miRNA was found to be able to increase viral replication and mortality, while at the same time weakening the synthesis of interferon-I *in vitro* and *in vivo*. Further studies showed that this miRNA prevents the formation of activated aggregates of mitochondrial antiviral signal protein (MAVS) and is a negative regulator of the antiviral system of innate immunity [22]. These and several other studies show the critical role of mitochondrial antiviral signaling protein (MAVS) in virus-induced apoptosis. Viral infection triggers the organism's defense mechanisms, the main of which is the mitochondrial antiviral sensor. The antiviral defense strategy of the organism is to initiate apoptosis of cells infected with RNA-containing viruses. The described protection

strategy can only be implemented with a functionally complete MAVS.

Inhibition of inflammation by reducing the number of apoptotic cells

After synthesis in the cell and its transport into the outer mitochondrial membrane, the mitochondrial antiviral sensor undergoes modification over time. The essence of the modification of this viral RNA sensor is its geranylation (addition of two residues of geranyl diphosphate) followed by palmitoylation (addition of two residues of palmitic acid). Such a modified mitochondrial antiviral sensor is not capable of aggregation under the influence of viral RNA and is not capable of activation and aggregation with the subsequent development of apoptosis of the virus of the infected cell [23]. Geranyl diphosphate is a linear ten-carbon molecule consisting of two isoprene residues formed in the organism in the way of cholesterol synthesis, therefore, preventive treatment of coronavirus infection may consist in pharmacological inhibition of the cholesterol synthesis pathway using statins. The timely use of preventive therapy against coronavirus infection (COVID-19) will help to avoid the severe course of the disease and the development of complications. The inflammatory process, with a functionally complete mitochondrial antiviral sensor, as we assume, will be localized in the upper respiratory tract and will not be spread in the organism. An important and relevant question about predicting the severity, complications and outcome of a coronavirus infection can be resolved after developing a test for the presence of a geranylated mitochondrial antiviral sensor. Uninfected people with a high level of modified (geranylated) MAVS may be at risk for coronavirus infection (SARS-CoV-2) and need in isolation and prescribing prophylactic therapy.

Neutrophilic extracellular traps

Neutrophilic extracellular traps are a form of response of pre-activated neutrophils to contact interactions with cells in a state of apoptosis. Neutrophils are pre-activated by receiving activation signals through various innate immunity receptors (TLRs). At the activation stage, neutrophils interact with various molecules of pathogens or modified molecules in our organism that recognize innate immunity receptors (TLRs) as pathogens. During the activation of neutrophils, occurs the expression of the genome, the synthesis of cytokines and enzymes, the generation of reactive oxygen (ROS) and nitrogen (NOS) species. However, this is not enough for the formation of neutrophilic extracellular traps.

Disclosure of neutrophilic extracellular traps occurs after interaction with apoptotic cells or their residues. A network of neutrophilic DNA fibers captures and holds apoptotic cells, and then other intact neutrophils and monocytes phagocytose this structure, hydrolyzing its components and presenting antigens. Interestingly, after phagocytosis, cells are no longer capable of opening neutrophilic extracellular traps [24–27]. A signal molecule that causes activated neutrophils to form neutrophilic extracellular traps is a membrane lipid phosphatidylserine located on the surface of apoptotic cells. The development of cell apoptosis is associated with the inversion of the membrane lipid — phosphatidylserine — normally located on the inner surface of the cell membrane. Phosphatidylserine is transferred from the inner cell membrane to the outer surface using phospholipid scramblase-1 (PLSCR1) and is an apoptotic signal for neutrophil activation with the opening of neutrophilic extracellular traps [26].

Excessive formation of neutrophilic extracellular traps causes hemocoagulation

The effect of phosphatidylserine on activated neutrophils is a key event in the pathogenesis of microvascular dysfunction. Studies have revealed a previously unrecognized relationship between hypercoagulation and the presence of phosphatidylserine in the blood, which causes a risk of thrombosis [28, 29]. Thrombotic complications are a serious danger in many diseases. Since the discovery of neutrophilic extracellular traps, the view on the pathophysiology of thrombosis has changed significantly. Networks generated by neutrophils, which consist of decondensed chromatin in the form of fibers, contribute to the formation of a blood clot, serving as a framework that activates platelets and coagulation. Thrombogenic vascular damage caused by excessive formation of neutrophilic extracellular traps has been described under various conditions of thrombosis, including stroke, myocardial infarction, and deep vein thrombosis [30]. To overcome thrombogenic vascular damage, it was proposed to use DNase I, which will limit the excessive formation of decondensed chromatin fibers and accelerate their hydrolysis [31]. The mechanisms underlying the development of systemic coagulopathy and acquired thrombophilia, characterized in most cases by a tendency to venous, arterial and microvascular thrombosis in COVID-19 pandemics, are unclear. Doctors and researchers are at the stage of collecting and analyzing information about this dangerous infection [32].

In the pathogenesis of coronavirus infection (COVID-19), there is a clear connection between the development of systemic coagulopathy and the formation of neutrophilic extracellular traps. Moreover, the most clinically severe patients are those who develop virus-induced apoptosis, only in some infected cells. These cells express phosphatidylserine on the surface and induce the neutrophilic extracellular traps formation that traps apoptotic cells and their residues. Another part of infected cells does not enter apoptosis due to functional deficiency of the mitochondrial antiviral sensor. These cells are involved in viral replication and support the spread of the virus throughout the human organism. The spread of the virus throughout the organism increases the number of apoptotic cells and, accordingly, the number of revealing neutrophilic extracellular traps. During the formation of extracellular traps, neutrophils secrete proinflammatory cytokines, enzymes, ROS, and peptides with pore-forming activity. Parts of the secreted products — ROS, peptides with pore-forming activity (such as LL-37), TNF α are designed to damage and destroy microorganisms. But in the absence of a bacterial infection, their own tissues and blood cells are damaged. Endothelial cells of capillaries of the pulmonary circulation become porous, which leads to interstitial pulmonary edema, the development of viral pneumonia, and an increase in the permeability of erythrocyte and platelet membranes causes hemoglobin loss and hemocoagulation. Our concept is supported by studies of patients with COVID-19 pneumonia, in which neutrophilic extracellular traps were found in microvessels of the pulmonary circulation together with damaged endothelial cells and fibrin deposits [33].

Development of immunodeficiency in patients with coronavirus infection

The study of blood cells in patients with severe coronavirus infection (COVID-19) showed that they have a reduced number of lymphocytes and an increased number of leukocytes. The

total number of T-lymphocytes was significantly reduced due to both CD4⁺ and CD8⁺ cells compared with the level of healthy donors [34]. Moreover, the degree of developing immunodeficiency depends on the severity and duration of the disease. Prolonged infectious inflammation causes significant changes in the population and subpopulation of T-lymphocytes, and causes the development of T-cell immunodeficiency. The decrease in the content of T-lymphocytes, as well as a subpopulation of peripheral blood CD4⁺ and CD8⁺ cells, is based on an insufficient expression of lymphocyte activation antigens (CD25, CD71, HLA-DR) and increased expression of activation apoptosis trigger receptor CD95 [35–37]. The action of these factors cause accelerated elimination of T-lymphocytes and cause the development of immunodeficiency. These observations indicate that the treatment strategy for patients should be aimed at reducing the time of inflammation.

Violations of IgG synthesis in patients with coronavirus infection

The formation of immunity in coronavirus infection (COVID-19) is an almost insoluble problem for doctors and researchers. Without a detailed analysis of the results of screening for antibodies in patients after a coronavirus infection, the main features of the deficiency in the formation of immunoglobulins can be identified. This is, first of all, the absence of virus-specific IgG in some patients, a low titer of virus-specific IgG, and in some patients, an extremely weakened immune response, which nevertheless causes the formation of a virus-specific IgG, but in some cases this occurs only after 4–5 or more weeks after admission to the hospital. Thus, it was reported that five of the six examined patients had a high titer of virus neutralizing antibody [38]. Examination of 208 plasma samples 14 days after the onset of the disease revealed the presence of virus-specific IgM and IgG in 85.4% and 77.9% of patients, respectively [39]. Being unable to analyze the obtained data, the authors cite a set of separate observations, from which it follows that virus-specific IgM and IgG antibodies in individual patients were recorded 6, 11, 18, 23, 24, 35, and 43 days after admission to the intensive care unit. As can be seen from the data provided, the late period for the appearance of specific IgG coincides with a higher viral load of patients [40]. The results of the studies showed that coronavirus infection (SARS-CoV-2) is accompanied by obvious violations of the production of specific immunoglobulins and this is the main mechanism of immunopathogenesis. The cause for the observed violations may be related to the excessive formation of neutrophilic extracellular traps during coronavirus infection. The formation of a network of DNA fibers is accompanied by the secretion of a number of compounds, including the secretion of enzymes. The main secreted enzymes are NADPH oxidase, myeloperoxidase, arginase. The physiological significance of NADPH oxidase, myeloperoxidase has been established and consists in the generation of reactive oxygen and nitrogen species that damage and inactivate various pathogens. The role of arginase is to disrupt antigenic presentation by antigen-presenting cells and inhibit T cells with helper induction function (CD4⁺ cells) in the initial period of inflammation. The role of arginase in inhibiting adaptive immunity has been described previously [41]. Investigating the early stages of inflammation, found pronounced reciprocity in relation to the activation of innate and adaptive immunity. The physiological role of arginase secreted by neutrophils is to organize the correct and consistent activation of two parts of the immune system [42, 43]. However, prolonged inflammation is dangerous not only by damage to one's own

tissues, but also by the development of hemocoagulation. As can be seen, there is a pronounced prolonged suppression of adaptive immunity, the result of which is the insufficient formation of virus-specific immunoglobulin in some patients.

A feature of coronavirus infection (COVID-19) is that damaged endothelial cells of the capillaries of the pulmonary circulation also contain arginase. Therefore, with inflammation accompanying a coronavirus infection, arginase enters the blood from two sources — neutrophils and endothelial cells. The suppression of adaptive immunity in this infection is especially pronounced. Overcoming the inhibition of adaptive immunity in patients in order to activate immunogenesis can be achieved, in our opinion, by the use of arginase inhibitors (like valine) in the acute period of the disease.

Asymptomatic coronavirus infection

A number of patients with coronavirus infection have an asymptomatic course. The danger is that asymptomatic virus carriers can infect other people. They can also be re-infected. So, 38 out of 112 COVID-19 positive patients have an asymptomatic course of the disease, while IgM antibodies were detected in 22 patients, 7 patients in this group had IgG antibodies, and 9 patients did not have virus-specific antibodies [44]. A group of 24 asymptomatic carriers of the SARS-CoV-2 virus was described. After hospitalization, in five cases (20.8%) symptoms appeared (fever, cough, fatigue), in twelve cases (50.0%) typical frosted glass images were found on CT scans, and in 5 (20.8%) observed bands of dimming in the lungs. No severe pneumonia was detected. None of the 24 cases revealed severe pneumonia. But in some family members of these asymptomatic carriers, severe coronavirus pneumonia was subsequently detected [45]. A study of the spread of coronavirus infection among recruits of the Swiss Armed Forces in the canton of Ticino (southern canton of Switzerland on the border with Italy) shows that young healthy people often show a moderate course of COVID-19 with a rapid alleviation of symptoms, but they were constant carriers of SARS-CoV-2 [46].

Asymptomatic course of the disease — activation of an alternative way to remove the virus from the organism

The asymptomatic course of COVID-19 disease is associated with activation of autophagy. Autophagy consists in the renewal of many cellular structures and is activated when the cell enters stressful conditions. At the same time, it is also a way to overcome viral infection due to accelerated hydrolysis of cellular proteins and other components with their subsequent synthesis. Autophagy is one of the first lines of cellular defense against the invasion of microorganisms, including viruses [47]. Many viruses have evolved to the point that they use autophagy for their own development. They acquired the ability to either inhibit autophagy in the cell, escaping the cellular hydrolysis of their components or, which is more common, to use autophagosomes for replication and assembly of viral particles. Moreover, some viruses can even cause additional activation of autophagy in an infected cell for their own development. Thus, Picornaviruses use the cell apparatus for reproduction, and then inhibit the fusion of autophagosomes with lysosomes, which leads to an increase in the formation of viral particles [48]. Enterovirus A71 (EV-A71) activates autophagy both *in vitro* and *in vivo*. EV-A71 triggers the formation of autolysosomes during infection in human rhabdomyosarcoma cells, which facilitates its replication [49]. Zika virus (ZIKV), upon infection of human umbilical vein endothelial cells, triggers cell autophagy

Table. The reaction of the antiviral system of innate immunity and the organism's inflammatory response

Cell response to infection with an RNA-containing virus	MAVS reaction	Mononuclear blood cells	Cytokines	Characterization of the inflammatory process
Apoptosis	MAVS induces prion-like polymerization	Activated neutrophils form neutrophilic extracellular traps	Pro-inflammatory	Acute inflammatory process
Cellular degeneration with necrotic changes	MAVS does not induce prion-like polymerization	Activated neutrophils do not form neutrophilic extracellular traps	Anti-inflammatory	No signs of inflammation, asymptomatic course of the disease

and enhances replication using autophagosomes. The use of inhibitors of autophagosome formation significantly reduces the formation of viral particles [50, 51]. Uzutu virus (USUV) is an African mosquito-borne flavivirus that is closely associated with West Nile fever virus and Japanese encephalitis virus, the carriers of which are mainly mosquitoes and birds. The presence of USUV in Africa was discovered more than 50 years ago, but in the last decade it has appeared in Europe, causing episodes of bird mortality and some cases of serious illness among people. USUV infection also stimulates autophagy. Pharmacological modulation of the autophagy pathway using the autophagy inducer Rapamycin led to an increase in the output of the virus. On the other hand, treatment with 3-methyladenine or Wortmannin, two different phosphatidylinositol-3-kinase inhibitors involved in autophagy, reduced the output of viral particles [52].

RIG-I (retinoic acid-inducible gene 1), which detects viral infections by recognition of viral RNA, MAVS and TRAF6 (TNF receptor-associated factor 6), a cytosolic adapter protein belonging to the family of factors related with TNF alpha receptor, takes part in virus-induced autophagy. Deficiency in the cells of any of these proteins disrupts the initiation of autophagy [53]. These and many other studies have shown that viruses circulating among the human population for a long time, use autophagy mechanisms for their own development. SARS-CoV-2 apparently does not yet have such mechanisms. Despite the fact that direct data on the interaction of SARS-CoV-2 with autophagy proteins or autophagosomes have not been obtained, however, the nature of the asymptomatic course of COVID-19 indicates that autophagy in this disease nevertheless fulfills its deterrent role and prevents the spread of the virus in the human organism.

Activation of autophagy causes cellular degeneration of virus infected cells

Short-term activation of autophagy promotes cell survival with insufficient intake of the necessary metabolites. Activation of virus-induced autophagy continues for a long time and leads to cellular degeneration and necrotic cell death [54–57]. Such cells do not exhibit phosphatidylserine on their surface and therefore are not able to cause the neutrophilic extracellular traps formation.

Therefore, secretion of inflammatory cytokines does not occur. Removal of such infected cells develops through phagocytosis by monocytes/macrophages secreting anti-inflammatory cytokines. The asymptomatic course of the disease is due to the reaction of the antiviral system of innate immunity in an alternative way. The results of the study are presented in the table.

The polarization of M0 macrophages into M2 phenotype producing anti-inflammatory cytokines develops with IFN γ deficiency, and in the presence of IFN γ , the differentiation of macrophages in M2 phenotype is weakened [58, 59], which explains the presence of anti-inflammatory cytokines in case of formation of neutrophilic extracellular traps.

The treatment strategy for asymptomatic COVID-19 patients may be directed to the activation of apoptosis in cells infected with the virus. For this, Resveratrol can be used, which is able to induce apoptosis, while inhibiting the anti-apoptotic protein Bcl2, and enhancing the expression of p53 in normal and tumor human cells [60–62].

We call on doctors and researchers to experimentally verify the theoretical basis of our concept and the treatment methods of COVID-19 resulting from our proposed antiviral system of innate immunity.

CONCLUSION

The data presented in this article allow us to describe the components and functioning of the antiviral system of innate immunity in the human organism. We suggest that the antiviral system of innate immunity has two main components: the mitochondrial antiviral sensor — the mitochondrial outer membrane protein and peripheral blood neutrophils capable of forming neutrophilic extracellular traps. Depending on the activation pathway of the mitochondrial antiviral sensor (MAVS), when a cell is infected with an RNA-containing virus (SARS-CoV-2), two possible variants of its death, apoptosis or cellular degeneration with necrotic changes develop. These variants of the predominant cell death determine the type of inflammation and the course of the disease. The development of virus-induced apoptosis of infected cells causes the formation of neutrophilic extracellular traps, the secretion of inflammatory cytokines, ROS generation, tissue damage, hemocoagulation and the development of an acute inflammatory process in the form of COVID-19 pneumonia. Violation of the prion-like reaction of MAVS in response to viral infection of the cell triggers an alternative pathway for the activation of autophagy. Cells under conditions of prolonged activation of autophagy experience necrotic changes and are eliminated from the organism by monocytes/macrophages that secrete anti-inflammatory cytokines. This type of reaction of the antiviral system of innate immunity corresponds to the asymptomatic course of the disease.

The given main stages of the pathogenesis of coronavirus infection make it possible to propose pathogenetically substantiated therapy that can significantly reduce the severity of the disease, activate immunity and reduce mortality.

References

- Cai X, Xu H, Chen ZJ. Prion-Like Polymerization in Immunity and Inflammation. *Cold Spring Harb Perspect Biol.* 2017; 9 (4). pii: a023580. DOI: 10.1101/cshperspect.a023580.
- He X, Zhu Y, Zhang Y, Geng Y, Gong J, Geng J, et al. RNF34 functions in immunity and selective mitophagy by targeting MAVS for autophagic degradation. *EMBO J.* 2019. pii: e100978. DOI: 10.15252/embj.2018100978.
- Cai X, Chen J, Xu H, Liu S, Jiang QX, Halfmann R, et al. Prion-like polymerization underlies signal transduction in antiviral immune defense and inflammasome activation. *Cell.* 2014; 156 (6): 1207–2. DOI: 10.1016/j.cell.2014.01.063.
- Cai X, Xu H, Chen ZJ. Prion-Like Polymerization in Immunity and Inflammation. *Cold Spring Harb Perspect Biol.* 2017; 9 (4). pii: a023580. DOI: 10.1101/cshperspect.a023580.
- Dutta M, Robertson SJ, Okumura A, Scott DP, Chang J, Weiss JM, et al. A Systems Approach Reveals MAVS Signaling in Myeloid Cells as Critical for Resistance to Ebola Virus in Murine Models of Infection. *Cell Rep.* 2017; 18 (3): 816–29. DOI: 10.1016/j.celrep.2016.12.069.
- Hu Y, Dong X, He Z, Wu Y, Zhang S, Lin J, et al. Zika virus antagonizes interferon response in patients and disrupts RIG-I-MAVS interaction through its CARD-TM domains. *Cell Biosci.* 2019; 9: 46. DOI: 10.1186/s13578-019-0308-9. eCollection 2019.
- Hu X, Peng X, Lu C, Zhang X, Gan L, Gao Y, et al. Type I IFN expression is stimulated by cytosolic MtDNA released from pneumolysin-damaged mitochondria via the STING signaling pathway in macrophages. *FEBS J.* 2019. DOI: 10.1111/febs.15001.
- Liu S, Cai X, Wu J, Cong Q, Chen X, Li T, et al. Phosphorylation of innate immune adaptor proteins MAVS, STING, and TRIF induces IRF3 activation. *Science.* 2015; 347 (6227): aaa2630. DOI: 10.1126/science.aaa2630.
- Diner EJ, Burdette DL, Wilson SC, Monroe KM, Kellenberger CA, Hyodo M, et al. The innate immune DNA sensor cGAS produces a noncanonical cyclic dinucleotide that activates human STING. *Cell Rep.* 2013; 3 (5): 1355–61. DOI: 10.1016/j.celrep.2013.05.009.
- Schwede F, Genieser HG, Rentsch A. The Chemistry of the Noncanonical Cyclic Dinucleotide 2'3'-cGAMP and Its Analogs. *Handb Exp Pharmacol.* 2017; 238: 359–84. DOI: 10.1007/164_2015_43.
- Eaglesham JB, Pan Y, Kupper TS, Kranzusch PJ. Viral and metazoan poxins are cGAMP-specific nucleases that restrict cGAS-STING signalling. *Nature.* 2019; 566 (7743): 259–63. DOI: 10.1038/s41586-019-0928-6.
- Oh DS, Kim TH, Lee HK. Differential Role of Anti-Viral Sensing Pathway for the Production of Type I Interferon — in Dendritic Cells and Macrophages Against Respiratory Syncytial Virus A2 Strain Infection. *Viruses.* 2019; 11 (1). pii: E62. DOI: 10.3390/v11010062.
- Goritzka M, Makris S, Kausar F, Durant LR, Pereira C, Kumagai Y, et al. Alveolar macrophage-derived type I interferons orchestrate innate immunity to RSV through recruitment of antiviral monocytes. *J Exp Med.* 2015 May 4; 212 (5): 699–714. DOI: 10.1084/jem.20140825.
- Goritzka M, Pereira C, Makris S, Durant LR, Johansson C. T cell responses are elicited against Respiratory Syncytial Virus in the absence of signalling through TLRs, RLRs and IL-1R/IL-18R. *Sci Rep.* 2015 Dec 21; 5: 18533. DOI: 10.1038/srep18533.
- Sturge CR, Benson A, Raetz M, Wilhelm CL, Mirpuri J, Vitetta ES, et al. TLR-independent neutrophil-derived IFN- γ is important for host resistance to intracellular pathogens. *Proc Natl Acad Sci USA.* 2013; 110 (26): 10711–6. DOI: 10.1073/pnas.1307868110.
- Kirsebom FCM, Kausar F, Nuriev R, Makris S, Johansson C. Neutrophil recruitment and activation are differentially dependent on MyD88/TRIF and MAVS signaling during RSV infection. *Mucosal Immunol.* 2019. DOI: 10.1038/s41385-019-0190-0.
- Gonzalez-Quintal R, Nguyen A, Kono DH1, Oldstone MBA, Theofilopoulos AN, Baccala R. Lupus acceleration by a MAVS-activating RNA virus requires endosomal TLR signaling and host genetic predisposition. *PLoS One.* 2018; 13 (9): e0203118. DOI: 10.1371/journal.pone.0203118. eCollection 2018.
- Lei Y, Moore CB, Liesman RM, O'Connor BP, Bergstralh DT, Chen ZJ, et al. MAVS-mediated apoptosis and its inhibition by viral proteins. *PLoS One.* 2009; 4 (5): e5466. DOI: 10.1371/journal.pone.0005466.
- El Maadidi S, Faletti L, Berg B, Wenzl C, Wieland K, Chen ZJ, et al. A novel mitochondrial MAVS/Caspase-8 platform links RNA virus-induced innate antiviral signaling to Bax/Bak-independent apoptosis. *J Immunol.* 2014; 192 (3): 1171–83. DOI: 10.4049/jimmunol.1300842.
- Dong W, Lv H, Li C, Liu Y, Wang C, Lin J, et al. MAVS induces a host cell defense to inhibit CSFV infection. *Arch Virol.* 2018 Jul; 163 (7): 1805–21. DOI: 10.1007/s00705-018-3804-z.
- Hirai-Yuki A, Whitmire JK, Joyce M, Tyrrell DL, Lemon SM. Murine Models of Hepatitis A Virus Infection. *Cold Spring Harb Perspect Med.* 2019; 9 (1). pii: a031674. DOI: 10.1101/cshperspect.a031674.
- Liu D, Tan Q, Zhu J, Zhang Y, Xue Y, Song Y, et al. MicroRNA-33/33* inhibit the activation of MAVS through AMPK in antiviral innate immunity. *Cell Mol Immunol.* 2019. DOI: 10.1038/s41423-019-0326-x.
- Yang S, Harding AT, Sweeney C, Miao D, Swan G, Zhou C, et al. Control of antiviral innate immune response by protein geranylgeranylation. *Sci Adv.* 2019; 5 (5): eaav7999. DOI: 10.1126/sciadv.aav7999.
- Maugeri N, Rovere-Querini P, Evangelista V, Covino C, Capobianco A, Bertilaccio MT, et al. Neutrophils phagocytose activated platelets in vivo: a phosphatidylserine, P-selectin and β_2 integrin-dependent cell clearance program. *Blood.* 2009; 113: 5254–65. DOI: 10.1182/blood-2008-09-180794.
- Manfredi AA, Covino C, Rovere-Querini P, Maugeri N. Instructive influences of phagocytic clearance of dying cells on neutrophil extracellular trap generation. *Clin Exp Immunol.* 2015; 179 (1): 24–9. DOI: 10.1111/cei.12320.
- Ma R, Xie R, Yu C, Si Y, Wu X, Zhao L, et al. Phosphatidylserine-mediated platelet clearance by endothelium decreases platelet aggregates and procoagulant activity in sepsis. *Sci Rep.* 2017; 7 (1): 4978. DOI: 10.1038/s41598-017-04773-8.
- Manfredi AA, Ramirez GA, Rovere-Querini P, Maugeri N. The Neutrophil's Choice: Phagocytosis vs Make Neutrophil Extracellular Traps. *Front Immunol.* 2018; 9: 288. DOI: 10.3389/fimmu.2018.00288. eCollection 2018.
- Strumwasser A, Bhargava A, Victorino GP. Attenuation of Endothelial Phosphatidylserine Exposure Decreases Ischemia-Reperfusion Induced Changes in Microvascular Permeability. *J Trauma Acute Care Surg.* 2018; 84 (6): 838–46. DOI: 10.1097/TA.0000000000001891.
- Tong D, Yu M, Li G, Li T, Li J, Novakovic VA, et al. Phosphatidylserine-exposing Blood and Endothelial Cells Contribute to the Hypercoagulable State in Essential Thrombocythemia Patients. *Ann Hematol.* 2018; 97 (4): 605–16. DOI: 10.1007/s00277-018-3228-6.
- Laridan E, Martinod K, De Meyer SF. Neutrophil Extracellular Traps in Arterial and Venous Thrombosis. *Semin Thromb Hemost.* 2019; 45 (1): 86–93. DOI: 10.1055/s-0038-1677040.
- Li B, Liu Y, Hu T, Zhang Y, Zhang C, Li T, et al. Neutrophil Extracellular Traps Enhance Procoagulant Activity in Patients With Oral Squamous Cell Carcinoma. *J Cancer Res Clin Oncol.* 2019; 145 (7): 1695–707. DOI: 10.1007/s00432-019-02922-2.
- Becker RC. COVID-19 Update: Covid-19-associated Coagulopathy. *J Thromb Thrombolysis.* 2020; 1–14. DOI: 10.1007/s11239-020-02134-3.
- Barnes BJ, Adrover JM, Baxter-Stoltzfus A, Borczuk A, Cools-Lartigue J, Crawford JM, et al. Targeting Potential Drivers of COVID-19: Neutrophil Extracellular Traps. *J Exp Med.* 2020; 217 (6): e20200652. DOI: 10.1084/jem.20200652.
- Qin C, Zhou L, Hu Z, Zhang S, Yang S, Tao Y, et al. Dysregulation of Immune Response in Patients With COVID-19 in Wuhan, China. *Clin Infect Dis.* 2020; ciaa248. DOI: 10.1093/cid/ciaa248.
- Kazimirskii AN, Poryadin GV, Salmasi JM. The mechanisms of development of immunodeficiency in non-specific inflammation of infectious origin. *Pathological physiology and experimental therapy.* 2003; 3: 23. Russian.

36. Poryadin GV, Salmasi JM, Kazimirskii AN. Activation markers of lymphocytes as indicators of dysregulation of the immune system during inflammation. *Pathological physiology and experimental therapy*. 2006; 1: 2–7. Russian.
37. Salmasi JM, Kazimirskii AN, Poryadin GV. The leading mechanisms of pathogenesis in inflammation of various origins. *Russian Immunological Journal*. 2019; 13-22 (2): 518–20. Russian.
38. Zhang L, Pang R, Xue X, Bao J, Ye S, Dai Y, et al. Anti-SARS-CoV-2 Virus Antibody Levels in Convalescent Plasma of Six Donors Who Have Recovered From COVID-19 Aging (Albany NY). 2020; 12 (8): 6536–42. DOI: 10.18632/aging.103102.
39. Guo L, Ren L, Yang S, Xiao M, Chang D, Yang F, et al. Profiling Early Humoral Response to Diagnose Novel Coronavirus Disease (COVID-19). *Clin Infect Dis*. 2020; ciaa310. DOI: 10.1093/cid/ciaa310.
40. Lee Y-L, Liao C-H, Liu P-Y, Cheng C-Y, Chung M-Y, Liu C-E, et al. Dynamics of anti-SARS-Cov-2 IgM and IgG Antibodies Among COVID-19 Patients. *J Infect*. 2020; S0163-4453(20)30230-9. DOI: 10.1016/j.jinf.2020.04.019.
41. Kazimirskii AN, Poryadin GV, Salmasi JM, Semenova LY. Endogenous regulators of the immune system (sCD100, malonic dialdehyde, and arginase). *Bulletin of Experimental Biology and Medicine*. 2018; 164 (5): 693–700. DOI: 10.1007/s10517-018-4061-6.
42. Kazimirskii AN, Salmasi JM, Poryadin GV. Coordination of Innate and Adaptive Immunity Depending on Neutrophilic Extracellular Traps Formation. *Austin J Clin Immunol*. 2019; 6 (1): 1037.
43. Kazimirskii AN, Salmasi JM, Poryadin GV. Neutrophil extracellular traps regulate the development of innate and adaptive immune system. *Russian Medical Review*. 2020; 4 (1): 38–41. DOI: 10.32364/2587-6821-2020-4-1-38-41. Russian.
44. Imai K, Tabata S, Ikeda M, Noguchi S, Kitagawa Y, Matuoka M, et al. Clinical Evaluation of an Immunochromatographic IgM/IgG Antibody Assay and Chest Computed Tomography for the Diagnosis of COVID-19. *J Clin Virol*. 2020; 128: 104393. DOI: 10.1016/j.jcv.2020.104393.
45. Hu Z, Song C, Xu C, Jin G, Chen Y, Xu X, et al. Clinical Characteristics of 24 Asymptomatic Infections With COVID-19 Screened Among Close Contacts in Nanjing, China. *Sci China Life Sci*. 2020; 63 (5): 706–11. DOI: 10.1007/s11427-020-1661-4.
46. Baettig SJ, Parini A, Cardona I, Morand GB. Case Series of Coronavirus (SARS-CoV-2) in a Military Recruit School: Clinical, Sanitary and Logistical Implications. *BMJ Mil Health*. 2020; DOI: 10.1136/bmjmilitary-2020-001482.
47. Rozières A, Viret C, Faure M. Autophagy in Measles Virus Infection. *Viruses*. 2017; 9 (12): 359. DOI: 10.3390/v9120359.
48. Mohamad Y, Shi J, Qu J, Poon T, Xue YC, Deng H, et al. Enteroviral Infection Inhibits Autophagic Flux via Disruption of the SNARE Complex to Enhance Viral Replication. *Cell Rep*. 2018; 22 (12): 3292–303. DOI: 10.1016/j.celrep.2018.02.090.
49. Lai JKF, Sam I-C, Verlhac P, Baguet J, Eskelinen E-L, Faure M, et al. 2BC Non-Structural Protein of Enterovirus A71 Interacts With SNARE Proteins to Trigger Autolysosome Formation. *Viruses*. 2017; 9 (7): 169. DOI: 10.3390/v9070169.
50. Peng H, Liu B, Yves TD, He Y, Wang S, Tang H, et al. Zika Virus Induces Autophagy in Human Umbilical Vein Endothelial Cells. *Viruses*. 2018; 10 (5): 259. DOI: 10.3390/v10050259.
51. Gratton R, Agrelli A, Tricarico PM, Brandão L, Crovella S. Autophagy in Zika Virus Infection: A Possible Therapeutic Target to Counteract Viral Replication. *Int J Mol Sci*. 2019; 20 (5): 1048. DOI: 10.3390/ijms20051048.
52. Blázquez A-B, Escribano-Romero E, Merino-Ramos T, Saiz J-C, Martín-Acebes MA. Infection With Usutu Virus Induces an Autophagic Response in Mammalian Cells. *PLoS Negl Trop Dis*. 2013; 7 (10): e2509. DOI: 10.1371/journal.pntd.0002509.
53. Lee N-R, Ban J, Lee N-J, Yi C-M, Choi J-Y, Kim H, et al. Activation of RIG-I-Mediated Antiviral Signaling Triggers Autophagy Through the MAVS-TRAF6-Beclin-1 Signaling Axis. *Front Immunol*. 2018 Sep 12; 9: 2096. DOI: 10.3389/fimmu.2018.02096.
54. Silva LM, Jung JU. Modulation of the Autophagy Pathway by Human Tumor Viruses. *Semin Cancer Biol*. 2013; 23 (5): 323–8. DOI: 10.1016/j.semcancer.2013.05.005.
55. Green DR, Llambi F. Cell Death Signaling Cold Spring Harb Perspect Biol. 2015; 7 (12): a006080. DOI: 10.1101/cshperspect.a006080.
56. Nishida K, Tamura A, Yui N. ER Stress-Mediated Autophagic Cell Death Induction Through Methylated β -Cyclodextrins-Threaded Acid-Labile Polyrotaxanes. *J Control Release*. 2018; 275: 20–31. DOI: 10.1016/j.jconrel.2018.02.010.
57. Wang Y, Jiang K, Zhang Q, Meng S, Ding C. Autophagy in Negative-Strand RNA Virus Infection. *Front Microbiol*. 2018; 9: 206. DOI: 10.3389/fmicb.2018.00206.
58. Müller-Quernheim UC, Potthast L, Müller-Quernheim J, Zissel G. Tumor-cell Co-Culture Induced Alternative Activation of Macrophages Is Modulated by Interferons in Vitro. *J Interferon Cytokine Res*. 2012; 32 (4): 169–77. DOI: 10.1089/jir.2011.0020.
59. Tarique AA, Logan J, Thomas E, Holt PG, Sly PD, Fantino E. Phenotypic, Functional, and Plasticity Features of Classical and Alternatively Activated Human Macrophages. *Am J Respir Cell Mol Biol*. 2015; 53 (5): 676–88. DOI: 10.1165/rcmb.2015-00120C.
60. Yang Y, Huang X, Chen S, Ma G, Zhu M, Yan F, Yu J. Resveratrol Induced Apoptosis in Human Gastric Carcinoma SGC-7901 Cells via Activation of Mitochondrial Pathway. *Asia Pac J Clin Oncol*. 2018; 14 (5): e317–e324. DOI: 10.1111/ajco.12841.
61. Wang D, Gao Z, Zhang X. Resveratrol Induces Apoptosis in Murine Prostate Cancer Cells via Hypoxia-Inducible Factor 1- α (HIF-1 α)/Reactive Oxygen Species (ROS)/P53 Signaling. *Med Sci Monit*. 2018; 24: 8970–6. DOI: 10.12659/MSM.913290.
62. Li C, Hu W-L, Lu M-X, Xiao G-F. Resveratrol Induces Apoptosis of Benign Prostatic Hyperplasia Epithelial Cell Line (BPH-1) Through p38 MAPK-FOXO3a Pathway. *BMC Complement Altern Med*. 2019; 19 (1): 233. DOI: 10.1186/s12906-019-2648-8.

Литература

1. Cai X, Xu H, Chen ZJ. Prion-Like Polymerization in Immunity and Inflammation. *Cold Spring Harb Perspect Biol*. 2017; 9 (4). pii: a023580. DOI: 10.1101/cshperspect.a023580.
2. He X, Zhu Y, Zhang Y, Geng Y, Gong J, Geng J, et al. RNF34 functions in immunity and selective mitophagy by targeting MAVS for autophagic degradation. *EMBO J*. 2019. pii: e100978. DOI: 10.15252/embj.2018100978.
3. Cai X, Chen J, Xu H, Liu S, Jiang QX, Halfmann R, et al. Prion-like polymerization underlies signal transduction in antiviral immune defense and inflammasome activation. *Cell*. 2014; 156 (6): 1207–2. DOI: 10.1016/j.cell.2014.01.063.
4. Cai X, Xu H, Chen ZJ. Prion-Like Polymerization in Immunity and Inflammation. *Cold Spring Harb Perspect Biol*. 2017; 9 (4). pii: a023580. DOI: 10.1101/cshperspect.a023580.
5. Dutta M, Robertson SJ, Okumura A, Scott DP, Chang J, Weiss JM, et al. A Systems Approach Reveals MAVS Signaling in Myeloid Cells as Critical for Resistance to Ebola Virus in Murine Models of Infection. *Cell Rep*. 2017; 18 (3): 816–29. DOI: 10.1016/j.celrep.2016.12.069.
6. Hu Y, Dong X, He Z, Wu Y, Zhang S, Lin J, et al. Zika virus antagonizes interferon response in patients and disrupts RIG-I-MAVS interaction through its CARD-TM domains. *Cell Biosci*. 2019; 9: 46. DOI: 10.1186/s13578-019-0308-9. eCollection 2019.
7. Hu X, Peng X, Lu C, Zhang X, Gan L, Gao Y, et al. Type I IFN expression is stimulated by cytosolic MtDNA released from pneumolysin-damaged mitochondria via the STING signaling pathway in macrophages. *FEBS J*. 2019. DOI: 10.1111/febs.15001.
8. Liu S, Cai X, Wu J, Cong Q, Chen X, Li T, et al. Phosphorylation of innate immune adaptor proteins MAVS, STING, and TRIF induces IRF3 activation. *Science*. 2015; 347 (6227): aaa2630. DOI: 10.1126/science.aaa2630.
9. Diner EJ, Burdette DL, Wilson SC, Monroe KM, Kellenberger CA, Hyodo M, et al. The innate immune DNA sensor cGAS produces a noncanonical cyclic dinucleotide that activates human STING. *Cell*

- Rep. 2013; 3 (5): 1355–61. DOI: 10.1016/j.celrep.2013.05.009.
10. Schwede F, Genieser HG, Rentsch A. The Chemistry of the Noncanonical Cyclic Dinucleotide 2'3'-cGAMP and Its Analogs. *Handb Exp Pharmacol.* 2017; 238: 359–84. DOI: 10.1007/164_2015_43.
 11. Eaglesham JB, Pan Y, Kupper TS, Kranzusch PJ. Viral and metazoan poxins are cGAMP-specific nucleases that restrict cGAS-STING signalling. *Nature.* 2019; 566 (7743): 259–63. DOI: 10.1038/s41586-019-0928-6.
 12. Oh DS, Kim TH, Lee HK. Differential Role of Anti-Viral Sensing Pathway for the Production of Type I Interferon — in Dendritic Cells and Macrophages Against Respiratory Syncytial Virus A2 Strain Infection. *Viruses.* 2019; 11 (1). pii: E62. DOI: 10.3390/v11010062.
 13. Goritzka M, Makris S, Kausar F, Durant LR, Pereira C, Kumagai Y, et al. Alveolar macrophage-derived type I interferons orchestrate innate immunity to RSV through recruitment of antiviral monocytes. *J Exp Med.* 2015 May 4; 212 (5): 699–714. DOI: 10.1084/jem.20140825.
 14. Goritzka M, Pereira C, Makris S, Durant LR, Johansson C. T cell responses are elicited against Respiratory Syncytial Virus in the absence of signalling through TLRs, RLRs and IL-1R/IL-18R. *Sci Rep.* 2015 Dec 21; 5: 18533. DOI: 10.1038/srep18533.
 15. Sturge CR, Benson A, Raetz M, Wilhelm CL, Mirpuri J, Vitetta ES, et al. TLR-independent neutrophil-derived IFN- γ is important for host resistance to intracellular pathogens. *Proc Natl Acad Sci USA.* 2013; 110 (26): 10711–6. DOI: 10.1073/pnas.1307868110.
 16. Kirsebom FCM, Kausar F, Nuriev R, Makris S, Johansson C. Neutrophil recruitment and activation are differentially dependent on MyD88/TRIF and MAVS signaling during RSV infection. *Mucosal Immunol.* 2019. DOI: 10.1038/s41385-019-0190-0.
 17. Gonzalez-Quintal R, Nguyen A, Kono DH1, Oldstone MBA, Theofilopoulos AN, Baccala R. Lupus acceleration by a MAVS-activating RNA virus requires endosomal TLR signaling and host genetic predisposition. *PLoS One.* 2018; 13 (9): e0203118. DOI: 10.1371/journal.pone.0203118. eCollection 2018.
 18. Lei Y, Moore CB, Liesman RM, O'Connor BP, Bergstralh DT, Chen ZJ, et al. MAVS-mediated apoptosis and its inhibition by viral proteins. *PLoS One.* 2009; 4 (5): e5466. DOI: 10.1371/journal.pone.0005466.
 19. El Maadidi S, Faletti L, Berg B, Wenzl C, Wieland K, Chen ZJ, et al. A novel mitochondrial MAVS/Caspase-8 platform links RNA virus-induced innate antiviral signaling to Bax/Bak-independent apoptosis. *J Immunol.* 2014; 192 (3): 1171–83. DOI: 10.4049/jimmunol.1300842.
 20. Dong W, Lv H, Li C, Liu Y, Wang C, Lin J, et al. MAVS induces a host cell defense to inhibit CSFV infection. *Arch Virol.* 2018 Jul; 163 (7): 1805–21. DOI: 10.1007/s00705-018-3804-z.
 21. Hirai-Yuki A, Whitmire JK, Joyce M, Tyrrell DL, Lemon SM. Murine Models of Hepatitis A Virus Infection. *Cold Spring Harb Perspect Med.* 2019; 9 (1). pii: a031674. DOI: 10.1101/cshperspect.a031674.
 22. Liu D, Tan Q, Zhu J, Zhang Y, Xue Y, Song Y, et al. MicroRNA-33/33* inhibit the activation of MAVS through AMPK in antiviral innate immunity. *Cell Mol Immunol.* 2019. DOI: 10.1038/s41423-019-0326-x.
 23. Yang S, Harding AT, Sweeney C, Miao D, Swan G, Zhou C, et al. Control of antiviral innate immune response by protein geranylgeranylation. *Sci Adv.* 2019; 5 (5): eaav7999. DOI: 10.1126/sciadv.aav7999.
 24. Maugeri N, Rovere-Querini P, Evangelista V, Covino C, Capobianco A, Bertilaccio MT, et al. Neutrophils phagocytose activated platelets in vivo: a phosphatidylserine, P-selectin and β 2 integrin-dependent cell clearance program. *Blood.* 2009; 113: 5254–65. DOI: 10.1182/blood-2008-09-180794.
 25. Manfredi AA, Covino C, Rovere-Querini P, Maugeri N. Instructive influences of phagocytic clearance of dying cells on neutrophil extracellular trap generation. *Clin Exp Immunol.* 2015; 179 (1): 24–9. DOI: 10.1111/cei.12320.
 26. Ma R, Xie R, Yu C, Si Y, Wu X, Zhao L, et al. Phosphatidylserine-mediated platelet clearance by endothelium decreases platelet aggregates and procoagulant activity in sepsis. *Sci Rep.* 2017; 7 (1): 4978. DOI: 10.1038/s41598-017-04773-8.
 27. Manfredi AA, Ramirez GA, Rovere-Querini P, Maugeri N. The Neutrophil's Choice: Phagocytose vs Make Neutrophil Extracellular Traps. *Front Immunol.* 2018; 9: 288. DOI: 10.3389/fimmu.2018.00288. eCollection 2018.
 28. Strumwasser A, Bhargava A, Victorino GP. Attenuation of Endothelial Phosphatidylserine Exposure Decreases Ischemia-Reperfusion Induced Changes in Microvascular Permeability. *J Trauma Acute Care Surg.* 2018; 84 (6): 838–46. DOI: 10.1097/TA.0000000000001891.
 29. Tong D, Yu M, Li G, Li T, Li J, Novakovic VA, et al. Phosphatidylserine-exposing Blood and Endothelial Cells Contribute to the Hypercoagulable State in Essential Thrombocythemia Patients. *Ann Hematol.* 2018; 97 (4): 605–16. DOI: 10.1007/s00277-018-3228-6.
 30. Laridan E, Martinod K, De Meyer SF. Neutrophil Extracellular Traps in Arterial and Venous Thrombosis. *Semin Thromb Hemost.* 2019; 45 (1): 86–93. DOI: 10.1055/s-0038-1677040.
 31. Li B, Liu Y, Hu T, Zhang Y, Zhang C, Li T, et al. Neutrophil Extracellular Traps Enhance Procoagulant Activity in Patients With Oral Squamous Cell Carcinoma. *J Cancer Res Clin Oncol.* 2019; 145 (7): 1695–707. DOI: 10.1007/s00432-019-02922-2.
 32. Becker RC. COVID-19 Update: Covid-19-associated Coagulopathy. *J Thromb Thrombolysis.* 2020; 1–14. DOI: 10.1007/s11239-020-02134-3.
 33. Barnes BJ, Adrover JM, Baxter-Stoltzfus A, Borczuk A, Cools-Lartigue J, Crawford JM, et al. Targeting Potential Drivers of COVID-19: Neutrophil Extracellular Traps. *J Exp Med.* 2020; 217 (6): e20200652. DOI: 10.1084/jem.20200652.
 34. Qin C, Zhou L, Hu Z, Zhang S, Yang S, Tao Y, et al. Dysregulation of Immune Response in Patients With COVID-19 in Wuhan, China. *Clin Infect Dis.* 2020; ciaa248. DOI: 10.1093/cid/ciaa248.
 35. Казимирский А. Н., Порядин Г. В., Салмаси Ж. М. Механизмы развития иммунодефицита при неспецифическом воспалении инфекционного генеза. *Патологическая физиология и экспериментальная терапия.* 2003; 3: 23.
 36. Порядин Г. В., Салмаси Ж. М., Казимирский А. Н. Активационные маркеры лимфоцитов как показатели дисрегуляции иммунной системы при воспалении. *Патологическая физиология и экспериментальная терапия.* 2006; 1: 2–7.
 37. Салмаси Ж. М., Казимирский А. Н., Порядин Г. В. Ведущие механизмы патогенеза при воспалении различного генеза. *Русский иммунологический журнал.* 2019; 13-22 (2): 518–20.
 38. Zhang L, Pang R, Xue X, Bao J, Ye S, Dai Y, et al. Anti-SARS-CoV-2 Virus Antibody Levels in Convalescent Plasma of Six Donors Who Have Recovered From COVID-19 Aging (Albany NY). 2020; 12 (8): 6536–42. DOI: 10.18632/aging.103102.
 39. Guo L, Ren L, Yang S, Xiao M, Chang D, Yang F, et al. Profiling Early Humoral Response to Diagnose Novel Coronavirus Disease (COVID-19). *Clin Infect Dis.* 2020; ciaa310. DOI: 10.1093/cid/ciaa310.
 40. Lee Y-L, Liao C-H, Liu P-Y, Cheng C-Y, Chung M-Y, Liu C-E, et al. Dynamics of anti-SARS-Cov-2 IgM and IgG Antibodies Among COVID-19 Patients. *J Infect.* 2020; S0163-4453(20)30230-9. DOI: 10.1016/j.jinf.2020.04.019.
 41. Казимирский А. Н., Порядин Г. В., Салмаси Ж. М., Семенова Л. Ю. Эндогенные регуляторы иммунной системы (sCD100, малоновый диальдегид, аргиназа). *Бюллетень экспериментальной биологии и медицины.* 2017; 164 (11): 652–60.
 42. Kazimirskii AN, Salmasi JM, Poryadin GV. Coordination of Innate and Adaptive Immunity Depending on Neutrophilic Extracellular Traps Formation. *Austin J Clin Immunol.* 2019; 6 (1): 1037.
 43. Казимирский А. Н., Салмаси Ж. М., Порядин Г. В. Нейтрофильные экстраклеточные ловушки — регуляторы формирования врожденного и адаптивного иммунитета. *РМЖ. Медицинское обозрение.* 2020; 1: 38–41. DOI: 10.32364/2587-6821-2020-4-1-38-41.
 44. Imai K, Tabata S, Ikeda M, Noguchi S, Kitagawa Y, Matuoka M, et al. Clinical Evaluation of an Immunochromatographic IgM/IgG Antibody Assay and Chest Computed Tomography for the Diagnosis of COVID-19. *J Clin Virol.* 2020; 128: 104393. DOI: 10.1016/j.jcv.2020.104393.

45. Hu Z, Song C, Xu C, Jin G, Chen Y, Xu X, et al. Clinical Characteristics of 24 Asymptomatic Infections With COVID-19 Screened Among Close Contacts in Nanjing, China. *Sci China Life Sci.* 2020; 63 (5): 706–11. DOI: 10.1007/s11427-020-1661-4.
46. Baettig SJ, Parini A, Cardona I, Morand GB. Case Series of Coronavirus (SARS-CoV-2) in a Military Recruit School: Clinical, Sanitary and Logistical Implications. *BMJ Mil Health.* 2020; DOI: 10.1136/bmjmilitary-2020-001482.
47. Rozières A, Viret C, Faure M. Autophagy in Measles Virus Infection. *Viruses.* 2017; 9 (12): 359. DOI: 10.3390/v9120359.
48. Mohamud Y, Shi J, Qu J, Poon T, Xue YC, Deng H, et al. Enteroviral Infection Inhibits Autophagic Flux via Disruption of the SNARE Complex to Enhance Viral Replication. *Cell Rep.* 2018; 22 (12): 3292–303. DOI: 10.1016/j.celrep.2018.02.090.
49. Lai JKF, Sam I-C, Verlhac P, Baguet J, Eskelinen E-L, Faure M, et al. 2BC Non-Structural Protein of Enterovirus A71 Interacts With SNARE Proteins to Trigger Autolysosome Formation. *Viruses.* 2017; 9 (7): 169. DOI: 10.3390/v9070169.
50. Peng H, Liu B, Yves TD, He Y, Wang S, Tang H, et al. Zika Virus Induces Autophagy in Human Umbilical Vein Endothelial Cells. *Viruses.* 2018; 10 (5): 259. DOI: 10.3390/v10050259.
51. Gratton R, Agrelli A, Tricarico PM, Brandão L, Crovella S. Autophagy in Zika Virus Infection: A Possible Therapeutic Target to Counteract Viral Replication. *Int J Mol Sci.* 2019; 20 (5): 1048. DOI: 10.3390/ijms20051048.
52. Blázquez A-B, Escribano-Romero E, Merino-Ramos T, Saiz J-C, Martín-Acebes MA. Infection With Usutu Virus Induces an Autophagic Response in Mammalian Cells. *PLoS Negl Trop Dis.* 2013; 7 (10): e2509. DOI: 10.1371/journal.pntd.0002509.
53. Lee N-R, Ban J, Lee N-J, Yi C-M, Choi J-Y, Kim H, et al. Activation of RIG-I-Mediated Antiviral Signaling Triggers Autophagy Through the MAVS-TRAF6-Beclin-1 Signaling Axis. *Front Immunol.* 2018 Sep 12; 9: 2096. DOI: 10.3389/fimmu.2018.02096.
54. Silva LM, Jung JU. Modulation of the Autophagy Pathway by Human Tumor Viruses. *Semin Cancer Biol.* 2013; 23 (5): 323–8. DOI: 10.1016/j.semcancer.2013.05.005.
55. Green DR, Llambi F. Cell Death Signaling. *Cold Spring Harb Perspect Biol.* 2015; 7 (12): a006080. DOI: 10.1101/cshperspect.a006080.
56. Nishida K, Tamura A, Yui N. ER Stress-Mediated Autophagic Cell Death Induction Through Methylated β -Cyclodextrins-Threaded Acid-Labile Polyrotaxanes. *J Control Release.* 2018; 275: 20–31. DOI: 10.1016/j.jconrel.2018.02.010.
57. Wang Y, Jiang K, Zhang Q, Meng S, Ding C. Autophagy in Negative-Strand RNA Virus Infection. *Front Microbiol.* 2018; 9: 206. DOI: 10.3389/fmicb.2018.00206.
58. Müller-Quernheim UC, Potthast L, Müller-Quernheim J, Zissel G. Tumor-cell Co-Culture Induced Alternative Activation of Macrophages Is Modulated by Interferons in Vitro. *J Interferon Cytokine Res.* 2012; 32 (4): 169–77. DOI: 10.1089/jir.2011.0020.
59. Tarique AA, Logan J, Thomas E, Holt PG, Sly PD, Fantino E. Phenotypic, Functional, and Plasticity Features of Classical and Alternatively Activated Human Macrophages. *Am J Respir Cell Mol Biol.* 2015; 53 (5): 676–88. DOI: 10.1165/rcmb.2015-0012OC.
60. Yang Y, Huang X, Chen S, Ma G, Zhu M, Yan F, Yu J. Resveratrol Induced Apoptosis in Human Gastric Carcinoma SGC-7901 Cells via Activation of Mitochondrial Pathway. *Asia Pac J Clin Oncol.* 2018; 14 (5): e317–e324. DOI: 10.1111/ajco.12841.
61. Wang D, Gao Z, Zhang X. Resveratrol Induces Apoptosis in Murine Prostate Cancer Cells via Hypoxia-Inducible Factor 1- α (HIF-1 α)/Reactive Oxygen Species (ROS)/P53 Signaling. *Med Sci Monit.* 2018; 24: 8970–6. DOI: 10.12659/MSM.913290.
62. Li C, Hu W-L, Lu M-X, Xiao G-F. Resveratrol Induces Apoptosis of Benign Prostatic Hyperplasia Epithelial Cell Line (BPH-1) Through p38 MAPK-FOXO3a Pathway. *BMC Complement Altern Med.* 2019; 19 (1): 233. DOI: 10.1186/s12906-019-2648-8.

NEW ANTI-MESOTHELIN SINGLE-DOMAIN ANTIBODIES AND CELL MODELS FOR DEVELOPING TARGETED BREAST CANCER THERAPY

Kravchenko YuE, Chumakov SP [✉], Frolova EI

Shemyakin-Ovchinnikov Institute of Bioorganic Chemistry of the Russian Academy of Sciences, Moscow, Russia

Most triple negative breast cancers (TNBC) are characterized by elevated expression of mesothelin (MSLN), a cell surface antigen and one of the preferred targets for the therapy of solid tumors. Most continuous TNBC cell lines are MSLN-negative, which obstructs the development of MSLN-targeted therapy for TNBC. The aim of this study was to identify TNBC cell lines with MSLN hyperexpression and to obtain single-domain antibodies (nanobodies) capable of recognizing MSLN in TNBC cells. Mesothelin expression levels were measured in the panel of TNBC cell lines by real-time reverse-transcription PCR. PCR results were verified by measuring concentrations of the megakaryocyte potentiating factor (the secreted fragment of the mesothelin precursor) using sandwich ELISA. Immune phage-display VHH fragment libraries were prepared from mononuclear cells of *Vicugna pacos* using a modified library enrichment protocol. Two nanobody variants with high specificity for the target and K_d of about 140 and 95 nM, respectively were obtained. Two MSLN⁺ and three MSLN⁻ cell lines were identified in the TNBC cell lines panel. The nanobodies demonstrated the ability to recognize the target antigen in MSLN⁺ cells and had the low ability to bind to MSLN⁻ cells. Thus, we found a convenient MSLN⁺ TNBC cell model for MSLN-targeted therapy testing. The new single-domain antibodies can be used as targeting components of chimeric antigen receptors.

Keywords: nanobody, chimeric antigen receptor, mesothelin, triple-negative breast cancer

Funding: the study was supported by the Russian Ministry of Education and Science (Project ID RFMEFI60418X0205).

Author contribution: Kravchenko JE — cell culture, real-time PCR and ELISA; Chumakov SP — preparation of immune libraries, protein purification, flow cytometry, manuscript preparation; Frolova EI — study design, immunization and blood collection, primary cultures, manuscript preparation.

Compliance with ethical standards: the study was conducted in compliance with the guidelines of the Association for Assessment and Accreditation of Laboratory Animal Care International and the Directive 86/609/EEC dated November 24, 1986.

✉ **Correspondence should be addressed:** Stepan P. Chumakov
Miklouho-Maclaya, 16/10, Moscow, 117997; hathkul@gmail.com

Received: 28.09.2020 **Accepted:** 20.10.2020 **Published online:** 30.10.2020

DOI: 10.24075/brsmu.2020.068

НОВЫЕ ОДНОДОМЕННЫЕ АНТИТЕЛА К МЕЗОТЕЛИНУ И КЛЕТОЧНЫЕ МОДЕЛИ ДЛЯ РАЗРАБОТКИ ТАРГЕТНОЙ ТЕРАПИИ РАКА МОЛОЧНОЙ ЖЕЛЕЗЫ

Ю. Е. Кравченко, С. П. Чумаков [✉], Е. И. Фролова

Институт биоорганической химии имени М. М. Шемякина и Ю. А. Овчинникова, Москва, Россия

Среди случаев трижды негативного рака молочной железы (ТНПМЖ) преобладают новообразования с повышенной экспрессией поверхностного антигена мезотелина (MSLN) — одной из предпочтительных мишеней для направленной терапии многих видов солидных опухолей. Разработка MSLN-опосредованной терапии ТНПМЖ осложнена тем, что большая часть перевиваемых клеточных культур этого субтипа MSLN-негативны. Целью работы было найти гиперэкспрессирующие MSLN модельные клеточные культуры ТНПМЖ и получить новые однодоменные антитела (наноантитела), распознающие MSLN на клетках ТНПМЖ. Уровни транскрипта мезотелина были определены на панели клеточных линий ТНПМЖ при помощи ОТ-ПЦР-РВ, результаты верифицированы непрямым иммуно-ферментным анализом на мегакариоцит-потенцирующий фактор, секретируемую часть белка-предшественника мезотелина. Для получения наноантител адаптировали метод предварительного обогащения иммунных библиотек фрагментов VHH-антител из мононуклеаров *Vicugna pacos* с селекцией при помощи фагового дисплея. В результате исследования получены два варианта наноантител, обладающих высокой специфичностью взаимодействия с мишенью и K_d около 140 и 95 нмоль. Были идентифицированы две линии клеток MSLN⁺ и три линии MSLN⁻ ТНПМЖ. Наноантитела оказались способны распознавать целевой антиген на MSLN⁺ клетках и обладали низким уровнем связывания с MSLN⁻-клеточными культурами. Установлена удобная клеточная модель MSLN⁺ ТНПМЖ для тестирования MSLN-опосредованной терапии; новые однодоменные антитела могут быть использованы в качестве нацеливающих частей химерных антигенных рецепторов.

Ключевые слова: наноантитела, химерный антигенный рецептор, мезотелин, трижды негативный рак молочной железы

Финансирование: работа выполнена при финансовой поддержке Министерства образования и науки РФ (уникальный код проекта RFMEFI60418X0205).

Вклад авторов: Ю. Е. Кравченко — работа с клеточными культурами, ПЦР-РВ, ИФА; С. П. Чумаков — получение иммунных библиотек, проведение селекции, очистка белковых препаратов, цитометрия, написание рукописи; Е. И. Фролова — планирование исследования, проведение манипуляций с животными, работа с первичными культурами, редактирование рукописи.

Соблюдение этических стандартов: работу с животными проводили в соответствии с принципами и требованиями Международной лаборатории по уходу за животными и Директивой совета европейских сообществ (86/609/EEC) от 24 ноября 1986 г.

✉ **Для корреспонденции:** Степан Петрович Чумаков
ул. Миклухо-Маклая, 16/10, г. Москва, 117997; hathkul@gmail.com

Статья получена: 28.09.2020 **Статья принята к печати:** 20.10.2020 **Опубликована онлайн:** 30.10.2020

DOI: 10.24075/vrgmu.2020.068

Mesothelin (MSLN) is a small cell-surface protein anchored to the cell membrane via its C-terminal glycosylphosphatidylinositol (the GPI-anchor) [1]. In humans, mesothelin expression is limited to the cells that line the pericardium, peritoneum and pleura. However, mesothelin is also abundantly expressed in many tumors, including 100% of mesotheliomas, up to 70% of

ovarian cancers, 60% of triple negative breast cancers, 50% of lung cancers, pancreatic and biliary cancers, and gastric cancer [2, 3]. The role of mesothelin in the initiation and progression of malignancies is not fully understood. Since mesothelin is a receptor for another cancer antigen, MUC16, it might promote the metastatic expansion of MUC16-expressing cells typically

seen in ovarian tumors [4]. Mesothelin can inhibit the TNF α -induced apoptosis of tumor cells [5], stimulate proliferation and invasion of malignant cells [6] and promote resistance to chemotherapy [7]. The evident prooncogenic effect of this protein, its elevated expression in the most aggressive subpopulations of cancer cells and limited expression in normal tissue make mesothelin an attractive target for cancer therapies that rely on monoclonal antibodies and immunocompetent cells expressing chimeric antigen receptors (CARs). Currently, a few types of immunotoxins and MSLN-CAR-T cells are being tested as candidate therapeutics against mesotheliomas, pancreatic, biliary, gastric and ovarian cancers [3].

Mesothelin can function as a biomarker for many TNBC [8]. TNBC is defined as a breast cancer negative for the estrogen (ER) and progesterone (PR) receptors and lacking HER2/neu (ERBB2) expression. TNBC is a very aggressive malignancy with a poor prognosis: there are no effective therapeutic regimens for this type of cancer. There were attempts to identify different gene expression patterns within this cancer subtype; for example, the claudin-low phenotype was identified a while ago [9]. This, however, did not result in the advent of a novel specific therapy for TNBC. Mesothelin is overexpressed in more than half of TNBC cases and in no more than 4% of ER⁺, PR⁺ and ERBB⁺ breast cancers; therefore, it could be considered a fairly selective TNBC marker and a promising therapeutic target [10].

In MSLN-targeted CAR-based therapy, the antigen-recognition domain of CAR is assembled from single-chain variable fragments (scFv) derived from anti-MSLN monoclonal antibodies [11]. This is a fast yet not perfect method for obtaining CAR prototypes and testing their efficacy. ScFv derived from traditional antibodies can have inferior physical and chemical properties due to the altered secondary structure and are characterized by reduced affinity and reduced specificity for the target protein [12]. Besides, it is argued that monoclonal antibodies for immunotherapy and immunodiagnostics should preferably be high-affinity (in the nanomolar range), whereas the most important factor for CAR engineering is antibody binding specificity (the optimal antibody affinity for the target can be much lower) [13]. This necessitates a search for new antibodies for CAR constructs.

Since antibodies for CAR therapy are designed as scFv, alternative immunoglobulin structures like single-domain antibodies (sdAb) of Camelidae have some advantages as candidates for CAR design [14]. These camelid antibodies consisting of variable heavy homodimers (VHH) arose from a point mutation in the hinge region of the heavy chain; in the course of evolution, they “learned” to effectively recognize antigens in the absence of light chain variable fragments [15]. Owing to the extended CDR3 length and the presence of an additional disulfide bond, VHH antibodies are capable of binding to their targets with the same specificity and affinity as traditional antibodies, but they are advantageously smaller in size and have good solubility. Their antigen-recognition sites are located on their single peptide chain, so they can be easily employed as scFv (VHH fragments or nanobodies) to create new CARs [16]. Today, there are two variants of anti-mesothelin nanobodies, but their application is still limited to immunodiagnostics [17, 18].

Once the antigen-recognition domain of an anti-MSLN CAR has been designed, the CAR construct needs to be tested using an adequate *ex vivo* model. According to the literature, the most commonly exploited model TNBC cell lines are MSLN⁻. The aim of this study was to identify the cell line with high MSLN expression in the panel of commercial TNBC cell lines, select VHH fragments against MSLN using phage display

and find a few sequence variants that could be used to create an anti-MSLN CAR.

METHODS

Cell culture

The cell lines used in this study, including HEK-293T (transformed human cells), MDA-MB-231, MDA-MB-468, MDA-MB-436, MDA-MB-157, MDA-MB-453, HCC1937, HCC1143, HCC38, HCC70, HCC1806, HCC1187, HCC1395, BT-549, BT-20, and Hs 578T (TNBC), were ordered from the American Type Culture Collection (ATCC; USA). The cells were grown in DMEM-F12 (PAA; Austria) supplemented with 10% fetal bovine serum (Gibco; USA), 2 mM alanylglutamine (PanEco; Russia), 20 mM HEPES, 100 μ g/ml penicillin and 100 μ g/ml streptomycin (PanEco; Russia).

RNA isolation and reverse transcription PCR

RNA was isolated using an RNeasy Mini kit and spin columns (Qiagen; USA) following the manufacturer's protocol or, alternatively, extracted in preparative amounts using an ExtractRNA reagent (Evrogen; Russia) following the manufacturer's protocol. The reverse cDNA sequence was generated from the purified RNA template using a ProtoScript II First Strand cDNA Synthesis Kit (NEB; USA). The purified RNA (500 ng per reaction) was mixed with other kit components, including the d(T)₂₃ primer, following the manufacturer's protocol. cDNA of VHH fragments was synthesized using a specific primer CH2-IgG-sp rev (GGTACGTGCTGTTGAACTGTTCC). The RNA/primer mix was incubated at 42 °C for one hour and then at 80 °C for 5 min. The amount of cDNA per each quantitative PCR (qPCR) reaction was no more than 50 ng.

Real-time PCR

For qPCR, we used HS-Taq polymerase (Evrogen; Russia) and a set of specific primers, including MSLN-qPCR dir (GCACTCCTCTTTCTGCCTGG), MSLN-qPCR rev (GCCATGGTCTGTGTAGATCCC) and MSLN-probe (5'-FAM-CCCACGGTGCCTCCCTCCCT-BHQ1-3') by DNA-synthesis, Russia. Primer and probe selection was aided by the Primer-BLAST tool (NIH NCBI; USA). Prediction of secondary structures was carried out using the OligoAnalyzer Tool (IDT; USA). All experiments were run in 6 replicates. The amount of the accumulated PCR product was compared between the samples based on the Ct values. *GAPDH* was used as an internal control for real-time PCR; the expression of target genes was normalized to *GAPDH* expression (Δ Ct). The Δ Ct value in the cDNA sample isolated from the MDA-MB-231 cell line was used as a calibration standard. Thus, changes in gene expression in the studied samples were calculated by the formula: $2^{-\Delta(\Delta C_{t\text{sample}} - \Delta C_{t\text{calib}})}$ [19]. PCR was performed in the MyiQ Single-Color Real-Time PCR Detection System (Bio-rad; USA).

MSLN producer and recombinant protein

cDNA prepared from the HCC1806 cell line was amplified in the presence of 2 primers for the membrane-anchored mesothelin domain sequence: MSLN full dir (GAAGTGGAGAAGACAGCCTGTCCTTCAGGC) and MSLN full rev (GCTGAGGTCTAGGACCGTAGCCGTTG) by DNA-synthesis, Russia. The initial denaturation step was performed at 95 °C for 120 s, followed by 30 cycles of 95 °C for 30 s, 66 °C

for 30 s and 72 °C for 60 s in the presence of Tersus polymerase (Evrogen; Russia). Then the reaction mix was loaded on 1% agarose gel and stained with the intercalating Sybr Gold dye (Thermo; USA); the target band (~890 bp) was identified using the Cleanup mini kit (Evrogen; Russia). The obtained DNA was subjected to PCR amplification in the presence of 2 primers: MSLN Xba dir (AGAGAGTCTAGAGAAGTGGAGAAGACAG CCTGTCTTCAGGC) and MSLN BglII rev (AGAGAGAGATC TGCTGAGGTCTAGGACCAGGTAGCCGTTG), following the protocol of 18 cycles described above. The PCR product was again purified using the Cleanup mini kit and cloned at the XbaI — BglII/BamHI restriction sites (enzymes by NEB; USA) of a pLCMV-HT-puro lentiviral expression vector (ligase T4, Evrogen; Russia). Plasmid pLCMV-MSLN-HT-puro DNA was purified using a Plasmid miniprep kit (Evrogen; Russia). To prepare the lentiviral vector, 106 HEK-293T cells were plated onto a 10 cm culture dish. Next day, the LCMV-MSLN-HT-puro plasmid was mixed with the psPAX2 and pMD2.G packaging plasmids (both were a gift from Didier Trono (Addgene plasmid # 12260; <http://n2t.net/addgene:12260>; RRID:Addgene_12260 and Addgene plasmid # 12259; <http://n2t.net/addgene:12259>; RRID:Addgene_12259) at the weight ratio of 5 : 3 : 2 (the total amount was 20 µg). Transfection was performed in the Opti-MEM medium (Gibco; USA) following the protocol adapted from [20]. Next day, the Opti-MEM medium was replaced with fresh serum-free DMEM-F12 supplemented with a Serum replacement solution, a Lipid mixture (both by Peprotech; USA) and 4 mM caffeine (Sigma Aldrich; USA). Forty-eight hours later, the medium enriched in the lentivirus was harvested, filtered, supplemented with 10 µg/ml polybrene (Sigma Aldrich; USA) and combined with intact HEK-293T cells (5×10^5) plated onto a 10 cm culture dish. After 24 h of incubation, the medium was replaced with a regular culture medium. Seventy-two hours after inoculation, the medium was supplemented with 1 µg/ml puromycin (Sigma Aldrich; USA), and the culture was left to incubate for 10 days. To obtain recombinant mesothelin, the cells were seeded onto six 15-cm culture dishes (2.5×10^7 cells per dish) containing DMEM-F12 supplemented with the Serum replacement solution and the Lipid mixture. Protein-containing liquid culture medium was harvested every 4 days for 16 days. The obtained recombinant mesothelin was purified on HIS Mag Sepharose Excel magnetic beads (Cytiva; USA) according to the manufacturer's protocol. Pooled mesothelin samples were run through PD-10 columns (Cytiva; USA) to transfer mesothelin to a phosphate buffer. Mesothelin concentrations were determined by measuring OD280 with a Nanodrop OneC spectrophotometer (Thermo; USA). For quality control, the protein was run in a polyacrylamide gel and stained with Coomassie Blue G-250 following the standard protocol.

Animal immunization and collection of biological samples

Biological specimens (venous blood samples) were collected from an alpaca (*Vicugna pacos*), the member of the Camelidae family. For primary immunization, 400 µg/500 µl mesothelin was mixed with an equal volume of complete Freund's adjuvant (Pierce; USA) until complete homogenization. For boosting, 250 µg/500 µl mesothelin was combined with an equal volume of incomplete Freund's adjuvant. A total of 3 booster doses were administered at 2-week intervals. The antigen was injected subcutaneously and intramuscularly into the thigh of the animal. Prior to each immunization, a venous blood sample (10 ml) was collected to measure serum concentration of anti-mesothelin antibodies. B cells were separated from peripheral blood mononuclear cells (PBMC) 5 days after the last booster

injection. PBMC were isolated from a fresh blood sample (100 ml) by density gradient centrifugation with Ficoll (1,077 g/ml) (PanEco; Russia) following the standard protocol.

Primary selection of B cells

Recombinant mesothelin was biotinylated with NHS-LC-biotin (Covachem; USA) following the standard protocol and then used for magnetic separation of B cells with an EasySep Biotin Positive Selection Kit II (Stemcell Technologies; Canada) according to the manufacturer's protocol. RNA was isolated from the separated cell fraction using the Satellite red co-precipitator (Evrogen; Russia).

Assembly of immune VHH library

The VHH library was prepared from cDNA synthesized in 8 independent reactions from a total of 4 µg mRNA. Target VHH sequences were amplified in the presence of high-fidelity Tersus polymerase (Evrogen; Russia) and the following primers: AlpVHH3 uni fwd (CCACCATGTCTAGASAGKTGCAGSTSGTR GAGTCTGKGGGAGG), AlpVHH-R1 (AATCCGGATCCGGGGG GTCTTCGCTGTGGTGCG) and AlpVHH-R2 (AATCCGGATCC GGTTGTGGTTTTGGTGTCTTGGG); the 2 later primers were based on the sequences published in [21]. The amplification protocol consisted of a denaturation step at 95 °C for 120 s, followed by 30 cycles of 95 °C for 30 s, 61 °C for 30 s and 72 °C for 30 s. The phagemid library was prepared by cloning the amplified VHH sequences into a pHEN2-XB phagemid using the XbaI and BamHI-HF endonucleases and the T4 Electroligase (NEB; USA). TG-1 cells were transformed with the phagemid library by electroporation using a GenePulser system (Bio-Rad; USA). Phage selection was performed following a previously published protocol [22] using the antigen immobilized on immuno tubes.

Expression and purification of candidate biotinylated antibodies

Sequences of VHH fragments from the selected individual phagemid clones were cloned into the pET-BAD expression vector at the XbaI and BamHI sites. The resultant constructs were used to transform biotin ligase-expressing BL21DE3-BirA cells. The water-soluble nanobodies were obtained from individual cell colonies grown in the liquid medium supplemented with 0.2 mM D-biotin (Covachem; USA). The culture protocol was previously described in [23]. The water-soluble nanobodies were isolated from the periplasm by lysing the bacterial cell sediment in the buffer composed of 50 mM Tris-HCl (pH 7.4), 150 mM NaCl, 0.1% Triton X-100 and 10 mg/ml lysozyme and PMSF, followed by triple sonication with a Soniprep-100 ultrasonic disintegrator (Soniprep; USA), subsequent purification on HIS Mag Sepharose Excel magnetic beads (Cytiva; USA) and transfer to a phosphate buffer.

ELISA

Megakaryocyte potentiating factor (MPF) concentrations in the liquid culture media were measured using a Human Mesothelin Propeptide/MPF DuoSet ELISA (RND Systems; USA) according to the manufacturer's protocol. To quantify anti-mesothelin serum antibodies, the collected serum samples were added to the wells of a well-plate coated with 5 µg/ml mesothelin and then treated with polyclonal sheep anti-alpaca antibodies; detection was carried out using HRP-conjugated donkey anti-

sheep antibodies (Santa Cruz; USA). Library enrichment was evaluated following a previously published protocol [22]. The wells of the well-plate were coated with 5 µg/ml mesothelin; detection was aided by HRP-conjugated anti-M13 antibodies (Sino Biological; China). For direct ELISA, the wells of the well-plate were coated with mesothelin and treated with 1 µg/ml nanobodies. Antigen detection was carried out using anti-c-myc biotinylated antibodies (SciStoreLab; Russia) and HRP-conjugated streptavidin (R&D Systems; USA) or, for biotinylated nanobodies, using HRP-conjugated streptavidin only. For sandwich ELISA, 5 µg/ml MesoVHH-1E3 was used as a capture antibody for antigen immobilization, 1 mg/ml MesoVHH-2H5B was used as a detection antibody, and HRP-conjugated streptavidin was added for additional probing. A ready-to-use tetramethylbenzidine solution (Sigma Aldrich; USA) was employed as a substrate for HRP conjugates. Colorimetric measurements were done with a Triad microplate reader (Dynex; USA).

Biolayer interferometry

Dissociation constants (Kd) for purified MesoVHH-1E3B and MesoVHH-2H5B nanobodies were determined using Streptavidin (SA) biosensors and a BLtz system (ForteBio; USA).

Nanobody cell staining and flow cytometry

Adherent cells were detached from the surface using TrypLE (Thermo; USA) and then fixed in 3.7% paraformaldehyde solution. Cells suspended in the phosphate buffer were incubated with 5 µg/ml nanobodies for one hour (except for control samples) and then washed with Streptavidin-FITC (MyBioSource; USA) for 40 min. After that, the unreacted reagent was removed and fluorescence was measured by means of a FACS Vantage SE flow cytometer (Beckton Dickinson; USA). The

data generated by flow cytometry were processed in Flowing Software (Perttu Terho; Finland).

Statistical analysis

Statistical analysis was done in Prism 8 software (GraphPad Software; USA).

RESULTS

To obtain nanobodies against mesothelin, a *Vicugna pacos* animal was challenged with recombinant mesothelin containing highly immunogenic full-sized regions II and III. The immune response was closely monitored at all time points after initial immunization and administration of booster doses. Production of anti-mesothelin serum antibodies slowed between the 2nd and 3rd booster injections (Fig. 1A), so blood samples for library preparation were collected on day 5 after the 3rd booster injection. The mononuclear cell fraction was divided into 2 equal parts, which were subsequently used to prepare 2 immune phage-display libraries. The first library was prepared from the total RNA isolated from mononuclear cells; the second library was prepared from the total RNA isolated from the cells that had undergone positive selection on magnetic beads coated with biotinylated mesothelin. This was necessary to clear the cell population of the B cells that secreted irrelevant antibodies. Both phage-display libraries were subjected to 3 rounds of selection on the immobilized antigen, with enrichment control between the rounds. The second library was characterized by higher abundance of MSLN-reactive clones and better enrichment with target sequences after as early as one round of selection (Fig. 1B). After positive selection, 48 clones were randomly chosen from each library and tested for response to mesothelin using ELISA; the clones characterized by the maximum level of signal intensity (Fig. 1C) were sequenced.

Sequencing revealed that all selected clones contained 2 types of VHH fragments, which we called MesoVHH-1E3 and MesoVHH-2H5.

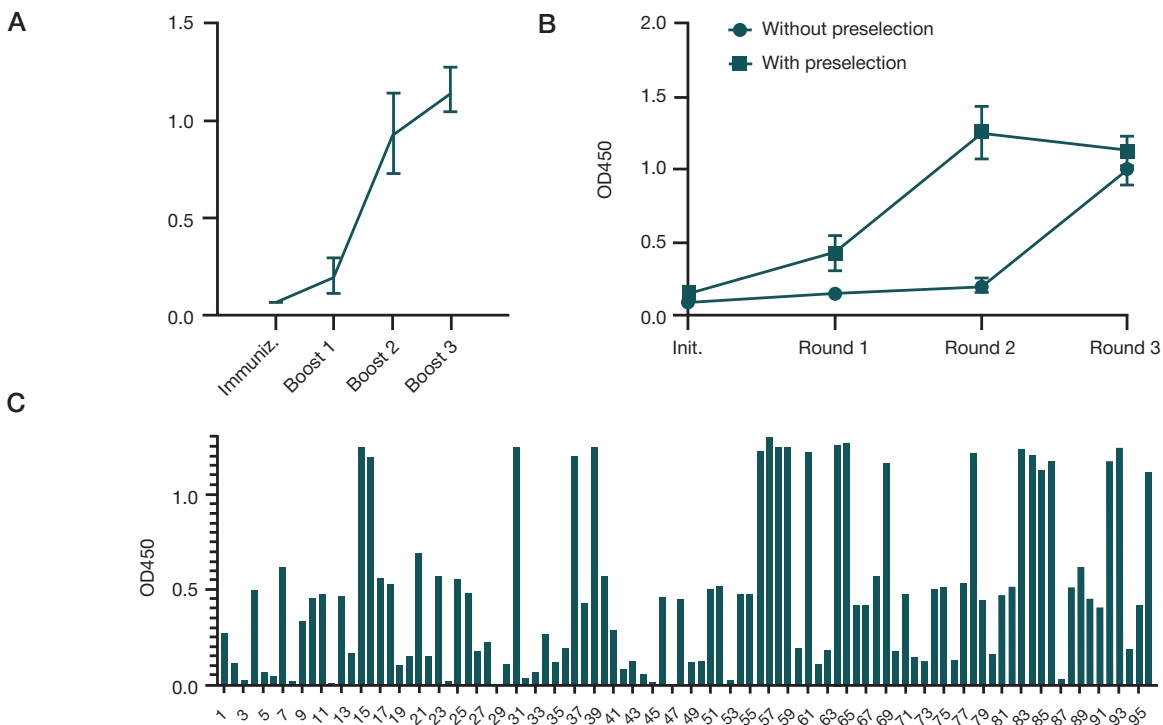


Fig. 1. Selection of nanobodies. **A.** Levels of anti-mesothelin serum antibodies in the blood of the immunized animal at the time of immunization and each booster injection. **B.** The dynamics of phage libraries enrichment with mesothelin-specific nanobodies after each round of selection. **C.** Results of screening of 96 randomly selected clones (direct ELISA for mesothelin). 1–48 — clones from the library that was not subjected to preselection; 49–96 — clones from the library that underwent preselection.

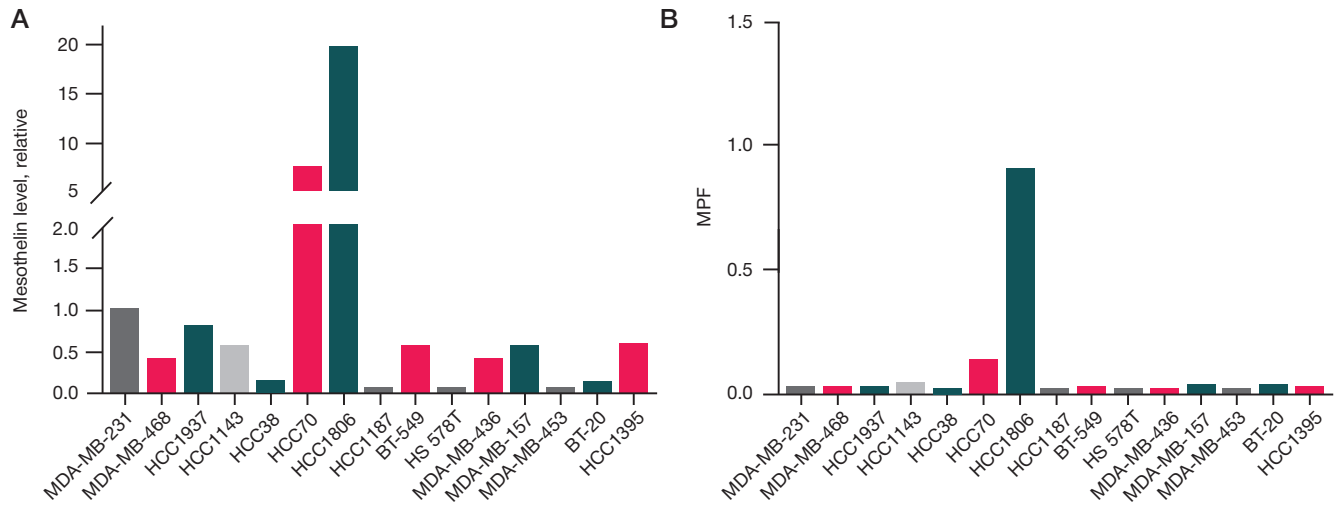


Fig. 2. Determination of mesothelin levels. **A.** Relative MSLN expression levels in TNBC cell lines evaluated by real-time PCR. **B.** MPF levels in the cultural media with TNBC. The graphs show median values and standard deviations between biological replicates

Both sequences were cloned into a pET-BAD expression vector in frame with biotinylation signal sequence of BirA biotin ligase. Biotinylated MesoVHH-1E3B and MesoVHH-2H5B antibodies purified by means of affinity chromatography were tested for their ability to bind to mesothelin using ELISA. We also attempted indirect antigen detection, in which MesoVHH-1E3 was used as a capture antibody and MesoVHH-2H5B was used as a detection antibody. Both tests were successful. Then, dissociation constants were determined for the purified antibodies by means of biolayer interferometry. For MesoVHH-1E3B, Kd was approximating 140 nmol, whereas for MesoVHH-2H5B it was about 95 nmol.

Mesothelin expression was measured in the panel of TNBC cell lines by real-time PCR in order to identify MSLN⁺ and MSLN⁻ cultures. The data generated by real-time PCR were normalized to the MDA-MB-231 cell line characterized by low mesothelin expression. The analysis showed that low mesothelin expression was typical for most of the tested TNBC cell lines (Fig. 2). Two cell lines (HCC70 and HCC1806) exhibited moderate expression and hyperexpression of MSLN, respectively, and therefore were chosen as model cell lines for further tests on the selected candidate anti-MSLN VHH antibodies. By contrast, the HCC1187, Hs 578T and MDA-MB-453 cell lines were characterized by significantly (> tenfold) reduced MSLN expression and therefore were chosen as negative controls. The levels of intracellular transcripts do

not always correlate with the actual amount of the protein on the cell surface, so the results of real-time PCR needed to be verified by ELISA using a secreted fragment of the mesothelin precursor MPF. Only 2 cell lines (HCC70 and HCC1806) were found to secrete MPF into the liquid culture medium after 6 days of incubation (Fig. 2B); MPF levels were well-correlated with the levels of mesothelin expression measured by real-time PCR.

Purified MesoVHH-1E3B and MesoVHH-2H5B antibodies were used to stain the selected cell cultures and perform flow cytometry. Both VHH fragments produced intense fluorescence in most cells (%) of the HCC1806 and HCC70 cell populations (Fig. 3); however, fluorescence was much less intense in HCC70 cells. No significant differences were observed between the histograms constructed for the MDA-MB-453, HCC1187 and Hs 578T cell lines that were used as a negative control to test the non-specific binding of the studied nanobodies and the histograms of corresponding samples that were not labeled with VHH fragments. These findings were consistent with the PCR data on mesothelin expression in TNBC cell lines used for the testing of VHH fragments. This suggests that the studied nanobodies had high specificity for the target antigen.

DISCUSSION

We have successfully identified two specific single-domain antibodies against mesothelin. The protocol for the pre-

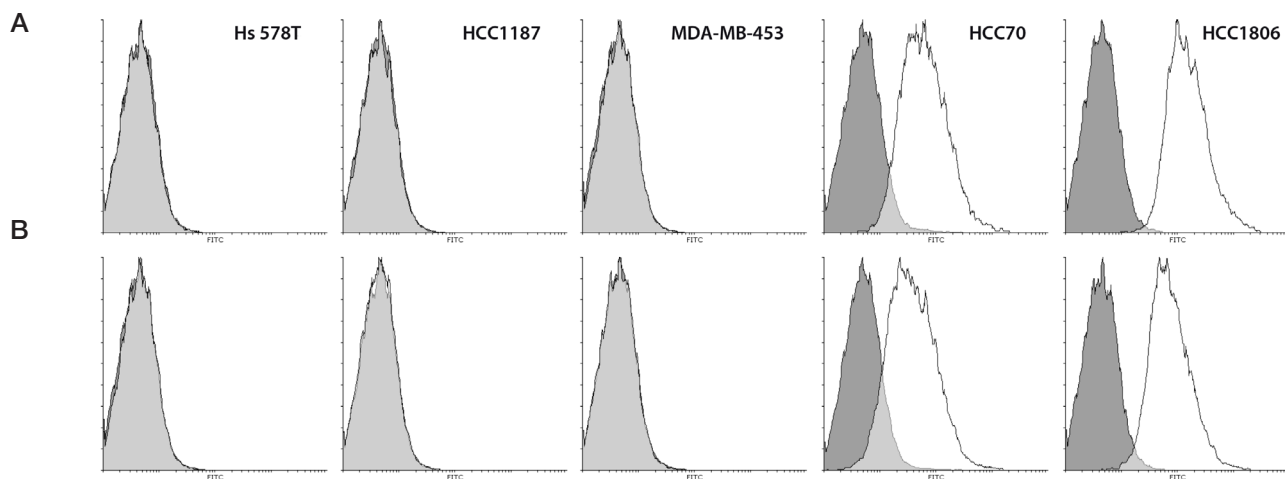


Fig. 3. Testing of the nanobodies in TNBC cell lines. The graphs show flow cytometry results for the model TNBC cell lines labeled with MesoVHH-2H5B (A) and MesoVHH-1E3B (B). Staining was done with Streptavidin-FITC

selection of immunocompetent cells was adapted from [24] and used to prepare immune libraries. Unlike the original protocol, we did not perform negative selection on magnetic beads to separate the B-cell fraction from mononuclear peripheral cells due to the absence of commercial kits for the isolation of alpaca B cells. The step involving the sorting of B cells labeled with fluorescently-conjugated antibodies was also skipped. Instead, we decided to isolate B cells expressing target B-cell receptors on their surface by performing positive selection on magnetic beads coated with biotinylated mesothelin. This approach allowed us to reduce the amount of the initial raw material 100-fold and create a smaller phage library devoid of irrelevant antibody fragments. Both anti-MSLN nanobodies were more abundant in the preselected library and were detected during the screening of individual clones as early as the first round of selection. We conclude that our simplified preselection procedure takes 3 times less time than usually needed to select a candidate clone. The relative abundance of clones with affinity for the target in the initial library can prevent the loss of rare sequences with unique properties.

Currently, there are a few known variants of anti-mesothelin VHH antibodies [17, 18]. These nanobodies show promise as immunodiagnostic tools, targeting molecules for nanoparticle-based therapy and components of bispecific therapeutic agents. The nanobodies identified in this study are slightly inferior to the already known nanobodies in terms of their specificity; however, this parameter is not definitive in allowing the use of a VHH fragment in a CAR construct. MesoVHH-1E3 and MesoVHH-2H5B have been successfully tested as capture and detection antibodies, respectively, in a sandwich ELISA. This suggests that the two nanobodies recognize different mesothelin epitopes and their simultaneous binding to the target is not impeded.

Mesothelin-targeting CARs are being actively tested as candidate therapies for solid tumors [3]. Recently, a number of studies have been published on the MSLN-targeted therapy for TNBC [10]. There is a need for a convenient MSLN⁺ TNBC cell model that could be employed for testing these therapeutic approaches *ex vivo* and *in vivo*. Although the proportion of primary MSLN⁺ TNBC cultures is substantial, the continuous cell lines of this subtype are mostly MSLN-negative [8]. By

screening the wide panel of TNBC cell lines, we were able to identify 2 candidate cell models and 3 cell lines with suppressed MSLN expression. For MSLN⁺-cell lines, real-time PCR results were consistent with the results of ELISA assays for the MPF, the secreted fragment of the mesothelin precursor present in the cell supernatant. Noteworthy, both MSLN⁺-cell lines can be used to induce cancer in immunodeficient BalbC/nude [25, 26] via an orthotopic injection, which makes this cell model suitable for *in vivo* experiments.

The selected anti-mesothelin nanobodies were tested on the MSLN⁺ TNBC model and demonstrated the ability to recognize the native TNBC antigen. The low level of background signal in the MSLN⁺ cell lines stained with the nanobodies indicates their high specificity for the target. The obtained data leads us to hypothesize that MesoVHH-1E3 and MesoVHH-2H5 might be used to create compact functionally active antigen receptors for mesothelin.

CONCLUSIONS

Using a modified protocol for the preselection of cells obtained from an immunized animal, we identified 2 nanobodies capable to specifically bind to mesothelin. The activity of these nanobodies was demonstrated in the *in vitro* experiment. The identified VHH fragments recognize different non-overlapping epitopes of MSLN and can be used for sandwich ELISA. Using biolayer interferometry, we determined the K_d values for MesoVHH-1E3B and MesoVHH-2H5B (about 140 and 95 nmol, respectively). The panel of TNBC cell lines was screened for candidate MSLN⁺ cell models, and 2 cell lines (HCC1806 and HCC70) were chosen as characterized by high and moderate hyperexpression of mesothelin. We also identified 3 cell lines (HCC1187, Hs 578T and MDA-MB-453) in which mesothelin expression was suppressed. The selected anti-mesothelin nanobodies were able to specifically stain native mesothelin on the surface of HCC1806 and HCC70 cells and had low levels of non-specific binding in MSLN⁻ breast cancer lines. Our findings suggest that the MesoVHH-1E3 and MesoVHH-2H5 nanobodies could be used for the molecular diagnosis of tumors and creation of compact and functionally active antigen receptors for mesothelin.

References

- Pastan I, Hassan R. Discovery of mesothelin and exploiting it as a target for immunotherapy. *Cancer Res.* 2014; 74 (11): 2907–12. DOI: 10.1158/0008-5472.CAN-14-0337. PubMed PMID: 24824231.
- Einama T, Homma S, Kamachi H, Kawamata F, Takahashi K, Takahashi N, et al. Luminal membrane expression of mesothelin is a prominent poor prognostic factor for gastric cancer. *Br J Cancer.* 2012; 107 (1): 137–42. DOI: 10.1038/bjc.2012.235. PubMed PMID: 22644300.
- Kelly RJ, Sharon E, Pastan I, Hassan R. Mesothelin-targeted agents in clinical trials and in preclinical development. *Mol Cancer Ther.* 2012; 11 (3): 517–25. DOI: 10.1158/1535-7163.MCT-11-0454. PubMed PMID: 22351743.
- Rump A, Morikawa Y, Tanaka M, Minami S, Umesaki N, Takeuchi M, et al. Binding of ovarian cancer antigen CA125/MUC16 to mesothelin mediates cell adhesion. *J Biol Chem.* 2004; 279 (10): 9190–8. DOI: 10.1074/jbc.M312372200. PubMed PMID: 14676194.
- Bharadwaj U, Marin-Muller C, Li M, Chen C, Yao Q. Mesothelin confers pancreatic cancer cell resistance to TNF-alpha-induced apoptosis through Akt/PI3K/NF-kappaB activation and IL-6/Mcl-1 overexpression. *Mol Cancer.* 2011; 10: 106. DOI: 10.1186/1476-4598-10-106. PubMed PMID: 21880146.
- Li M, Bharadwaj U, Zhang R, Zhang S, Mu H, Fisher WE, et al. Mesothelin is a malignant factor and therapeutic vaccine target for pancreatic cancer. *Mol Cancer Ther.* 2008; 7 (2): 286–96. DOI: 10.1158/1535-7163.MCT-07-0483. PubMed PMID: 18281514.
- Cheng WF, Huang CY, Chang MC, Hu YH, Chiang YC, Chen YL, et al. High mesothelin correlates with chemoresistance and poor survival in epithelial ovarian carcinoma. *Br J Cancer.* 2009; 100 (7): 1144–53. DOI: 10.1038/sj.bjc.6604964. PubMed PMID: 19293794.
- Wang M, Li A, Sun G, Mbuagbaw L, Reid S, Lovrics PJ, et al. Association between mesothelin expression and survival outcomes in patients with triple-negative breast cancer: a protocol for a systematic review. *Syst Rev.* 2016; 5 (1): 133. DOI: 10.1186/s13643-016-0313-6. PubMed PMID: 27514374.
- Fougner C, Bergholtz H, Norum JH, Sorlie T. Re-definition of claudin-low as a breast cancer phenotype. *Nat Commun.* 2020; 11 (1): 1787. DOI: 10.1038/s41467-020-15574-5. PubMed PMID: 32286297.
- Tchou J, Wang LC, Selven B, Zhang H, Conejo-Garcia J, Borghaei H, et al. Mesothelin, a novel immunotherapy target for

- triple negative breast cancer. *Breast Cancer Res Treat.* 2012; 133 (2): 799–804. DOI: 10.1007/s10549-012-2018-4. PubMed PMID: 22418702.
11. Lanitis E, Poussin M, Hagemann IS, Coukos G, Sandaltzopoulos R, Scholler N, et al. Redirected antitumor activity of primary human lymphocytes transduced with a fully human anti-mesothelin chimeric receptor. *Mol Ther.* 2012; 20(3): 633–43. DOI: 10.1038/mt.2011.256. PubMed PMID: 22127019.
 12. Fujiwara K, Masutani M, Tachibana M, Okada N. Impact of scFv structure in chimeric antigen receptor on receptor expression efficiency and antigen recognition properties. *Biochem Biophys Res Commun.* 2020; 527 (2): 350–7. DOI: 10.1016/j.bbrc.2020.03.071. PubMed PMID: 32216966.
 13. Maus MV, Plotkin J, Jakka G, Stewart-Jones G, Riviere I, Merghoub T, et al. An MHC-restricted antibody-based chimeric antigen receptor requires TCR-like affinity to maintain antigen specificity. *Mol Ther Oncolytics.* 2016; 3: 1–9. DOI: 10.1038/mto.2016.23. PubMed PMID: 29675462.
 14. Tillib SV. Prospective Applications of Single-Domain Antibodies in Biomedicine. *Mol Biol (Mosk).* 2020; 54 (3): 362–73. Epub 2020/06/04. DOI: 10.31857/S0026898420030167. PubMed PMID: 32492000.
 15. Hamers-Casterman C, Atarhouch T, Muyldermans S, Robinson G, Hamers C, Songa EB, et al. Naturally occurring antibodies devoid of light chains. *Nature.* 1993; 363 (6428): 446–8. DOI: 10.1038/363446a0. PubMed PMID: 8502296.
 16. Liu W, Song H, Chen Q, Yu J, Xian M, Nian R, et al. Recent advances in the selection and identification of antigen-specific nanobodies. *Mol Immunol.* 2018; 96: 37–47. DOI: 10.1016/j.molimm.2018.02.012. PubMed PMID: 29477934.
 17. Prantner AM, Turini M, Kerfelec B, Joshi S, Baty D, Chames P, et al. Anti-Mesothelin Nanobodies for Both Conventional and Nanoparticle-Based Biomedical Applications. *J Biomed Nanotechnol.* 2015; 11 (7): 1201–12. DOI: 10.1166/jbn.2015.2063. PubMed PMID: 26307843.
 18. Prantner AM, Yin C, Kamat K, Sharma K, Lowenthal AC, Madrid PB, et al. Molecular Imaging of Mesothelin-Expressing Ovarian Cancer with a Human and Mouse Cross-Reactive Nanobody. *Mol Pharm.* 2018; 15 (4): 1403–11. DOI: 10.1021/acs.molpharmaceut.7b00789. PubMed PMID: 29462558.
 19. Pfaffl MW. A new mathematical model for relative quantification in real-time RT-PCR. *Nucleic Acids Res.* 2001; 29 (9): e45. DOI: 10.1093/nar/29.9.e45. PubMed PMID: 11328886.
 20. Fukumoto Y, Obata Y, Ishibashi K, Tamura N, Kikuchi I, Aoyama K, et al. Cost-effective gene transfection by DNA compaction at pH 4.0 using acidified, long shelf-life polyethylenimine. *Cytotechnology.* 2010; 62 (1): 73–82. DOI: 10.1007/s10616-010-9259-z. PubMed PMID: 20309632.
 21. Maass DR, Sepulveda J, Pernthaner A, Shoemaker CB. Alpaca (Lama pacos) as a convenient source of recombinant camelid heavy chain antibodies (VHHs). *J Immunol Methods.* 2007; 324 (1–2): 13–25. Epub 2007/06/15. DOI: S0022-1759(07)00119-6 [pii] 10.1016/j.jim.2007.04.008. PubMed PMID: 17568607.
 22. Benhar I, Reiter Y. Phage display of single-chain antibody constructs. *Curr Protoc Immunol.* 2002; 10 (10): 9B. DOI: 10.1002/0471142735.im1019bs48. PubMed PMID: 18432867.
 23. Studier FW. Protein production by auto-induction in high density shaking cultures. *Protein Expr Purif.* 2005; 41 (1): 207–34. PubMed PMID: 15915565.
 24. Zost SJ, Gilchuk P, Chen RE, Case JB, Reidy JX, Trivette A, et al. Rapid isolation and profiling of a diverse panel of human monoclonal antibodies targeting the SARS-CoV-2 spike protein. *Nat Med.* 2020; 26 (9): 1422–7. DOI: 10.1038/s41591-020-0998-x. PubMed PMID: 32651581.
 25. Liu R, Zhi X, Zhou Z, Zhang H, Yang R, Zou T, et al. Mithramycin A suppresses basal triple-negative breast cancer cell survival partially via down-regulating Kruppel-like factor 5 transcription by Sp1. *Scientific reports.* 2018; 8 (1): 1138. DOI: 10.1038/s41598-018-19489-6. PubMed PMID: 29348684.
 26. Simon N, Antignani A, Sarnovsky R, Hewitt SM, FitzGerald D. Targeting a Cancer-Specific Epitope of the Epidermal Growth Factor Receptor in Triple-Negative Breast Cancer. *J Natl Cancer Inst.* 2016; 108 (8). DOI: 10.1093/jnci/djw028. PubMed PMID: 27075852.

Литература

1. Pastan I, Hassan R. Discovery of mesothelin and exploiting it as a target for immunotherapy. *Cancer Res.* 2014; 74 (11): 2907–12. DOI: 10.1158/0008-5472.CAN-14-0337. PubMed PMID: 24824231.
2. Einama T, Homma S, Kamachi H, Kawamata F, Takahashi K, Takahashi N, et al. Luminal membrane expression of mesothelin is a prominent poor prognostic factor for gastric cancer. *Br J Cancer.* 2012; 107 (1): 137–42. DOI: 10.1038/bjc.2012.235. PubMed PMID: 22644300.
3. Kelly RJ, Sharon E, Pastan I, Hassan R. Mesothelin-targeted agents in clinical trials and in preclinical development. *Mol Cancer Ther.* 2012; 11 (3): 517–25. DOI: 10.1158/1535-7163.MCT-11-0454. PubMed PMID: 22351743.
4. Rump A, Morikawa Y, Tanaka M, Minami S, Umesaki N, Takeuchi M, et al. Binding of ovarian cancer antigen CA125/MUC16 to mesothelin mediates cell adhesion. *J Biol Chem.* 2004; 279 (10): 9190–8. DOI: 10.1074/jbc.M312372200. PubMed PMID: 14676194.
5. Bharadwaj U, Marin-Muller C, Li M, Chen C, Yao Q. Mesothelin confers pancreatic cancer cell resistance to TNF-alpha-induced apoptosis through Akt/PI3K/NF-kappaB activation and IL-6/Mcl-1 overexpression. *Mol Cancer.* 2011; 10: 106. DOI: 10.1186/1476-4598-10-106. PubMed PMID: 21880146.
6. Li M, Bharadwaj U, Zhang R, Zhang S, Mu H, Fisher WE, et al. Mesothelin is a malignant factor and therapeutic vaccine target for pancreatic cancer. *Mol Cancer Ther.* 2008; 7 (2): 286–96. DOI: 10.1158/1535-7163.MCT-07-0483. PubMed PMID: 18281514.
7. Cheng WF, Huang CY, Chang MC, Hu YH, Chiang YC, Chen YL, et al. High mesothelin correlates with chemoresistance and poor survival in epithelial ovarian carcinoma. *Br J Cancer.* 2009; 100 (7): 1144–53. DOI: 10.1038/sj.bjc.6604964. PubMed PMID: 19293794.
8. Wang M, Li A, Sun G, Mbuagbaw L, Reid S, Lovrics PJ, et al. Association between mesothelin expression and survival outcomes in patients with triple-negative breast cancer: a protocol for a systematic review. *Syst Rev.* 2016; 5 (1): 133. DOI: 10.1186/s13643-016-0313-6. PubMed PMID: 27514374.
9. Fougner C, Bergholtz H, Norum JH, Sorlie T. Re-definition of claudin-low as a breast cancer phenotype. *Nat Commun.* 2020; 11 (1): 1787. DOI: 10.1038/s41467-020-15574-5. PubMed PMID: 32286297.
10. Tchou J, Wang LC, Selven B, Zhang H, Conejo-Garcia J, Borghaei H, et al. Mesothelin, a novel immunotherapy target for triple negative breast cancer. *Breast Cancer Res Treat.* 2012; 133 (2): 799–804. DOI: 10.1007/s10549-012-2018-4. PubMed PMID: 22418702.
11. Lanitis E, Poussin M, Hagemann IS, Coukos G, Sandaltzopoulos R, Scholler N, et al. Redirected antitumor activity of primary human lymphocytes transduced with a fully human anti-mesothelin chimeric receptor. *Mol Ther.* 2012; 20(3): 633–43. DOI: 10.1038/mt.2011.256. PubMed PMID: 22127019.
12. Fujiwara K, Masutani M, Tachibana M, Okada N. Impact of scFv structure in chimeric antigen receptor on receptor expression efficiency and antigen recognition properties. *Biochem Biophys Res Commun.* 2020; 527 (2): 350–7. DOI: 10.1016/j.bbrc.2020.03.071. PubMed PMID: 32216966.
13. Maus MV, Plotkin J, Jakka G, Stewart-Jones G, Riviere I, Merghoub T, et al. An MHC-restricted antibody-based chimeric antigen receptor requires TCR-like affinity to maintain antigen specificity. *Mol Ther Oncolytics.* 2016; 3: 1–9. DOI: 10.1038/mto.2016.23. PubMed PMID: 29675462.
14. Tillib SV. Prospective Applications of Single-Domain Antibodies in Biomedicine. *Mol Biol (Mosk).* 2020; 54 (3): 362–73. Epub

- 2020/06/04. DOI: 10.31857/S0026898420030167. PubMed PMID: 32492000.
15. Hamers-Casterman C, Atarhouch T, Muyldermans S, Robinson G, Hamers C, Songa EB, et al. Naturally occurring antibodies devoid of light chains. *Nature*. 1993; 363 (6428): 446–8. DOI: 10.1038/363446a0. PubMed PMID: 8502296.
 16. Liu W, Song H, Chen Q, Yu J, Xian M, Nian R, et al. Recent advances in the selection and identification of antigen-specific nanobodies. *Mol Immunol*. 2018; 96: 37–47. DOI: 10.1016/j.molimm.2018.02.012. PubMed PMID: 29477934.
 17. Prantner AM, Turini M, Kerfelec B, Joshi S, Baty D, Chames P, et al. Anti-Mesothelin Nanobodies for Both Conventional and Nanoparticle-Based Biomedical Applications. *J Biomed Nanotechnol*. 2015; 11 (7): 1201–12. DOI: 10.1166/jbn.2015.2063. PubMed PMID: 26307843.
 18. Prantner AM, Yin C, Kamat K, Sharma K, Lowenthal AC, Madrid PB, et al. Molecular Imaging of Mesothelin-Expressing Ovarian Cancer with a Human and Mouse Cross-Reactive Nanobody. *Mol Pharm*. 2018; 15 (4): 1403–11. DOI: 10.1021/acs.molpharmaceut.7b00789. PubMed PMID: 29462558.
 19. Pfaffl MW. A new mathematical model for relative quantification in real-time RT-PCR. *Nucleic Acids Res*. 2001; 29 (9): e45. DOI: 10.1093/nar/29.9.e45. PubMed PMID: 11328886.
 20. Fukumoto Y, Obata Y, Ishibashi K, Tamura N, Kikuchi I, Aoyama K, et al. Cost-effective gene transfection by DNA compaction at pH 4.0 using acidified, long shelf-life polyethylenimine. *Cytotechnology*. 2010; 62 (1): 73–82. DOI: 10.1007/s10616-010-9259-z. PubMed PMID: 20309632.
 21. Maass DR, Sepulveda J, Pernthaler A, Shoemaker CB. Alpaca (Lama pacos) as a convenient source of recombinant camelid heavy chain antibodies (VHHs). *J Immunol Methods*. 2007; 324 (1–2): 13–25. Epub 2007/06/15. DOI: S0022-1759(07)00119-6 [pii] 10.1016/j.jim.2007.04.008. PubMed PMID: 17568607.
 22. Benhar I, Reiter Y. Phage display of single-chain antibody constructs. *Curr Protoc Immunol*. 2002; 10 (10): 9B. DOI: 10.1002/0471142735.im1019bs48. PubMed PMID: 18432867.
 23. Studier FW. Protein production by auto-induction in high density shaking cultures. *Protein Expr Purif*. 2005; 41 (1): 207–34. PubMed PMID: 15915565.
 24. Zost SJ, Gilchuk P, Chen RE, Case JB, Reidy JX, Trivette A, et al. Rapid isolation and profiling of a diverse panel of human monoclonal antibodies targeting the SARS-CoV-2 spike protein. *Nat Med*. 2020; 26 (9): 1422–7. DOI: 10.1038/s41591-020-0998-x. PubMed PMID: 32651581.
 25. Liu R, Zhi X, Zhou Z, Zhang H, Yang R, Zou T, et al. Mithramycin A suppresses basal triple-negative breast cancer cell survival partially via down-regulating Kruppel-like factor 5 transcription by Sp1. *Scientific reports*. 2018; 8 (1): 1138. DOI: 10.1038/s41598-018-19489-6. PubMed PMID: 29348684.
 26. Simon N, Antignani A, Sarnovsky R, Hewitt SM, FitzGerald D. Targeting a Cancer-Specific Epitope of the Epidermal Growth Factor Receptor in Triple-Negative Breast Cancer. *J Natl Cancer Inst*. 2016; 108 (8). DOI: 10.1093/jnci/djw028. PubMed PMID: 27075852.

IMMUNOHISTOCHEMICAL EXPRESSION OF NANOG PROTEIN IN PROSTATE CANCER CELLS OF DISTINCT GRADE GROUPS

Kudryavtsev GYu^{1,3}✉, Kudryavtseva LV¹, Mikhaleva LM², Kudryavtseva YaYu¹, Solovyeva NA¹, Osipov VA³, Babichenko II¹

¹ Peoples' Friendship University of Russia, Moscow, Russia

² Research Institute of Human Morphology, Moscow, Russia

³ Hospital for War Veterans № 2, Moscow, Russia

Prostate cancer is the most common type of cancer among men, which is mainly due to extensive use of screening tests and high total number of prostate biopsies. Verification of tumors with poorer prognosis is the primary goal of prostate cancer management. The study was aimed to determine the clinical and morphological associations and the prognostic value of the Nanog protein expression in prostate cancer of distinct Grade Groups. We used the prostate tissue specimens obtained during surgery, and the biopsy specimens, the total of 89 cases. Histological and immunohistochemical assessment was performed using antibodies to Ki-67 and Nanog. Correlations between the expression of markers and the Grade Groups were revealed using the Spearman's rank correlation coefficient, and the correlation with clinical and morphological characteristics was determined using the chi-squared test (χ^2). There was a positive correlation between the expression of Ki-67 and Nanog, and the Grade Group numerical order ($r_s = 0.619, p < 0.001$ and $r_s = 0.786, p < 0.001$ respectively). We managed to find the relationship between the high Nanog expression and the extraprostatic extension ($p = 0.041$). High expression of Nanog protein in the prostate cancer cells was associated with a higher-grade adenocarcinoma and indicated a poor prognosis.

Keywords: prostate cancer, prostate adenocarcinoma, Ki-67, Nanog, Gleason index, Grade Groups

Author contribution: Kudryavtsev GYu, Kudryavtseva YaYu, Solovyeva NA — literature survey, manuscript writing; Kudryavtseva LV, Osipov VA — statistical data processing; Mikhaleva LM — sample collection and processing; Babichenko II — study concept and design.

Compliance with ethical standards: the study was approved by the Ethics Committee of Medical Institute of the Peoples' Friendship University of Russia (protocol № 13 dated December 19, 2019); the study design was consistent with the Declaration of Helsinki guidelines regarding the research involving identifiable human tissue samples. The informed consent was submitted by all patients.

✉ **Correspondence should be addressed:** Georgy Yu. Kudryavtsev
Baikalskaya, 35, apt. 216, Moscow, 107207; kgosha@mail.ru

Received: 06.10.2020 **Accepted:** 20.10.2020 **Published online:** 30.10.2020

DOI: 10.24075/brsmu.2020.067

ИММУНОГИСТОХИМИЧЕСКАЯ ЭКСПРЕССИЯ БЕЛКА NANOG В КЛЕТКАХ РАКА ПРЕДСТАТЕЛЬНОЙ ЖЕЛЕЗЫ РАЗЛИЧНЫХ ПРОГНОСТИЧЕСКИХ ГРУПП

Г. Ю. Кудрявцев^{1,3}✉, Л. В. Кудрявцева¹, Л. М. Михалева², Я. Ю. Кудрявцева¹, Н. А. Соловьева¹, В. А. Осипов³, И. И. Бабиченко¹

¹ Российский университет дружбы народов, Москва, Россия

² Научно-исследовательский институт морфологии человека, Москва, Россия

³ Госпиталь для ветеранов войн № 2, Москва, Россия

Рак предстательной железы — наиболее часто выявляемое онкологическое заболевание среди мужчин, этому во многом способствуют распространение скрининговых исследований и высокая частота биопсий органа. Верификация опухолей с потенциально более неблагоприятным прогнозом течения является первостепенной задачей при лечении рака предстательной железы. Целью исследования было определить клиничко-морфологические ассоциации и прогностическую значимость экспрессии белка Nanog при раке предстательной железы в различных прогностических группах. Работа выполнена на материале ткани предстательной железы, полученном после оперативного вмешательства, а также образцах ткани биопсии (всего 89 случаев). Было проведено гистологическое и иммуногистохимическое исследование с использованием антител к белкам Ki-67 и Nanog. Корреляционные связи между выраженностью экспрессии указанных маркеров и прогностической группой определяли с помощью коэффициента Спирмена, а связь с клиничко-морфологическими проявлениями — с использованием критерия хи-квадрат (χ^2). Обнаружена статистически значимая прямая корреляционная связь между выраженностью экспрессии Ki-67 и Nanog и порядковым номером прогностической группы ($r_s = 0,619, p < 0,001$ и $r_s = 0,786, p < 0,001$ соответственно). Удалось обнаружить связь между высокой степенью экспрессии Nanog и экстрапростатическим распространением опухоли ($p = 0,041$). Повышенная экспрессия белка Nanog в клетках рака предстательной железы связана с более злокачественными формами аденокарциномы и свидетельствует о неблагоприятном прогнозе.

Ключевые слова: рак предстательной железы, аденокарцинома простаты, Ki-67, Nanog, индекс Глисона, прогностические группы

Вклад авторов: Г. Ю. Кудрявцев, Я. Ю. Кудрявцева, Н. А. Соловьева — обзор литературы, написание текста; Л. В. Кудрявцева, В. А. Осипов — статистическая обработка данных; Л. М. Михалева — сбор и обработка материалов; И. И. Бабиченко — концепция и дизайн исследования.

Соблюдение этических стандартов: исследование было одобрено Комитетом по этике Медицинского института РУДН (протокол № 13 от 19 декабря 2019 г.), дизайн исследования соответствовал правилам Хельсинкской декларации об использовании тканей человека. От всех пациентов было получено письменное информированное согласие.

✉ **Для корреспонденции:** Георгий Юрьевич Кудрявцев
ул. Байкальская, д. 35, кв. 216, г. Москва, 107207; kgosha@mail.ru

Статья получена: 06.10.2020 **Статья принята к печати:** 20.10.2020 **Опубликована онлайн:** 30.10.2020

DOI: 10.24075/vrgmu.2020.067

According to statistics, there were 42,518 newly-reported cases of prostate cancer in the year 2018 in Russia, and the higher incidence rates among males were demonstrated only by tracheal, bronchial and lung malignant neoplasms [1].

Prostate cancer is the most common cancer in men all over the world, the prevalence of the disease in the developed world exceeds 200 cases per 100,000 men. Although the clinical course of the tumor varies from slow-growing localized types

to highly aggressive cases with fast spreading, the disease is one of the major causes of morbidity and mortality among men [2, 3].

The USA is one of the countries with the highest rate of prostate cancer. The disease occurs in one of every six American men during his lifetime. However, only one of those patients actually dies of prostate cancer and its complications, in other patients the tumor usually demonstrates no clinical manifestations [4]. These data were confirmed by autopsy studies in which the postmortem diagnosis of prostate cancer was established in one third of patients aged 50–60, and in 60% of people who died over the age of 80 [5].

Prior to wide-scale introduction of the prostate-specific antigen (PSA) level assessment, the prostate cancer was often diagnosed after the patients had shown symptoms of locally advanced or metastatic disease, and the overall 5-year relative survival rate was 70% [6]. The extensive use of PSA screening tests led to a dramatic increase in the prostate cancer detection involving mostly localized cancer. However, the described method does not have high specificity and often contributes to the increased number of invasive procedures in patients with clinically insignificant cancer types [7]. Therefore there is a need to continue search for biological markers in order to refine the various prostate cancer types progression model and choose the appropriate treatment tactics.

The promising strategy to address the problem is the in-depth study of major histogenesis patterns for the most common type of prostate cancer, the adenocarcinoma.

At the current stage, the stochastic model of carcinogenesis suggesting that each individual tumor cell possesses the amplification capacity and is able to produce a new tumor pool is relegated to the background [8]. It is being substituted by hierarchical approach to tumor progression. This approach involves the model in which the tumor consists of atypical cells, polymorphic in their proliferative activity and differentiation potential. The theory described implies that there are cancer stem cells (CSC), which, like normal stem cells, are able to divide indefinitely, inter alia they divide asymmetrically, and therefore they are capable of multipotent differentiation in the tumor tissue. It is believed that cancer stem cells potentiate tumor growth [9].

Early observations (1960s) based on the studies of hemoblastosis proved the heterogeneity of cells in the tumor mass suggesting the existence of immature cell population. The first evidence based on the acute myeloid leukemia research that supported the cancer stem cells (CSC) existence hypothesis was obtained in the 1990s [10]. More recent studies indicated that CSCs were present in tumors of other types, particularly in prostate cancer.

The CSC multipotency maintenance patterns are not well understood, however, the regulatory proteins responsible for similar properties of embryonic stem cells (ESC) may play a vital part.

The Nanog protein is a transcription factor involved in self-renewal of stem cells. It was first discovered in mouse embryonic stem cells and considered an important transcriptional regulator responsible for cell differentiation [11, 12].

The described protein encoded by the gene *NANOG1* consists of 305 amino acids and possesses three functional domains: the N-terminal domain, the C-terminal domain and the conservative homeodomain motif required for binding to promoter region of DNA target regions and transcription regulation [13].

Together with other transcription factors, the most conservative of which are SOX2 and OCT4, Nanog plays a critical role in maintaining ESC properties [14]. These three key

factors usually function together through transcriptional network formation to control the expression of a set of pluripotent-related genes in ESC. High expression of Nanog is observed in the pluripotent stem cells and embryonal carcinoma cells, and its expression is downregulated upon cell maturation [11]. Overexpression of Nanog protein not only contributes to maintenance of ESC pluripotency in murine models in the absence of such strong extrinsic factors as leukemia inhibitory factor (LIF), but also promotes the human ESC growth in the controlled environment in feeder-free conditions, i.e. in the absence of feeder, the functional basis represented by primary embryonic fibroblasts [15]. Thus, the level of Nanog protein is involved in determining the cell fate in pluripotent cells under physiological conditions.

Identification of cells possessing the stemness-related signs and markers in the tumor tissue might help to predict the unfavourable prostate cancer outcome.

The study was aimed to determine the prognostic value of the Nanog protein expression in the cells of prostate adenocarcinoma.

METHODS

From September 2017 to May 2019 at two hospitals (City Clinical Hospital № 31 and Hospital for War Veterans № 2) we had been collecting specimens obtained from 89 urological patients during surgery and diagnostic procedures.

The average age of patients at the time of tissue sampling was 69.3 years (47–89 years). Inclusion criteria: prostate cancer patients with morphologically verified diagnosis who received no neoadjuvant therapy. Exclusion criteria: cases with no clinical and instrumental examination data (PSA levels, tumor extension), as well as the cases with tissue amounts insufficient for immunohistochemical analysis and further interpretation of results. Surgery was performed in 48 patients (23 patients underwent transurethral resection, and 25 patients underwent radical prostatectomy), and the diagnostic transrectal multifocal biopsy was performed in 41 patients. Morphological assessment of prostate cancer included not only the cancer grade evaluation according to the Gleason score, but also, according to the WHO recommendations, the Grade Group characteristics were provided in each observation.

Immunohistochemical assessment was carried out according to standard protocol. The rabbit monoclonal Nanog antibody (Clone EPR2027 (2), Epitomics; USA) was used as a primary antibody. The seminomatous testis tissue specimens were used as a positive control. The cell proliferative activity assessment was performed using the anti-Ki-67 rabbit monoclonal antibody (Clone SP6, Cell Marque; USA). The reaction with the tonsils lymphoid tissue (tonsillar germinal center cells) was used as a positive control. Immunohistochemical reaction was carried out using the QUANTO detection system in the Autostainer 360 unit (Thermo Fisher Scientific; USA). The slices were stained with Mayer's hematoxylin. The specimens were examined under the Axioplan 2 imaging microscope (Karl Zeiss; Germany) with the AxioCam ERc 5s stand-alone camera (Karl Zeiss; Germany).

Quantification of proliferative activity was performed by counting the percentage of positively stained nuclei per 300 cells at x400 magnification. The following scoring system was used: no expression (score 0), weak expression (score 1) — less than 10% of cell nuclei were stained, moderate expression (score 2) — more than 10% but less than 33% of cell nuclei were positive, strong expression (score 3) — more than 33% of the cell nuclei were positive.

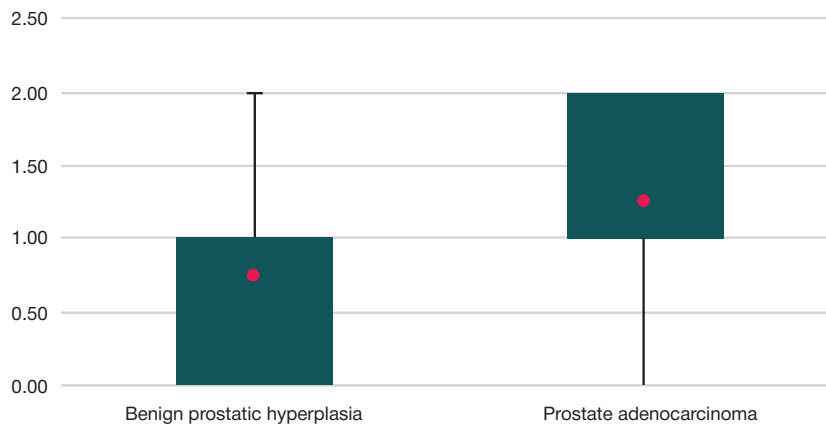


Fig. 1. Expression of Ki-67 in patients with benign prostatic hyperplasia and prostate adenocarcinoma

The Nanog expression assessment was also performed by counting the number of immunopositive cells at high magnification (x400, the minimum number of cells was 300). However, the results were adjusted for staining intensity. The 0–3 scale was used: 0 was no staining, 1 was weak staining, 2 and 3 were moderate and strong staining respectively. Then the H-score (histochemical score) was calculated using the following formula:

$$\text{H-score} = \sum (P_i \times i),$$

where i was the staining intensity ranged from 0 to 3, and P_i was the proportion of cells stained to different intensities (%). The H-score value ranged between 0 and 300 [16].

Statistical analysis was carried out using the Statistica 10.0 (StatSoft; USA) software for Windows 10. The significance of differences in the samples was determined using the Mann–Whitney U -test. The differences were considered significant at $p < 0.05$. Correlation relationships were determined using the Spearman's rank correlation coefficient, the Chaddock scale was used to evaluate the strength of relationship for correlation coefficients. The chi-square (χ^2) and Fisher's exact tests were used to reveal correlations between the studied markers expression and the clinical and morphological characteristics of patients.

RESULTS

After histological examination 68 patients were diagnosed with prostate cancer, the other patients were diagnosed with benign prostatic hyperplasia combined with inflammatory changes of varying severity. In accordance with the recommendations, after morphologic evaluation all observations were distinguished into five prognostic Grade Groups: Grade Group 1 included 18 cases (26.5%), Grade Group 2 included 16 cases (23.6%), and Grade Group 3 included 15 cases (22.1%). Grade Groups 4 and 5 included 10 (14.7%) and 9 (13.2%) cases respectively. The cancer extent was determined based on the clinical and morphological data: tumors detected accidentally during examination, as well as carcinomas limited to the tissue of origin were considered localized cancer (T1 and T2 tumor-node-metastasis stage according to AJCC, 8th edition). Extraprostatic extension was considered a sign of advanced cancer (T3 and T4). The serum PSA level of 10 ng/mL was used as a threshold value.

The expression of Ki-67 was detected in 82 cases (92.1%). In the group of patients with benign prostatic hyperplasia the expression of Ki-67 was detected in 14 observations

(66.7%), and in vast majority of cases the expression was weak. Comparison of the described marker expression between groups of patients with benign prostate lesions and prostate cancer revealed significant differences, and the overall proliferative activity in the prostate cancer group turned out to be much higher ($p < 0.001$) (Fig. 1).

Comparison of proliferative activity between different Grade Groups revealed the progressive increase of the mean Ki-67 expression with the Grade Group numerical order (Fig. 2). Correlation analysis revealed strong positive correlation between the parameters compared ($r_s = 0.619$; $p < 0.001$).

Expression of Nanog

In our study no expression of Nanog was detected in patients with benign prostatic hyperplasia, whereas among 68 cases of prostate cancer the 26 specimens (38.2%) turned out to be Nanog-positive. No expression of Nanog was detected in Grade Group 1, in Grade Group 2 there were three positive cases (18.75%), in Grade Group 3 there were 6 positive cases (40%), in Grade Group 4 there were 8 positive cases (80%), and in Grade Group 5 there were 9 positive cases out of 9. The mean Nanog expression values adjusted for staining intensity are presented in Fig. 3.

Comparison of H-scores for Nanog expression in the cells of prostate adenocarcinoma made it possible to reveal positive correlation with the Grade Group numerical order ($r_s = 0.786$, $p < 0.001$).

The studied markers expression for the most common Gleason patterns is shown in Fig. 4.

Matching the clinical and morphological properties with the studied markers expression (Table) revealed significant correlation between the Ki-67 expression level and the extraprostatic extension ($p = 0.046$) together with high serum PSA level (> 10 ng/mL; $p < 0.001$). At the same time, high H-scores for Nanog expression were associated with advanced cancer ($p = 0.041$). However, no significant correlation between Nanog reactivity and the serum PSA level was observed.

DISCUSSION

The study of cancer stem cells (CSC) peculiarities made it possible to revise the fundamentals of tumor organization and metabolism. Heterogeneity of tumor cell population is due to hierarchical organization partially modeling the normal histoarchitectonics of the tissue of origin. Symmetric and asymmetric division of CSC contributes both to maintaining the tumor cell population and to tumor volume increase due to loss of stemness by certain cells [17].

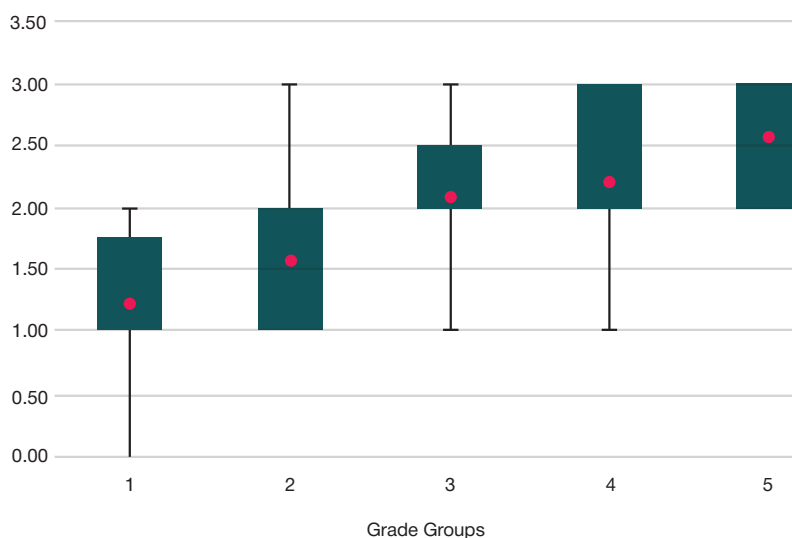


Fig. 2. Comparison of Ki-67 expression between different prostate cancer Grade Groups

It has been shown that in certain cancer types the Nanog expression level in CSC is higher compared to the rest of tumor cell population [18, 19].

The functional studies have demonstrated that Nanog is not only the marker of CSC, but is also able to enhance CSC-like properties in some cancer types. For example, the embryonic *NANOG* gene activation forces the colorectal cancer cell subpopulation to acquire a stem cell-like phenotype [20].

The expression of Nanog was detected in various tumors, including breast cancer, cervical cancer, oral cavity cancer, renal cancer, prostate cancer, lung cancer, gastric cancer, brain cancer and ovarian cancer [21]. High expression of Nanog indicates poor survival prognosis in patients with serous ovarian carcinoma, colorectal cancer and breast cancer. In patients with oral squamous cell carcinoma and lung adenocarcinoma, higher expression of Nanog and Oct4 is associated with advanced stage and worse overall survival [22, 23].

Aberrant expression of Nanog in cancer cells was associated with higher proliferation rate *in vitro* and tumor growth *in vivo*. It had been shown that the parallel overexpression of Nanog and Oct4 in the cells of lung adenocarcinoma enhanced clonogenicity and induced the spheroid formation [24], and the Nanog knockdown in the breast cancer cells reduced clonogenicity and cell proliferation [25]. The Nanog knockdown was associated with downregulation of a number of cell-cycle genes (such as cyclins D1, D2, D3 and E1, as well as cyclin-dependent

kinases 1 and 6) and the p53 signaling pathway (for example, Bcl6 and Atf3), which could indicate the Nanog involvement in the cell cycle regulation [25, 26].

Our study made it possible to identify the Nanog protein expression in the prostate cancer cells. This protein was absent both in normal prostatic tissue and in observations of benign prostatic hyperplasia. The Nanog protein expression heterogeneity suggests that distinct adenocarcinoma variants distinguished primarily by the degree of anaplasia have different histochemical profiles. Considering that this transcription factor is generally inherent in embryonic cells, finding it in the cells of tumor mass speaks well for the theory of specific pool of cells showing signs of "stem-like" phenotype. The comparison of distinct prognostic Grade Groups has revealed that the Nanog expression rate and intensity increases with the growth of the degree of anaplasia. This is reflected by the Gleason score of the tumor and contributes to the Grade Group selection. Such positive correlation confirms that there is a significant subpopulation of CSC, multipotent due to presence of Nanog, in the cell mass of the most poorly differentiated prostate adenocarcinomas. The study also demonstrates the significant correlation between the Nanog expression level and the extraprostatic extension, which is an important factor affecting the outcome. Most observations, which turned out to be considerably immunoreactive for the described protein expression, also showed high expression of Ki-67. That indicated the high proliferative capacity of anaplastic cancer

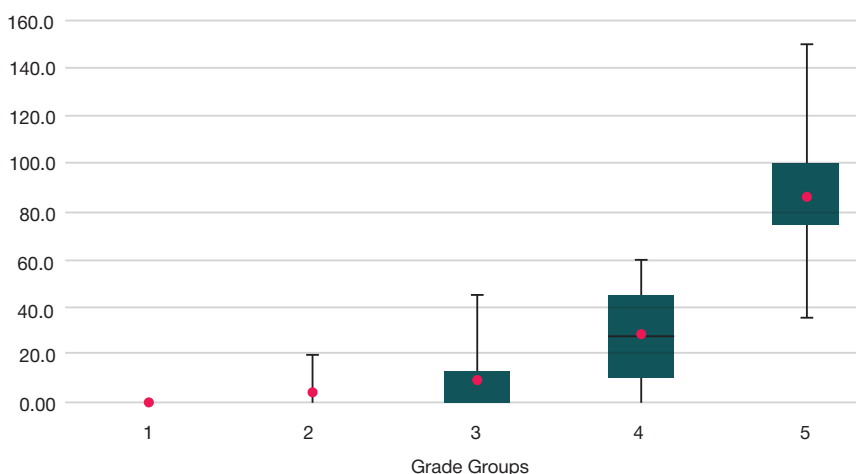


Fig. 3. Comparison of Nanog expression between different prostate cancer Grade Groups

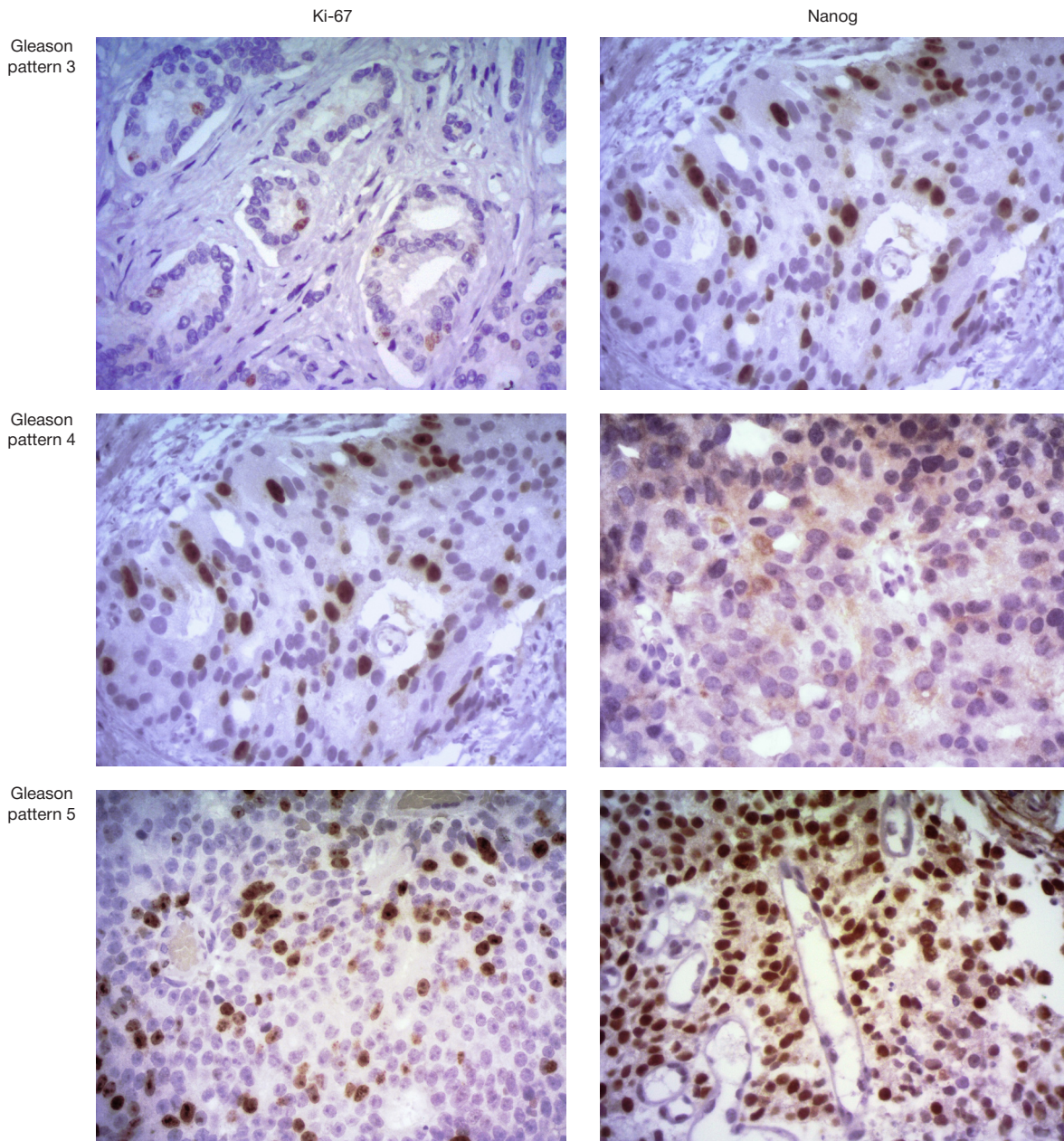


Fig. 4. Expression of Ki-67 and Nanog in the prostate cancer cells for the most common Gleason patterns (magnification x400)

cells, among them the CSC. Immunohistochemical reaction with markers Nanog and Ki-67 in the Grade Groups 1 и 2 turned out to be much lower compared to Grade Group 5, which indicated the better prognosis in well-differentiated carcinomas.

CONCLUSION

Identification of cancer stem cells in the prostate cancer tissue is a promising diagnosis and outcome prediction method. High expression of Nanog is associated with higher proliferative

Table. Relationship between the expression of Ki-67 and Nanog and the major clinical and morphological characteristics

Clinical and morphological characteristics	Number of cases, N (%), 68 in total	Expression of Ki-67				Expression of Nanog (histochemical score)		
		Score 1	Score 2	Score 3	Significance level, <i>p</i>	Weak (<40)	Strong (>40)	Significance level, <i>p</i>
Tumor extension								
Localized cancer (T1, T2)	39 (57.4%)	19 (27.9%)	17 (25%)	5 (7.4%)	0.046	8 (11.8%)	2 (2.9%)	0.041
Advanced cancer (T3, T4)	29 (42.6%)	6 (8.8%)	11 (16.2%)	9 (13.2%)		5 (7.4%)	11 (16.2%)	
PSA level								
<10 ng/mL	51 (75%)	23 (33.8%)	21 (30.9%)	4 (5.9%)	<0.001	9 (13.2%)	5 (7.4%)	0.238
>10 ng/mL	17 (25%)	2 (2.9%)	7 (10.3%)	10 (14.7%)		4 (5.9%)	8 (11.8%)	

activity and worse prognosis of the tumor. The polypotent cancer stem cells may constitute the source for tumor cell population self-renewal and contribute to metastasis and

chemoresistance. The detection of cells possessing such properties requires the selection of more aggressive treatment algorithm aimed primarily at radical tumor removal.

References

1. Kaprin AD, Starinskiy VV, Petrova GV, editors. Malignant tumors in Russia in 2018 (morbidity and fatality). Moscow: FGBU «Moskovskiy nauchno-issledovatel'skiy onkologicheskiy institut im. P.A. Gertsena» — filial FGBU «Natsional'nyy meditsinskiy issledovatel'skiy radiologicheskiy tsentr» Minzdrava Rossii, 2019; 250 p. Russian.
2. Zhou CK, Check DP, Lortet-Tieulent J, Laversanne M, Jemal A, Ferlay J, et al. Prostate cancer incidence in 43 populations worldwide: an analysis of time trends overall and by age group. *Int J Cancer*. 2016; 138 (6): 1388–400.
3. Heidegger I, Heidenreich A, Pfister D. New biomarkers for selecting the best therapy regimens in metastatic castration-resistant prostate cancer. *Target Oncol*. 2017; 12 (1): 37–45.
4. Horner MJ, Ries LAG, Krapcho M, Neyman N, Aminou R, Howlader N, et al (eds). SEER Cancer Statistics Review, 1975–2006, National Cancer Institute. Bethesda, MD. Available from: http://seer.cancer.gov/csr/1975_2006/
5. Bell KJL, Del Mar C, Wright G, Dickinson J, Glasziou P. Prevalence of incidental prostate cancer: a systematic review of autopsy studies. *Int J Cancer*. 2015; 137 (7): 1749–57.
6. Howlader N, Noone AM, Krapcho M, Miller D, Bishop K, Altekruse SF, et al. SEER Cancer Statistics Review 1975–2013 National Cancer Institute SEER Cancer Statistics Review 1975–2013, National Cancer Institute. Bethesda, 2016. Available from: https://seer.cancer.gov/csr/1975_2014/.
7. Thompson IM, Pauler DK, Goodman PJ, et al. Prevalence of Prostate Cancer among Men with a Prostate-Specific Antigen Level \leq 4.0 ng per Milliliter. *N Engl J Med*. 2004; 350 (22): 2239–46.
8. Kreso A, Dick JE. Evolution of the cancer stem cell model. *Cell Stem Cell*. 2014; 14 (3): 275–91. DOI: 10.1016/j.stem.2014.02.006.
9. Aguilar-Gallardo C, Simón C. Cells, stem cells, and cancer stem cells. *Seminars in Reproductive Medicine*. 2013; 31 (01): 005–013. DOI: 10.1055/s-0032-1331792.
10. Bonnet D, Dick JE. Human acute myeloid leukemia is organized as a hierarchy that originates from a primitive hematopoietic cell. *Nat Med*. 1997; 3: 730–7. DOI: 10.1038/nm0797-730.
11. Chambers I, Colby D, Robertson M, Nichols J, Lee S, Tweedie S, Smith A. Functional expression cloning of Nanog, a pluripotency sustaining factor in embryonic stem cells. *Cell*. 2003; 113: 643–55. PubMed PMID: 12787505.
12. Mitsui K, Tokuzawa Y, Itoh H, et al. The homeoprotein Nanog is required for maintenance of pluripotency in mouse epiblast and ES cells. *Cell*. 2003; 113: 631–42.
13. Gawlik-Rzemieniewska N, Bednarek I. The role of NANOG transcriptional factor in the development of malignant phenotype of cancer cells. *Cancer Biol Ther*. 2015; 17 (1): 1–10. DOI:10.1080/15384047.2015.1121348.
14. Boiani M, Scholer HR. Regulatory networks in embryo-derived pluripotent stem cells. *Nat Rev Mol Cell Biol*. 2005; 6: 872–84.
15. Gong S, Li Q, Jeter CR, Fan Q, Tang DG, Liu B. Regulation of NANOG in cancer cells. *Mol Carcinog*. 2015; 54 (9): 679–87. DOI: 10.1002/mc.22340.
16. Hirsch FR, Varella-Garcia M, Bunn PA, et al. Epidermal growth factor receptor in non-small-cell lung carcinomas: correlation between gene copy number and protein expression and impact on prognosis. *J Clin Oncol*. 2003; 21 (20): 3798–807.
17. Battle E, Clevers H. Cancer stem cells revisited. *Nat Med*. 2017; 23 (10): 1124–34. DOI:10.1038/nm.4409.
18. Zhang J, Espinoza LA, Kinders RJ, et al. NANOG modulates stemness in human colorectal cancer. *Oncogene*. 2013 Sep 12; 32 (37): 4397–405.
19. Niu CS, Li DX, Liu YH, Fu XM, Tang SF, Li J. Expression of NANOG in human gliomas and its relationship with undifferentiated glioma cells. *Oncol Rep*. 2011; 26 (3): 593–601.
20. Ibrahim EE, Babaei-Jadidi R, Saadeddin A, et al. Embryonic NANOG activity defines colorectal cancer stem cells and modulates through AP1- and TCF-dependent mechanisms. *Stem Cells*. 2012; 30 (10): 2076–87.
21. Grubelnik G, Boštjančič E, Pavlič A, Kos M, Zidar N. NANOG expression in human development and cancerogenesis. *Exp Biol Med*. 2020; 245 (5): 456–64.
22. Chiou SH, Yu CC, Huang CY, et al. Positive correlations of Oct-4 and Nanog in oral cancer stem-like cells and high-grade oral squamous cell carcinoma. *Clin Cancer Res*. 2008; 14 (13): 4085–95.
23. Gillis AJ, Stoop H, Biermann K, et al. Expression and interdependencies of pluripotency factors LIN28, OCT3/4, NANOG and SOX2 in human testicular germ cells and tumours of the testis. *Int J Androl*. 2011; 34 (4 Pt 2): e160–e174.
24. Chiou SH, Wang ML, Chou YT, et al. Coexpression of oct4 and nanog enhances malignancy in lung adenocarcinoma by inducing cancer stem cell-like properties and epithelial-mesenchymal transdifferentiation. *Cancer Res*. 2010; 70 (24): 10433–4.
25. Han J, Zhang F, Yu M, et al. RNA interference-mediated silencing of NANOG reduces cell proliferation and induces G0/G1 cell cycle arrest in breast cancer cells. *Cancer Lett*. 2012; 321 (1): 80–8.
26. Choi SC, Choi JH, Park CY, Ahn CM, Hong SJ, Lim DS. Nanog regulates molecules involved in stemness and cell cycle-signaling pathway for maintenance of pluripotency of P19 embryonal carcinoma stem cells. *J Cell Physiol*. 2012; 227 (11): 3678–92.

Литература

1. Каприн А. Д., Старинский В. В., Петрова Г. В., редакторы. Злокачественные новообразования в России в 2018 году (заболеваемость и смертность). М.: ФГБУ «Московский научно-исследовательский онкологический институт им. П.А. Герцена» — филиал ФГБУ «Национальный медицинский исследовательский радиологический центр» Минздрава России, 2019; 250 с.
2. Zhou CK, Check DP, Lortet-Tieulent J, Laversanne M, Jemal A, Ferlay J, et al. Prostate cancer incidence in 43 populations worldwide: an analysis of time trends overall and by age group. *Int J Cancer*. 2016; 138 (6): 1388–400.
3. Heidegger I, Heidenreich A, Pfister D. New biomarkers for selecting the best therapy regimens in metastatic castration-resistant prostate cancer. *Target Oncol*. 2017; 12 (1): 37–45.
4. Horner MJ, Ries LAG, Krapcho M, Neyman N, Aminou R, Howlader N, et al (eds). SEER Cancer Statistics Review, 1975–2006, National Cancer Institute. Bethesda, MD. Available from: http://seer.cancer.gov/csr/1975_2006/
5. Bell KJL, Del Mar C, Wright G, Dickinson J, Glasziou P. Prevalence of incidental prostate cancer: a systematic review of autopsy studies. *Int J Cancer*. 2015; 137 (7): 1749–57.
6. Howlader N, Noone AM, Krapcho M, Miller D, Bishop K, Altekruse SF, et al. SEER Cancer Statistics Review 1975–2013 National Cancer Institute SEER Cancer Statistics Review 1975–2013, National Cancer Institute. Bethesda, 2016. Available from: https://seer.cancer.gov/csr/1975_2014/.
7. Thompson IM, Pauler DK, Goodman PJ, et al. Prevalence of Prostate Cancer among Men with a Prostate-Specific Antigen

- Level \leq 4.0 ng per Milliliter. *N Engl J Med.* 2004; 350 (22): 2239–46.
8. Kreso A, Dick JE. Evolution of the cancer stem cell model. *Cell Stem Cell.* 2014; 14 (3): 275–91. DOI: 10.1016/j.stem.2014.02.006.
 9. Aguilar-Gallardo C, Simón C. Cells, stem cells, and cancer stem cells. *Seminars in Reproductive Medicine.* 2013; 31 (01): 005–013. DOI: 10.1055/s-0032-1331792.
 10. Bonnet D, Dick JE. Human acute myeloid leukemia is organized as a hierarchy that originates from a primitive hematopoietic cell. *Nat Med.* 1997; 3: 730–7. DOI: 10.1038/nm0797-730.
 11. Chambers I, Colby D, Robertson M, Nichols J, Lee S, Tweedie S, Smith A. Functional expression cloning of Nanog, a pluripotency sustaining factor in embryonic stem cells. *Cell.* 2003; 113: 643–55. PubMed PMID: 12787505.
 12. Mitsui K, Tokuzawa Y, Itoh H, et al. The homeoprotein Nanog is required for maintenance of pluripotency in mouse epiblast and ES cells. *Cell.* 2003; 113: 631–42.
 13. Gawlik-Rzemieniewska N, Bednarek I. The role of NANOG transcriptional factor in the development of malignant phenotype of cancer cells. *Cancer Biol Ther.* 2015; 17 (1): 1–10. DOI:10.1080/15384047.2015.1121348.
 14. Boiani M, Scholer HR. Regulatory networks in embryo-derived pluripotent stem cells. *Nat Rev Mol Cell Biol.* 2005; 6: 872–84.
 15. Gong S, Li Q, Jeter CR, Fan Q, Tang DG, Liu B. Regulation of NANOG in cancer cells. *Mol Carcinog.* 2015; 54 (9): 679–87. DOI: 10.1002/mc.22340.
 16. Hirsch FR, Varella-Garcia M, Bunn PA, et al. Epidermal growth factor receptor in non-small-cell lung carcinomas: correlation between gene copy number and protein expression and impact on prognosis. *J Clin Oncol.* 2003; 21 (20): 3798–807.
 17. Batlle E, Clevers H. Cancer stem cells revisited. *Nat Med.* 2017; 23 (10): 1124–34. DOI:10.1038/nm.4409.
 18. Zhang J, Espinoza LA, Kinders RJ, et al. NANOG modulates stemness in human colorectal cancer. *Oncogene.* 2013 Sep 12; 32 (37): 4397–405.
 19. Niu CS, Li DX, Liu YH, Fu XM, Tang SF, Li J. Expression of NANOG in human gliomas and its relationship with undifferentiated glioma cells. *Oncol Rep.* 2011; 26 (3): 593–601.
 20. Ibrahim EE, Babaei-Jadidi R, Saadeddin A, et al. Embryonic NANOG activity defines colorectal cancer stem cells and modulates through AP1- and TCF-dependent mechanisms. *Stem Cells.* 2012; 30 (10): 2076–87.
 21. Grubelnik G, Boštjančič E, Pavlič A, Kos M, Zidar N. NANOG expression in human development and cancerogenesis. *Exp Biol Med.* 2020; 245 (5): 456–64.
 22. Chiou SH, Yu CC, Huang CY, et al. Positive correlations of Oct-4 and Nanog in oral cancer stem-like cells and high-grade oral squamous cell carcinoma. *Clin Cancer Res.* 2008; 14 (13): 4085–95.
 23. Gillis AJ, Stoop H, Biermann K, et al. Expression and interdependencies of pluripotency factors LIN28, OCT3/4, NANOG and SOX2 in human testicular germ cells and tumours of the testis. *Int J Androl.* 2011; 34 (4 Pt 2): e160–e174.
 24. Chiou SH, Wang ML, Chou YT, et al. Coexpression of oct4 and nanog enhances malignancy in lung adenocarcinoma by inducing cancer stem cell-like properties and epithelial-mesenchymal transdifferentiation. *Cancer Res.* 2010; 70 (24): 10433–4.
 25. Han J, Zhang F, Yu M, et al. RNA interference-mediated silencing of NANOG reduces cell proliferation and induces G0/G1 cell cycle arrest in breast cancer cells. *Cancer Lett.* 2012; 321 (1): 80–8.
 26. Choi SC, Choi JH, Park CY, Ahn CM, Hong SJ, Lim DS. Nanog regulates molecules involved in stemness and cell cycle-signaling pathway for maintenance of pluripotency of P19 embryonal carcinoma stem cells. *J Cell Physiol.* 2012; 227 (11): 3678–92.

PROSPECTIVE PHARMACOLOGICAL EFFECTS OF PSORALEN PHOTOOXIDATION PRODUCTS AND THEIR CYCLOADDUCTS WITH AMINOTHIOLS: CHEMOINFORMATIC ANALYSIS

Skarga W^{1,2}✉, Zadorozhny AD¹, Shilov BV¹, Nevezhin EV¹, Negrebetsky VV¹, Maslov MA², Lagunin AA^{1,3}, Malakhov MV¹

¹ Pirogov Russian National Research Medical University, Moscow, Russia

² MIREA — Russian Technological University, Moscow, Russia

³ Institute of Biomedical Chemistry (IBMC), Moscow, Russia

Psoralens are medicinal photosensitizing furocoumarins which are used in photochemotherapy and photoimmunotherapy of dermatoses. Psoralen photooxidation products may be involved in therapeutic effects, but the possible mechanisms of their action remain unclear. The study was aimed to assess the prospective pharmacological effects and mechanisms of activity for six previously identified ortho-hydroxyformyl-containing psoralen photooxidation products and their cycloadducts with aminothiols, as well as for structurally similar compounds (furocoumaric acid and tucaresol). Chemoinformatic analysis of the prospective pharmacological effects and mechanisms of action of these compounds was performed using the PASS and PharmaExpert software. The predicted pharmacological effects partially confirmed by previous studies highlight the possible involvement of psoralen photooxidation products in the effects of PUVA therapy or photopheresis during the course of dermatoses and proliferative disorders treatment. A broad spectrum of pharmacological effects found for furocoumaric acid and cycloadducts of coumarinic and benzofuranic photoproducts of psoralen with cysteine and homocysteine appoints new directions of research relating to therapeutic use of psoralens.

Keywords: psoralens, coumarins, benzofurans, aldehydes, furocoumaric acid, aminothiols, (Q)SAR, PASS, PharmaExpert

Funding: the study was supported by RFBR, project number 19-33-90277.

Author contribution: Skarga W — literature analysis, data analysis and interpretation, manuscript writing and editing; Zadorozhny AD, Shilov BV — data acquisition and analysis; Nevezhin EV — literature analysis, data interpretation; Negrebetsky VV — data interpretation, manuscript writing; Maslov MA — study design; Lagunin AA — study design, literature analysis, manuscript writing; Malakhov MV — study design, literature analysis, data interpretation, manuscript writing and editing.

✉ **Correspondence should be addressed:** Vladislav V. Skarga
Ostrovityanova, 1, Moscow, 117437; skargavlad@gmail.com

Received: 27.08.2020 **Accepted:** 22.09.2020 **Published online:** 09.10.2020

DOI: 10.24075/brsmu.2020.059

ПОТЕНЦИАЛЬНЫЕ ФАРМАКОЛОГИЧЕСКИЕ ЭФФЕКТЫ ПРОДУКТОВ ФОТООКИСЛЕНИЯ ПСОРАЛЕНА И ИХ ЦИКЛОАДДУКТОВ С АМИНОТИОЛАМИ: ХЕМОИНФОРМАЦИОННЫЙ АНАЛИЗ

В. В. Скарга^{1,2}✉, А. Д. Задорожный¹, Б. В. Шилов¹, Е. В. Невежин¹, В. В. Негребетский¹, М. А. Маслов², А. А. Лагунин^{1,3}, М. В. Малахов¹

¹ Российский национальный исследовательский медицинский университет имени Н. И. Пирогова, Москва, Россия

² МИРЭА — Российский технологический университет, Москва, Россия

³ Научно-исследовательский институт биомедицинской химии имени В. Н. Ореховича, Москва, Россия

Псоралены, медицинские фотосенсибилизаторы фурукумаринового ряда, используют для фотохимиотерапии и фотоиммунотерапии дерматозов. Продукты фотоокисления псораленов могут принимать участие в реализации терапевтических эффектов, однако возможные механизмы их действия остаются неизвестными. Основной целью работы было оценить потенциальные фармакологические эффекты и возможные механизмы действия шести ранее идентифицированных продуктов фотоокисления псоралена, характеризующихся наличием орто-гидроксиформильной группировки, их циклоаддуктов с аминотиолами, а также структурно родственных соединений (фурукумариновой кислоты и тукарезола). Хемоинформационный анализ потенциальных фармакологических эффектов и возможных механизмов действия указанных соединений был проведен с использованием программ PASS и PharmaExpert. Предсказанные фармакологические эффекты, частично подтверждаемые результатами ранее проведенных исследований, свидетельствуют о возможном участии продуктов фотоокисления псораленов в реализации эффектов PUVA-терапии или фотофереза при лечении ряда дерматозов и пролиферативных патологий. Широкий спектр фармакологических эффектов, обнаруженный для фурукумариновой кислоты и циклоаддуктов кумариновых и бензофурановых фотопродуктов псоралена с цистеином и гомоцистеином, определяет новые направления исследований в области терапевтического применения псораленов.

Ключевые слова: псоралены, кумарины, бензофураны, альдегиды, фурукумариновая кислота, аминотиолы, (Q)SAR, PASS, PharmaExpert

Финансирование: исследование выполнено при финансовой поддержке РФФИ в рамках научного проекта № 19-33-90277.

Вклад авторов: В. В. Скарга — анализ литературы, анализ и интерпретация данных, подготовка и окончательная редакция текста рукописи; А. Д. Задорожный, Б. В. Шилов — сбор и анализ данных; Е. В. Невежин — анализ литературы, интерпретация данных; В. В. Негребетский — интерпретация данных, подготовка текста рукописи; М. А. Маслов — дизайн исследования; А. А. Лагунин — дизайн исследования, анализ литературы, подготовка текста рукописи; М. В. Малахов — дизайн исследования, анализ литературы, интерпретация данных, подготовка и окончательная редакция текста рукописи.

✉ **Для корреспонденции:** Владислав Викторович Скарга
ул. Островитянова, д. 1, г. Москва, 117437; skargavlad@gmail.com

Статья получена: 27.08.2020 **Статья принята к печати:** 22.09.2020 **Опубликована онлайн:** 09.10.2020

DOI: 10.24075/vrgmu.2020.059

Psoralens are plant-derived or synthetic linear furanocoumarins which are able to sensitize biological objects to near-ultraviolet radiation (UVA, 320–400 nm) [1]. PUVA (*Psoralen and UV-A*) therapy and extracorporeal photopheresis, both based on photosensitizing effects of psoralens, are widely used in medicine

for treatment of such disorders as psoriasis, vitiligo, atopic dermatitis, eczema, cutaneous T-cell lymphoma, scleroderma (systemic sclerosis), graft-versus-host reaction and a number of other diseases [2–9]. PUVA therapy and photopheresis are now understood to be based on antiproliferative and apoptotic

effects towards keratinocytes and immunocompetent cells, as well as on induction of immunosuppression, i.e. the described treatment methods should be considered as photochemotherapy and photoimmunotherapy [2–9]. It is important to emphasize that for the reasons of versatility, cost-efficiency and safety, the clinical significance of PUVA therapy and photopheresis does not depreciate in the modern era of biologicals development and use [6, 7, 9].

During PUVA therapy or photopheresis, the patient's skin or leukapack derived therefrom, respectively, are exposed to PUVA treatment. Previously, we have proposed the treatment modality for psoriasis, atopic dermatitis and eczema based on oral administration to patients of psoralen preliminary photooxidized *in vitro* (POP) and able to induce the immunotherapeutic effect *in vivo* [10, 11]. The described effect was studied in the murine model of contact hypersensitivity to dinitrofluorobenzene (DNFB) being an experimental analogue of atopic dermatitis in humans [11, 12]. It was shown that POP modulated the production of secretory cytokines by the lymph node cells of DNFB-sensitized mice. POP reduced production of IL2, IL4 and IFN- γ , increased secretion of IL17, but did not affect the production of IL6 and IL10 [11]. Furthermore, it was found that administration of POP to DNFB-sensitized mice resulted in reduced number of cells in the regional lymph nodes, decreased proliferative activity of cells, and apoptosis induction [11]. The results obtained were consistent with the modern concepts on the molecular basis of PUVA therapy and photopheresis [2–9], and made it possible to consider POP as a prospective agent for treatment of pathologies caused by T-cell immunity hyperresponsiveness.

It is known that POP is a complex mixture of photoproducts produced during the photolysis of aerated psoralen solution *in vitro* [13, 14]. However, only some of those were isolated from mixture and chemically identified due to extremely low yield in photoreactions and instability during separation and/or analytical procedures [13–16]. The *in vitro* analysis of photooxidized psoralens revealed their apoptotic activity [16, 17], as well as the ability to affect cell proliferation and differentiation [15, 17]. It is noteworthy that apoptotic effect was observed only in the transformed T-cell lines (Jurkat cell line), whereas in normal lymphocytes derived from healthy donors no apoptotic effects were detected [16]. That observation makes it possible to suggest that the apoptotic activity of psoralen photoproducts is specific, and that photoproducts play a vital part in PUVA therapy and photopheresis effects.

Currently, chemoinformatics is widely used to predict the biological activity of organic compounds. The software products created for this purpose enable the precise prediction of biological activity profiles based on the structural formulae of low molecular weight compounds under study [18–22].

The present study was aimed to assess the prospective pharmacological effects and mechanisms of action for previously identified psoralen photooxidation products and their cycloadducts with aminothiols, to reveal correlations between the results of chemoinformatic analysis and previously reported immunotropic (therapeutic) effects of such products, as well as to appoint new directions of research in this field.

METHODS

The prospective pharmacological effects were predicted using the PASS (*Prediction of Activity Spectra for Substances*) software ver. 2019 (IBM; Russia) [18, 19] making it possible to assess the biological activity profile of an organic compound based on its structural formula. Assessment is based on

the structure–activity relationship analysis of the training set including more than one million of compounds tested for biological activity. In the PASS software, the biological activity is presented qualitatively (active/inactive). The chemical structure is represented by the MNA (*Multilevel Neighborhoods of Atoms*) descriptors [20]. The algorithm of the structure–activity relationship modeling based on the training set compounds, and the new compounds activity prediction uses the modified Bayesian algorithm [18, 19]. The used version of PASS software (PASS 2019) predicts over 5000 different types of biological activity, including therapeutic effects, 3818 mechanisms of action, and side effects with average accuracy of about 95% (leave-one-out cross-validation procedure).

The information on structural formula of the compound presented in the Molfile format is used as the PASS input data. The list of predicted activities with probabilities “to be active” P_a and “to be inactive” P_i varying from 0 to 1 is generated as the output. The probabilities P_a and P_i are also estimates of the type I and type II error probabilities, respectively, and may be considered as a measure of the predicted compound assignment to the subset of “active” or “inactive” substances. For specific type of activity, the greater P_a value and the smaller P_i value are predicted, the higher is the chance to confirm the predicted activity by experiment.

In the present study, prediction and analysis of prospective pharmacological effects and corresponding mechanisms of action were performed using the PharmaExpert ver. 2019 software (IBM; Russia) [21] with 50% cut-off probability of predicted activity signs (the activity was considered probable when the P_a value was above 0.5 and exceeded the P_i value). The PharmaExpert software is intended for analysis of PASS prediction results, which are based on the “target-pathway-effect” relationships stored in the PharmaExpert database (current version, issued in 2019, contains information for more than 15,000 such relationships).

The molecular structures of compounds under study were used in the search for identical and similar compounds in PubChem, the largest free database containing data (both experimental and patent) on molecular structure and biological activity for more than 100 million chemical compounds [22]. The search for identical and similar compounds is based on their structure description as PubChem fingerprints (881-bit vectors describing the structural features of the compounds). It is known that compounds with similar structure may exhibit similar activity, and identification of similar compounds with known biological activity may help in planning experimental studies. In the present study, the PubChem built-in tool using the Tanimoto coefficient calculated from PubChem fingerprints as a measure of structural similarity was used for similarity-based search [23]:

$$T(X, Y) = (N(X \cap Y)) / (N(X \cup Y)),$$

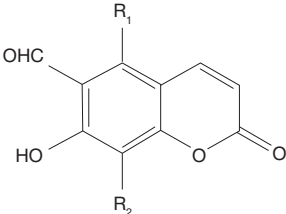
where $N(X \cap Y)$ was the number of common descriptors for compounds X and Y , and $N(X \cup Y)$ was the total number of unique descriptors for compounds X and Y . The Tanimoto coefficient values exceeding 0.9 and 0.8 were used as a threshold for similarity evaluation.

RESULTS

Rationale for selection of research objects

It is known that the formation of photoproducts possessing immunotropic (therapeutic) effect strictly depends on the

Table 1. Coumarinic POP products

	$R_1 = H$ $R_2 = H$ 1	$R_1 = H$ $R_2 = OMe$ 2	$R_1 = OMe$ $R_2 = H$ 3
Pharmacological effects	P_a / P_i		
Immunosuppressive	-	-	0.541/0.036
Apoptotic	0.899/0.004	0.915/0.004	0.764/0.010
Antitumor	0.741/0.019	0.763/0.017	0.751/0.018
Cytostatic	0.538/0.020	0.586/0.015	0.516/0.023
Antimutagenic	0.807/0.004	0.760/0.005	0.774/0.004
Radioprotective	0.701/0.010	-	0.766/0.006
Analeptic	0.791/0.005	0.769/0.007	0.687/0.011
Antifungal	0.620/0.016	0.631/0.015	0.584/0.020
Antiprotozoal (Trypanosoma)	0.537/0.014	-	-
Antiparasitic	0.513/0.014	0.519/0.014	-
Anthelmintic (nematodes)	0.512/0.015	-	-
Antimycobacterial	0.506/0.018	-	-

presence of oxygen during irradiation of psoralen solution [10]. That makes it possible to limit the search by previously characterized psoralen photooxidation products (POP products). Photolysis products of furocoumarins and the pathways leading to their formation are exhaustively reviewed [13]. This review demonstrated that all processes involving oxidative modification of psoralen and other furocoumarins could be divided into three sets. The first set consists of oxidative furan or pyrone ring opening photoproducts classified as coumarins and benzofurans, respectively. The second set includes photoproducts formed by addition of a solvent molecule to the furan ring of photooxidation intermediate. The third set consists of photoproducts formed during double modification of psoralen molecule, with at least one being oxidative.

After the analysis of literature data on biological activity had been done, we decided to focus on POP products referring to the first set. Coumarins and benzofurans formed during photooxidation of furocoumarins are known to contain *ortho*-hydroxyformyl (OHF) arrangement as the fingerprint and possess the biological activity described above [13, 15, 16]. It was suggested [13] that biological activity of POP products from the first set was due to presence of OHF, similarly to well known immunomodulator tucarezol [24]. That was partially confirmed by the paper reporting the apoptogenic effect of several OHF-containing compounds [16]. Previously, we have shown that OHF-containing photooxidation products of protoporphyrin IX possessed immunotropic activity inducing suppression of contact hypersensitivity reaction in mice [25].

Thus, we determined the set of compounds for chemoinformatic analysis using the PASS and PharmaExpert software. This set includes the OHF-containing coumarinic POP products (compounds 1–3) previously identified for psoralen, 8-methoxypsoralen (8-MOP) and 5-methoxypsoralen (5-MOP), the main furocoumarinic photosensitizers used in medicine [2–9]. The set also includes the known OHF-containing benzofuranic POP products of the three psoralens listed above (compounds 4–6). The OHF-containing tucarezol (compound 7) was added to the set as a reference compound with the known immunotropic effect based on T-cells stimulation by means of Schiff base formation with T-cell receptors [24]. Furthermore, the

prospective pharmacological effects of the furocoumaric acid (compound 8), the psoralen photoproduct suspected of being an intermediate on the pathway to compound 4 during the psoralen photooxidation, were analyzed [26]. A distinct group includes cycloadducts of the OHF-containing POP products with cysteine and homocysteine (compounds 9–12 and 13–16 for coumarinic and benzofuranic POP products, respectively). In the present study, the choice of cysteine and homocysteine is not random. It is known that the OHF-containing coumarins (in particular, 8-formylumbelliferone) are used for fluorometric analysis of above-mentioned amino acids in biological objects [27], and their adducts with amines possess biological activity [28].

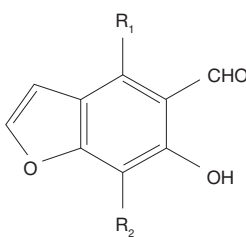
Predicted pharmacological effects of POP products, furocoumaric acid and tucarezol

Tables 1 and 2 summarize the major results of chemoinformatic analysis for the target POP products (compounds 1–6). The only compound with predicted immunotropic (immunosuppressive) activity is coumarinic POP product of 5-MOP. Instead, the high probability of apoptosis inducing activity is predicted for all compounds, with P_a/P_i values for the described type of activity being higher in coumarinic POP products compared to benzofuranic POP products. Furthermore, the antitumor and cytostatic effects are predicted for compounds 1–6.

In addition to the types of antiproliferative activity listed above, the high probability of respiratory (compounds 1–5) and to a lesser extent cardiovascular (compounds 1, 2) analeptic activities, as well as antimutagenic (compounds 1–6) and radioprotective (compounds 1, 3, 4 and 6) activities are predicted. Several other protective types of activity are expected for benzofuranic POP products, especially for compound 4 (vasoprotective, neuroprotective and cardioprotective activities).

The results of analysis demonstrate the broad spectrum of expected antibiotic activity: antifungal activity is predicted for compounds 1–6, and compound 1 is characterized by five types of antibiotic activity at once. When comparing, it can be noted that the antibiotic activity of coumarinic POP products is higher compared to benzofuranic POP products, both in qualitative and quantitative terms.

Table 2. Benzofuranic POP products

	$R_1 = H$ $R_2 = H$ 4	$R_1 = H$ $R_2 = OMe$ 5	$R_1 = OMe$ $R_2 = H$ 6
Pharmacological effects	P_a / P_i		
Apoptotic	0.884/0.005	0.906/0.004	0.702/0.015
Antitumor	0.565/0.053	0.635/0.038	0.613/0.042
Cytostatic	–	0.532/0.021	–
Antimutagenic	0.780/0.004	0.724/0.005	0.741/0.005
Radioprotective	0.662/0.012	–	0.746/0.008
Analeptic	0.580/0.021	0.532/0.027	–
Antifungal	0.531/0.026	0.548/0.024	–
Antimycobacterial	0.510/0.180	–	–
Vasoprotective	0.732/0.009	0.550/0.028	0.523/0.034
Neuroprotective	0.640/0.058	–	0.586/0.080
Cardioprotective	0.539/0.008	–	–

Analysis of predicted mechanisms of action for the types of activity described above leads to the conclusion that antiproliferative activities of the studied compounds may be mediated by their action as apoptosis agonists, and as inhibitors of a number of enzymes (phosphatases, kinases, monophenol oxygenase) and transcription factors (for example, NF- κ B transcription factor). Radioprotective properties may be associated with the ability to inhibit the permeability and promote the integrity of membranes, as well as to act as a free radical scavenger. Antibiotic activity presumably results from the effect of compounds on transmembrane processes and functioning of kinases and membrane proteins (for example, inhibiting the ampH penicillin-binding protein).

Table 3 presents the results on prediction of major pharmacological effects for tucaresol. According to the analysis,

with a high probability tucaresol possesses anti-inflammatory activity in intestine, as well as neurotropic protective effects (antineurotoxic and neuroprotective activities).

The profiles of the pharmacological effects predicted for furocoumaric acid were found to be surprisingly broad (Table 4). It is assumed that acting mainly as a free radical scavenger and maintaining the integrity of membranes furocoumaric acid provides a wide range of protective effects (including antimutagenic, neuroprotective, vasoprotective, radioprotective, anticarcinogenic, etc.), affects metabolic pathways (regulates lipid metabolism, reduces cholesterolemia), provides anti-inflammatory and antioxidant protection, and also possesses prospective dermatologic (in particular, antipsoriatic) therapeutic activity due to anti-inflammatory effect and regulation of enzymatic activity.

Table 3. Tucaresol

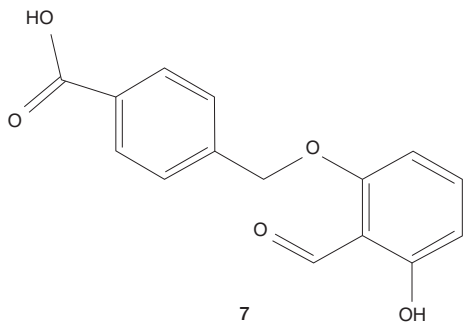
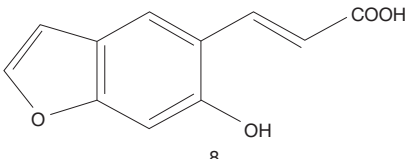
	7
Pharmacological effects	P_a / P_i
Anti-inflammatory (intestine)	0.800/0.004
Treatment of sickle cell disease	0.738/0.002
Antineurotoxic	0.677/0.035
Neuroprotective	0.662/0.039
Antiprotozoal (leishmania)	0.608/0.004
Treatment of precancerous lesions	0.556/0.026
Cytoprotective	0.533/0.020
Radioprotective	0.502/0.022

Table 4. Furocoumaric acid

 8	
Pharmacological effects	P_a / P_i
Antimutagenic	0.896/0.002
Neuroprotective	0.754/0.018
Vasoprotective	0.720/0.006
Regulation of lipid metabolism	0.676/0.012
Antihypercholesterolemic	0.669/0.011
Radioprotective	0.643/0.011
Anticarcinogenic	0.631/0.013
Antipyretic	0.566/0.009
Dermatologic	0.530/0.028
Anti-inflammatory	0.523/0.033
Antioxidant	0.520/0.006

Predicted pharmacological effects of OHF-containing POP products adducts with aminothiols

Tables 5 and 6 present pharmacological effects predicted for cycloadducts of the OHF-containing POP products with aminothiols. Reaction of coumarinic compound 1 with cysteine and homocysteine results in formation of corresponding cycloadducts (see Table 5, compounds 9 and 11). Oxidation of compounds 9 and 11 leads to formation of compounds 10 and 12, respectively (see Table 5). Similarly, the appropriate cycloadducts may be obtained for benzofuranic compound 4 (see Table 6, compounds 13–16).

According to the analysis, compounds 9–15 may function as radioprotectors, with such property being associated with the ability to scavenge free radicals is more likely for nonoxidized cycloadducts (compounds 9, 11, 13, 15). In

addition, it is assumed that compounds 9, 11, 13 and 15 (but not their oxidized forms 10, 12, 14 and 16) possess antitumor activity against a number of malignant neoplasms, such as prostate cancer, liver cancer, and melanoma. For compounds 9–16 hepatoprotective activity is predicted, which may be used for treatment of liver diseases. As with radioprotective properties, this pharmacological effect is attributed to the functioning of compounds 9–16 as reducing agents and free radical scavengers. According to prediction, coumarinic cycloadducts 9–12 possess spasmolytic activity which is realized in urinary tract, with such type of activity not being predicted for benzofuranic cycloadducts 13–16. All oxidized forms of cycloadducts (compounds 10, 12, 14 and 16) are presumably applicable for treatment of neurodegenerative diseases, and compounds 10 and 12 are also potentially active when used in dermatology.

Table 5. Coumarinic POP products cycloadducts with aminothiols

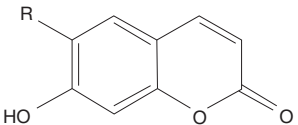
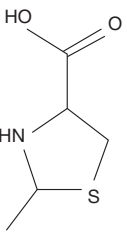
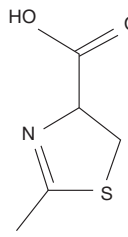
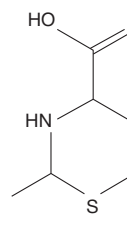
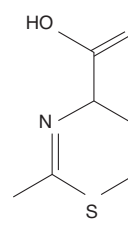
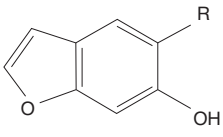
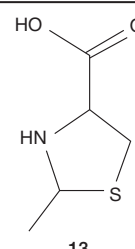
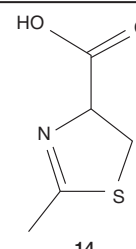
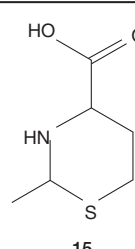
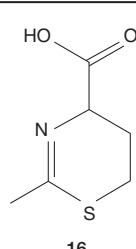
	R			
	 9	 10	 11	 12
Pharmacological effects	P_a / P_i			
Radioprotective	0.857/0.003	0.569/0.015	0.800/0.005	0.513/0.021
Treatment of prostate cancer	0.734/0.004	–	0.640/0.005	–
Antitumor (melanoma)	0.661/0.004	–	0.540/0.006	–
Antitumor (liver cancer)	0.563/0.003	–	0.503/0.003	–
Treatment of liver diseases	0.700/0.004	0.683/0.004	0.555/0.008	0.614/0.005
Antispasmodic (urinary tract)	0.525/0.021	0.577/0.013	0.512/0.023	0.563/0.015
Treatment of neurodegenerative diseases	–	0.528/0.027	–	0.603/0.016
Dermatologic	–	0.522/0.029	–	0.585/0.019

Table 6. Benzofuranic POP products products cycloadducts with aminothiols

	R			
	 13	 14	 15	 16
Pharmacological effects	P_a / P_i			
Radioprotective	0.843/0.004	0.531/0.019	0.783/0.005	–
Treatment of prostate cancer	0.710/0.004	–	0.621/0.006	–
Antitumor (melanoma)	0.670/0.004	–	0.549/0.005	–
Antitumor (liver cancer)	0.579/0.003	–	0.510/0.003	–
Treatment of liver diseases	0.689/0.004	0.672/0.004	0.542/0.008	0.601/0.005
Treatment of neurodegenerative diseases	–	0.658/0.011	–	0.707/0.008

DISCUSSION

The described results of the present study are consistent with literature data. Previously, it has been found that compounds 1 and 2 were apoptosis inducers [16], and the psoralen derivatives were able to inhibit the activity of NF- κ B transcription factor [29]. Furthermore, the predicted antitumor and cytostatic activity of compounds 1–6 may explain some previously detected effects of POP and individual photoproducts. Thus, antitumor activity of POP was revealed in the *in vivo* experiments with murine EL-4 lymphoma as a model of human cutaneous T-cell lymphoma [10], and the benzofuranic POP product (compound 4) possessed teratogenic effect in the experiments on the *Xenopus laevis* embryos [15].

In addition, it has been previously shown that tucareol used by us as the reference compound with known immunotropic activity, possessed antiprotozoal activity in the experimental model of visceral leishmaniasis [30], and was also applicable for treatment of patients with sickle cell anemia [31]. It is noteworthy that the possible use of psoralen photooxidation products for treatment of β -thalassemia and sickle cell anemia has also been reported [17].

Of particular interest is the unexpected discovery of the prospective dermatologic (in particular, antipsoriatic) therapeutic activity of furocoumaric acid resulting from anti-inflammatory effect and regulation of enzymatic activity. The latter two types of biological activity are typical for cinnamic acid derivatives [32], and presumably implemented by furocoumaric acid by means of free radical scavenging, inhibiting lipoxygenase and transcription factors, and maintaining the integrity of membranes.

Oxidized forms of coumarinic cycloadducts with aminothiols potentially possess dermatologic therapeutic activity, but the

predicted activity of the OHF-containing psoralen photooxidation products on homocysteine is of greater interest. It is known that elevated level and/or accumulation of homocysteine may result in a variety of pathologic conditions (Alzheimer's disease, senile dementia, vascular disorders, nephropathy, etc.) [33]. Hence, the predicted therapeutic activity of oxidized cycloadducts resulting from reaction of the OHF-containing psoralen photooxidation products with homocysteine may determine the prospects of their practical usage for therapy of the above-mentioned pathologies.

CONCLUSION

In the present study, chemoinformatic assessment of prospective pharmacological effects and mechanisms of action for previously identified psoralen photooxidation products and their cycloadducts with aminothiols was performed using the PASS and PharmaExpert software. Several predicted pharmacological effects are confirmed with the results of earlier studies, which indicate high prediction efficiency of the analysis. In terms of actual usage of psoralens for treatment of various dermatoses and proliferative disorders, the data obtained are indicative of the possible involvement of psoralen photooxidation products in the realization of the therapeutic effects of PUVA therapy and photopheresis, and therefore are especially valuable. Of special interest is the surprisingly broad spectrum of pharmacological effects found for furocoumaric acid and cycloadducts of coumarinic and benzofuranic photoproducts of psoralen with aminothiols, which appoints new directions of research related to therapeutic use of psoralens.

References

1. Bruni R, Barreca D, Protti M, Brighenti V, Righetti L, Anceschi L, et al. Botanical Sources, Chemistry, Analysis, and Biological Activity of Furanocoumarins of Pharmaceutical Interest. *Molecules*. 2019; 24 (11): 2163. DOI: 10.3390/molecules24112163.
2. Trautinger F, Just U, Knobler R. Photopheresis (extracorporeal photochemotherapy). *Photochem Photobiol Sci*. 2013; 12 (1): 22–8. DOI: 10.1039/c2pp25144b.
3. Racz E, Prens EP. Phototherapy and photochemotherapy for psoriasis. *Dermatol Clin*. 2015; 33 (1): 79–89. DOI: 10.1016/j.det.2014.09.007.
4. Bae JM, Jung HM, Hong BY, Lee JH, Choi WJ, Lee JH, et al. Phototherapy for Vitiligo: A Systematic Review and Meta-analysis. *JAMA Dermatol*. 2017; 153 (7): 666–674. DOI: 10.1001/jamadermatol.2017.0002.
5. Chaowattapanit S, Choonhakarn C, Foocharoen C, Julanon N. Phototherapy in systemic sclerosis: Review. *Photodermatol*

- Photoimmunol Photomed. 2017; 33 (6): 296–305. DOI: 10.1111/phpp.12331.
6. Guitart J. Psoralen Plus UV-A Therapy in the 21st Century: Use It or Lose It. *JAMA Dermatol.* 2019; 155 (5): 529–31. DOI: 10.1001/jamadermatol.2018.5844.
 7. Richard EG. The Science and (Lost) Art of Psoralen Plus UVA Phototherapy. *Dermatol Clin.* 2020; 38 (1): 11–23. DOI: 10.1016/j.det.2019.08.002.
 8. Vieyra-Garcia PA, Wolf P. Extracorporeal Photopheresis: A Case of Immunotherapy Ahead of Its Time. *Transfus Med Hemother.* 2020; 47 (3): 226–35. DOI: 10.1159/000508479.
 9. Torres AE, Lyons AB, Hamzavi IH, Lim HW. Role of phototherapy in the era of biologics. *J Am Acad Dermatol.* 2020; S0190-9622 (20): 30711–8. DOI: 10.1016/j.jaad.2020.04.09.
 10. Potapenko AY, Kyagova AA, Bezdetsnaya LN, Lysenko EP, Chernyakhovskaya IYu, Bekhalo VA, et al. Products of psoralen photooxidation possess immunomodulative and antileukemic effects. *Photochem Photobiol.* 1994; 60 (2): 171–4. DOI: 10.1111/j.1751-1097.1994.tb05086.x.
 11. Pyatnitskiy IA, Pavlova SI, Albegova DZ, Kozlov IG, Potapenko AY, Kyagova AA. Suppressive effects of psoralene photooxidation products on contact sensitivity reaction in mice: lymphocyte proliferation inhibition and apoptosis induction. *Russian journal of skin and venereal diseases.* 2013; 6: 59–63. Russian.
 12. Honda T, Egawa G, Grabbe S, Kabashima K. Update of immune events in the murine contact hypersensitivity model: toward the understanding of allergic contact dermatitis. *J Invest Dermatol.* 2013; 133 (2): 303–15. DOI: 10.1038/jid.2012.284.
 13. Caffieri S. Furocoumarin photolysis: chemical and biological aspects. *Photochem Photobiol Sci.* 2002; 1 (3): 149–57. DOI: 10.1039/b107329j.
 14. Potapenko AY, Malakhov MV, Kyagova AA. Photobiophysics of furocoumarins. *Biophysic.* 2004; 49 (2): 307–24.
 15. Marley KA, Larson RA, Davenport R. Alternative mechanisms of psoralen phototoxicity. *ACS Symposium Series.* 1995; 616 (15): 179–88. DOI: 10.1021/bk-1995-0616.ch015.
 16. Caffieri S, Di Lisa F, Bolesani F, Facco M, Semenzato G, Dall'Acqua F, et al. The mitochondrial effects of novel apoptogenic molecules generated by psoralen photolysis as a crucial mechanism in PUVA therapy. *Blood.* 2007; 109 (11): 4988–94. DOI: 10.1182/blood-2006-08-037192.
 17. Viola G, Salvador A, Vedaldi D, Dall'Acqua F, Bianchi N, Zuccato C, et al. Differentiation and apoptosis in UVA-irradiated cells treated with furocoumarin derivatives. *Ann NY Acad Sci.* 2009; 1171: 334–44. DOI: 10.1111/j.1749-6632.2009.04894.x.
 18. Filimonov DA, Lagunin AA, Glorizova TA, Rudik AV, Druzhilovskij DS, Pogodin PV i dr. Predskazanie spektrov biologicheskoy aktivnosti organicheskikh soedinenij ispol'zuja veb-resurs PASS Online. *Himija geterociklicheskih soedinenij.* 2014; 50 (3): 483–99. DOI: 10.1007/s10593-014-1496-1.
 19. Filimonov DA, Druzhilovskij DS, Lagunin AA, Glorizova TA, Rudik AV, Dmitriev AV, Pogodin PV, Poroikov VV. Computer prediction of the spectra of biological activity of chemical compounds: possibilities and limitations. *Biomedical Chemistry: Research and Methods.* 2018; 1 (1): e00004. DOI: 10.18097/BMCRM00004.
 20. Filimonov D, Poroikov V, Borodina Yu, Glorizova T. Chemical Similarity Assessment through Multilevel Neighborhoods of Atoms: Definition and Comparison with the Other Descriptors. *J Chem Inf Comput Sci.* 1999; 39 (4): 666–70. DOI: 10.1021/ci980335o.
 21. Lagunin AA, Goel RK, Gawande DY, Pahwa P, Glorizova TA, Dmitriev AV, et al. Chemo- and bioinformatics resources for in silico drug discovery from medicinal plants beyond their traditional use: a critical review. *Nat Prod Rep.* 2014; 31 (11): 1585–611. DOI: 10.1039/c4np00068d.
 22. Kim S, Chen J, Cheng T, Gindulyte A, He J, He S, et al. PubChem 2019 update: improved access to chemical data. *Nucleic Acids Res.* 2019; 47 (D1): D1102–9. DOI: 10.1093/nar/gky1033.
 23. Willett P. Similarity-based virtual screening using 2D fingerprints. *Drug Discov Today.* 2006; 11 (23–24): 1046–53.
 24. Chen H, Hall S, Zheng B, Rhodes J. Potentiation of the Immune System by Schiff Base-Forming Drugs. *BioDrugs.* 1997; 7 (3): 217–31. DOI: 10.2165/00063030-199707030-00005.
 25. Kyagova AA, Mansurova GV, Kozir LA, Ponomarev GV, Pavlov VY, Konstantinov IO, et al. Systemic suppression of the contact hypersensitivity by the products of protoporphyrin IX photooxidation. *Photochem Photobiol.* 2005; 81 (6): 1380–5. DOI: 10.1562/2005-04-26-RA-500.
 26. Nevezhin EV, Vlasova NV, Pyatnitskiy IA, Lysenko EP, Malakhov MV. On the mechanism of erythrocyte hemolysis induced by photooxidized psoralen. *Biochemistry (Moscow).* 2015; 80 (6): 763–8. DOI: 10.1134/S0006297915060115.
 27. Yin C, Huo F, Zhang J, Martinez-Mañez R, Yang Y, Lv H, et al. Thiol-addition reactions and their applications in thiol recognition. *Chem Soc Rev.* 2013; 42 (14): 6032–59. DOI: 10.1039/c3cs60055f.
 28. Patil SA, Prabhakara CT, Halasangi BM, Toragalmath SS, Badami PS. DNA cleavage, antibacterial, antifungal and anthelmintic studies of Co(II), Ni(II) and Cu(II) complexes of coumarin Schiff bases: synthesis and spectral approach. *Spectrochim Acta A Mol Biomol Spectrosc.* 2015; 137: 641–51. DOI: 10.1016/j.saa.2014.08.028.
 29. Marzaro F, Lampronti I, Borgatti M, Manzini P, Gambari R, Chilin A. Psoralen derivatives as inhibitors of NF κB DNA interaction — the critical role of the furan ring. *Mol Divers.* 2015; 19 (3): 551–61. DOI: 10.1007/s11030-015-9586-2.
 30. Smith AC, Yardley V, Rhodes J, Croft SL. Activity of the novel immunomodulatory compound tucareol against experimental visceral leishmaniasis. *Antimicrob Agents Chemother.* 2000; 44 (6): 1494–8. DOI: 10.1128/aac.44.6.1494-1498.2000.
 31. Arya R, Rolan PE, Wootton R, Posner J, Bellingham AJ. Tucareol increases oxygen affinity and reduces haemolysis in subjects with sickle cell anaemia. *Br J Haematol.* 1996; 93 (4): 817–21. DOI: 10.1046/j.1365-2141.1996.d01-1744.x.
 32. Sova M. Antioxidant and antimicrobial activities of cinnamic acid derivatives. *Mini Rev Med Chem.* 2012; 12 (8): 749–67. DOI: 10.2174/138955712801264792.
 33. Zaric BL, Obradovic M, Bajic V, Haidara MA, Jovanovic M, Isenovic ER. Homocysteine and Hyperhomocysteinemia. *Curr Med Chem.* 2019; 26 (16): 2948–61. DOI: 10.2174/0929867325666180313105949.

Литература

1. Bruni R, Barreca D, Protti M, Brighenti V, Righetti L, Anceschi L, et al. Botanical Sources, Chemistry, Analysis, and Biological Activity of Furanocoumarins of Pharmaceutical Interest. *Molecules.* 2019; 24 (11): 2163. DOI: 10.3390/molecules24112163.
2. Trautinger F, Just U, Knobler R. Photopheresis (extracorporeal photochemotherapy). *Photochem Photobiol Sci.* 2013; 12 (1): 22–8. DOI: 10.1039/c2pp25144b.
3. Racz E, Prens EP. Phototherapy and photochemotherapy for psoriasis. *Dermatol Clin.* 2015; 33 (1): 79–89. DOI: 10.1016/j.det.2014.09.007.
4. Bae JM, Jung HM, Hong BY, Lee JH, Choi WJ, Lee JH, et al. Phototherapy for Vitiligo: A Systematic Review and Meta-analysis. *JAMA Dermatol.* 2017; 153 (7): 666–674. DOI: 10.1001/jamadermatol.2017.0002.
5. Chaowattanapanit S, Choonhakarn C, Foocharoen C, Julanon N. Phototherapy in systemic sclerosis: Review. *Photodermatol Photoimmunol Photomed.* 2017; 33 (6): 296–305. DOI: 10.1111/phpp.12331.
6. Guitart J. Psoralen Plus UV-A Therapy in the 21st Century: Use It or Lose It. *JAMA Dermatol.* 2019; 155 (5): 529–31. DOI: 10.1001/jamadermatol.2018.5844.
7. Richard EG. The Science and (Lost) Art of Psoralen Plus UVA Phototherapy. *Dermatol Clin.* 2020; 38 (1): 11–23. DOI: 10.1016/j.det.2019.08.002.
8. Vieyra-Garcia PA, Wolf P. Extracorporeal Photopheresis: A Case of Immunotherapy Ahead of Its Time. *Transfus Med Hemother.* 2020; 47 (3): 226–35. DOI: 10.1159/000508479.
9. Torres AE, Lyons AB, Hamzavi IH, Lim HW. Role of phototherapy in the era of biologics. *J Am Acad Dermatol.* 2020; S0190-9622 (20): 30711–8. DOI: 10.1016/j.jaad.2020.04.09.

10. Potapenko AYа, Kyagova AA, Bezdetnaya LN, Lysenko EP, Chernyakhovskaya IYu, Bekhalo VA, et al. Products of psoralen photooxidation possess immunomodulative and antileukemic effects. *Photochem Photobiol.* 1994; 60 (2): 171–4. DOI: 10.1111/j.1751-1097.1994.tb05086.x.
11. Пятницкий И. А., Павлова С. И., Албегова Д. З., Козлов И. Г., Потепенко А. Я., Кягова А. А. Супрессорное действие продуктов фотоокисления псоралена на реакцию контактной чувствительности у мышей: ингибирование пролиферации и индукция апоптоза лимфоцитов. *Российский журнал кожных и венерических болезней.* 2013; 6: 59–63.
12. Honda T, Egawa G, Grabbe S, Kabashima K. Update of immune events in the murine contact hypersensitivity model: toward the understanding of allergic contact dermatitis. *J Invest Dermatol.* 2013; 133 (2): 303–15. DOI: 10.1038/jid.2012.284.
13. Caffieri S. Furocoumarin photolysis: chemical and biological aspects. *Photochem Photobiol Sci.* 2002; 1 (3): 149–57. DOI: 10.1039/b107329j.
14. Potapenko AYа, Malakhov MV, Kyagova AA. Photobiophysics of furocoumarins. *Biophysics.* 2004; 49 (2): 307–24.
15. Marley KA, Larson RA, Davenport R. Alternative mechanisms of psoralen phototoxicity. *ACS Symposium Series.* 1995; 616 (15): 179–88. DOI: 10.1021/bk-1995-0616.ch015.
16. Caffieri S, Di Lisa F, Bolesani F, Facco M, Semenzato G, Dall'Acqua F, et al. The mitochondrial effects of novel apoptogenic molecules generated by psoralen photolysis as a crucial mechanism in PUVA therapy. *Blood.* 2007; 109 (11): 4988–94. DOI: 10.1182/blood-2006-08-037192.
17. Viola G, Salvador A, Vedaldi D, Dall'Acqua F, Bianchi N, Zuccato C, et al. Differentiation and apoptosis in UVA-irradiated cells treated with furocoumarin derivatives. *Ann NY Acad Sci.* 2009; 1171: 334–44. DOI: 10.1111/j.1749-6632.2009.04894.x.
18. Филимонов Д. А., Лагунин А. А., Глорозова Т. А., Рудик А. В., Дружиловский Д. С., Погодин П. В. и др. Предсказание спектров биологической активности органических соединений используя веб-ресурс PASS Online. *Химия гетероциклических соединений.* 2014; 50 (3): 483–99. DOI: 10.1007/s10593-014-1496-1.
19. Филимонов Д. А., Дружиловский Д. С., Лагунин А. А., Глорозова Т. А., Рудик А. В. и др. Компьютерное прогнозирование спектров биологической активности химических соединений: возможности и ограничения. *Biomedical Chemistry: Research and Methods.* 2018; 1 (1): e00004. DOI: 10.18097/BMCRM00004.
20. Filimonov D, Poroikov V, Borodina Yu, Glorizova T. Chemical Similarity Assessment through Multilevel Neighborhoods of Atoms: Definition and Comparison with the Other Descriptors. *J Chem Inf Comput Sci.* 1999; 39 (4): 666–70. DOI: 10.1021/ci980335o.
21. Lagunin AA, Goel RK, Gawande DY, Pahwa P, Glorizova TA, Dmitriev AV, et al. Chemo- and bioinformatics resources for in silico drug discovery from medicinal plants beyond their traditional use: a critical review. *Nat Prod Rep.* 2014; 31 (11): 1585–611. DOI: 10.1039/c4np00068d.
22. Kim S, Chen J, Cheng T, Gindulyte A, He J, He S, et al. PubChem 2019 update: improved access to chemical data. *Nucleic Acids Res.* 2019; 47 (D1): D1102–9. DOI: 10.1093/nar/gky1033.
23. Willett P. Similarity-based virtual screening using 2D fingerprints. *Drug Discov Today.* 2006; 11 (23–24): 1046–53.
24. Chen H, Hall S, Zheng B, Rhodes J. Potentiation of the Immune System by Schiff Base-Forming Drugs. *BioDrugs.* 1997; 7 (3): 217–31. DOI: 10.2165/00063030-199707030-00005.
25. Kyagova AA, Mansurova GV, Kozir LA, Ponomarev GV, Pavlov VY, Konstantinov IO, et al. Systemic suppression of the contact hypersensitivity by the products of protoporphyrin IX photooxidation. *Photochem Photobiol.* 2005; 81 (6): 1380–5. DOI: 10.1562/2005-04-26-RA-500.
26. Nevezhin EV, Vlasova NV, Pyatnitskiy IA, Lysenko EP, Malakhov MV. On the mechanism of erythrocyte hemolysis induced by photooxidized psoralen. *Biochemistry (Moscow).* 2015; 80 (6): 763–8. DOI: 10.1134/S0006297915060115.
27. Yin C, Huo F, Zhang J, Martínez-Máñez R, Yang Y, Lv H, et al. Thiol-addition reactions and their applications in thiol recognition. *Chem Soc Rev.* 2013; 42 (14): 6032–59. DOI: 10.1039/c3cs60055f.
28. Patil SA, Prabhakara CT, Halasangi BM, Toragalmath SS, Badami PS. DNA cleavage, antibacterial, antifungal and anthelmintic studies of Co(II), Ni(II) and Cu(II) complexes of coumarin Schiff bases: synthesis and spectral approach. *Spectrochim Acta A Mol Biomol Spectrosc.* 2015; 137: 641–51. DOI: 10.1016/j.saa.2014.08.028.
29. Marzaro F, Lampronti I, Borgatti M, Manzini P, Gambari R, Chilin A. Psoralen derivatives as inhibitors of NF κB DNA interaction — the critical role of the furan ring. *Mol Divers.* 2015; 19 (3): 551–61. DOI: 10.1007/s11030-015-9586-2.
30. Smith AC, Yardley V, Rhodes J, Croft SL. Activity of the novel immunomodulatory compound tucaresol against experimental visceral leishmaniasis. *Antimicrob Agents Chemother.* 2000; 44 (6): 1494–8. DOI: 10.1128/aac.44.6.1494-1498.2000.
31. Arya R, Rolan PE, Wootton R, Posner J, Bellingham AJ. Tucaresol increases oxygen affinity and reduces haemolysis in subjects with sickle cell anaemia. *Br J Haematol.* 1996; 93 (4): 817–21. DOI: 10.1046/j.1365-2141.1996.d01-1744.x.
32. Sova M. Antioxidant and antimicrobial activities of cinnamic acid derivatives. *Mini Rev Med Chem.* 2012; 12 (8): 749–67. DOI: 10.2174/138955712801264792.
33. Zaric BL, Obradovic M, Bajic V, Haidara MA, Jovanovic M, Isenovic ER. Homocysteine and Hyperhomocysteinaemia. *Curr Med Chem.* 2019; 26 (16): 2948–61. DOI: 10.2174/0929867325666180313105949.

EFFECT OF NEUROMODULATION ON NEUROTROPHIC FACTORS IN PATIENTS WITH CHRONIC DISORDERS OF CONSCIOUSNESS

Iazeva EG [✉], Legostaeva LA, Bakulin IS, Poydasheva AG, Abaimov DA, Suponeva NA, Shabalina AA, Ryabinkina YV, Piradov MA

Research Center of Neurology, Moscow, Russia

Transcranial magnetic stimulation (TMS) is one of rehabilitation approaches for patients with chronic disorders of consciousness (DOC). The aim of our study was to assess neurotrophic factors and the changes of those after TMS course in patients with chronic DOC. We enrolled 26 patients with chronic DOC of various etiology and 21 healthy volunteers. Blood serum and cerebrospinal fluid (CSF) were collected from all patients before and after the TMS course, the levels of BDNF, NSE, NGF, PDGF, GDNF and NT3 were assessed in the biomaterial. The blood BDNF, NSE, PDGF, GDNF and NT3 in patients with chronic DOC were higher compared to healthy volunteers ($p < 0.05$). We found no correlations between the type of DOC and neurotrophic factors concentrations in blood and CSF. The CSF level of BDNF in patients after traumatic brain injury (TBI) was higher compared to patients with non-traumatic chronic DOC ($p < 0.05$). We also found the increase of CSF BDNF after the TMS course in patients after TBI ($p < 0.05$). No other significant differences between groups and another blood and cerebrospinal fluid biomarker levels were detected. Thus, the serum BDNF, NSE, PDGF, GDNF and NT3 levels in patients with chronic DOC were higher compared to healthy volunteers. The BDNF level in CSF was higher in patients with traumatic DOC, and it also increased after the course of high-frequency TMS in this group. This fact may indicate the long-term neuronal plasticity processes in patients after TBI, as well as more favorable rehabilitation prognosis.

Keywords: disorders of consciousness, vegetative state, unresponsive wakefulness syndrome, minimally consciousness state, BDNF, NSE, PDGF, NT3, neurotrophic factors, transcranial magnetic stimulation

Funding: the study was supported by Russian Science Foundation (RSF) grant 16-15-00274.

Author contribution: Iazeva EG — clinical practice, clinical assessment, collecting biomaterials, manuscript writing; Legostaeva LA — clinical practice, clinical assessment, collecting biomaterials; Bakulin IS, Poydasheva AG — rTMS, manuscript writing; Abaimov DA, Shabalina AA — laboratory tests; Suponeva NA, Ryabinkina YV, Piradov MA — study planning and management.

Compliance with ethical standards: the study was approved by the Ethics Committee of the Research Center of Neurology (protocol No. 9-5.16 dated October 26, 2016). Patients were included in the study after obtaining the informed consent from their legal representatives.

✉ **Correspondence should be addressed:** Elizaveta G. Iazeva
Volokolamskoye shosse, 80, Moscow, 125367; yazeva@neurology.ru

Received: 19.08.2020 **Accepted:** 05.09.2020 **Published online:** 23.09.2020

DOI: 10.24075/brsmu.2020.056

ВЛИЯНИЕ КУРСА НЕЙРОМОДУЛЯЦИИ НА ПРОФИЛЬ НЕЙРОТРОФИЧЕСКИХ ФАКТОРОВ У ПАЦИЕНТОВ С ХРОНИЧЕСКИМИ НАРУШЕНИЯМИ СОЗНАНИЯ

Е. Г. Язева [✉], Л. А. Легостаева, И. С. Бакулин, А. Г. Пойдашева, Д. А. Абаимов, Н. А. Супонева, А. А. Шабалина, Ю. В. Рябинкина, М. А. Пирадов

Научный центр неврологии, Москва, Россия

Одним из методов реабилитации пациентов с хроническим нарушением сознания (ХНС) является транскраниальная магнитная стимуляция (ТМС). Целью работы было изучить нейротрофические факторы у пациентов с ХНС и их изменение на фоне применения курса ТМС. Пациентам с ХНС различной этиологии в хронических сроках (26 человек) и здоровым добровольцам (21 человек) проводили курс ритмической ТМС левой ангулярной извилины. У всех участников собирали образцы сыворотки крови и ликвора до и после курса. В биоматериале исследовали уровни BDNF, NSE, NGF, PDGF, GDNF, NT3. Показано, что уровни BDNF, NSE, PDGF, GDNF, NT3 в крови у пациентов с ХНС выше, чем у здоровых добровольцев ($p < 0,05$). Не выявлено различий в концентрации нейротрофических факторов в крови и ликворе в зависимости от формы ХНС. У пациентов с последствиями черепно-мозговой травмы уровень BDNF в ликворе оказался выше, чем у пациентов с нетравматической этиологией ХНС ($p < 0,05$). После проведения курса ТМС показано увеличение уровня BDNF в ликворе у посттравматических пациентов ($p < 0,05$). Других значимых изменений по группам и другим биомаркерам в крови и ликворе выявлено не было. Таким образом, уровни нейротрофических факторов BDNF, NSE, PDGF, GDNF, NT3 в сыворотке крови пациентов с ХНС выше, чем у здоровых добровольцев. Уровень BDNF в ликворе пациентов был выше при посттравматическом ХНС и увеличивался после проведения курса высокочастотной ТМС у этой группы. Это может свидетельствовать о длительных процессах нейропластичности, происходящих у пациентов после черепно-мозговой травмы, и более благоприятном реабилитационном прогнозе.

Ключевые слова: хронические нарушения сознания, вегетативное состояние, синдром ареактивного бодрствования, состояние минимального сознания, BDNF, NSE, PDGF, NT3, нейротрофические факторы, транскраниальная магнитная стимуляция

Финансирование: работа выполнена при поддержке гранта Российского научного фонда (РНФ) 16-15-00274.

Вклад авторов: Е. Г. Язева — клиническая работа, клиническая оценка, сбор биоматериалов, подготовка рукописи; Л. А. Легостаева — клиническая работа, клиническая оценка, сбор биоматериалов; И. С. Бакулин, А. Г. Пойдашева — выполнение rTMS, подготовка рукописи; Д. А. Абаимов, А. А. Шабалина — выполнение лабораторных исследований; Н. А. Супонева, Ю. В. Рябинкина, М. А. Пирадов — планирование и руководство исследованием.

Соблюдение этических стандартов: исследование одобрено этическим комитетом Научного центра неврологии (протокол № 9-5.16 от 26 октября 2016 г.). Пациентов включали в исследование после получения от их родственников добровольного письменного информированного согласия.

✉ **Для корреспонденции:** Elizaveta Grigorievna Iazeva
Волоколамское шоссе, д. 80, г. Москва, 125367; yazeva@neurology.ru

Статья получена: 19.08.2020 **Статья принята к печати:** 05.09.2020 **Опубликована онлайн:** 23.09.2020

DOI: 10.24075/vrgmu.2020.056

Advancements in intensive care led to increased number of patients who survived severe brain injury and numerous disabled patients with chronic disorders of consciousness (DOC) including the vegetative state (VS), also known as unresponsive wakefulness syndrome (UWS), the minimally conscious state (MCS) and the emergence from MCS (eMCS). As is well known, the spontaneous opening of eyes with no signs of self- or environmental awareness is typical for VS. MCS is distinguished by minimal but clearly discernible evidence of awareness [1–4]. Patients with chronic DOC pose many significant challenges for health professionals and society, such as development of approaches to social adaptation of patients, and search for rehabilitation methods with proven effectiveness. That creates a large field for clinical and fundamental neuroscientific research.

Currently, most studies of chronic DOC are focused on neurophysiological and neuroimaging features of the impaired consciousness, as well as on implementation of various methods for the consciousness level improvement. Of those, the noninvasive neuromodulation techniques attract most attention, such as transcranial magnetic stimulation (TMS) and transcranial direct current stimulation (tDCS) [5]. However, the study of biochemical changes in the nervous tissue is relegated to the background. To date, a large number of neurotrophic factors are known. The factors are involved in the central nervous system (CNS) functional regeneration, and may be used as neuronal plasticity markers.

In the context of chronic DOC and recovery of consciousness the brain-derived neurotrophic factor (BDNF) is of particular interest. It is known as one of the most active neuroprotective factors, and is involved in regeneration of neurons both during the acute phase of brain tissue damage and in chronic one [6]. Among other neurotrophins involved in neural plasticity process are neurotrophin-3 (NT3), glial cell derived neurotrophic factor (GDNF), platelet derived growth factor (PDGF), and nerve growth factor (NGF). Neurotrophic factors are generally studied in the context of search for possible neurodegenerative diseases treatment methods [6], however, the experience of using them for treatment of injuries to nervous tissue had been also reported [7]. NT3 is known mainly as a factor responsible for stimulation of fetal neurogenesis. It is involved in generation of neurons from stem cells and in regeneration of neurons in adults [8]. GDNF increases the survival rate of dopaminergic and motor neurons, therefore, it is also considered a factor promoting the nervous tissue repair [9]. PDGF is best known for its effect on angiogenesis and mesenchymal stem cells. Furthermore, PDGF stimulates glial cells (oligodendrocytes, for instance), which affects the neurons functioning and regeneration [10]. NGF stimulates growth and repair of neurons [6]. Another potentially interesting protein is the marker of neuronal injury, the neuron specific enolase (NSE). NSE is commonly studied in the context of acute conditions (acute traumatic brain injury, cardiac arrest). It shows the prognostic value during the acute brain injury both for subsequent consciousness recovery and brain death [11, 12].

Very few studies so far assessed neurotrophic factors in patients with chronic DOC, and their potential role in the recovery of consciousness remains unknown. As previously mentioned, one of the major approaches to rehabilitation of such patients is the noninvasive brain stimulation, particularly TMS. A number of papers report the changes of plasma BDNF, NT3, GDNF and PDGF levels in patients after TMS, which might be interesting in terms of studying the damaged nervous tissue repair mechanisms [13–15].

Currently, the prognostic value of biochemical markers for chronic DOC generally remains understudied, as well as their correlations with repair processes. The study was

aimed to assess the neurotrophic factors levels in blood and cerebrospinal fluid (CSF) of patients with chronic DOC and their change during the course of repetitive TMS (rTMS).

METHODS

Inclusion criteria were: age over 18 years; chronic DOC (vegetative state or minimally conscious state); within a period of more than 3 months for non-traumatic brain injury or more than 12 months after traumatic brain injury (TBI); traumatic and non-traumatic etiology (after hypoxia, CNS infections, stroke, etc.); stable condition of the patient; no current infectious complications, disfunctions of organs and systems; no contraindications of rTMS. We performed routine EEG to ensure the safety of rTMS in patients with organic lesions of the CNS [16]. Exclusion criteria: patients with epileptiform discharges on EEG screening were excluded.

Patients after admission were examined with the validated Russian version of the Coma Recovery Scale — Revised (CRS-R) score [17], then we conducted venipuncture for blood sampling and lumbar puncture in accordance with standard protocol for CSF sampling. After that we delivered the high-frequency rTMS protocol over the left angular gyrus [18]. The patient's rehabilitation also included standard procedures, such as physical exercises, massage therapy and verticalization. After the rTMS course the patients were assessed with the CRS-R score again. The second sampling of serum and CSF was performed within 24 hours after the last rTMS session.

After sampling of biomaterials, blood was subjected to centrifugation in order to obtain serum. The serum and CSF samples were subsequently frozen at -71°C . The levels of BDNF, NSE, NGF, PDGF, GDNF, NT3 were evaluated. Detection and quantification were performed by sandwich enzyme linked immunosorbent assay (ELISA). The R&D Systems (USA, China) and Vector-Best (Russia) reagent kits were used. The calibrators provided by the reagent manufacturers were used in all studies. The duplicate readings were performed with VICTOR 2 system (PerkinElmer; USA) using the lyophilized control serum/plasma samples with low and high values of studied parameters.

The control group included healthy volunteers, from whom serum samples were obtained.

Statistical analysis was carried out by means of the SPSS Statistics v23 software. We performed the biomarker levels intergroup comparisons using the Mann–Whitney *U*-test. We tested differences between biomarkers' levels before and after the rTMS course using the Wilcoxon signed-rank test (the differences between groups were accepted when $p < 0.05$). Quantitative data were reported as median, lower and upper quartiles (Me [LQ, UQ]).

RESULTS

We enrolled 26 patients and 21 healthy volunteers. The surveyed patients' demographics and structure of diagnosis are listed in Table 1. The sex ratio in the group of healthy volunteers (M/F) was 8/13, and the average age was 30 [27; 36] years. We didn't find significant gender and age differences between healthy volunteers and the patients.

The blood and CSF analysis results are listed in Tables 2 and 3. The levels of BDNF, NSE, PDGF, GDNF, and NT3 in serum were significantly higher in patients with chronic DOC, than in healthy volunteers, but there were no differences in NGF levels.

We didn't find any differences in serum BDNF, NSE, NGF, PDGF, GDNF, NT3 both between groups of patients with VS/UWS and MCS, and due to DOC etiology.

Table 1. Baseline characteristics of patients included in the study of biochemical markers in chronic DOC

Parameter	Total DOC	Type of DOC			DOC Etiology		
		VS/UWS	MCS	<i>p</i>	TBI	Non-traum.	<i>p</i>
Type of DOC (VS/ MCS)	26	14	12		10	16	0.02
Age, yr.	27 [23; 41]	25 [23; 33]	29 [24; 44]	0.86	24 [21; 25]	33 [25; 47]	0.01
Sex (M/F)	16/10	7/7	9/3	0.05	7/3	7/7	0.18
Etiology (TBI/non-traum.)	10/16	3/11	7/5	0.06	10	16	
Time postinjury, months	12 [8; 22]	12 [8; 19]	14 [9; 23]	0.63	14 [12; 21]	12 [7; 22]	0.7
CRS-R score before rTMS	7 [6; 11.75]	6 [6; 6]	13 [10; 17]	<0.01	12 [7; 15]	6 [6; 9]	0.03

Note: VS — vegetative state; non-traum. — non-traumatic; MCS — minimally conscious state; DOC — chronic disorder of consciousness; TBI — traumatic brain injury.

We detected significantly higher level of CSF BDNF in patients after TBI compared to patients with non-traumatic DOC. There were no differences in other studied markers CSF levels between groups.

We analysed the biomarker levels in blood and CSF before and after the rTMS course. It was possible to obtain CSF samples before and after rTMS only in 21 people. Withdrawal of the informed consent by relatives, the refusal of the second lumbar puncture, or inability to complete the rTMS protocol were the reasons to get less samples. There were 11 VS/UWS patients and 10 MCS patients in rTMS group. Eight patients had traumatic etiology of DOC, and in 13 ones had the non-traumatic etiology. Comparison of CRS-R scores before TMS course in the groups due to the chronic DOC type (VS/UWS or MCS) and etiology didn't show any differences. The patients after TBI were significantly younger than ones with non-traumatic etiology. There were no other significant differences between the groups.

We didn't find any significant changes of biomarker levels in serum and CSF after rTMS application in the whole group, in VS/UWS and MCS patients distinctly, traumatic and non-traumatic DOC. The only difference was in BDNF level: we saw the significant increase of CSF BDNF level after rTMS course in patients with TBI (see Figure).

The level of consciousness in MCS patients improved after the rTMS course: their CRS-R score increased by 2.1 points

on average regardless of etiology, at the same time, the VS/UWS patients didn't show any changes (the clinical results are reported in the paper [18]). We didn't find any correlations in biomarker levels before rTMS course and patients' improvement via CRS-R score after the course.

Thus, we found that the CSF BDNF level is significantly higher in patients with posttraumatic chronic DOC compared to non-traumatic chronic DOC, and it was increasing after the rTMS course in that group. There were no differences in concentrations of other studied biomarkers (NSE, NGF, PDGF, GDNF и NT3) in CSF and serum, both between groups of patients and after the rTMS course.

DISCUSSION

The study of biochemical markers injury and repair of the central nervous system may contribute to a deeper understanding of appropriate patterns.

In our study we measured the levels of BDNF, NSE, NGF, PDGF, GDNF, and NT3. In patients with traumatic chronic DOC the concentration of BDNF in CSF was significantly higher compared to patients with non-traumatic DOC, and the concentration increased after the rTMS course in the discussed group. When comparing the factors' blood levels in patients and healthy volunteers, it turned out that the levels of all factors except NGF were significantly higher in the patients,

Table 2. Serum biomarkers levels in patients with chronic DOC and healthy volunteers

Biomarker	Total group			Type of DOC			DOC Etiology		
	DOC, <i>n</i> = 26	Healthy, <i>n</i> = 21	<i>p</i>	VS/UWS, <i>n</i> = 14	MCS, <i>n</i> = 12	<i>p</i>	TBI, <i>n</i> = 10	Non-traum., <i>n</i> = 16	<i>p</i>
BDNF, pg/ml	770 [640; 950]	54 [40; 62]	< 0.01	800 [510; 1010]	770 [675; 915]	1	750 [645; 875]	820 [560; 980]	0.9
NSE, ng/ml	53 [30; 64]	10 [9; 13]	< 0.01	40 [28; 54]	61 [51; 71]	0.13	55 [30; 63]	52 [30; 62]	0.86
NGF, pg/ml	222 [145; 267]	128 [103; 211]	0.54	219 [103; 261]	229 [184; 282]	0.35	229 [186; 260]	219 [144; 313]	1
PDGF, pg/ml	223 [200; 267]	72 [64; 90]	< 0.01	243 [191; 282]	213 [200; 246]	0.86	205 [200; 239]	235 [198; 289]	0.45
GDNF, pg/ml	5.3 [3.7; 6.4]	1.1 [1; 1.5]	< 0.01	4.6 [3.6; 5.7]	5.8 [4.1; 6.5]	0.3	5.8 [4.5; 6.4]	4.6 [3.6; 5.9]	0.39
NT 3, pg/ml	365 [329; 504]	89 [69; 103]	< 0.01	360 [322; 472]	388 [356; 518]	0.43	388 [332; 524]	362 [339; 491]	0.78

Note: VS — vegetative state; non-traum. — non-traumatic; MCS — minimally conscious state; DOC — chronic disorder of consciousness; TBI — traumatic brain injury.

Table 3. Cerebrospinal fluid biomarkers levels in patients with chronic DOC

Biomarker	Total DOC group, <i>n</i> = 26	Type of DOC			DOC Etiology		
		VS/UWS, <i>n</i> = 14	MCS, <i>n</i> = 12	<i>p</i>	TBI, <i>n</i> = 10	Non-traum., <i>n</i> = 16	<i>p</i>
BDNF, ng/ml	18 [11; 30]	14 [11; 31]	21 [12; 27]	0.49	28 [21; 38]	13 [11; 20]	0.04
NSE, ng/ml	96 [81; 131]	95 [78; 104]	98 [90; 156]	0.27	110 [94; 154]	95 [79; 101]	0.2
NGF, ng/ml	178 [137; 233]	178 [120; 210]	189 [143; 242]	0.53	177 [137; 233]	178 [144; 219]	0.82
GDNF, pg/ml	170 [135; 250]	160 [135; 240]	193 [140; 258]	0.56	235 [158; 261]	145 [123; 215]	0.17
NT 3, ng/ml	163 [111; 215]	145 [110; 199]	195 [145; 240]	0.19	195 [128; 219]	153 [110; 211]	0.34

Note: VS — vegetative state; non-traum. — non-traumatic; MCS — minimally conscious state; DOC — chronic disorder of consciousness; TBI — traumatic brain injury.

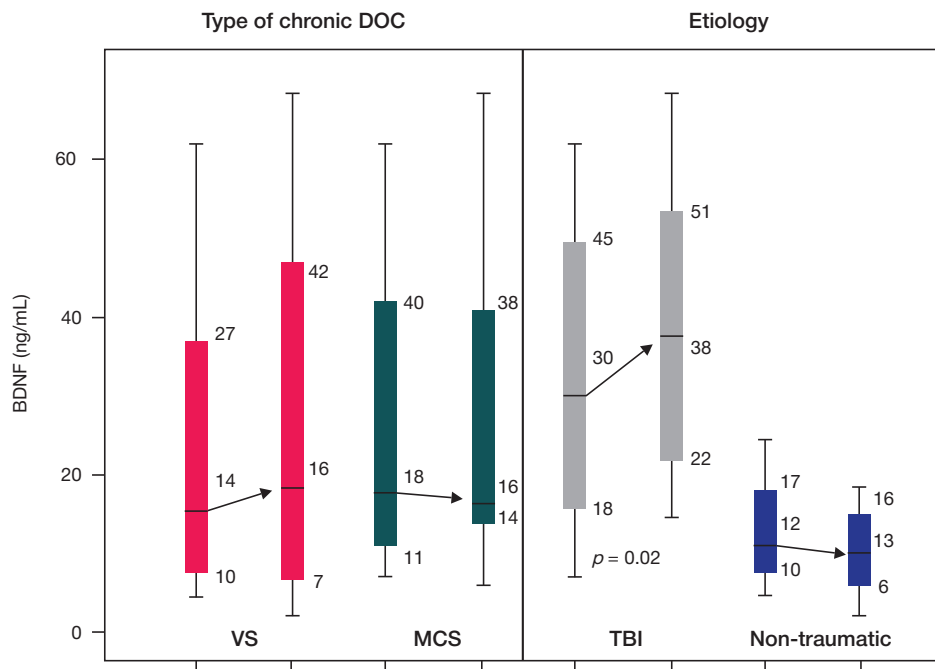


Figure. Change of BDNF levels in the cerebrospinal fluid of patients with chronic DOC after the course of rTMS by groups according to DOC type and etiology. VS — vegetative state; MCS — minimally conscious state; DOC — disorder of consciousness; TBI — traumatic brain injury

which indicated the long-existing nervous tissue damage and ongoing repair processes.

In this context it should be understood that the synthesis and level of neurotrophins in patients with severe CNS injury is likely to be affected by the cause of the disorder, its duration, and the patient's age. Thus, it is difficult enough to obtain homogeneous results in the heterogenous group of patients with chronic DOC. It can be assumed however that the overall brain injury and nervous tissue repair process are similar in all patients with chronic DOC.

It is well known that in the nervous system neurotrophins are involved in the neurons survival and regeneration process [6], therefore, in patients with severe nervous system injury the elevated levels of neurotrophins are observed. This may be due to damaged blood-brain barrier, and suggests that neurotrophins may have a neuroprotective role [19–21]. During the analysis of patients by groups we detected significant differences in the CSF BDNF concentration. There were no significant differences in the other factors concentrations between patients with VS/UWS and MCS, traumatic and non-traumatic etiology, before and after rTMS course.

The role of BDNF as a neuroprotective factor promoting the nervous tissue repair is widely discussed in literature. Thus, its role in the spinal cord injury recovery is being actively studied, the elevated BDNF level after traumatic injury is reported [22, 23]. During the experiments on rats the researchers tried to repair the spinal cord by delivery of BDNF to the affected area [7]. The BDNF level increased proportional to severity of paresis after stroke [21]; the other study reported elevated BDNF after moderate TBI proportional to neurologic deficit [19]. Interesting data were reported on critically ill patients without brain injury: there were no correlations between elevated BDNF and other neurotrophins, as in our study [24]. The authors concluded that the discussed marker correlated with the patients' mortality. In another study with patients after TBI, the authors made the opposite conclusion: they didn't detect any correlation between the injury severity and the level of BDNF [25].

Thus, literature contains contradictory information on the role of BDNF and the changes of its concentration in various

disorders. Unlike any other authors, we revealed the changes in the concentration of this factor in the CSF, but not in the blood serum. This fact may indicate that our chronic patients have already recovered the blood-brain barrier, but the neural plasticity processes still go on. The interesting fact is that the most active changes are seen in patients with TBI. This may be due to various factors. Firstly, the trauma patients have longer recovery period, therefore, the disorder of consciousness is considered persistent after 12 months in patients with TBI and after 3 months in patients with non-traumatic DOC [3]. Secondly, it is known that such patients have more favourable prognosis compared to patients with hypoxia [26]. Therefore, we can assume that recovery process is more active and lasts longer, that is what our results may indirectly indicate. It should be noted that among patients with TBI there were three people with VS/UWS and eight people with MCS. At first glance, it is reasonable to assume that elevated BDNF and the associated recovery processes were detected in the group with TBI due to higher proportion of patients with MCS. However, the comparison of groups with VS/UWS and MCS revealed no differences in the BDNF concentration. It can therefore be concluded that elevated CSF BDNF results not from type of DOC, but from etiology.

The changed BDNF level after the rTMS course is of particular interest. Literature contains contradictory information: elevated BDNF in serum after rTMS [27, 28], and elevated BDNF mRNA in the hippocampus and parietal cortex after the long-term rTMS [29] have been reported. It is considered that magnetic field during the high-frequency rTMS can stimulate activity of glutamatergic receptors and trigger the synthesis of BDNF, and the low-frequency rTMS, on the contrary, inhibits the BDNF synthesis [30]. Nevertheless, the results of meta-analysis across studies of BDNF level during rTMS are contradictory [30]. The authors note that BDNF level may be also related to etiology of the disorder and patient's age. Therefore, the described biomarker requires further research.

In our study, we found elevated CSF BDNF after rTMS in patients with posttraumatic chronic DOC. Taking into account the protein's neuroprotective properties, this may be due to

process underlying more favorable recovery that is known for DOC patients after TBI.

The study limitations include the small number of patients, as well as the lack of control group of healthy volunteers for assessment of neurotrophic factor levels in CSF. For more accurate results, especially for group comparison, further study of neurotrophins is required with the inclusion of more participants.

CONCLUSION

The study of neurotrophic factors in patients with severe brain injury revealed significantly higher serum BDNF, NSE, PDGF, GDNF and NT3 levels in patients with chronic DOC compared to healthy volunteers. The level of BDNF in CSF in patients

with chronic DOC was higher in posttraumatic patients, and it significantly increased after the course of high-frequency rTMS. Generally, our results confirm the previous findings about better recovery and more favorable prognosis in patients with TBI compared to patients with non-traumatic DOC. The data obtained on the neurotrophic factors concentration in the CSF in chronic DOC patients can indirectly indicate that the neuronal plasticity process remains active even in chronic terms of severe brain injuries. This could be considered one of the arguments in favour of recommendations to perform long-term rehabilitation of patients after severe TBI even in the chronic disorder of consciousness setting, since the potential for improvement in this group may persist beyond the first year after trauma.

References

- Giacino JT, Ashwal S, Childs N, Cranford R, Jennett B, Katz DI, et al. The minimally conscious state: definition and diagnostic criteria. *Neurology*. 2002; 58 (3): 349–53. DOI: 10.1212/WNL.58.3.349.
- Turner-Stokes L, Wade D, Playford D, Kitzinger J, Allanson J, Pundole A, et al. Prolonged disorders of consciousness guidelines. London, 2020.
- Giacino JT, Katz DI, Schiff ND, Whyte J, Ashman EJ, Ashwal S, et al. Practice guideline update recommendations summary: Disorders of consciousness. *Neurology*. 2018; 91 (10): 450–60. DOI: 10.1212/WNL.0000000000005926.
- Piradov MA, Suponeva NA, Vosnyuk IA, Kondratyev AN, Scshegolev AV, Belkin AA, et al. Chronic disorders of consciousness: terminology and diagnostic criteria. The results of the first meeting of the Russian Working Group for Chronic Disorders of Consciousness. *Annals of clinical and experimental neurology*. 2020; 14 (1): 5–16. DOI: 10.25692/ACEN.2020.1.1. Russian.
- Thibaut A, Schiff N, Giacino J, Laureys S, Gosseries O. Therapeutic interventions in patients with prolonged disorders of consciousness. *The Lancet Neurology*. 2019; 18 (6): 600–14. DOI: 10.1016/S1474-4422(19)30031-6.
- Skaper SD. Neurotrophic factors: An overview. *Methods in Molecular Biology*. 2018. DOI: 10.1007/978-1-4939-7571-6_1.
- Ye JH, Houle JD. Treatment of the chronically injured spinal cord with neurotrophic factors can promote axonal regeneration from supraspinal neurons. *Experimental Neurology*. 1997. DOI: 10.1006/exnr.1996.6353.
- Chen Q, Zhou L, Shine HD. Expression of neurotrophin-3 promotes axonal plasticity in the acute but not chronic injured spinal cord. *Journal of Neurotrauma*. 2006. DOI: 10.1089/neu.2006.23.1254.
- Pascual A, Hidalgo-Figueroa M, Gómez-Díaz R, López-Barneo J. GDNF and protection of adult central catecholaminergic neurons. *Journal of Molecular Endocrinology*. 2011. DOI: 10.1530/JME-10-0125.
- Sil S, Periyasamy P, Thangaraj A, Chivero ET, Buch S. PDGF/PDGFR axis in the neural systems. *Molecular Aspects of Medicine*. 2018. DOI: 10.1016/j.mam.2018.01.006.PMID:29409855.
- Daubin C, Quentin C, Alouche S, Etard O, Gaillard C, Seguin A, et al. Serum neuron-specific enolase as predictor of outcome in comatose cardiac-arrest survivors: a prospective cohort study. *BMC Cardiovasc Disord*. 2011; 11: 48. DOI: 10.1186/1471-2261-11-48.
- Pfeifer R, Borner A, Krack A, Sigusch HH, Surber R, Figulla HR. Outcome after cardiac arrest: predictive values and limitations of the neuroproteins neuron-specific enolase and protein S-100 and the Glasgow Coma Scale. *Resuscitation*. 2005; 65 (1): 49–55. DOI: 10.1016/j.resuscitation.2004.10.011.
- Gaede G, Hellweg R, Zimmermann H, Brandt AU, Dorr J, Bellmann-Strobl J, et al. Effects of deep repetitive transcranial magnetic stimulation on brain-derived neurotrophic factor serum concentration in healthy volunteers. *Neuropsychobiology*. 2014; 69 (2): 112–9. DOI: 10.1159/000358088.
- Lee JY, Park HJ, Kim JH, Cho BP, Cho SR, Kim SH. Effects of low- and high-frequency repetitive magnetic stimulation on neuronal cell proliferation and growth factor expression: A preliminary report. *Neurosci Lett*. 2015; 604: 167–72. DOI: 10.1016/j.neulet.2015.07.038.
- Takahashi T. Monoamines, monoamine metabolites, neuron specific enolase and myelin basic protein concentrations in cerebrospinal fluid of resuscitated patients. *Nihon Shinkei Seishin Yakurigaku Zasshi*. 1997; 17 (1): 7–16.
- Suponeva NA, Bakulin IS, Pojdasheva AG, Piradov MA. Bezopasnost' transkraniial'noj magnitnoj stimuljacii: obzor mezhdunarodnyh rekomendacij i novye dannye. *Nervno-myshechnye bolezni*. 2017; 7 (2): 21–36.
- Iazeva EG, Legostaeva LA, Zimin AA, Sergeev DV, Domashenko MA, Samorukov VY, et al. A Russian validation study of the Coma Recovery Scale-Revised (CRS-R). *Brain Injury*. 2019. DOI: 10.1080/02699052.2018.1539248.
- Legostaeva L, Poydasheva A, Iazeva E, Sinitsyn D, Sergeev D, Bakulin I, et al. Stimulation of the angular gyrus improves the level of consciousness. *Brain Sciences*. 2019; 9 (5). DOI: 10.3390/brainsci9050103.
- Karakulova YV, Selyanina NV. Monitoring of neurotrophic factors and cognitive function in patients with traumatic brain injury. *Zh Nevrol Psikhiatr im S. S. Korsakova*. 2017;117(10):34-37. doi:10.17116/jnevro201711710134-37.
- Mokhtarzade M, Motl R, Negaresh R, Zimmer P, Khodadoost M, Baker JS, et al. Exercise-induced changes in neurotrophic factors and markers of blood-brain barrier permeability are moderated by weight status in multiple sclerosis. *Neuropeptides*. 2018. DOI: 10.1016/j.npep.2018.05.010.PMID:29880392.
- King M, Kelly LP, Wallack EM, Hasan SMM, Kirkland MC, Curtis ME, et al. Serum levels of insulin-like growth factor-1 and brain-derived neurotrophic factor as potential recovery biomarkers in stroke. *Neurological Research*. 2019. DOI: 10.1080/01616412.2018.1564451.
- Xu L, Zhang Y, Zhang R, Zhang H, Song P, Ma T, et al. Elevated plasma BDNF levels are correlated with NK cell activation in patients with traumatic spinal cord injury. *International Immunopharmacology*. 2019. DOI: 10.1016/j.intimp.2019.105722.PMID:31255880.
- Sasaki M, Radtke C, Tan AM, Zhao P, Hamada H, Houkin K, et al. BDNF-hypersecreting human mesenchymal stem cells promote functional recovery, axonal sprouting, and protection of corticospinal neurons after spinal cord injury. *Journal of Neuroscience*. 2009. DOI: 10.1523/JNEUROSCI.2769-09.2009.
- Ritter C, Miranda AS, Giombelli VR, Tomasi CD, Comim CM, Teixeira AL, et al. Brain-derived neurotrophic factor plasma levels are associated with mortality in critically ill patients even in the absence of brain injury. *Critical Care*. 2012. DOI: 10.1186/cc11902.
- Simon D, Do Nascimento RIM, Filho EMR, Bencke J,

- Regner A. Plasma brain-derived neurotrophic factor levels after severe traumatic brain injury. *Brain Injury*. 2016. DOI: 10.3109/02699052.2015.1077993.
26. Giacino JT, Katz DI, Schiff ND, Whyte J, Ashman EJ, Ashwal S, et al. Comprehensive systematic review update summary: Disorders of consciousness: Report of the Guideline Development, Dissemination, and Implementation Subcommittee of the American Academy of Neurology; The American Congress of Rehabilitation Medicine; and the National Institute on Disability, Independence. 2018; 91 (10): 461–470. DOI: 10.1016/j.apmr.2018.07.002
27. Yukimasa T, Tamagawa A, Uozumi T, Shinkai K, Ueda N, Tsuji S, et al. High-frequency repetitive transcranial magnetic stimulation improves refractory depression by influencing catecholamine and brain-derived neurotrophic factors. *Pharmacopsychiatry*. 2006. DOI: 10.1055/s-2006-931542.
28. Zanardini R, Gazzoli A, Ventriglia M, Perez J, Bignotti S, Maria Rossini P, et al. Effect of repetitive transcranial magnetic stimulation on serum brain derived neurotrophic factor in drug resistant depressed patients. *Journal of Affective Disorders*. 2006. DOI: 10.1016/j.jad.2005.12.029.
29. Müller MB, Toschi N, Kresse AE, Post A, Keck ME. Long-term repetitive transcranial magnetic stimulation increases the expression of brain-derived neurotrophic factor and cholecystokinin mRNA, but not neuropeptide tyrosine mRNA in specific areas of rat brain. *Neuropsychopharmacology*. 2000. DOI: 10.1016/S0893-133X(00)00099-3.
30. Jiang B, He D. Repetitive transcranial magnetic stimulation (rTMS) fails to increase serum brain-derived neurotrophic factor (BDNF). *Neurophysiologie Clinique*. 2019; 49 (4): 295–300. DOI: 10.1016/j.neucli.2019.05.068.

Литература

1. Giacino JT, Ashwal S, Childs N, Cranford R, Jennett B, Katz DI, et al. The minimally conscious state: definition and diagnostic criteria. *Neurology*. 2002; 58 (3): 349–53. DOI: 10.1212/WNL.58.3.349.
2. Turner-Stokes L, Wade D, Playford D, Kitzinger J, Allanson J, Pundole A, et al. Prolonged disorders of consciousness guidelines. London, 2020.
3. Giacino JT, Katz DI, Schiff ND, Whyte J, Ashman EJ, Ashwal S, et al. Practice guideline update recommendations summary: Disorders of consciousness. *Neurology*. 2018; 91 (10): 450–60. DOI: 10.1212/WNL.0000000000005926.
4. Пирадов М. А., Супонева Н. А., Вознюк И. А., Кондратьев А. Н., Щёголев А. В., Белкин А. А., и др. Хронические нарушения сознания: терминология и диагностические критерии. Результаты первого заседания Российской рабочей группы по проблемам хронических нарушений сознания. *Анналы клинической и экспериментальной неврологии* 2020; 14 (1): 5–16. DOI: 10.25692/ACEN.2020.1.1.
5. Thibaut A, Schiff N, Giacino J, Laureys S, Gosseries O. Therapeutic interventions in patients with prolonged disorders of consciousness. *The Lancet Neurology*. 2019; 18 (6): 600–14. DOI: 10.1016/S1474-4422(19)30031-6.
6. Skaper SD. Neurotrophic factors: An overview. *Methods in Molecular Biology*. 2018. DOI: 10.1007/978-1-4939-7571-6_1.
7. Ye JH, Houle JD. Treatment of the chronically injured spinal cord with neurotrophic factors can promote axonal regeneration from supraspinal neurons. *Experimental Neurology*. 1997. DOI: 10.1006/exnr.1996.6353.
8. Chen Q, Zhou L, Shine HD. Expression of neurotrophin-3 promotes axonal plasticity in the acute but not chronic injured spinal cord. *Journal of Neurotrauma*. 2006. DOI: 10.1089/neu.2006.23.1254.
9. Pascual A, Hidalgo-Figueroa M, Gómez-Díaz R, López-Barneo J. GDNF and protection of adult central catecholaminergic neurons. *Journal of Molecular Endocrinology*. 2011. DOI: 10.1530/JME-10-0125.
10. Sil S, Periyasamy P, Thangaraj A, Chivero ET, Buch S. PDGF/PDGFR axis in the neural systems. *Molecular Aspects of Medicine*. 2018. DOI: 10.1016/j.mam.2018.01.006.PMID:29409855.
11. Daubin C, Quentin C, Allouche S, Etard O, Gaillard C, Seguin A, et al. Serum neuron-specific enolase as predictor of outcome in comatose cardiac-arrest survivors: a prospective cohort study. *BMC Cardiovasc Disord*. 2011; 11: 48. DOI: 10.1186/1471-2261-11-48.
12. Pfeifer R, Borner A, Krack A, Sigusch HH, Surber R, Figulla HR. Outcome after cardiac arrest: predictive values and limitations of the neuroproteins neuron-specific enolase and protein S-100 and the Glasgow Coma Scale. *Resuscitation*. 2005; 65 (1): 49–55. DOI: 10.1016/j.resuscitation.2004.10.011.
13. Gaede G, Hellweg R, Zimmermann H, Brandt AU, Dorr J, Bellmann-Strobl J, et al. Effects of deep repetitive transcranial magnetic stimulation on brain-derived neurotrophic factor serum concentration in healthy volunteers. *Neuropsychobiology*. 2014; 69 (2): 112–9. DOI: 10.1159/000358088.
14. Lee JY, Park HJ, Kim JH, Cho BP, Cho SR, Kim SH. Effects of low- and high-frequency repetitive magnetic stimulation on neuronal cell proliferation and growth factor expression: A preliminary report. *Neurosci Lett*. 2015; 604: 167–72. DOI: 10.1016/j.neulet.2015.07.038.
15. Takahashi T. Monoamines, monoamine metabolites, neuron specific enolase and myelin basic protein concentrations in cerebrospinal fluid of resuscitated patients. *Nihon Shinkei Seishin Yakurigaku Zasshi*. 1997; 17 (1): 7–16.
16. Супонева Н. А., Бакулин И. С., Пойдашева А. Г., Пирадов М. А. Безопасность транскраниальной магнитной стимуляции: обзор международных рекомендаций и новые данные. *Нервно-мышечные болезни*. 2017; 7 (2): 21–36.
17. Iazeva EG, Legostaeva LA, Zimin AA, Sergeev DV, Domashenko MA, Samorukov VY, et al. A Russian validation study of the Coma Recovery Scale-Revised (CRS-R). *Brain Injury*. 2019. DOI: 10.1080/02699052.2018.1539248.
18. Legostaeva L, Poydasheva A, Iazeva E, Sinitsyn D, Sergeev D, Bakulin I, et al. Stimulation of the angular gyrus improves the level of consciousness. *Brain Sciences*. 2019; 9 (5). DOI: 10.3390/brainsci9050103.
19. Каракулова Ю. В., Селянина Н. В. Мониторинг нейротрофических факторов и когнитивных функций у пациентов с черепно-мозговой травмой. *Журнал неврологии и психиатрии им. С. С. Корсакова*. 2017; 117 (10): 34–37.
20. Mokhtarzade M, Motl R, Negaresh R, Zimmer P, Khodadoost M, Baker JS, et al. Exercise-induced changes in neurotrophic factors and markers of blood-brain barrier permeability are moderated by weight status in multiple sclerosis. *Neuropeptides*. 2018. DOI: 10.1016/j.npep.2018.05.010.PMID:29880392.
21. King M, Kelly LP, Wallack EM, Hasan SMM, Kirkland MC, Curtis ME, et al. Serum levels of insulin-like growth factor-1 and brain-derived neurotrophic factor as potential recovery biomarkers in stroke. *Neurological Research*. 2019. DOI: 10.1080/01616412.2018.1564451.
22. Xu L, Zhang Y, Zhang R, Zhang H, Song P, Ma T, et al. Elevated plasma BDNF levels are correlated with NK cell activation in patients with traumatic spinal cord injury. *International Immunopharmacology*. 2019. DOI: 10.1016/j.intimp.2019.105722.PMID:31255880.
23. Sasaki M, Radtke C, Tan AM, Zhao P, Hamada H, Houkin K, et al. BDNF-hypersecreting human mesenchymal stem cells promote functional recovery, axonal sprouting, and protection of corticospinal neurons after spinal cord injury. *Journal of Neuroscience*. 2009. DOI: 10.1523/JNEUROSCI.2769-09.2009.
24. Ritter C, Miranda AS, Giombelli VR, Tomasi CD, Comim CM, Teixeira AL, et al. Brain-derived neurotrophic factor plasma levels are associated with mortality in critically ill patients even in the absence of brain injury. *Critical Care*. 2012. DOI: 10.1186/cc11902.
25. Simon D, Do Nascimento RIM, Filho EMR, Bencke J, Regner A. Plasma brain-derived neurotrophic factor levels after severe traumatic brain injury. *Brain Injury*. 2016. DOI: 10.3109/02699052.2015.1077993.
26. Giacino JT, Katz DI, Schiff ND, Whyte J, Ashman EJ, Ashwal S, et

- al. Comprehensive systematic review update summary: Disorders of consciousness: Report of the Guideline Development, Dissemination, and Implementation Subcommittee of the American Academy of Neurology; The American Congress of Rehabilitation Medicine; and the National Institute on Disability, Independence. 2018; 91 (10): 461–470. DOI: 10.1016/j.apmr.2018.07.002
27. Yukimasa T, Tamagawa A, Uozumi T, Shinkai K, Ueda N, Tsuji S, et al. High-frequency repetitive transcranial magnetic stimulation improves refractory depression by influencing catecholamine and brain-derived neurotrophic factors. *Pharmacopsychiatry*. 2006. DOI: 10.1055/s-2006-931542.
28. Zanardini R, Gazzoli A, Ventriglia M, Perez J, Bignotti S, Maria Rossini P, et al. Effect of repetitive transcranial magnetic stimulation on serum brain derived neurotrophic factor in drug resistant depressed patients. *Journal of Affective Disorders*. 2006. DOI: 10.1016/j.jad.2005.12.029.
29. Müller MB, Toschi N, Kresse AE, Post A, Keck ME. Long-term repetitive transcranial magnetic stimulation increases the expression of brain-derived neurotrophic factor and cholecystokinin mRNA, but not neuropeptide tyrosine mRNA in specific areas of rat brain. *Neuropsychopharmacology*. 2000. DOI: 10.1016/S0893-133X(00)00099-3.
30. Jiang B, He D. Repetitive transcranial magnetic stimulation (rTMS) fails to increase serum brain-derived neurotrophic factor (BDNF). *Neurophysiologie Clinique*. 2019; 49 (4): 295–300. DOI: 10.1016/j.neucli.2019.05.068.

EFFECT OF ROBOT-ASSISTED GAIT TRAINING ON BIOMECHANICS OF ANKLE JOINT IN PATIENTS WITH POST-STROKE HEMIPARESIS

Klochkov AS ✉, Zimin AA, Khizhnikova AE, Suponeva NA, Piradov MA

Research Center of Neurology, Moscow, Russia

The key factor promoting post-stroke gait disturbances is motor impairment of the ankle joint (AJ) which results in pathological synergies. Robotic devices used for gait training are equipped with hip and knee joint actuators. However, there is no consensus in the literature on their effect on AJ movements. The aim of this study was to investigate the effect of robot-assisted gait training on AJ movements in patients with post-stroke paresis. The study recruited 22 hemispheric stroke survivors. They motor function was assessed using clinical scales and motion capture analysis. All patients received 11 robot-assisted gait training session. After rehabilitation, the total score on the Fugl-Meyer Assessment scale increased from 146.5 to 152 points ($p < 0.05$); for the lower limb, the score increased from 18 to 20.5 points ($p < 0.05$). The muscle tone of ankle extensors decreased from 2.5 to 2.0 points on the modified Ashworth scale ($p < 0.05$). The duration of the stance phase increased from 28.0 to 33.5% relative to the total gait cycle (GC). The main difference in the GC structure before and after rehabilitation is the presence of 3 GC parts instead of 5, suggesting consolidation of patients' goniograms at 1-61% of GC. Comparison of joint angles before and after rehabilitation revealed that only the interquartile ranges (IR) were different ($p < 0.05$). The authors conclude that robot-assisted training with knee and hip joint actuators indirectly affects the kinematic parameters of AJ by promoting a shift towards the average gait kinematics.

Keywords: stroke, neurorehabilitation, adaptation, gait disturbances, robot-assisted therapy, movement biomechanics, motion analysis

Funding: this study was state-funded.

Author contribution: Klochkov AS — study planning, patient recruitment, literature analysis, data interpretation, manuscript preparation; Zimin AA — statistical analysis, data interpretation, manuscript preparation; Khizhnikova AE — literature analysis, data interpretation, manuscript preparation; Suponeva NA, Piradov MA — manuscript preparation.

Compliance with ethical standards: the study was approved by the Ethics Committee of the Research Center of Neurology (Protocol № 14/09 dated December 23, 2009). Informed consent was obtained from all study participants.

✉ **Correspondence should be addressed:** Anton S. Klochkov
Volokolamskoe shosse, 80, Moscow, 125367; klochkov@neurology.ru

Received: 28.09.2020 **Accepted:** 14.10.2020 **Published online:** 29.10.2020

DOI: 10.24075/brsmu.2020.066

ВЛИЯНИЕ РОБОТИЗИРОВАННЫХ ТРЕНИРОВОК НА БИОМЕХАНИКУ ГОЛЕНОСТОПНОГО СУСТАВА У ПАЦИЕНТОВ С ПОСТИНСУЛЬТНЫМ ПАРЕЗОМ

А. С. Клочков ✉, А. А. Зимин, А. Е. Хижникова, Н. А. Супонева, М. А. Пирадов

Научный центр неврологии, Москва, Россия

Ключевым фактором нарушений походки после острых нарушений мозгового кровообращения (ОНМК) является нарушение движений в голеностопном суставе (ГС), приводящее к формированию патологической синергии. В настоящее время при роботизированных тренировках ходьбы используют приводы тазобедренного и коленного суставов. Однако по данным литературы нет единого мнения об их влиянии на движения в ГС. Целью исследования было изучить влияние роботизированных тренировок ходьбы на движения ГС у пациентов с постинсультным парезом. В исследовании приняло участие 22 пациента с ОНМК полушарной локализации. Для оценки двигательной функции применяли клинические шкалы и видеоанализ ходьбы. Всем пациентам проводили курс из 11 роботизированных тренировок ходьбы. На фоне тренировок выявлено увеличение общего балла по шкале Фугл-Майера со 146,5 до 152 баллов ($p < 0,05$) и отдельно для нижней конечности с 18 до 20,5 баллов ($p < 0,05$), а также снижение мышечного тонуса разгибателей ГС с 2,5 до 2,0 баллов по модифицированной шкале Эшворта ($p < 0,05$). На фоне роботизированных тренировок отмечено увеличение длительности фазы опоры пациентов с 28,0 до 33,5% от цикла шага (ЦШ). Кроме того, основным различием структуры ЦШ до и после курса тренировок стало наличие трех частей шага вместо пяти, что подтверждает консолидацию гониограмм пациентов в периоде от 1 до 61% ЦШ. Сравнение значений углов до и после показало достоверные различия только по межквартильному интервалу ($p < 0,05$). Авторы пришли к выводу, что роботизированные тренировки с применением активных приводов для тазобедренного и коленного суставов опосредованно способствуют изменениям кинематических параметров ГС за счет приближения показателей паттерна к некоему усредненному шаблону движений.

Ключевые слова: инсульт, нейрореабилитация, нарушения ходьбы, роботизированная терапия, биомеханика движений, видеоанализ движений

Финансирование: в рамках государственной НИР.

Вклад авторов: А. С. Клочков — планирование исследования, набор пациентов, проведение исследования, анализ литературы, интерпретация данных, подготовка рукописи; А. А. Зимин — статистическая обработка, интерпретация данных, подготовка рукописи; А. Е. Хижникова — анализ литературы, интерпретация данных, подготовка рукописи; Н. А. Супонева, М. А. Пирадов — подготовка рукописи.

Соблюдение этических стандартов: исследование одобрено этическим комитетом Научного центра неврологии (протокол № 14/09 от 23 декабря 2009 г.). Все пациенты подписали добровольное информированное согласие.

✉ **Для корреспонденции:** Антон Сергеевич Клочков
Волоколамское шоссе, д. 80, г. Москва, 125367; klochkov@neurology.ru

Статья получена: 28.09.2020 **Статья принята к печати:** 14.10.2020 **Опубликована онлайн:** 29.10.2020

DOI: 10.24075/vrgmu.2020.066

Gait disturbances are among the most debilitating sequelae of stroke [1, 2]. According to a study, over 30% of stroke survivors were totally unable or required assistance to walk after completing a standard rehabilitation program which

did not include robot-assisted gait training [3]. Recent research has shown that exercising with electromechanical gait trainers significantly increases the chance of regaining independent walking [4]. Many authors hold the opinion that

the altered biomechanics of the ankle joint are the key factor in gait disturbances, causing the pelvis, the trunk and the hip joint to move in an abnormal, energy-inefficient pattern, which negatively affects the quality and speed of walking and results in compensatory synergies [5–8]. Gait rehabilitation is a stepwise process; compensatory strategies used by the patient at the early stages of rehabilitation are perpetuated over time, becoming pathological due to weakness and spasticity in some muscle groups [9].

Currently, robot-assisted gait training is recognized as the gold standard of locomotor poststroke rehabilitation. Meta-analyses confirm the efficacy of electromechanical devices in restoring the impaired walking function, especially in patients who are unable to ambulate independently [4, 10]. Today, two major types of robotic devices are used in neurorehabilitation: exoskeletons and end-effectors, in which a patient's feet are fixed to footplates that simulate walking. Exoskeletons can be divided into 2 categories: mobile and stationary. The list of mobile exoskeletons includes but is not limited to ExoAtlet, HAL and Bionic leg, which have proved to be effective in clinical rehabilitation [11, 12]. Our literature analysis did not include publications on mobile exoskeletons because the gait pattern simulated by this technology differs from physiological gait; mobile exoskeletons exploit the zero-moment point concept, i.e. a locomotion model in which the net force is directed towards the surface to ensure safe locomotion; consequently, the ankle joint torque is limited [13–16]. Despite the growing variety of mobile exoskeletons, stationary exoskeletons like Lokomat and ReoAmbulator are more common in clinical practice. So far, both exoskeletons and end-effectors have proved to be clinically effective in helping stroke patients regain their walking function; there is no convincing evidence that one is more beneficial for such patients than the other [17, 18]. Research shows that end-effector-based training increases ankle joint power and kinetics, expands the range of motion of the knee joint, and improves mobility, walking speed and gait symmetry [19, 20]. In turn, stationary exoskeletons ensure precise control over the biomechanics of the assisted movement, reproducing the natural motor pattern and thus allowing the patient to correct the pathological gait pattern [21].

There is ongoing debate about the mechanism underlying the effect of robotic devices for the active training of the hip and knee joints on the changes in the biomechanics of the ankle joint, which is not normally actively involved in the training process. Early works looking into the effect of feedback-enhanced robot-assisted training with an exoskeleton on the biomechanics of voluntary movements during walking demonstrated that the natural kinematic patterns of the hip and knee joints were almost identical to the kinematics prescribed by the robot, whereas torque patterns in the joint remained abnormal, indirectly suggesting that the gait pattern prescribed by the robot could not replace the pattern developed by the patient [22].

The need to involve all joints, including the ankle joint, into training and the hypotheses about the beneficial effects of robotic therapy on the proximal/distal leg joints are a common subject of debate. At present, there are a few commercial robotic exoskeletons with ankle joint drives available on the

market. However, they are less popular than exoskeletons with hip and knee joints actuators and have some drawbacks. On the whole, there is no unanimous opinion on whether to equip a gait trainer with an ankle joint actuator and on whether it is enough to stimulate only the proximal paretic leg in order to “overwrite” the pathological gait pattern.

At the same time, it is known that locomotor movements are highly automatized and synergistic. So, it would be logical to hypothesize that gait training that provides active robotic assistance and performance feedback for only some movements generated by muscle synergy also produces an indirect effect on the components that do not participate in performing the trained movement.

The aim of our study was to investigate the possibility of improving ankle joint movements by means of gait training with prescribed knee and hip joints patterns in patients with poststroke paresis.

METHODS

The study conducted in 2010–2017 recruited 22 hemispheric stroke survivors (18 men and 4 women). The median age was 50.5 years (41; 56.5), the median time elapsed after stroke was 6.0 months (2.8; 12.9). Details are provided in Table 1.

The following inclusion criteria were applied: first-time hemispheric stroke, hemiparesis; gait disturbances.

Exclusion criteria (contraindications to training with the Lokomat) were as follows: weight under 50 kg or over 135 kg; height below 160 cm or above 185 cm; lower limb contractures; persistent skin lesions of lower limbs and the trunk; orthostatic hypotension; severe cardiac pathology; severe cognitive impairment; mechanical ventilation; comorbidities and disorders of the locomotor system, including leg length discrepancy > 3 cm; deep vein thrombosis of lower limbs; hip, knee or ankle arthrodesis; osteoporosis; ununited fractures of lower limbs; prescribed bedrest.

The patients were offered a series of robot-assisted gait training sessions with partial body weight support on the Lokomat (Hocoma; Switzerland) equipped with electromechanical drives in the hip and knee joints for flexion and extension and elastic foot lifters for toe clearance support. A total of 11 sessions were conducted; exoskeleton setup and adjustment took 15 min of the first session; the rest of the session (30 min) was spent on reduced-intensity gait training to allow each patient to adapt to the prescribed gait pattern. The remaining 10 sessions were 45 min long and consisted of only active gait training with sensory feedback. All sessions were one-on-one personal Lokomat trainings sessions conducted by a therapist, with comfortable walking speed and biofeedback based on the hip and knee potentiometers data. Body weight support was adjusted during each session at the minimal amount of support in order to prevent patients from stumbling. Foot support was ensured by tension springs attached distally to the metatarsal. The degree of spring tension was set up by the therapist during each session to assist the patient's voluntary effort during dorsiflexion and to ensure safe foot clearance.

Table 1. Patients characteristics

Sex		Stroke type		Hemisphere		Lesion site	
Male	18 (82%)	Ischemic	16 (72.7%)	Right	13 (59.1%)	Corticosubcortical	8 (36.4%)
Female	4 (18%)	Hemorrhagic	6 (27.3%)	Left	9 (40.9%)	Deeper brain structures	14 (63.6%)

For performance feedback, the patients were shown graphs illustrating the level of activity and synchronization of their hip and knee joints with the movements of the exoskeleton. The patients were tasked to perform active movements in the hip and knee joints in synch with the exoskeleton. The graphs reflected active movements of the patient; in the absence of active or synchronized movements, the curve dipped. Apart from robotic therapy, all patients received massages for paretic limbs and ten 30-minute long physical therapy sessions to regain their arm function, balance and walking. Within one hour before and after each Lokomat training session, no other therapeutic procedures were carried out.

The clinical efficacy of robot-assisted rehabilitation was assessed using the validated Russian versions of the Fugl-Meyer Assessment (FMA) scale, the modified Ashworth (MAS) scale for spasticity in the gastrocnemius and soleus muscles, the modified Rankin (MR) scale, and the Functional Ambulation Categories (FAC) scale [23, 24]. Measurements were performed before the beginning of the rehabilitation program and on the day following its completion.

The biomechanics of walking were evaluated using the motion analysis system (Biosoft-3D; Russia) [25, 26].

For motion capture, we used reflective markers and 2 synchronized infrared digital cameras. The patients were video-recorded for 30 seconds during a 2-minute walking trial on the treadmill at a comfortable speed before and after rehabilitation. The reflective markers were 2 cm in diameter; they were

attached to the anatomic landmarks (projections of joint centers) on the lateral side of the body, including the coracoid process, the most prominent part of the greater trochanter, above the tip of the lateral malleolus, at the heel, and the distal aspect of the foot at the site of the fifth metatarsal head. The kinematic parameters of locomotion were calculated in the XYZ coordinates (Z — vertical axis; Y — sagittal axis, running from right to left; X — frontal axis). The following kinematic parameters were calculated:

- marker coordinates on the X, Y, Z axes and their movement trajectories;
- angles between body segments and the X, Y, Z axes;
- joint angles.

The second-order low-pass Butterworth filter was applied to the obtained raw data. Kinematic parameters were calculated based on the 3-D coordinates of the reflective markers and the constructed kinetogram of the human body. Temporal characteristics of gait (duration of the stance and swing phases) were used as basic parameters for primary gait analysis; they were calculated based on the local vertical acceleration maximum for the markers attached to the lateral malleolus and the heel plus the local horizontal acceleration maximum for the markers attached to the fifth metatarsal head. Other primary kinematic parameters included maximums and ranges of torque and joint angles in the sagittal plane of the ankle joint. For secondary data analysis, cluster analysis and nonparametric analysis of ten- percentile intervals were used.

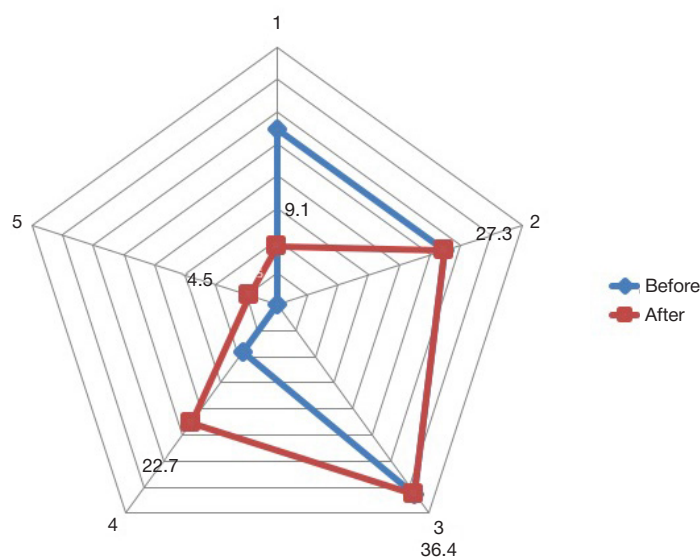


Fig. 1. Distribution of patients on the FAC scale before and after gait rehabilitation

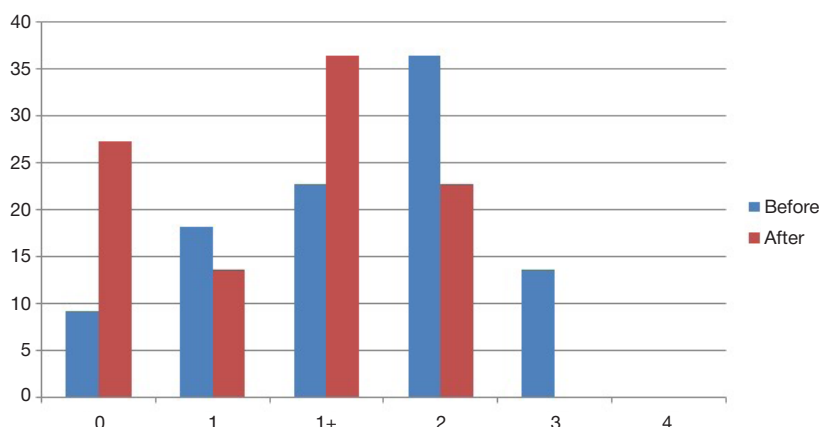


Fig. 2. Distribution of patients on the modified Ashworth scale (represented as percentage)

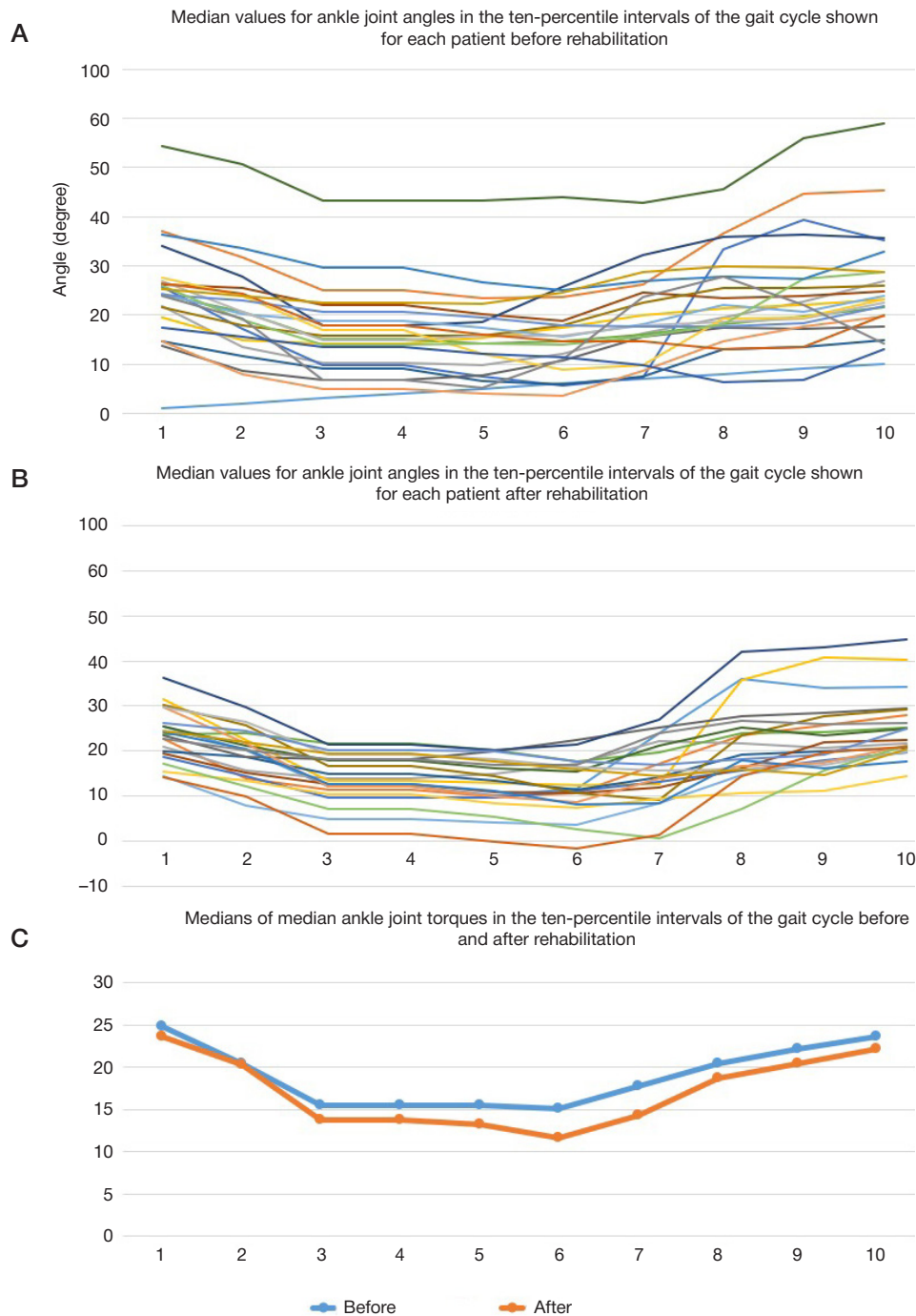


Fig. 3. Goniograms of ankle joint flexion/extension in the ten-percentile intervals of the gait cycle before (A) and after (B) rehabilitation; comparison of median values before and after rehabilitation (C)

Cluster analysis is widely used to study gait in general and the gait cycle in particular in healthy and diseased individuals [27–35]. In this work, cluster analysis was applied to identify the structure of the gait cycle and to compare its characteristics before and after rehabilitation. Nonparametric analysis of ten-percentile intervals of the gait cycle was conducted to study the characteristics of the cycle in greater detail and compare them before and after gait rehabilitation.

The obtained data were processed using nonparametric tests: the Mann–Whitney U test for independent variables and the Wilcoxon test for dependent variables. The Bonferroni correction was used to adjust for multiple comparisons. Categorical variables were analyzed using the Fisher exact test. To identify the hierarchy of the obtained data, cluster analysis was applied. Specifically, Ward's method followed by the Mann–Whitney test and the Bonferroni

correction procedure was used to identify the components of the gait cycle and subgroups of patients. The strength of associations was evaluated using Spearman's correlation coefficient. Results are presented below as median values, upper and lower quartiles. Differences were considered significant at $p < 0.05$. The analysis was carried out in Statistica v. 7.0 (StatSoft Inc; Russia) and SPSS 22 software (IBM; USA).

RESULTS

Clinical efficacy of gait training

The analysis of clinical data showed that patients' mobility had improved following the rehabilitation program; another finding was an insignificant yet reliable increase in the range of

Table 2. Comparison of gait cycle parts before and after rehabilitation

Part of gait cycle		Median, degrees		Q1, degrees		Q3, degrees		IR, degrees	
before	after	before	after	before	after	before	after	before	after
1–7	1–61	25.1	16.1	22.2	12.7	27.4	19.6	5.2	6.9*
8–19		21.0		16.1		24.6		8.5	
20–55		15.6		10.9		19.7		8.8	
56–74	62–75	16.9	16.6	14.2	13.1	22.5	20.8	8.3	7.7
75–97	76–97	22.1	20.1	18.8	18.7	27.4	24.7	8.6	6*

Note: the data were compared using the Mann–Whitney U and Tukey's tests. * — $p < 0.05$.

active motion and function of the lower limb and a reduction in gastrocnemius and soleus spasticity in all the participants; the initial degree of disability on the Rankin scale remained unchanged. After gait rehabilitation, a higher proportion of patients could ambulate without assistance than before they joined the program (3, 4 and 5 points on the FAC scale; Fig. 1).

We also observed an increase in active motion on the FM scale after rehabilitation. The total motor score increased from 146.5 (128; 163.5) to 152 (134.3; 176.8) ($p < 0.05$), whereas for the lower extremity, the score increased from 18 (16; 21) to 20.5 (18; 24.3) ($p < 0.05$).

The tone of the gastrocnemius and soleus muscles decreased significantly from 2.5 (1; 3) to 2.0 (0; 2) points on the MAS ($p < 0.05$). Details on the distribution of muscle tone parameters are provided in Fig. 2.

Assessment of gait biomechanics

Temporal and spatial characteristics of gait changed following robot-assisted gait rehabilitation: the duration of the stance phase increased from 28.0% (25; 36) to 33.5% (30; 42) relative to the gait cycle (GC) ($p = 0.0001$).

The analysis of kinematic parameters did not reveal any significant differences in the maximum values for ankle joint flexion and extension during GC. Maximum angle ranges before and after rehabilitation were 59.12° and 45.30°, respectively, the difference being insignificant ($p = 0.228$). Minimum angle ranges were 3.33° and -1.79°, respectively ($p = 0.072$). The differences between the maximum and minimum values were 55.79° and 47.09°, respectively ($p = 0.190$). However, comparison of the median values of GC ten-percentile intervals before and after rehabilitation revealed that initially different

patients' goniograms looked more similar after rehabilitation (Fig. 3A–C).

Considering the absence of significant differences in the primary kinematic parameters, we conducted an in-depth analysis of goniogram variability and ankle joint torques (Table 2).

To determine the degree of data variability, we analyzed the correlation coefficients for the angles between each two consecutive GC parts. Based on the graph (Fig. 4), we concluded that differences between the patients were the most pronounced at 51%–58% and 65%–82% of the gait cycle.

For a more in-depth analysis of ankle joint goniograms constructed before and after rehabilitation, we broke down the gait cycle into parts using cluster analysis and correlation coefficients for each 2 consecutive angles. Using Ward's clustering technique, the gait cycle before rehabilitation was divided into 5 parts corresponding to 1–7%, 8–19%, 20–55%, 56–74%, and 75–100% of GC. The first part corresponded to the time of foot contact with the treadmill and the beginning of the stance phase; the second part corresponded to the middle of the stance phase; the third part, to the end of the stance phase and the beginning of the swing phase; the fourth part, to the middle of the swing phase; the fifth part, to the end of the swing phase. Cluster analysis was applied to each GC part. Descriptive statistics for GC parts before clustering are provided in Table 3.

After 5 parts were identified in the pre-rehabilitation gait cycle, the patients were clustered into subgroups for each of those parts. Two clusters were identified in the first part of the cycle (1–7%). The second part (8–19%) was represented by 3 clusters, differing in their medians. In the third (20–55%) and fourth (56–74%) parts, 3 and 4 clusters were identified, respectively, differing in medians. The fifth part (75–97%) was

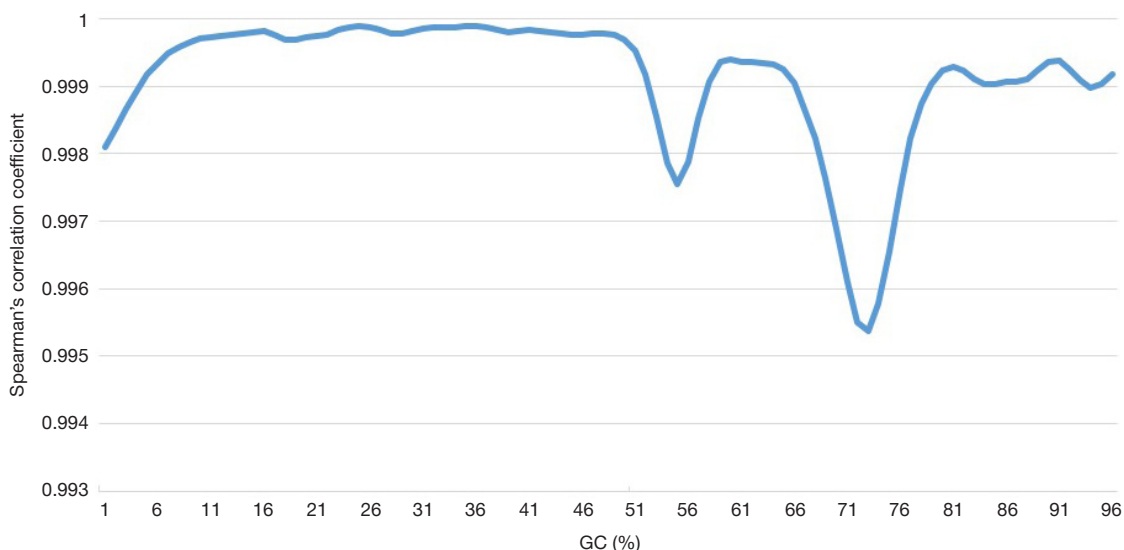
**Fig. 4.** The ankle joint angle range correlation coefficient for each two consecutive GC parts on the goniograms

Table 3. Statistical characteristics of GC parts

Part of gait cycle	Median, degrees	Q1, degrees	Q3, degrees	IR, degrees
1–7%	25.1	22.2	27.4	5.2
8–19%	21.0	16.1	24.6	8.5
20–55%	15.6	10.9	19.7	8.8
56–74%	16.9	14.2	22.5	8.3
75–100%	22.1	18.8	27.4	8.6

represented by 3 clusters. Based on the post-rehabilitation goniograms, Ward's clustering identified 3 parts in the post-rehabilitation gait cycle at 1–61%, 62–75% and 76–97% of the cycle. There were 3 clusters identified in the first part, 2 clusters in the second, and 3 clusters in the third. Thus, the main difference in the GC structure before and after rehabilitation was the presence of 3 parts instead of 5, suggesting consolidation of the goniograms at 1–61% of the gait cycle. Angle comparison before and after rehabilitation demonstrated significant differences in IR only ($p < 0.05$).

The analysis of torque medians in the ten-percentile intervals of the gait cycle before and after rehabilitation also revealed consolidation of these parameters after completion of the rehabilitation program; the most pronounced differences in torques were observed during dorsiflexion in the swing phase (Fig. 5A–C).

Comparison of torque medians in the ten-percentile GC intervals for each patient before and after rehabilitation revealed that torque patterns became more similar after rehabilitation. In almost all our patients, torque peaked during the 7th ten-percentile interval of the gait cycle (71–80%), which corresponds to the middle of the swing phase. The second, not so pronounced peak was observed in the 10th ten-percentile interval of the cycle (91–97%), which corresponds to the end of the swing phase. Statistical analysis showed that the observed changes were associated with Q3 changes and joint torque peaks. During the second half of pre-rehabilitation GC, 3 torque peaks were detected at 55%, 75% (the absolute maximum) and 95% of the cycle. After rehabilitation, there were also 3 torque peaks; however, the first and second peaks almost “fused” into a single peak. After rehabilitation, the first and the second torque peaks were lower than before the program; the third peak was almost the same before and after rehabilitation (Fig. 6).

Summing up, there was an increase in voluntary activity of the lower limb on the FMA scale, a reduction in gastrocnemius and soleus muscles spasticity on the MAS and functional improvement on the FAC scale in patients with post-stroke hemiparesis after robot-assisted gait rehabilitation.

Thorough analysis of movement biomechanics allowed us to identify changes in the GC structure (an increase in the duration of the stance phase) and ankle joint angles/torques (a reduction in the variability and fusion of torque peaks).

DISCUSSION

GC asymmetry is one of the most common gait disturbances beside reduced walking speed and shorter step length observed in stroke survivors. In GC asymmetry, the stance phase becomes shorter, whereas the swing phase of the paretic limb becomes longer, which is reflected in the temporal characteristics of the gait cycle before rehabilitation [2]. The increase in the duration of the stance phase from 28.0% (25; 36) to 33.5% (30; 42) relative to the entire length of the GC following gait training might be the result of improved strength

in the muscles supporting the paretic limb, improved weight shifting, reduced spasticity, and better coordination between the joints. It is known that high muscle tone of ankle flexors prevents the foot from dorsiflexion, forcing the body to stop its forward propulsion; the center of gravity is thus left behind the ankle joint line, the swing phase of the healthy leg becomes shorter, resulting in a shorter step. According to some authors [36], robot-assisted training can reduce spasticity in ankle extensor muscles and indirectly affect the recovery of gait symmetry. This hypothesis is supported by our findings concerning muscle tone reduction in the gastrocnemius and soleus muscles. Reduced muscle tone might promote ankle dorsiflexion during the stance phase. However, no significant differences in the range of motion during the stance phase were detected, which might be explained by the limited amplitude of the ankle dorsiflexion movement in the middle of the stance phase (the range of motion does not exceed 10° at the moment when the center of mass passes the center of pressure) [37]. At the same time, consolidation of ankle joint goniograms before the time point corresponding to 61% of the gait cycle (this part includes the stance phase and the beginning of the swing phase) indirectly suggests a positive effect of the prescribed physiological pattern of the center of mass movement on the ankle joint kinematics during the stance phase.

Apart from the stance and swing phases, some researchers identify 6 phases in the physiological gait biomechanics designated by the peak values of its dynamic parameters [38, 39]. Among these phases, the part at 60–73% of the GC corresponds to the acceleration phase, which begins when the foot leaves the ground and ends when the swing leg is adjacent to the stance leg. In this phase, the body gains up speed to advance the leg forward. In the next part of the cycle (73–87%) the foot passively advances further. This phase begins when the swing leg is adjacent to the stance leg and ends when the swing leg is in front of the body and its tibia is vertical [2, 40].

We found that in patients with poststroke paresis the biomechanics of the ankle joint were changed after gait rehabilitation: the joint was stable during the stance phase and the dorsiflexion movement was faster and smoother as the leg was advancing forward, ensuring sufficient foot clearance. Such changes might be promoted by the synergy of the hip and knee joints prescribed by the robotic trainer and the lack of opportunity to use compensatory strategies for better foot clearance. Perhaps, robot-assisted gait training has a certain universal tuning effect on the ankle joint movement resulting from the correction of the compensatory synergy of the hip and knee joints, reflected in the reduced data variability ($p < 0.05$; Mann–Whitney U), smaller number of the identified clusters and less differing medians after rehabilitation. However, patient clusters identified before and after rehabilitation were very different. This leads us to hypothesize that since patients move to other clusters as they continue gait training, the effect is achieved through different mechanisms, despite the overall “leveling” effect of rehabilitation on the gait pattern.

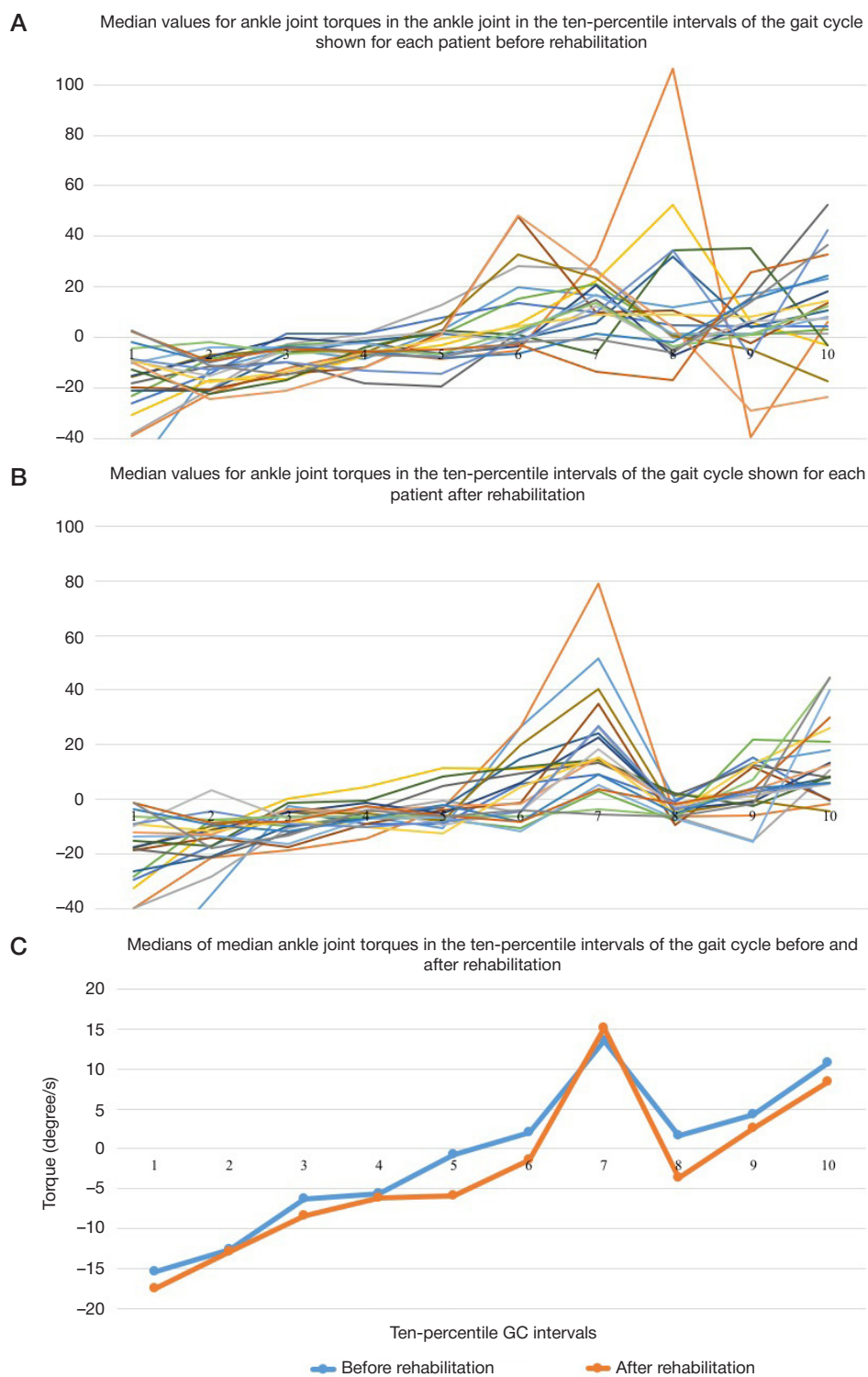


Fig. 5. Characteristics of the ten-percentile intervals of the gait cycle in the ankle joint of the paretic limb before (A) and after (B) rehabilitation; comparison of median values before and after rehabilitation (C)

Comparison of the total sum of angles in the gait cycle reveals that peak values leveled out as other patients showed a shift towards the median. Therefore, we conclude that there were no significant changes in the total sum of ankle joint angles after rehabilitation ($p = 0.521$; Mann-Whitney U). This suggests that structural changes in the gait pattern are not determined by quantitative parameters but are largely the result of the shift in the gait pattern towards the values characteristics of the average gait pattern. Some studies demonstrate that ankle joint angles change following gait rehabilitation, leading to improved dorsiflexion, but those

changes were detected in patients with moderate motor deficit in the ankle joint [40].

Hypothetically, therapy can target not the compensatory muscle synergy as a whole, but some of its components. If its components are more or less equally important, it does not matter which one is directly targeted. However, if the compensatory muscle synergy is not completely formed, the best correctional effect can be achieved by targeting the movement that initiated the development of compensatory synergies.

Our study has a few limitations. During motion capture, the patients were walking on the treadmill which was not equipped

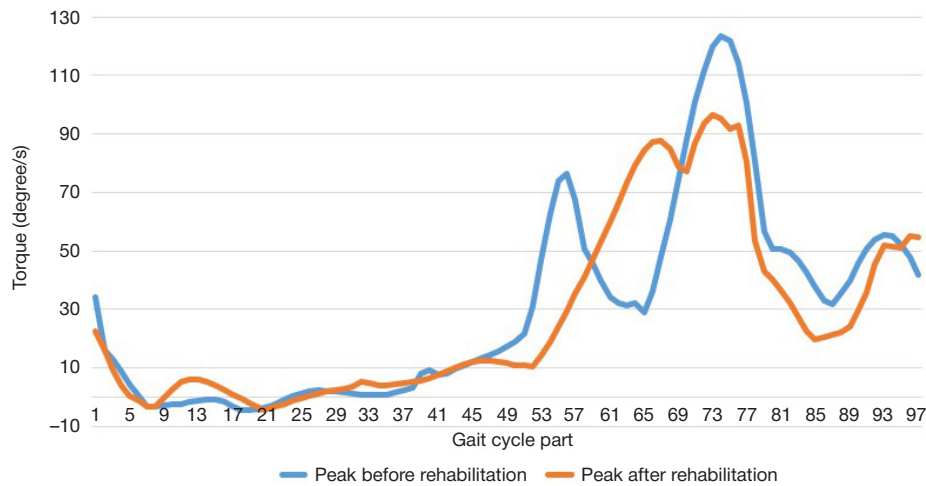


Fig. 6. Torque peaks during ankle flexion/extension of the paretic limb at different gait cycle timepoints before and after rehabilitation

with force plates, so we were unable to analyze support reaction forces. To better understand the biomechanics of the studied joints, further research should be focused on comparing patients and healthy individuals and analyzing the follow-up data and EMG results for muscle activity.

CONCLUSIONS

Robot-assisted gait training of the hip and knee joints can cause changes in ankle goniograms and ankle joint torques

in patients with pathological synergies, improving the biomechanics of the ankle joint. Further research should focus on the comprehensive analysis of the movements of the paretic and healthy leg, pelvis and trunk. Besides, in order to understand the mechanisms promoting changes in muscle synergies, the study protocol should include groups with different exposure to training. The analysis of the effect that robotic therapy has on complex movements will allow to design new training protocols accounting for the presence and severity of pathological compensatory gait patterns.

References

- Balaban B, Tok F. Gait Disturbances in Patients With Stroke. *J PM&R*. 2014; 6 (7): 635–42.
- Beyaert C, Vasa R, Frykberg GE. Gait post-stroke: Pathophysiology and rehabilitation strategies. *J Neurophysiol Clin*. 2015; 45 (4–5): 335–55.
- Jørgensen HS, Nakayama H, Raaschou H, et al. Recovery of walking function in stroke patients: The copenhagen stroke study. *J Arch Phys Med Rehabil*. 1995; 76 (1): 27–32.
- Mehrholz J, Thomas S, Werner C, et al. Electromechanical-assisted training for walking after stroke. *Cochrane Database Syst Rev*. 2017; 5.
- Skvortsov DV. *Klinicheskiy analiz dvizheniy. Analiz pokhodki*. Ivanovo: Stimul, 1996; 344 s. Russian.
- Kim CM, Eng JJ. Magnitude and pattern of 3D kinematic and kinetic gait profiles in persons with stroke: relationship to walking speed. *Gait Posture*. 2004; 20 (2): 140–6.
- Milot M-H, Nadeau S, Gravel D. Muscular utilization of the plantarflexors, hip flexors and extensors in persons with hemiparesis walking at self-selected and maximal speeds. *J Electromyogr Kinesiol*. 2007; 17 (2): 184–193.
- Sadeghi H, Allard P, Duhaime M. Muscle power compensatory mechanisms in below-knee amputee gait. *Am J Phys Med Rehabil*. 2001; 80 (1): 25–32.
- Brunnstrom S. *Movement Therapy in Hemiplegia: A Neurophysiological Approach*. Harper & Row. 1970; 192.
- Bruni MF, Corrado M, De Cola MC, et al. What does best evidence tell us about robotic gait rehabilitation in stroke patients: A systematic review and meta-analysis. *J Clin Neurosci*. 2018; 48: 11–17.
- Tan CH, Kadone H, Watanabe H, Marushima A, et al. Lateral Symmetry of Synergies in Lower Limb Muscles of Acute Post-stroke Patients After Robotic Intervention. *Frontiers in Neuroscience*. 2018; 12: 276.
- Pismennaya EV, Petrushanskaya KA, Kotov SV, et al. Clinical and biomechanical foundation of application of the exoskeleton exoatlet at walking of patients with poststroke disturbances. *Russian Journal of biomechanics*. 2019; 23 (2): 204–30. Russian.
- Vukobratović M, Borovac B. Zero-moment point—thirty five years of its life. *International Journal of Humanoid Robotics*. 2004; 1 (1): 157–73.
- Mokhtari M, Taghizadeh M, Mazare M. Hybrid Adaptive Robust Control Based on CPG and ZMP for a Lower Limb Exoskeleton. *Robotica*. 2020: 1–19.
- Al-Shuka H, Corves B, Vanderborgh B, et al. Zero-Moment Point-Based Biped Robot with Different Walking Patterns. *International Journal of Intelligent Systems and Applications (IJISA)*. 2015; 7: 31–41.
- Eratur K, Kurt O. Natural ZMP Trajectories for Biped Robot Reference Generation. *IEEE Transactions on Industrial Electronics*. 2009; 56 (3): 835–45.
- Schwartz I, Meiner Z. Robotic-Assisted Gait Training in Neurological Patients: Who May Benefit? *Ann Biomed Eng*. 2015; 43 (5): 1260–9.
- Moucheboeuf G, Griffier R, Gasq D. Effects of robotic gait training after stroke: a meta-analysis. *Ann Phys Rehabil Med*. 2020; S.1877–0657(20)30065-8. DOI: 10.1016/j.rehab.2020.02.008.
- Aprile I, Iacovelli C, Goffredo M, et al. Efficacy of end-effector Robot-Assisted Gait Training in subacute stroke patients: Clinical and gait outcomes from a pilot bi-centre study. *NeuroRehabilitation*. 2019; 45 (2): 201–12.
- De Luca A, Vernetti H, Capra C, et al. Recovery and compensation after robotic assisted gait training in chronic stroke survivors. *Disabil Rehabil Assist Technol*. 2019; 14 (8): 826–38.
- Klochkov AS, Telenkov AA, Chernikova LA. Effect of Lokomat trainings on the severity of gait disorders in patients after stroke. *Annals of Clinical and Experimental Neurology*. 2011; 5 (3): 20–25.
- Neckel ND, Blonien N, Nichols D, et al. Abnormal joint torque patterns exhibited by chronic stroke subjects while walking with a prescribed physiological gait pattern. *J Neuroeng Rehabil*. 2008; 5 (1): 1–13.

23. Suponeva NA, Yusupova DG, Zhironova ES, et al. Validation of the modified Rankin Scale in Russia. *J Neurology, Neuropsychiatry, Psychosomatics*. 2018; 10 (4): 36–39.
24. Suponeva NA, Yusupova DG, Ilyina KA, et al. Validation of the Modified Ashworth scale in Russia. *J Annals of clinical and experimental neurology*. 2020; 14 (1): 89–96.
25. Shpakov AV, Artamonov AA, Orlov DO, i dr. Novye podhody v obrabotke biomehanicheskikh harakteristik lokomocij cheloveka, poluchennykh s ispol'zovaniem videoanaliza dvizhenij. Upravlenie dvizheniem *Motor Control 2020 materialy VIII Rossijskoj s mezhdunarodnym uchastiem konferencii po upravleniju dvizheniem*. 2020; 65–66.
26. Docenko VI, Voronov AV, Titarenko NYu, i dr. Komp'juternyj videoanaliz dvizhenij v sportivnoj medicine i nejroreabilitacii. *Medicinskij alfavit*. 2005; 3: 12–14.
27. Ferrarin M, Bovi G, Rabuffetti M, et al. Gait pattern classification in children with Charcot-Marie-Tooth disease type 1A. *Gait and Posture*. 2012; 35: 131–7.
28. Kaczmarczyk K, Wit A, Krawczyk M, et al. Gait classification in poststroke patients using artificial neural networks. *Gait and Posture*. 2009; 30 (2): 207–10.
29. Toro B, Nester CJ, Farren PC. Cluster analysis for the extraction of sagittal gait patterns in children with cerebral palsy. *Gait and Posture*. 2007; 25: 157–65.
30. Giacomozzi C, Martelli F, Nagel A, et al. Cluster analysis to classify gait alterations in rheumatoid arthritis using peak pressure curves. *Gait and Posture*. 2009; 29: 220–4.
31. Fong-Chin S, Wen-Lan W, Yuh-Min C, et al. Fuzzy clustering of gait patterns of patients after ankle arthrodesis based on kinematic parameters. *Med Eng Phys*. 2001; 23: 83–90.
32. Rozumalski A, Schwartz M. Crouch gait patterns defined using k-means cluster analysis are related to underlying clinical pathology. *Gait and Posture*. 2009; 30: 155–60.
33. Mulroy S, Gronley J, Weiss W, et al. Use of cluster analysis for gait pattern classification of patients in the early and late recovery phases following stroke. *Gait and Posture*. 2003; 18: 114–25.
34. Phinyomark A, Osis S, Hettinga BA, Ferber R. Kinematic gait patterns in healthy runners: A hierarchical cluster analysis. *J Biomech*. 2015; 48 (14): 3897–904.
35. Watari R, Osis ST, Phinyomark A, Ferber R. Runners with patellofemoral pain demonstrate sub-groups of pelvic acceleration profiles using hierarchical cluster analysis: an exploratory cross-sectional study. *BMC Musculoskeletal Disorders*. 2018; 19: 120.
36. Trompetto C, Marinelli L, Mori L, et al. Postactivation depression changes after robotic-assisted gait training in hemiplegic stroke patients. *Gait Posture*. 2013; 38 (4): 729–33.
37. Skvortsov DV. Diagnostika dvigatel'noj patologii instrumental'nymi metodami: analiz pokhodki stabilometriya. M., 2007; 640 s.
38. Vitenson AS, Petrushanskaya KA. Physiological foundations of a method of artificial correction of movements by means of programmable electrical stimulation of muscles during walking. *Russian Journal of biomechanics*. 2005; 9 (1): 7–26.
39. Vorontcova OI, Lozovskaya MV. Structure of gait cycle based on kinetic and kinematical parameters. *Journal of new medical technologies*. 2017; 3: 9–15.
40. Bonnyaud C, Zory R, Boudarham J, et al. Effect of a robotic restraint gait training versus robotic conventional gait training on gait parameters in stroke patients. *Exp Brain Res*. 2014; 232 (1): 31–42.

Литература

1. Balaban B, Tok F. Gait Disturbances in Patients With Stroke. *J PM&R*. 2014; 6 (7): 635–42.
2. Beyaert C, Vasa R, Frykberg GE. Gait post-stroke: Pathophysiology and rehabilitation strategies. *J Neurophysiol Clin*. 2015; 45 (4–5): 335–55.
3. Jørgensen HS, Nakayama H, Raaschou H, et al. Recovery of walking function in stroke patients: The copenhagen stroke study. *J Arch Phys Med Rehabil*. 1995; 76 (1): 27–32.
4. Mehrholz J, Thomas S, Werner C, et al. Electromechanical-assisted training for walking after stroke. *Cochrane Database Syst Rev*. 2017; 5.
5. Скворцов Д. В. Клинический анализ движений. Анализ походки. Иваново: Стимул, 1996; 344 с.
6. Kim CM, Eng JJ. Magnitude and pattern of 3D kinematic and kinetic gait profiles in persons with stroke: relationship to walking speed. *Gait Posture*. 2004; 20 (2): 140–6.
7. Milot M-H, Nadeau S, Gravel D. Muscular utilization of the plantarflexors, hip flexors and extensors in persons with hemiparesis walking at self-selected and maximal speeds. *J Electromyogr Kinesiol*. 2007; 17 (2): 184–193.
8. Sadeghi H, Allard P, Duhaime M. Muscle power compensatory mechanisms in below-knee amputee gait. *Am J Phys Med Rehabil*. 2001; 80 (1): 25–32.
9. Brunnstrom S. *Movement Therapy in Hemiplegia: A Neurophysiological Approach*. Harper & Row. 1970; 192.
10. Bruni MF, Corrado M, De Cola MC, et al. What does best evidence tell us about robotic gait rehabilitation in stroke patients: A systematic review and meta-analysis. *J Clin Neurosci*. 2018; 48: 11–17.
11. Tan CH, Kadone H, Watanabe H, Marushima A, et al. Lateral Symmetry of Synergies in Lower Limb Muscles of Acute Post-stroke Patients After Robotic Intervention. *Frontiers in Neuroscience*. 2018; 12: 276.
12. Письменная Е. В., Петрушанская К. А., Котов С. В. и др. Клинико-биомеханическое обоснование применения экзоскелета «Экзоатлет» при ходьбе больных с последствиями ишемического инсульта. *Российский журнал биомеханики*. 2019; 23 (2): 204–30.
13. Vukobratović M, Borovac B. Zero-moment point-thirty five years of its life. *International Journal of Humanoid Robotics*. 2004; 1 (1): 157–73.
14. Mokhtari M, Taghizadeh M, Mazare M. Hybrid Adaptive Robust Control Based on CPG and ZMP for a Lower Limb Exoskeleton. *Robotica*. 2020: 1–19.
15. Al-Shuka H, Corves B, Vanderborgh B, et al. Zero-Moment Point-Based Biped Robot with Different Walking Patterns. *International Journal of Intelligent Systems and Applications (IJISA)*. 2015; 7: 31–41.
16. Erbatun K, Kurt O. Natural ZMP Trajectories for Biped Robot Reference Generation. *IEEE Transactions on Industrial Electronics*. 2009; 56 (3): 835–45.
17. Schwartz I, Meiner Z. Robotic-Assisted Gait Training in Neurological Patients: Who May Benefit? *Ann Biomed Eng*. 2015; 43 (5): 1260–9.
18. Moucheboeuf G, Griffier R, Gasq D. Effects of robotic gait training after stroke: a meta-analysis. *Ann Phys Rehabil Med*. 2020; S.1877–0657(20)30065-8. DOI: 10.1016/j.rehab.2020.02.008.
19. Aprile I, Iacovelli C, Goffredo M, et al. Efficacy of end-effector Robot-Assisted Gait Training in subacute stroke patients: Clinical and gait outcomes from a pilot bi-centre study. *NeuroRehabilitation*. 2019; 45 (2): 201–12.
20. De Luca A, Vernetti H, Capra C, et al. Recovery and compensation after robotic assisted gait training in chronic stroke survivors. *Disabil Rehabil Assist Technol*. 2019; 14 (8): 826–38.
21. Клочков А. С., Теленков А. А., Черникова Л. А. Влияние тренировок на системе «Локотат» на выраженность двигательных нарушений у пациентов, перенесших инсульт. *Анналы клинической и экспериментальной неврологии*. 2011; 5 (3): 20–25.
22. Neckel ND, Blonien N, Nichols D, et al. Abnormal joint torque patterns exhibited by chronic stroke subjects while walking with a prescribed physiological gait pattern. *J Neuroeng Rehabil*. 2008; 5 (1): 1–13.
23. Супонева Н. А., Юсупова Д. Г., Жирова Е. С. и др. Валидация модифицированной шкалы Рэнкина (The Modified Rankin Scale, MRS) в России. *Неврология, нейропсихиатрия, психосоматика*. 2018; 10 (4): 36–39.
24. Супонева Н. А., Юсупова Д. Г., Ильина К. А. и др. Валидация

- модифицированной шкалы Эшворта (modified ashworth scale) в России. *Анналы клинической и экспериментальной неврологии*. 2020; 14 (1): 89–96.
25. Шпаков А. В., Артамонов А. А., Орлов Д. О. и др. Новые подходы в обработке биомеханических характеристик локомоций человека, полученных с использованием видеоанализа движений. *Управление движением Motor Control 2020 материалы VIII Российской с международным участием конференции по управлению движением*. 2020; 65–66.
 26. Доценко В. И., Воронов А. В., Титаренко Н. Ю. и др. Компьютерный видеоанализ движений в спортивной медицине и нейрореабилитации. *Медицинский алфавит*. 2005; 3: 12–14.
 27. Ferrarin M, Bovi G, Rabuffetti M, et al. Gait pattern classification in children with Charcot-Marie-Tooth disease type 1A. *Gait and Posture*. 2012; 35: 131–7.
 28. Kaczmarsczyk K, Wit A, Krawczyk M, et al. Gait classification in poststroke patients using artificial neural networks. *Gait and Posture*. 2009; 30 (2): 207–10.
 29. Toro B, Nester CJ, Farren PC. Cluster analysis for the extraction of sagittal gait patterns in children with cerebral palsy. *Gait and Posture*. 2007; 25: 157–65.
 30. Giacomozzi C, Martelli F, Nagel A, et al. Cluster analysis to classify gait alterations in rheumatoid arthritis using peak pressure curves. *Gait and Posture*. 2009; 29: 220–4.
 31. Fong-Chin S, Wen-Lan W, Yuh-Min C, et al. Fuzzy clustering of gait patterns of patients after ankle arthrodesis based on kinematic parameters. *Med Eng Phys*. 2001; 23: 83–90.
 32. Rozumalski A, Schwartz M. Crouch gait patterns defined using k-means cluster analysis are related to underlying clinical pathology. *Gait and Posture*. 2009; 30: 155–60.
 33. Mulroy S, Gronley J, Weiss W, et al. Use of cluster analysis for gait pattern classification of patients in the early and late recovery phases following stroke. *Gait and Posture*. 2003; 18: 114–25.
 34. Phinyomark A, Osis S, Hettinga BA, Ferber R. Kinematic gait patterns in healthy runners: A hierarchical cluster analysis. *J Biomech*. 2015; 48 (14): 3897–904.
 35. Watari R, Osis ST, Phinyomark A, Ferber R. Runners with patellofemoral pain demonstrate sub-groups of pelvic acceleration profiles using hierarchical cluster analysis: an exploratory cross-sectional study. *BMC Musculoskeletal Disorders*. 2018; 19: 120.
 36. Trompetto C, Marinelli L, Mori L, et al. Postactivation depression changes after robotic-assisted gait training in hemiplegic stroke patients. *Gait Posture*. 2013; 38 (4): 729–33.
 37. Скворцов Д. В. Диагностика двигательной патологии инструментальными методами: анализ походки стабилметрия. М., 2007; 640 с.
 38. Витензон А. С., Петрушанская К. А. К фазовому анализу ходьбы и некоторых ритмических движений человека. *Российский журнал биомеханики*. 2005; 9 (1): 7–26.
 39. Воронцова О. И., Лозовская М. В. Структура шагового цикла по данным анализа кинетических и кинематических параметров походки человека. *Вестник новых медицинских технологий*. 2017; 3: 9–15.
 40. Bonnyaud C, Zory R, Boudarham J, et al. Effect of a robotic restraint gait training versus robotic conventional gait training on gait parameters in stroke patients. *Exp Brain Res*. 2014; 232 (1): 31–42.

TAXONOMIC DYSBIOSIS OF GUT MICROBIOTA AND SERUM BIOMARKERS REFLECT SEVERITY OF CENTRAL NERVOUS SYSTEM INJURY

Chernevskaya EA , Meglei AYu, Buyakova IV, Kovaleva NYu, Gorshkov KM, ZakharchenkoVE, Beloborodova NV

Federal Research and Clinical Center of Intensive Care Medicine and Rehabilitology, Moscow, Russian

The term “chronic critical illness” (CCI) refers to patients with prolonged dependence on intensive care. In most patients, CCI is triggered by severe brain injury. Ever more studies researching the microbiota in pathologic conditions are published every year, but a lot is yet to be elucidated about the composition of the gut microbiota in CCI. The aim of this study was to investigate possible correlations between changes in the taxonomic abundance of the gut microbiota, levels of proinflammatory and neurological serum biomarkers and the severity of central nervous system injury in patients with CCI. Our prospective observational pilot study included 29 patients with CCI. Using real-time PCR allowed us to detect changes in the taxonomic abundance of the gut microbiota. The correlation analysis of serum biomarkers and the taxonomic composition of the gut microbiota revealed statistically significant correlations between cortisol levels and the abundance of *F. prausnitzii* ($r = -0.62$; $p < 0.05$) and *B. thetaiotaomicron* ($r = -0.57$; $p < 0.05$) in vegetative state patients; between the CRP/albumin ratio and the abundance of *S. aureus* ($r = 0.72$; $p < 0.05$); between the abundance of *B. fragilis group/F. prausnitzii* and S100 levels ($r = 0.45$; $p < 0.05$) in conscious patients; between Glasgow coma scale scores and the abundance of *Enterococcus spp.* ($r = -0.77$; $p < 0.05$) in both groups. Thus, the association between the changes in the taxonomic composition of the gut microbiota and the severity of neurologic deficit can be evaluated using PCR-based diagnostic techniques and blood serum biomarkers. This approach will help to optimize antibacterial treatment regimens and/or develop alternative strategies to minimize the aggressive effect of antibiotics on the gut microbiota.

Keywords: gut microbiota, gut-brain axis, chronic critical illness, biomarkers, procalcitonin, cortisol, CRP/albumin ratio, real-time PCR, *Feacalibacterium prausnitzii*, *Bacteroides thetaiotaomicron*, *Enterococcus spp.*

Author contribution: Chernevskaya EA, Meglei AYu — taxonomic microbiota profiling, serum biomarker tests, data analysis, manuscript preparation; Beloborodova NV — study design, final version of the manuscript; Buyakova IV, Kovaleva NYu, Gorshkov KM — patient recruitment and treatment, clinical data collection; ZakharchenkoVE — sample collection, final version of the manuscript. All authors read and approved the final version of the manuscript.

Compliance with ethical standards: the study was approved by the Ethics Committee of the Federal Research and Clinical Center of Intensive Care Medicine and Rehabilitology (Protocol № 2/19/2 dated June 20, 2019). Informed consent was obtained from all study participants or their legal representatives.

 **Correspondence should be addressed:** Ekaterina A. Chernevskaya
Petrovka, 25, s. 2, Moscow, 127051; echernevskaya@fnkcr.ru

Received: 20.08.2020 **Accepted:** 03.09.2020 **Published online:** 16.09.2020

DOI: 10.24075/brsmu.2020.053

ТАКСОНОМИЧЕСКИЙ ДИСБИОЗ МИКРОБИОТЫ И СЫВОРОТОЧНЫЕ БИОМАРКЕРЫ КАК ОТРАЖЕНИЕ ТЯЖЕСТИ ПОРАЖЕНИЯ ЦЕНТРАЛЬНОЙ НЕРВНОЙ СИСТЕМЫ

Е. А. Черневская , А. Ю. Меглей, И. В. Буйакова, Н. Ю. Ковалева, К. М. Горшков, В. Е. Захарченко, Н. В. Белобородова

Федеральный научно-клинический центр реаниматологии и реабилитологии, Москва, Россия

Синдром «хронического критического состояния» (ХКС) объединяет пациентов с длительной зависимостью от жизнеобеспечивающих методов терапии. У значительной доли пациентов пусковым фактором ХКС служат тяжелые повреждения головного мозга. Число исследований по изучению микробиоты при различных патологических состояниях растет с каждым годом, однако особенности микробиоты кишечника при ХКС все еще недостаточно изучены. Целью работы было выявить связь изменений таксономического состава микробиоты кишечника, воспалительных и неврологических сывороточных биомаркеров с тяжестью поражения центральной нервной системы у пациентов в ХКС. В сравнительном проспективном исследовании у 29 пациентов с поражением ЦНС в ХКС методом ПЦР в реальном времени (ПЦР-РВ) обнаружены изменения таксономического состава микробиоты. Корреляционный анализ уровней биомаркеров и представителей микробиоты кишечника выявил статистически значимые корреляции: кортизола с *F. prausnitzii* ($r = -0.62$; $p < 0.05$) и *B. thetaiotaomicron* ($r = -0.57$; $p < 0.05$) в группе пациентов в вегетативном состоянии; коэффициента СРБ/альбумин с *S. aureus* ($r = 0.72$; $p < 0.05$), *B. fragilis group/F. prausnitzii* с S100 ($r = 0.45$; $p < 0.05$) в группе пациентов с сохраненным сознанием; результатов по шкале комы Глазго с уровнем *Enterococcus spp.* ($r = -0.77$; $p < 0.05$) в обеих группах. Таким образом, комплексная диагностика с применением метода ПЦР-РВ и современных биомаркеров позволяет оценить связь таксономических изменений состава микробиоты кишечника со степенью неврологического дефицита. Данный подход позволит оптимизировать использование антибактериальных препаратов и/или разработать альтернативные стратегии для менее агрессивного воздействия на микробиоту кишечника.

Ключевые слова: микробиота кишечника, ось «кишечник – мозг», хроническое критическое состояние, биомаркеры, прокальцитонин, кортизол, коэффициент СРБ/альбумин, ПЦР в реальном времени, *Feacalibacterium prausnitzii*, *Bacteroides thetaiotaomicron*, *Enterococcus spp.*

Вклад авторов: Е. А. Черневская, А. Ю. Меглей — оценка таксономического состава микробиоты и уровня биомаркеров, анализ полученных данных, написание текста рукописи; Н. В. Белобородова — дизайн исследования, редактирование рукописи; И. В. Буйакова, Н. Ю. Ковалева, К. М. Горшков — отбор и работа с пациентами, сбор клинических данных; В. Е. Захарченко — получение данных для анализа, редактирование рукописи. Все авторы прочли и одобрили рукопись.

Соблюдение этических стандартов: исследование одобрено этическим комитетом Федерального научно-клинического центра реаниматологии и реабилитологии (протокол № 2/19/2 от 20 июня 2019 г.). Все пациенты или их законные представители подписали добровольное информированное согласие.

 **Для корреспонденции:** Екатерина Александровна Черневская
ул. Петровка, д. 25, с. 2, г. Москва, 127051; echernevskaya@fnkcr.ru

Статья получена: 20.08.2020 **Статья принята к печати:** 03.09.2020 **Опубликована онлайн:** 16.09.2020

DOI: 10.24075/vrgmu.2020.053

Over the past decades, advances in intensive care have substantially improved survival in acutely critically ill patients but, at the same time, expanded the population of patients with prolonged dependence on intensive care. This engendered the concept of chronic critical illness (CCI) [1]. CCI criteria include at least 2 weeks in an intensive care unit (ICU); protracted (14–28 days) mechanical ventilation (MV); persistent inflammation; immunosuppression; hypermetabolism and hypercatabolism; increased susceptibility to infection [2–4].

Most survivors of severe brain injury meet CCI criteria. They are also at risk for CCI-attributed neurological deficit aggravated by their underlying condition and caused by functional or metabolic impairment mediated by pro- or noninflammatory factors, including microglia hyperactivation, blood brain barrier (BBB) disruption and altered neurotransmission [3]. These disturbances are detected based on the elevated markers of brain inflammation/injury [5]. Currently, there is no all-in-one biomarker for evaluating the complex pathophysiology of critical illness. Therefore, CCI patient monitoring relies on the whole array of different biomarkers. Of them, the most commonly used are S100 proteins and neuron-specific enolase (NSE) [6–8], which indicate neuronal injury, and non-specific markers of inflammation, like interleukin-6 (IL6) [9] and C-reactive protein (CRP) [10].

Changes in the gut microbiota might be an important contributor to CCI. Microbiota has the ability to affect CNS function in humans, which makes it an attractive object for research [11, 12]. The gastrointestinal (GI) tract may be involved in the development and progression of organ failures in critically ill patients [13, 14]. CCI patients have metabolic disorders leading to protein-energy malnutrition [15] and GI comorbidities caused, among other things, by nasogastric nutrition [16], which could be the underlying cause of dysbiosis observed in such patients [17]. Ever more studies researching the microbiota of critically ill patients are published every year; still, a lot is yet to be elucidated [18].

Human microbiota can be studied using a broad arsenal of methods, from classic culture-based analysis to state-of-the-art next generation sequencing (NGS). Real-time PCR is a promising alternative to culture-based methods that allows creating both qualitative and quantitative profiles of the gut microbiota [19].

The aim of this study was to investigate possible correlations between changes in the taxonomic abundance of the gut microbiota, levels of proinflammatory and neurological serum biomarkers and the severity of CNS injury in patients with CCI.

METHODS

Our prospective observational study included patients with CNS injury of various etiology ($n = 29$) receiving medical care at the ICU of the Federal Research and Clinical Center of Intensive Care Medicine and Rehabilitology from June 2019 to March 2020.

The following inclusion criteria were applied: patients with CNS injury of various etiology meeting CCI criteria (at least 2 weeks in ICU and/or 14–28 days of MV) aged 18–75 years and admitted to ICU for intensive neurological care. Exclusion criteria: age over 75 years; chemotherapy/hormonal therapy with steroids; neurological infection; therapy with antibiotics, pro-, pre- or probiotics at the time of admission.

The age range was from 20 to 75 years (median: 56 (32–63) years); 17 study participants were female (58.6%) and 12 were male (41.4%). Among the pathologies included in the study were an acute cerebrovascular event (ACVE) (15 patients), severe traumatic brain injury (TBI) (7 patients), neurosurgery

complications in the postoperative period (4 patients), anoxic brain injury after a successful CPR effort to reverse clinical death (3 patients). Ten patients were on MV and 19 had a tracheostomy tube. All patients were on enteral feeding; over half of them ($n = 15$) were fed through a nasogastric or gastrostomy tube (GT). Antibacterial therapy was administered to 21 patients who had urinary or lower respiratory tract infection (Table 1). All patients received a metabiotic containing active metabolites of *Bacillus subtilis*, a sorbent and a prebiotic.

The level of consciousness was assessed using the Glasgow coma scale (GCS): 15 points — fully awake and aware, 14–13 points — clouding of consciousness, 12–9 points — sopor, 8–6 points — coma; antibiotic prescriptions were done on the day of blood/stool collection.

Sample collection

One stool sample and one venous blood sample were collected from each patient on the day of admission (prior to antimicrobial therapy) and then every 7 days until transfer from ICU. In total, 2 to 7 samples of biological specimens were obtained from each patient. Sample collection, transport and storage were performed following standard guidelines [20]. Stool samples were collected into a disposable sterile container. The containers were transported to the lab and stored at $+2 - +8$ °C until further use. Time from sample collection to sample analysis did not exceed 24 h. DNA was extracted from the supernatant: 0.1 g of the stool sample was mixed with 800 μ l of the isotonic solution and vortexed until homogeneity. The resultant mixture was centrifuged at 12,045 g for 30 s. Further analysis was carried out following the protocol provided by the assay manufacturer (Colonoflor-16 by AlphaLab, Russia). Blood was collected from a venous catheter into an anticoagulant-free test tube. Serum samples were obtained by centrifuging the blood at 1,500 g for 10 min. Serum aliquots (500 μ l) were poured into disposable Eppendorf tubes, frozen and stored at -20 °C until further use.

Analysis of gut microbiota taxonomic abundance

Composition of the gut microbiota was analyzed using Colonoflor-16 kits (AlphaLab; Russia), which include reagents for DNA extraction, PCR primers specific for all bacterial DNA (total bacterial mass) and species-specific primers. Measurements were performed using a CFX 96 Real-Time PCR Detection System (BioRad; USA).

Analysis of serum biomarkers

Concentrations of NSE, S100, procalcitonin (PCT), IL6, and cortisol were measured in 200 μ l serum samples using reagent kits by Roche Diagnostics, Switzerland, and a Cobas e411 automated analyzer, which relies on the ElectroChemiluminescence technology (Roche; Switzerland).

Albumin and CRP levels were determined using an automated AU 480 chemistry analyzer (Beckman Coulter; USA) and reagent kits by the same manufacturer.

Statistical analysis was carried out in Statistica 13.0 (Stat Soft Inc.; USA). The obtained data are presented below as median values and lower and upper quartiles. Intergroup comparisons were made using the Mann–Whitney U test. Correlation strength was measured using Spearman's rank correlation coefficient. Differences were considered significant at $p \leq 0.05$.

Table 1. Patient characteristics. MV — mechanical ventilation, TST — tracheostomy tube, ACVE — acute cerebrovascular event, TBI — traumatic brain injury

Vegetative state patients (n = 10)					
Patient ID	Age/sex	Diagnosis	Respiration	Antibacterial therapy	GCS score
1	40 / f	Anoxic brain injury	MV	Oxazolidinone (linezolid), cephalosporins, carbapenems	9
2	64 / f	ACVE	MV, TST	Cephalosporins, carbapenems, aminoglycosides, glycopeptides (vancomycin)	10
3	32 / f	Post-op complications	MV, TST	Fosfomycins (monurol), carbapenems, aminoglycosides, glycopeptides (vancomycin)	12–15
4	61 / f	ACVE	TST	Nitrofurans (macmiror), carbapenems, glycopeptides, rifampicin	13
5	38 / f	ACVE	MV	Carbapenems	6
6	31 / f	TBI	TST	–	13–15
7	69 / f	ACVE	MV, TST	Carbapenems, aminoglycosides, tetracyclines	9–12
8	51 / m	TBI	TST	Carbapenems, glycopeptides (vancomycin), tetracyclines	13
9	62 / m	Post-op complications	MV, TST	Glycopeptides (vancomycin), aminoglycosides, cephalosporins, fosfomycins (monurol)	9–14
10	26 / f	TBI	TST	Carbapenems, tetracyclines, glycopeptides (vancomycin), sulfonamides	10–12
Conscious patients (n = 19)					
1	26 / m	ACVE	TST	Macrolides, glycopeptides	15
2	56 / m	Anoxic brain injury	TST	–	15
3	58 / f	ACVE	TST	–	15
4	60 / m	ACVE	TST	Nitrofurans, enterol	15
5	22 / f	TBI	TST	–	15
6	42 / f	ACVE	TST	–	–
7	20 / m	TBI	TST	Cephalosporins	–
8	63 / f	ACVE	TST	Carbapenems, aminoglycosides	12–14
9	74 / m	ACVE	TST	–	14
10	32 / m	Post-op complications	TST	–	15
11	44 / m	Anoxic brain injury	TST	Carbapenems, tetracyclines	15
12	69 / f	TBI	MV	–	13
13	58 / m	ACVE	TST	Fluoroquinolones, aminoglycosides	14–15
14	74 / m	ACVE	MV	Aminoglycosides, sulfonamides, nitrofurans, tetracyclines, cephalosporins, antimycotics	10
15	76 / m	ACVE	TST	Cephalosporins, glycopeptides, fosfomycins	10–14
16	72 / f	Post-op complications	MV	Carbapenems, glycopeptides, antimycotics	14
17	23 / f	TBI	TST	Carbapenems, glycopeptides	15
18	51 / f	ACVE	MV, TST	Cephalosporins, glycopeptides, aminoglycosides	11–15
19	57 / m	ACVE	TST	Tetracyclines, carbapenems, glycopeptides	10

RESULTS

Our study included 29 patients (see Table 1). Patients with etiologically different severe CNS injury formed a single group due to similar CCI manifestations regardless of the underlying condition. No significant differences in the taxonomic abundance of the gut microbiota were observed between the subgroups of patients receiving or not receiving antimicrobial therapy (Table 2). Therefore, the subsequent intergroup comparisons were based on neurologic assessment scores.

Based on the level of consciousness, the patients were divided into 2 subgroups [21] (see Table 1): vegetative state or minimally responsive patients ($n = 10$) and conscious patients with pronounced cognitive and mental impairment ($n = 19$). The latter is a clinical sign of CCI. The subgroups were comparable in terms of age (Table 3).

The following features of the gut microbiota taxonomy were identified during the analysis aided by real-time PCR (Fig. 1):

- total bacterial mass was comparable to the reference ranges provided by the manufacturer of the assay;

- gut microbiota of CCI patients contains *Clostridium spp.*, *Fusobacterium nucleatum*, and *Parvimonas micra*, which are not detected in healthy individuals;

- for 6 microorganisms (*Klebsiella spp.*, *Candida spp.*, *Staphylococcus aureus*, *Proteus spp.*, *Enterobacter spp./Citrobacter spp.*), base 10 logarithms of CFU concentrations (lg CFU/G) were 1.5–2 times above the upper reference limit;

- *Bacteroides thetaiotimicron* were low in comparison with the reference values;

- significant differences were observed in *F. prausnitzii* concentrations between the subgroups of patients with different level of consciousness ($p = 0.015$);

Levels of serum biomarkers (cortisol, albumin, CRP, CRP to albumin ratio) differed significantly between the groups (see Table 3). PCT was within the reference range in both conscious and vegetative state patients, but the differences between these two groups were significant ($p = 0.009$) (see Table 3).

Based on their GCS scores, our patients were divided into 3 subgroups: 15 points — fully awake and aware patients ($n = 37$), 14–13 points — clouding of consciousness ($n = 33$), 12–6

Table 2. Taxonomic abundance of the gut microbiota in patients receiving or not receiving antibacterial therapy

Parameter	Reference range	Patients, median (Q1; Q3)	
		Received antibiotics (n = 19)	Did not receive antibiotics (n = 21)
Total bacterial mass	< 10 ¹²	2×10 ¹² (3×10 ¹¹ –8×10 ¹²)	2.5×10 ¹² (2×10 ¹¹ –10 ¹³)
<i>Lactobacillus spp.</i>	10 ⁷ –10 ⁸	4×10 ⁷ (2×10 ⁶ –10 ⁸)	3×10 ⁷ (7×10 ⁶ –6.5×10 ⁹)
<i>Bifidobacterium spp.</i>	10 ⁹ –10 ¹⁰	4×10 ⁹ (3×10 ⁸ –3×10 ¹⁰)	9×10 ⁸ (9.5×10 ⁷ –8.5×10 ⁹)
<i>Escherichia coli</i>	10 ⁷ –10 ⁸	5×10 ⁸ (7×10 ⁷ –3×10 ⁹)	3×10 ⁸ (4.5×10 ⁷ –3.5×10 ⁹)
<i>Bacteroides fragilis group</i>	10 ⁹ –10 ¹²	1.5×10 ¹² (2×10 ¹¹ –8×10 ¹²)	4×10 ¹² (3×10 ¹¹ –10 ¹³)
<i>Faecalibacterium prausnitzii</i>	10 ⁸ –10 ¹¹	5×10 ⁷ (9.5×10 ⁶ –6×10 ⁸)	10 ⁸ (10 ⁷ –3×10 ¹⁰)
<i>Klebsiella pneumoniae</i>	< 10 ⁴	3×10 ⁸ (2×10 ⁵ –10 ⁹)	6×10 ⁵ (2×10 ⁵ –10 ⁶)
<i>Klebsiella oxytoca</i>	< 10 ⁴	1.5×10 ¹¹ (2×10 ⁶ –10 ¹³)	2×10 ¹⁴ (1.1×10 ⁶ –4.5×10 ¹⁴)
<i>Candida spp.</i>	< 10 ⁴	2×10 ⁷ (6×10 ⁶ –5×10 ⁷)	2×10 ⁷ (7×10 ⁶ –2×10 ⁷)
<i>Staphylococcus aureus</i>	< 10 ⁴	4×10 ⁸ (3×10 ⁷ –6×10 ¹¹)	2×10 ⁸ (3×10 ⁷ –10 ⁹)
<i>Enterococcus spp.</i>	< 10 ⁸	8×10 ⁵ (7×10 ⁵ –9×10 ⁶)	1.2×10 ⁶ (2×10 ⁵ –2×10 ⁹)
<i>Bacteroides thetaiotaomicron</i>	10 ⁹ –10 ¹²	6×10 ⁸ (2×10 ⁷ –4×10 ⁹)	2.5×10 ⁸ (2.5×10 ⁷ –2×10 ⁹)
<i>Akkermansia muciniphila</i>	< 10 ¹¹	8×10 ⁸ (10 ⁷ –3×10 ⁹)	5.1×10 ⁸ (5.1×10 ⁷ –5.5×10 ⁹)
<i>Clostridium difficile</i>	–	2×10 ⁸ (10 ⁷ –2×10 ⁹)	4×10 ⁷ (2×10 ⁵ –10 ⁹)
<i>Clostridium perfringens</i>	–	–	6×10 ⁸ (6×10 ⁵ –2×10 ⁹)
<i>Proteus spp.</i>	< 10 ⁴	10 ⁹ (2.5×10 ⁸ –2×10 ¹⁰)	6.5×10 ⁸ (10 ⁸ –10 ¹⁰)
<i>Enterobacter spp. / Citrobacter spp.</i>	< 10 ⁴	4.5×10 ⁷ (6.5×10 ⁶ –6.5×10 ⁸)	5×10 ⁸ (2×10 ⁷ –4×10 ⁹)
<i>Fusobacterium nucleatum</i>	–	2×10 ⁷ (5×10 ⁶ –2×10 ⁸)	1.95×10 ⁶ (3×10 ⁵ –4.5×10 ⁷)
<i>Parvimonas micra</i>	–	2.55×10 ⁸ (7.5×10 ⁶ –10 ¹⁴)	10 ⁷ (2×10 ⁵ –2×10 ¹²)
<i>Bacteroides fragilis group to Faecalibacterium prausnitzii ratio</i>	0.1–100	5000 (100–100 000)	667 (100–15 000)

points — sopor/coma (n = 40). Differences in the CRP/albumin ratio (Fig. 2), cortisol and IL6 (Fig. 3) observed between these groups were statistically significant.

To test correlations in the gut-brain axis system, we applied the correlation analysis to the levels of serum biomarkers and gut microbiota representatives. In vegetative state patients, significant negative correlations were discovered for cortisol and *F. prausnitzii* (r = -0.62) and cortisol and *B. thetaiotaomicron* (r = -0.57). In conscious patients, the CRP/albumin ratio value was directly correlated with the abundance of *S. aureus* (r = 0.72); S100 levels were directly correlated with *B. fragilis group/F. prausnitzii* (r = 0.45).

A strong negative correlation was discovered between the abundance of *Enterococcus spp.* and GCS scores (r = -0.77; ρ ≤ 0.05).

DISCUSSION

Based on our findings, we conclude that the taxonomic abundance of the gut microbiota in CCI patients differs significantly from the reference values, regardless of their neurological status. Pronounced dysbiosis in patients with CCI is characterized by increased levels of *Proteobacteria*, *Candida spp.*, opportunistic *Firmicutes* and *Bacteroides*, and reduced abundance of commensal microorganisms (see Fig. 1) producing low molecular weight metabolites (*F. prausnitzii*). These data are consistent with the findings of previous gut microbiota studies that employed 16S RNA sequencing and were conducted in patients undergoing intensive care [22] and critically ill patients with brain injury [23]. It is reported that pronounced dysbiosis developed by stroke survivors and

Table 3. Blood serum parameters in patients with CCI

Parameter, unit	Reference range	Patients, median (Q1; Q3)		p
		Conscious (n = 19)	Vegetative state (n = 10)	
Age, years	–	57 (32–69)	51 (38–62)	0.82
PCT, ng/ml*	<0.25	0.058 (0.039–0.095)	0.107 (0.08–0.177)	0.009
Cortisol, nmol/L*	166–507	367 (244–623)	682 (492–816)	0.001
IL6, pg/ml	<7	31 (15–47)	35 (14–67)	0.293
S100, µg/ml	<0.1	0.097 (0.05–0.16)	0.105 (0.06–0.19)	0.423
NSE, ng/ml	15.7–17	17.8 (12.8–23)	15.2 (9.7–22)	0.248
CRP, mg/L*	<5	35 (18–78)	76 (33–147)	0.004
Albumin, g/L*	35–55	33 (28–35)	28 (25–35)	0.038
CRP/albumin, rel.un.	<1	1.2 (0.5–2.2)	2.5 (0.9–5.8)	0.003

Note: * — differences are statistically significant.

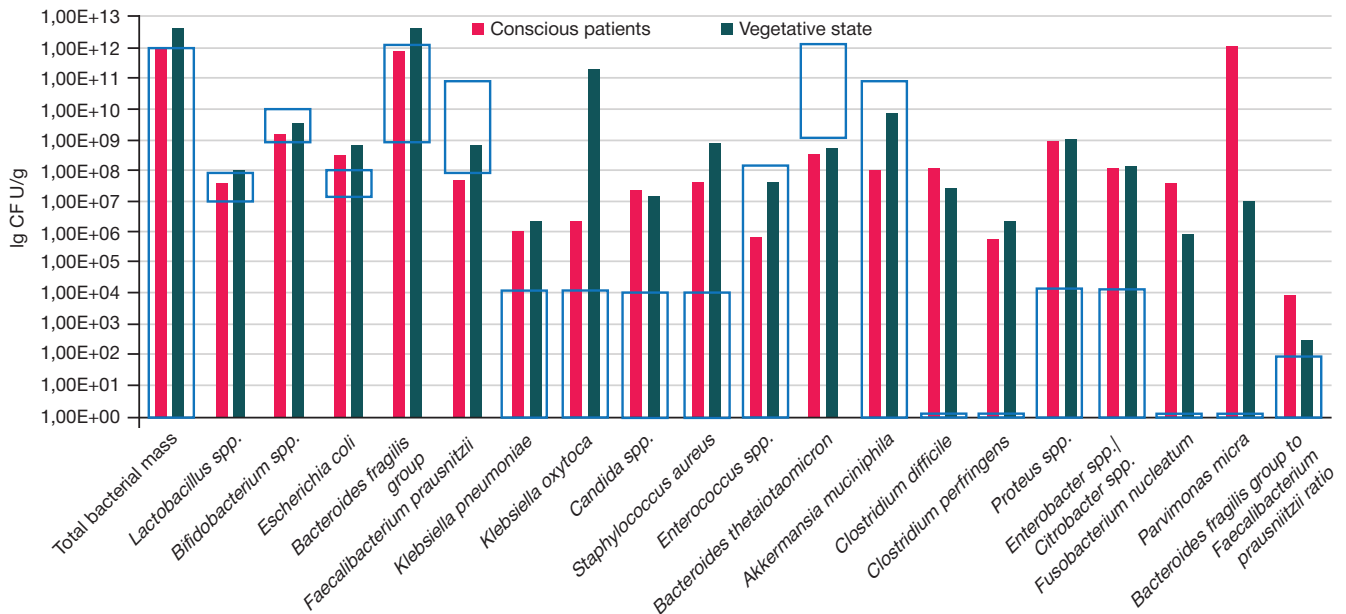


Fig. 1. The taxonomic composition of the gut microbiota in conscious patients ($n = 19$) and vegetative state patients ($n = 10$) compared to the reference ranges (shown in blue) provided by the manufacturer. Twenty parameters were compared

manifested as the dominance of short-chain fatty acids producers, including *Odoribacter* and *Akkermansia*, was correlated with their clinical outcomes [24]. However, the cited study evaluated the composition of the gut microbiota in the first 48h after stroke, and we were unable to find any publications describing microbiota composition in chronically ill neurological patients; these facts underscores the novelty of our findings.

Biomarker analysis uncovered significant differences in the levels of cortisol, CRP, albumin and the CRP/albumin ratio between conscious and vegetative state patients (see Table 3). The studied biomarkers were significantly correlated with the abundance of some gut microbiota representatives (see Table 3), supporting the gut-brain axis concept. The established negative correlations between cortisol levels and the abundance of *F. prausnitzii* and *B. thetaiotaomicron* in vegetative state patients are consistent with earlier reports demonstrating that a decline in the abundance of the foregoing taxa compromises

the neuroprotective function of the gut microbiota and therefore leads to nervous tissue injury [25], an immune response shift towards inflammation and autoimmunity [26]. In turn, elevated cortisol exerts a negative effect on the metabolism of critically ill patients, shifting the balance towards catabolism and promoting the hypermetabolism-hypercatabolism syndrome [27, 28].

In our study, CRP and cortisol levels, as well as the CRP/albumin ratio value, were twice as high in vegetative state patients, whereas their albumin levels were lower than in conscious participants, indicating more pronounced inflammation and catabolism in vegetative state. PCT levels were within the reference range in both groups, although the difference between the groups was significant, suggesting aseptic inflammation unrelated to systemic bacterial infection (see Table 3).

The CRP/albumin ratio is widely studied as a combined marker of systemic inflammation and nutritional status and also

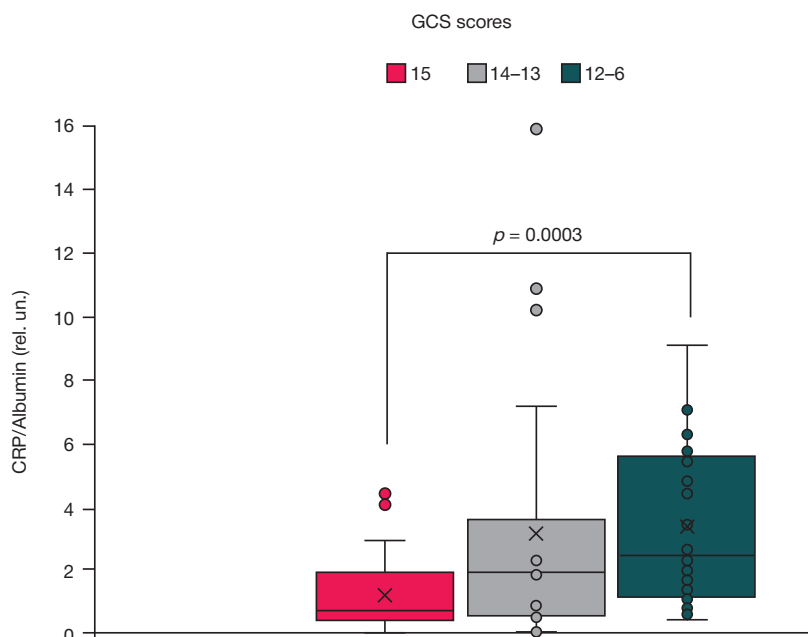


Fig. 2. Association between the CRP/albumin ratio and GCS scores ($p < 0.05$ for comparison of the groups that scored 15 and 12–6 points)

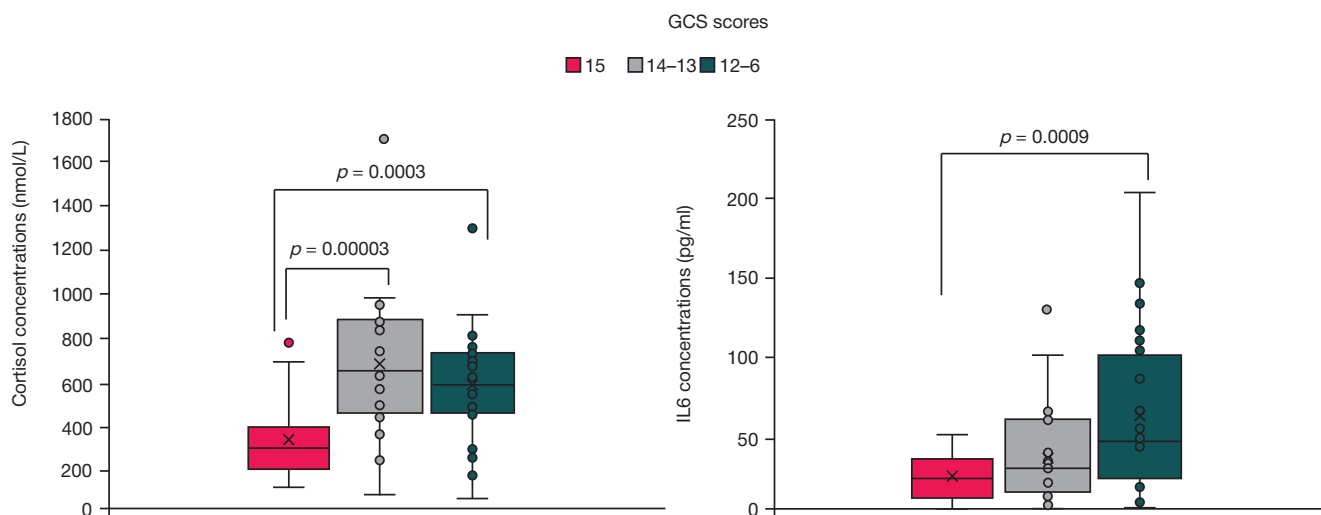


Fig. 3. Blood serums concentrations of IL6 and cortisol in patients with different GCS scores ($p < 0.05$ for comparison between groups scoring 15 and 14–13 points and between groups scoring 15 and 12–6 points)

as an independent prognostic marker in patients with infection, malignancies or undergoing intensive care [10, 29, 30]. We have demonstrated that the CRP/albumin ratio indicates the severity of consciousness impairment on GCS in critically ill patients (see Fig. 2) and correlates with the abundance of opportunistic *S. aureus* in the gut microbiota of such patients. S100 and NSE are traditionally used as markers of acute nervous tissue injury [31]. In our CCI patients, their only slightly changed levels were within the reference range, which might be reflective of the perpetuation of brain tissue injury. The observed direct correlation between S100 levels and the *Bacteroides fragilis* to *Faecalibacterium prausnitzii* ratio (a potential marker of proinflammatory type dysbiosis) and the strong negative correlation between GCS scores and *Enterococcus spp.* abundance confirm the association between dysbiosis and brain dysfunction. However, the link between the taxonomic abundance of the gut microbiota, the levels of neurologic biomarkers and the degree of neurologic deficit is not fully clear and needs to be further elucidated. We found no data on the correlation between the studied taxa and the levels of serum biomarkers in patients with CCI in the available literature.

To sum up, the gut microbiota of chronically critically ill patients with brain dysfunction undergoes certain transformations and can be deemed a “damaged organ”. The small study sample size and different therapeutic regimens did not allow us to assess the contribution of antibiotics to the changes in the gut microbiota. However, a complex approach based on the use of state-of-the-art technologies might help to optimize antibiotic therapies in the future.

CONCLUSIONS

1. Regardless of CNS injury severity, patients with CCI have pronounced imbalances in the taxonomic composition of their gut microbiota.
2. The established significant correlations between the studied serum biomarkers, GCS scores and certain gut microbiota representatives support the gut-brain axis concept.
3. Complex PCR-based diagnostics allows performing rapid dynamic assessment of the taxonomic composition of the gut microbiota.
4. Further research is needed to confirm the role of the gut microbiota in the pathogenesis of neurological deficit. Microbiota-targeted therapies might improve the efficacy of neurorehabilitation even in patients with severe brain damage.

References

1. Nelson JE, Cox CE, Hope AA, Carson SS. Chronic critical illness. *Am J Respir Crit Care Med.* 2010; 182 (4): 446–54.
2. Beloborodova NV. Metabolizm mikrobioty pri kriticheskikh sostojanijah (obzor i postulaty). *Obshhaja reanimatologija.* 2019; 15 (6): 62–79. Russian.
3. Parfjonov AL, Petrova MV, Solovjova NN, Stepanjuk TA, Zachepilova K O, Saidov ShH, i dr. Belkovo-jenergeticheskaja nedostatochnost' i struktura letal'nosti u pacientov v hronicheskom kriticheskom sostojanii. *Zdorov'e i obrazovanie v XXI veke.* 2018; 20 (8): 55–60. Russian.
4. Cox CE. Persistent systemic inflammation in chronic critical illness. *Respir Care.* 2012; 57 (6): 859–66.
5. Duda I, Krzych Ł, Jędrzejowska-Szypułka H, Lewin-Kowalik J. Serum levels of the S100B protein and neuron-specific enolase are associated with mortality in critically ill patients. *Acta Biochimica Polonica.* 2017; 64 (4): 681–52.
6. Beloborodova NV, Ostrova IV. Sepsis-associrovannaja jencefalopatija (obzor). *Obshhaja reanimatologija.* 2017; 13 (5): 121–39. Russian.
7. Thomas PAW, Moffatt CE, Rudd D, Marshman LAG. S-100β in chronic subdural haematoma: Prospective cohort study. *J Clin Neurosci.* 2019; 67: 145–50.
8. Shaik AJ, Reddy K, Mohammed N, Tandra SR, Rukmini MK, Baba KS. Neuron specific enolase as a marker of seizure related neuronal injury. *Neurochem Int.* 2019; 131: 104509.
9. Kiiski H, Långsjö J, Tenhunen J, Ala-Peijari M, Huhtala H, Hämäläinen M, et al. Time-courses of plasma IL-6 and HMGB-1 reflect initial severity of clinical presentation but do not predict poor neurologic outcome following subarachnoid hemorrhage. *eNeurologicalSci.* 2017; 6: 55–62.
10. Park JE, Chung KS, Song JH, Kim SY, Kim EY, Jung JY, et al. The C-reactive protein/albumin ratio as a predictor of mortality in critically ill patients. *J Clin Med.* 2018; 7 (10): 333.
11. Giau VV, Wu SY, Jamerlan A, Soo SA, Kim AN, Sang YK, et al. Gut microbiota and their neuroinflammatory implications in Alzheimer's disease. 2018; 10 (11): 1765.
12. Kohler J, Borchers F, Endres M, Weiss B, Spies C, Emmrich JV. Cognitive deficits following intensive care. *Dtsch Arztebl Int.* 2019; 116 (38): 627–34.
13. Meng M, Klingensmith NJ, Coopersmith CM. New insights into the gut as the driver of critical illness and organ failure. *Curr Opin*

- Crit Care. 2017; 23 (2): 143–8.
14. Otani S, Coopersmith CM. Gut integrity in critical illness. *J Intensive Care*. 2019; 20 (7): 7.
 15. Parfenov AL, Petrova MV, Pichugina IM, Luginina EV. Comorbidity Development in Patients with Severe Brain Injury Resulting in Chronic Critical Condition (Review). *General Reanimatology*. 2020; 16 (4): 72–89.
 16. Levy H, Hayes J, Boivin M, Tomba T. Transpyloric feeding tube placement in critically ill patients using electromyogram and ery-thromycin infusion. *Chest*. 2004; 125 (2): 587–91.
 17. Luft V. M. Sovremennye vozmozhnosti nutricionnoj podderzhki bol'nyh v intensivnoj medicine. *Vestnik anesteziologii i reanimatologii*. 2010; 7 (5): 42–51.
 18. Chemevskaya E, Beloborodova N, Klimenko N, Pautova A, Shilkin D, Gusarov V, et al. Serum and fecal profiles of aromatic microbial metabolites reflect gut microbiota disruption in critically ill patients: a prospective observational pilot study. *Crit Care*. 2020; 24: 312.
 19. Kurina I, Popenko A, Klimenko N, Koshechkin S, Chuprikova L, Filipenko M, et al. Development of qPCR platform with probes for quantifying prevalent and biomedically relevant human gut microbial taxa. *Mol Cell Probes*. 2020; 52: 101570.
 20. Metodicheskie ukazaniya «Organizatsiya raboty laboratorij, ispol'zujushih metody amplifikacii nukleinovyh kislot pri rabote s materialom, sodержashhim mikroorganizmy I-IV grupp patogenosti» МУ 1.3.2569-09. Moskva, 2009. Available from: <http://docs.cntd.ru/document/1200077791>. Russian.
 21. Kondrateva EA, Avdjunina IA, Kondratev AN, Ulitin AYU, Ivanova NE, Petrova MV, i dr. Opredelenie priznakov soznaniya i prognozirovaniya ishoda u pacientov v vegetativnom sostojanii. *Vestnik RAMN*. 2016; 71 (4): 273–80. Russian.
 22. Zaborin A, Smith D, Garfield K, Quensen J, Shakhsher B, Kade M, et al. Membership and behavior of ultra-low-diversity pathogen communities present in the gut of humans during prolonged critical illness. *mBio*. 2014; 5 (5): e01361–14.
 23. Ravi A, Halstead FD, Bamford A, Casey A, Thomson NM, Schaik W, et al. Loss of microbial diversity and pathogen domination of the gut microbiota in critically ill patients. *Microb Genom*. 2019; 5 (9): e000293.
 24. Li N, Wang X, Sun C, Wu X, Lu M, Si Y, et al. Change of intestinal microbiota in cerebral ischemic stroke patients. *BMC Microbiol*. 2019; 19 (1): 191.
 25. Benakis C, Brea D, Caballero S, Faraco G, Moore J, Murphy M, et al. Commensal microbiota affects ischemic stroke outcome by regulating intestinal $\gamma\delta$ T cells. *Nature Medicine*. 2016; 22 (5): 516–23.
 26. Sitkin SI, Vahitov TYa, Demjanova EV. Mikrobiom, disbioz tolstoj kishki i vospalitel'nye zabolevaniya kishchnika: kogda funkciya vazhnee taksonomii. *Al'manah klinicheskoy mediciny*. 2018; 46 (5): 396–425. Russian.
 27. Selivanova AV, Yakovlev VN, Moroz VV, Marchenkov YuV, Alekseev VG. Izmeneniya gormonal'no-metabolicheskikh pokazatelej u pacientov, nahodjashhhsja v kriticheskom sostojanii. *Obshhaja reanimatologija*. 2012; 8 (5). Russian.
 28. Ryabov GA. Jenergeticheskij metabolizm pri neotlozhnyh sostojaniyah. V knige: Ermolova AS, Abakumova MM, redaktory. *Iskusstvennoe pitanie v neotlozhnoj hirurgii i travmatologii*. Moskva: Nil SP im. NV Sklifosovskogo, 2001; c. 21–82. Russian.
 29. Llop-Talaveron J, Badia-Tahull MB, Leiva-Badosa E. An inflammation-based prognostic score, the C-reactive protein/albumin ratio predicts the morbidity and mortality of patients on parenteral nutrition. *Clin Nutr*. 2018; 37 (5): 1575–83.
 30. Oh TK, Song IA, Lee J.H. Clinical usefulness of C-reactive protein to albumin ratio in predicting 30-day mortality in critically ill patients: A retrospective analysis. *Sci Rep*. 2018; 8 (1): 14977.
 31. Golubev AM, Petrova MV, Grechko AV, Zaharchenko VE, Kuzovlev AN, Ershov AV. Molekuljarnye markery ishemicheskogo insul'ta. *Obshhaja reanimatologija*. 2019; 15 (5): 11–22. Russian.

Литература

1. Nelson JE, Cox C.E., Hope A.A., Carson S.S. Chronic critical illness. *Am J Respir Crit Care Med*. 2010; 182 (4): 446–54.
2. Белобородова Н. В. Метаболизм микробиоты при критических состояниях (обзор и постулаты). *Общая реаниматология*. 2019; 15 (6): 62–79.
3. Парфёнов А. Л., Петрова М. В., Соловьёва Н. Н., Степанюк Т. А., Зачепилова К. О., Саидов Ш. Х., и др. Белково-энергетическая недостаточность и структура летальности у пациентов в хроническом критическом состоянии. *Здоровье и образование в XXI веке*. 2018; 20 (8): 55–60.
4. Cox CE. Persistent systemic inflammation in chronic critical illness. *Respir Care*. 2012; 57 (6): 859–66.
5. Duda I, Krzych Ł, Jędrzejowska-Szypułka H, Lewin-Kowalik J. Serum levels of the S100B protein and neuron-specific enolase are associated with mortality in critically ill patients. *Acta Biochimica Polonica*. 2017; 64 (4): 681–52.
6. Белобородова Н. В., Острова И. В. Сепсис-ассоциированная энцефалопатия (обзор). *Общая реаниматология*. 2017; 13 (5): 121–39.
7. Thomas PAW, Moffatt CE, Rudd D, Marshman LAG. S-100 β in chronic subdural haematoma: Prospective cohort study. *J Clin Neurosci*. 2019; 67: 145–50.
8. Shaik AJ, Reddy K, Mohammed N, Tandra SR, Rukmini MK, Baba KS. Neuron specific enolase as a marker of seizure related neuronal injury. *Neurochem Int*. 2019; 131: 104509.
9. Kiiski H, Långsjö J, Tenhunen J, Ala-Peijari M, Huhtala H, Hämäläinen M, et al. Time-courses of plasma IL-6 and HMGB-1 reflect initial severity of clinical presentation but do not predict poor neurologic outcome following subarachnoid hemorrhage. *eNeurologicalSci*. 2017; 6: 55–62.
10. Park JE, Chung KS, Song JH, Kim SY, Kim EY, Jung JY, et al. The C-reactive protein/albumin ratio as a predictor of mortality in critically ill patients. *J Clin Med*. 2018; 7 (10): 333.
11. Giau VV, Wu SY, Jamerlan A, Soo SA, Kim AN, Sang YK, et al. Gut microbiota and their neuroinflammatory implications in Alzheimer's disease. 2018; 10 (11): 1765.
12. Kohler J, Borchers F, Endres M, Weiss B, Spies C, Emmrich JV. Cognitive deficits following intensive care. *Dtsch Arztebl Int*. 2019; 116 (38): 627–34.
13. Meng M, Klingensmith NJ, Coopersmith CM. New insights into the gut as the driver of critical illness and organ failure. *Curr Opin Crit Care*. 2017; 23 (2): 143–8.
14. Otani S, Coopersmith CM. Gut integrity in critical illness. *J Intensive Care*. 2019; 20 (7): 7.
15. Парфенов А. Л., Петрова М. В., Пичугина И. М., Лугинина Е. В. Формирование коморбидности у пациентов с тяжелым повреждением мозга и исходом в хроническое критическое состояние (обзор). *Общая реаниматология*. 2020; 16 (4): 72–89.
16. Levy H, Hayes J, Boivin M, Tomba T. Transpyloric feeding tube placement in critically ill patients using electromyogram and ery-thromycin infusion. *Chest*. 2004; 125 (2): 587–91.
17. Луфт В. М. Современные возможности нутриционной поддержки больных в интенсивной медицине. *Вестник анестезиологии и реаниматологии*. 2010; 7 (5): 42–51.
18. Chemevskaya E, Beloborodova N, Klimenko N, Pautova A, Shilkin D, Gusarov V, et al. Serum and fecal profiles of aromatic microbial metabolites reflect gut microbiota disruption in critically ill patients: a prospective observational pilot study. *Crit Care*. 2020; 24: 312.
19. Kurina I, Popenko A, Klimenko N, Koshechkin S, Chuprikova L, Filipenko M, et al. Development of qPCR platform with probes for quantifying prevalent and biomedically relevant human gut microbial taxa. *Mol Cell Probes*. 2020; 52: 101570.
20. Методические указания «Организация работы лабораторий, использующих методы амплификации нуклеиновых кислот при работе с материалом, содержащим микроорганизмы I-IV групп патогенности» МУ 1.3.2569-09. Москва, 2009. Доступно по ссылке: <http://docs.cntd.ru/document/1200077791>.
21. Кондратьева Е. А., Авдюнина И. А., Кондратьев А. Н., Улитин А. Ю., Иванова Н. Е., Петрова М. В., и др. Определение признаков сознания и прогнозирования исхода у пациентов в вегетативном состоянии. *Вестник РАМН*. 2016; 71 (4): 273–80.
22. Zaborin A, Smith D, Garfield K, Quensen J, Shakhsher B, Kade M,

- et al. Membership and behavior of ultra-low-diversity pathogen communities present in the gut of humans during prolonged critical illness. *mBio*. 2014; 5 (5): e01361–14.
23. Ravi A, Halstead FD, Bamford A, Casey A, Thomson NM, Schaik W, et al. Loss of microbial diversity and pathogen domination of the gut microbiota in critically ill patients. *Microb Genom*. 2019; 5 (9): e000293.
 24. Li N, Wang X, Sun C, Wu X, Lu M, Si Y, et al. Change of intestinal microbiota in cerebral ischemic stroke patients. *BMC Microbiol*. 2019; 19 (1): 191.
 25. Benakis C, Brea D, Caballero S, Faraco G, Moore J, Murphy M, et al. Commensal microbiota affects ischemic stroke outcome by regulating intestinal $\gamma\delta$ T cells. *Nature Medicine*. 2016; 22 (5): 516–23.
 26. Ситкин С. И., Вахитов Т. Я., Демьянова Е. В. Микробиом, дисбиоз толстой кишки и воспалительные заболевания кишечника: когда функция важнее таксономии. *Альманах клинической медицины*. 2018; 46 (5): 396–425.
 27. Селиванова А. В., Яковлев В. Н., Мороз В. В., Марченков Ю. В., Алексеев В. Г. Изменения гормонально-метаболических показателей у пациентов, находящихся в критическом состоянии. *Общая реаниматология*. 2012; 8 (5).
 28. Рябов Г. А. Энергетический метаболизм при неотложных состояниях. В книге: Ермолова А. С., Абакумова М. М., редакторы. *Искусственное питание в неотложной хирургии и травматологии*. Москва: НИИ СП им. Н. В. Склифосовского, 2001; с. 21–82.
 29. Llop-Talaveron J, Badia-Tahull MB, Leiva-Badosa E. An inflammation-based prognostic score, the C-reactive protein/albumin ratio predicts the morbidity and mortality of patients on parenteral nutrition. *Clin Nutr*. 2018; 37 (5): 1575–83.
 30. Oh TK, Song IA, Lee J.H. Clinical usefulness of C-reactive protein to albumin ratio in predicting 30-day mortality in critically ill patients: A retrospective analysis. *Sci Rep*. 2018; 8 (1): 14977.
 31. Голубев А. М., Петрова М. В., Гречко А. В., Захарченко В. Е., Кузовлев А. Н., Ершов А. В. Молекулярные маркеры ишемического инсульта. *Общая реаниматология*. 2019; 15 (5): 11–22.

SEMEN MICROBIOTA: CLUSTER ANALYSIS OF REAL-TIME PCR DATA

Voroshilina ES^{1,2}✉, Zornikov DL¹, Ivanov AV³, Pochernikov DG⁵, Panacheva EA^{1,2}¹ Ural State Medical University, Yekaterinburg, Russia² Medical Center "Garmonia", Yekaterinburg, Russia³ Yeltsin Ural Federal University, Yekaterinburg, Russia⁴ Krasovskii Institute of Mathematics and Mechanics, Yekaterinburg, Russia⁵ Ivanovo State Medical Academy, Ivanovo, Russia

To this day semen microbiota is still poorly understood, and clinical significance of detecting specific microorganism groups has not been clearly determined. The aim of this work was to conduct cluster analysis of semen microbiota detected using real-time PCR. 634 semen samples of reproductive age men were analyzed using the Androflor kit. Microbial DNA in the quantity of no less than 10³ GE/ml was detected in 460 samples (72.5%). From 1 to 14 microorganism groups were detected in 350 samples (55.2%) in the quantities that exceeded the threshold values (the detection rate of specific groups: 3.3–21.0%). In these 350 samples 4 stable microbiota clusters were determined. Each of the clusters was characterized by the prevalence of a specific microorganism group: obligate anaerobes (cluster 1; $n = 172$; detection rate — 49.1%), *Lactobacillus spp.* (cluster 2; $n = 78$; detection rate — 22.3%), gram-positive facultative anaerobes (cluster 3; $n = 62$; detection rate — 17.7%), *Enterobacteriaceae / Enterococcus* (cluster 4; $n = 62$; detection rate — 10.9%). Cluster 1 was less stable and was characterized by the larger species diversity compared to other clusters.

Keywords: semen microbiota, real-time PCR, cluster analysis, semen analysis

Acknowledgments: the authors would like to thank VN Khayutin, director of "Garmonia" Medical Center, for allowing them to conduct the study in the clinic's laboratory department.

Author contribution: Voroshilina ES — organization of the study, data analysis, article authoring; Zornikov DL — data analysis, article authoring; Ivanov AV — statistical processing, data analysis, article authoring; Pochernikov DG — patients' clinical profile, clinical data collection, data analysis, article authoring; Panacheva EA — literature review, data analysis, conducting PCR tests, article authoring.

Compliance with ethical standards: the study was approved by the Ethics Committee of Ural State Medical University, Federal State Budget Educational Institution of Higher Education under the Ministry of Health of the Russian Federation (Protocol № 7 of September 20, 2019). All patients signed the informed written consent to participation in the study.

✉ **Correspondence should be addressed:** Ekaterina S. Voroshilina
Furmanova, 30, Yekaterinburg, 620142; voroshilina@gmail.com

Received: 21.09.2020 **Accepted:** 08.10.2020 **Published online:** 27.10.2020

DOI: 10.24075/brsmu.2020.064

МИКРОБИОТА ЭЯКУЛЯТА: КЛАСТЕРНЫЙ АНАЛИЗ РЕЗУЛЬТАТОВ, ПОЛУЧЕННЫХ ПРИ ИССЛЕДОВАНИИ МЕТОДОМ ПЦР-РВ

Е. С. Ворошилина^{1,2}✉, Д. Л. Зорников¹, А. В. Иванов^{3,4}, Д. Г. Почерников⁵, Е. А. Паначева^{1,2}¹ Уральский государственный медицинский университет, Екатеринбург, Россия² Медицинский центр «Гармония», Екатеринбург, Россия³ Уральский федеральный университет имени первого Президента России Б. Н. Ельцина, Екатеринбург, Россия⁴ Институт математики и механики имени Н. Н. Красовского Уральского отделения Российской академии наук, Екатеринбург, Россия⁵ Ивановская государственная медицинская академия, Иваново, Россия

Микробиота эякулята до сих пор недостаточно изучена, а клиническая значимость выявления отдельных групп микроорганизмов окончательно не установлена. Целью работы было провести кластерный анализ микробиоты эякулята, выявленной методом ПЦР-РВ. С помощью теста «Андрофлор» («ДНК-Технология») исследовали 634 образца эякулята мужчин репродуктивного возраста. Микробную ДНК в количестве не менее 10³ ГЭ/мл обнаружили в 460 (72,5%) образцов. В 350 (55,2%) пробах выявили от 1 до 14 групп микроорганизмов в надпороговых значениях (частота выявления отдельных групп составила 3,3–21,0%). Среди 350 образцов выделили четыре устойчивых кластера микробиоты, в каждом из которых преобладала определенная группа микроорганизмов: облигатных анаэробов (кластер 1, $n = 172$; частота выявления — 49,1%), *Lactobacillus spp.* (кластер 2, $n = 78$; частота выявления — 22,3%) грамположительных факультативных анаэробов (кластер 3, $n = 62$; частота выявления — 17,7%), *Enterobacteriaceae / Enterococcus* (кластер 4, $n = 38$; частота выявления — 10,9%). Кластер 1 характеризовался меньшей устойчивостью и большим видовым разнообразием в сравнении с другими кластерами.

Ключевые слова: микробиота эякулята, ПЦР-РВ, кластерный анализ, спермограмма

Благодарности: авторы благодарят директора медицинского центра «Гармония» (г. Екатеринбург) В. Н. Хаютина за возможность выполнения исследования на базе центра.

Вклад авторов: Е. С. Ворошилина — организация исследования, анализ данных, написание статьи; Д. Л. Зорников — анализ данных, написание статьи; А. В. Иванов — статистическая обработка, анализ данных, написание статьи; Д. Г. Почерников — клиническая характеристика пациентов, сбор клинических данных, анализ данных, написание статьи; Е. А. Паначева — анализ литературы, проведение ПЦР, анализ данных, написание статьи.

Соблюдение этических стандартов: исследование одобрено этическим комитетом Уральского государственного медицинского университета (протокол № 7 от 20 сентября 2019 г.). Все участники исследования подписали добровольное информированное согласие на проведение исследования.

✉ **Для корреспонденции:** Екатерина Сергеевна Ворошилина
ул. Фурманова, д. 30, г. Екатеринбург, 620142; voroshilina@gmail.com

Статья получена: 21.09.2020 **Статья принята к печати:** 08.10.2020 **Опубликована онлайн:** 27.10.2020

DOI: 10.24075/vrgmu.2020.064

Male genital tract microbiota and semen microbiota in particular are still poorly understood compared to the microbiota of other human body biotopes [1]. For a long time, semen in healthy men was considered to be sterile, and any microorganisms (MO) detected there were associated with pathologies. Nevertheless, recent studies indicate that microbiota can be present in the semen of healthy or asymptomatic men with normal semen parameters [1–7]. It has been shown that polymicrobial communities of various bacteria genera and even phyla constitute semen microbiota [1, 2, 5, 7]. Some authors even cautiously conclude that certain MO groups could be associated with norm and pathology [1, 2, 5]. There are also researchers who believe that it is the presence of certain microbial associations, not species, that is associated with genital tract inflammatory diseases [4].

These results became possible due to the implementation of molecular-based techniques since many of the microbes detected in semen are difficult to culture or non-culturable (including obligate anaerobic bacteria which are rarely found in a routine culture-based test) [4, 7, 8]. However, clinical significance of the detection of these MO in semen samples has not been clearly established.

Most of the research dedicated to analyzing semen microbiota are based on 16S rRNA gene specific Next generation sequencing [1–5, 7]. While it is highly informative, this approach has a number of disadvantages such as: complicated sample preparation, difficult sample intake control, complicated result interpretation, long analysis process, high cost of equipment and reagents. These disadvantages make using NGS-sequencing in routine medical practice virtually impossible. Quantitative real-time PCR (qPCR) is far more suitable for this. In several previous studies, the potential of the Androflor commercial kit (qPCR kit for the detection of 24 MO groups) for semen microbiota analysis was shown [9–11]. Among other things, Androflor kit is more informative compared to culture-based tests [10]. While analyzing semen microbiota using qPCR has many benefits compared to other microbiological techniques, practical interpretation of the results remains difficult, which prevents this method from becoming part of the routine practice.

Semen culture colony count of 10^3 CFU/1 ml or higher is considered to be the above the threshold value for detecting opportunistic microbiota in culture-based testing [12]. The high sensitivity of molecular-based techniques and their capability to detect non-culturable and non-viable MO makes it difficult to use threshold values similar to those used in culture-based techniques when interpreting qPCR results. It is necessary to establish whether the presence of non-culturable MOs in quantities exceeding the threshold value is typical for normal and pathological conditions. We also need to determine the persistent types of microbial groups associated with infertility in men when identifying certain MO groups.

To answer these questions, semen analysis results (clinical and molecular-based), both from patients with infertility and healthy males, need to be comprehensively studied. Aim of the study: to conduct cluster analysis of semen microbiota detected by means of real-time PCR (Androflor kit)

METHODS

Patient groups

From January 2019 to March 2020, semen samples from 634 men were examined (mean age 34 ± 6.7 years). During this period, the patients came to the “Garmonia” Medical Center

(Yekaterinburg, $n = 429$) and to the urological clinic of the Ivanovo State Medical Academy of the Ministry of Health of Russian Federation (Ivanovo, $n = 205$) either seeking preconception care or for infertility treatment. All patients gave their consent to participate in the study.

Inclusion criteria: reproductive-age men; infertility or undergoing preconception care; all examined patients during the last four weeks did not receive medications that could affect the semen microbiota, such as hormonal, antibacterial drugs; consumption of substances with alcohol content over 30 ml in terms of pure ethanol was excluded.

Exclusion criteria: hypogonadotropic and hypergonadotropic hypogonadism, type 1 and 2 diabetes, hypo- and hyperthyroidism; sexually transmitted infections (*Chlamydia trachomatis*, *Neisseria gonorrhoeae*, *Mycoplasma genitalium*, *Trichomonas vaginalis*); clinical manifestations of prostatitis such as pain and dysuria; karyotype abnormalities, mutations in the CFTR gene, microdeletions in the AZF locus of the Y chromosome.

Semen sampling

Preparation for semen sampling: sexual abstinence for a period of 2–5 days. Prior to semen collection, patients urinated. Semen was collected through masturbation into a sterile container. Patients were instructed to avoid contact with the walls and the lid of the container.

DNA extraction

PREP-NA-PLUS kit (DNA-Technology; Russia) was used for DNA-extraction. Semen samples were prepared using the following technique: 1.0 ml of semen was put into an Eppendorf tube with 1.0 ml of transport medium (“Transport media with mucolytic agent”, InterLabService Ltd.; Russia) which was then shaken in the vortex until the substances mixed completely. The tube was centrifuged at 13,000 rpm for 10 minutes (Mini-Spin centrifuge, Eppendorf; Germany). After removing the supernatant, 50 μ l of the precipitate was used for extraction of the DNA.

Semen microbiota evaluation

The study was conducted using the Androflor reagent kit (DNA-Technology; Russia) and the DTprime detection thermal cycler (DNA-Technology; Russia) following the manufacturer's instructions. Once the amplification is over, the special software (DNA-Technology; Russia) automatically calculates the quantities (expressed in genome equivalents per 1 ml (GE/ml)) of the total bacterial load (TBL), lactobacilli and each of the detected opportunistic microorganisms (OM) in a given sample.

The Androflor kit allows detecting the following MO groups: Gram-positive facultative anaerobes (*Streptococcus spp.*, *Staphylococcus spp.*, *Corynebacterium spp.*); Gram-negative facultative anaerobes (*Haemophilus spp.*, *Pseudomonas aeruginosa* / *Ralstonia spp.* / *Burkholderia spp.*); *Enterobacteriaceae* / *Enterococcus spp.* group; obligate anaerobes (*Gardnerella vaginalis*, *Eubacterium spp.*, *Sneathia spp.* / *Leptotrichia spp.* / *Fusobacterium spp.*, *Megasphaera spp.* / *Veillonella spp.* / *Dialister spp.*, *Bacteroides spp.* / *Porphyromonas spp.* / *Prevotella spp.*, *Anaerococcus spp.*, *Peptostreptococcus spp.*, *Atopobium cluster*), mycoplasmas (*Mycoplasma hominis*, *Ureaplasma urealyticum*, *Ureaplasma parvum*), transient microbiota (*Lactobacillus spp.*), yeast-like fungi (*Candida spp.*).

Table 1. Detection rate for individual MO groups present in quantities exceeding the threshold value ($n = 634$)*

MO Group	n	%
<i>Corynebacterium spp.</i>	133	21.0
<i>Bacteroides spp. / Porphyromonas spp. / Prevotella spp.</i>	131	20.7
<i>Lactobacillus spp.</i>	125	19.7
<i>Eubacterium spp.</i>	108	17.0
<i>Peptostreptococcus spp. / Parvimonas spp.</i>	107	16.9
<i>Megasphaera spp. / Veillonella spp. / Dialister spp.</i>	94	14.8
<i>Streptococcus spp.</i>	81	12.8
<i>Enterobacteriaceae spp. / Enterococcus spp.</i>	74	11.7
<i>Anaerococcus spp.</i>	68	10.7
<i>Gardnerella vaginalis</i>	67	10.6
<i>Ureaplasma parvum</i>	63	9.9
<i>Atopobium cluster</i>	57	9.0
<i>Staphylococcus spp.</i>	52	8.2
<i>Sneathia spp. / Leptotrichia spp. / Fusobacterium spp.</i>	41	6.5
<i>Haemophilus spp.</i>	36	5.7
<i>Mycoplasma hominis</i>	25	3.9
<i>Ureaplasma urealyticum</i>	24	3.8
<i>Pseudomonas aeruginosa / Ralstonia spp. / Burkholderia spp.</i>	21	3.3

Note: * — for *Ureaplasma urealyticum*, *Ureaplasma parvum*, *Mycoplasma hominis* threshold is > 0 , for the other MO groups threshold is $\geq 10^3$ GE/ml.

Sterile deionized water was used as the negative control sample. Positive signals were detected in the negative control sample for some MO groups no earlier than in the 35th amplification cycle. In these cases, the bacterial load was less than 10^3 GE/ml. Thus, the quantity of MOs needed to be at least 10^3 GE/ml for it to be considered above threshold, which meant that a positive signal was received in qPCR before the 35th cycle. The exceptions were *U. urealyticum*, *U. parvum*, *M. hominis* since there was no positive signal for these MOs in the negative control sample. If the signal was detected at any amplification cycle for these MO groups, qPCR result for them was regarded as positive. Yeast-like fungi of the *Candida spp.* were not included in this study.

Statistical methods

The analysis of the structural characteristics of semen microbiota was carried out using the MSSC clustering model, which minimizes the sum over all clusters of intra-cluster sums of squared distances from cluster elements to their centroids [13]. The clustering problem was solved using the k-means++ algorithm [14], implemented in the scikit-learn machine learning library. The optimal clustering was selected on the basis of internal assessments of the clustering quality: the Silhouette index [15] and the Davies–Bouldin index (DBI) [16]. For optimal clustering, the stability of clusters to changes in the sample size was analyzed.

RESULTS

Detection rate for specific MO groups

TBL was detected in quantities exceeding the threshold value (at least 10^3 GE/ml) in 460 (72.5%) out of 634; samples the quantities of specific MO groups were below the threshold value in 110 (17.4%) of these 460 samples. Bacterial DNA was present in the quantities lower than 10^3 GE/ml in 174 (27.5%) samples.

From 1 to 14 MO groups were detected in quantities, exceeding the threshold value, simultaneously in 350 (55.2%) samples. Detection rate for specific MO groups is given in Table 1.

Different MO groups were found in a variety of associations with each other. Thus, we have decided to carry out cluster analysis in order to identify the microbial communities typical of semen microbiota.

Cluster analysis of semen microbiota

For cluster analysis, 350 samples were selected in accordance with the following criteria: TBL in the quantity of at least 10^3 GE / ml, at least one group of MO in the quantity of at least 10^3 GE / ml.

To run the k-means++ clustering algorithm, each examined sample was represented as a vector $(p, s) \in R^{50}$, consisting of a vector of primary characteristics $p \in R^{19}$, (taken from the data on the semen microbiota analyses by means of qPCR) and secondary characteristics vector $s \in R^{31}$, calculated on the basis of primary characteristics.

The absolute values of the parameters determined by the Androflor kit (TBL and 18 MO groups) were regarded as primary characteristics.

The following secondary characteristics were calculated on the basis of the primary ones: corrected TBL (CTBL), equal to the total mass of the 18 MO groups detected by the kit; mass percentages of the MOs in relation to the CTBL; masses of the MO groups consolidated in accordance with the Androflor kit's configuration: lactobacilli, gram-positive facultative anaerobes (GPFA), obligate anaerobes (OA), gram-negative facultative anaerobes (GNFA), *Enterobacteriaceae / Enterococcus* (EE), and mycoplasmas; mass percentages of the consolidated MO groups in relation to the CTBL.

The optimal number of clusters in the examined dataset was determined on the basis of the values of the Silhouette and Davies-Bouldin indices (Table 2). The best clustering quality corresponds to the highest Silhouette Index and the lowest

Davies-Bouldin Index. In accordance with the obtained values of the indices, it was optimal to select 4 main clusters of the semen microbiota.

One consolidated MO group was predominant in each of the obtained clusters. The diagrams in Fig. 1 show the range of characteristics of the objects in their respective clusters.

Cluster 1 — the OA-dominated variant. The absolute quantity of all OA was comparable to the TBL and amounted to $10^{4.3}$ GE / ml in the centroid (Fig. 1A). The proportion of OA in the centroid reached 82.8% in relation to the CTBL. This microbiota variant was identified in 172 (49.1%) out of 350 samples.

Cluster 2 — the lactobacilli-dominated variant. The absolute quantity of all lactobacilli was comparable to the CTBL and amounted to $10^{4.0}$ GE / ml in the centroid (Fig. 1B). The proportion of lactobacilli in the centroid reached 80.9% in relation to the CTBL. This microbiota variant was identified in 78 (22.3%) out of 350 samples.

Cluster 3, characterized by the predominance of GPFA, was identified in 62 (17.7%) out of 350 samples. The absolute quantity of all GPFA was comparable to the CTBL and amounted to $10^{3.6}$ GE / ml in the centroid (Fig. 1C). The proportion of GPFA in the centroid reached 89.4% in relation to the CTBL.

Cluster 4 — the EE-dominated variant. The absolute quantity of all EE was less than the CTBL and amounted to $10^{3.5}$ GE / ml in the centroid (Fig. 1D). The proportion of EE in the centroid reached 64.5% in relation to the CTBL. This microbiota variant was identified in 38 (10.9%) out of 350 samples.

Analysis of the microbial clusters' stability

To analyze the stability of the identified clusters, subsamples of samples of $f = 1,100$ volume of the original sample were generated (1000 random subsamples without return for each value of the volume). The generated subsamples were divided into 4 clusters. For each ($m = 1,1000$) generated subsample of volume f samples (let us denote this subsample by X_m^f) stability index of the k cluster was calculated using the following formula:

$$Stability\ Index(X_m^f, k) = \frac{\sum_{i=1}^n \sum_{j=1}^n \mathbf{1}_{\{true\}}([A(x_i), A(x_j) \in k] \wedge [\exists l A_m^l(x_i), A_m^l(x_j) \in l])}{\sum_{i=1}^n \sum_{j=1}^n \mathbf{1}_{\{true\}}([A(x_i), A(x_j) \in k]) \cdot \mathbf{1}_{\{true, false\}}([\exists l A_m^l(x_i), A_m^l(x_j) \in l])}, \quad (1)$$

where n is the number of samples in the subsample X_m^f ; $\mathbf{1}_{\{true\}}: \{true, false\} \rightarrow \{0, 1\}$; is the indicator function of the logical argument; $x \in X_m^f$ is the sample from the subsample X_m^f , $A(x)$; $A^l(x)$ is the label of the cluster where the sample is contained as a result of clustering of the original sample set and the subsample X_m^f , respectively; $k = \{1, 2, 3, 4\}$, $l = \{1, 2, 3, 4\}$, are the cluster labels.

Table 2. Clustering quality values

Number of Clusters	Silhouette Index	Davies–Bouldin Index
2	0.21606	1.88844
3	0.29118	1.55122
4	0.32952	1.27021
5	0.29094	1.642083
6	0.30307	1.51617
7	0.29392	1.58818
8	0.29052	1.51856
9	0.28759	1.43542
10	0.29666	1.48578

In addition, the stability index of the k cluster, common for the subsamples of the f volume, was calculated. The calculations were carried out using the following formula:

$$Stability\ Index(k) = \frac{\sum_{m=1}^{1000} \sum_{i=1}^n \sum_{j=1}^n \mathbf{1}_{\{true\}}([A(x_i), A(x_j) \in k] \wedge [\exists l A_m^l(x_i), A_m^l(x_j) \in l])}{\sum_{m=1}^{1000} \sum_{i=1}^n \sum_{j=1}^n \mathbf{1}_{\{true\}}([A(x_i), A(x_j) \in k]) \cdot \mathbf{1}_{\{true, false\}}([\exists l A_m^l(x_i), A_m^l(x_j) \in l])}. \quad (2)$$

Fig. 2 shows the graphs depicting cluster stability indices calculated according to formulas (1) and (2). The obtained 4 clusters are stable: on sufficiently small volumes of subsamples, the probability of assigning two arbitrary observations to the same cluster with 4-clustering of the initial sample and an arbitrary subsample tends to 1. As follows from the graphs in Fig. 2, the most stable are the clusters with the predominance of lactobacilli (cluster 2, Fig. 2B), the predominance of GPFA (cluster 3, Fig. 2C) and with the predominance of EE (cluster 4, Fig. 2D). The least stable cluster is cluster 1 with the predominance of OA (Fig. 2A).

DISCUSSION

The presence of bacterial DNA both in the environment and in the reagents used for conducting the test (KITome) and high sensitivity of the PCR method limit our capability for interpreting results when analyzing the samples with low bacterial load [17]. Since positive signals were received for most MO groups after the 35th cycle in qPCR when analyzing negative control samples (which corresponded to the bacterial load of less than 10^3 GE/ml), the value of 10^3 GE/ml was regarded as the threshold value. All the other results were regarded as negative. The exceptions were *U. urealyticum*, *U. parvum*, *M. hominis* since there was no positive signal for these MOs in the negative control sample. If the signal was detected at any amplification cycle for these MO groups, qPCR result for them was regarded as positive.

The bacterial load in quantities exceeding the threshold value was identified only in 460 (72.5%) samples. The quantities of all the MO groups were below the threshold value in 110 of these 460 samples. Almost half of all the semen samples (44.8%) had bacterial DNA in the quantities below the threshold value (less than 10^3 GE/ml) which is regarded as a variant of the norm [12].

From 1 to 14 MO groups were detected simultaneously in quantities exceeding the threshold value in 350 (55.2%) samples, which corresponds with the results obtained by other researchers, who note that semen microbiota is heterogenous [1, 2, 5, 7]. The following MO groups were detected more often than others: *Corynebacterium spp.* (21,0%), *Bacteroides spp.* / *Porphyromonas spp.* / *Prevotella spp.* (20,7%), *Lactobacillus spp.* (19,7%), *Eubacterium spp.* (17,0%), *Peptostreptococcus spp.* /

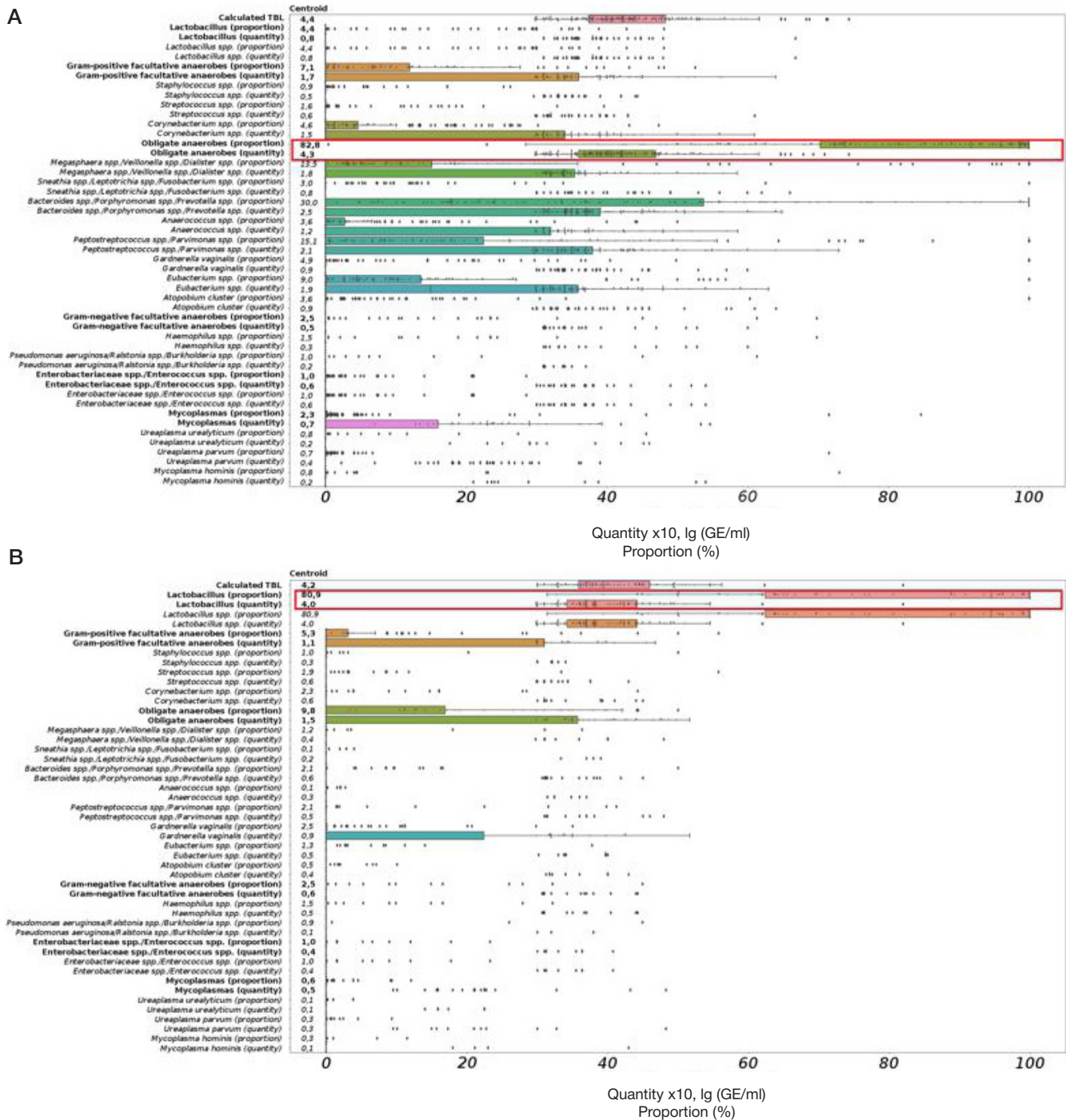


Fig. 1. Results of cluster analysis of semen microbiota analyzed by means of qPCR ($n = 350$). The ordinate shows the values of the features in the centroid. Diagrams of the predominant groups of microorganisms are highlighted using red rectangles. Cluster 1 ($n = 172$; Fig. **A**) is characterized by the predominance of obligate anaerobes, cluster 2 ($n = 78$; Fig. **B**) is characterized by the predominance of lactobacilli, cluster 3 ($n = 62$; Fig. **C**) is characterized by the predominance of gram-positive facultative anaerobes, cluster 4 ($n = 38$; Fig. **D**) is characterized by the predominance of enterobacteria / enterococci

Parvimonas spp. (16,9%). Other MO groups were detected less often, with the rate of 3.3–14.8%. Previous studies have also shown that *Lactobacillus* spp. and obligate anaerobes along with facultative anaerobes and are often detected in the semen when using molecular-based methods [1, 2, 5, 7, 18].

Cluster analysis of semen microbiota in samples, containing TBL and at least one of the MO groups in quantities exceeding the threshold value, showed that division into 4 clusters was optimal. Each cluster was characterized by the predominance of one of the consolidated MO groups: cluster 1 — OA, cluster 2 — lactobacilli, cluster 3 — GPFA, cluster 4 — EE. Similar data were obtained in earlier studies using the NGS sequencing method

to evaluate the semen microbiota composition [1, 2]. Having studied the seminal fluid of healthy men and men with infertility, Hou D. et al. also identified several clusters of MOs, including those with predominance of GPFA, OA, and *Lactobacillus* spp. [2].

Clusters 2 (with the predominance of lactobacilli), 3 (with the predominance of GPFA), and 4 (with the predominance of EE) were characterized by high stability. Moreover, for clusters 2 and 3, the presence of other MO groups in the quantities comparable to those of the ones forming the cluster was atypical. At the same time, cluster 4 was characterized by the presence of other groups of bacteria, along with EE: GPFA, OA, and gram-negative facultative anaerobes.

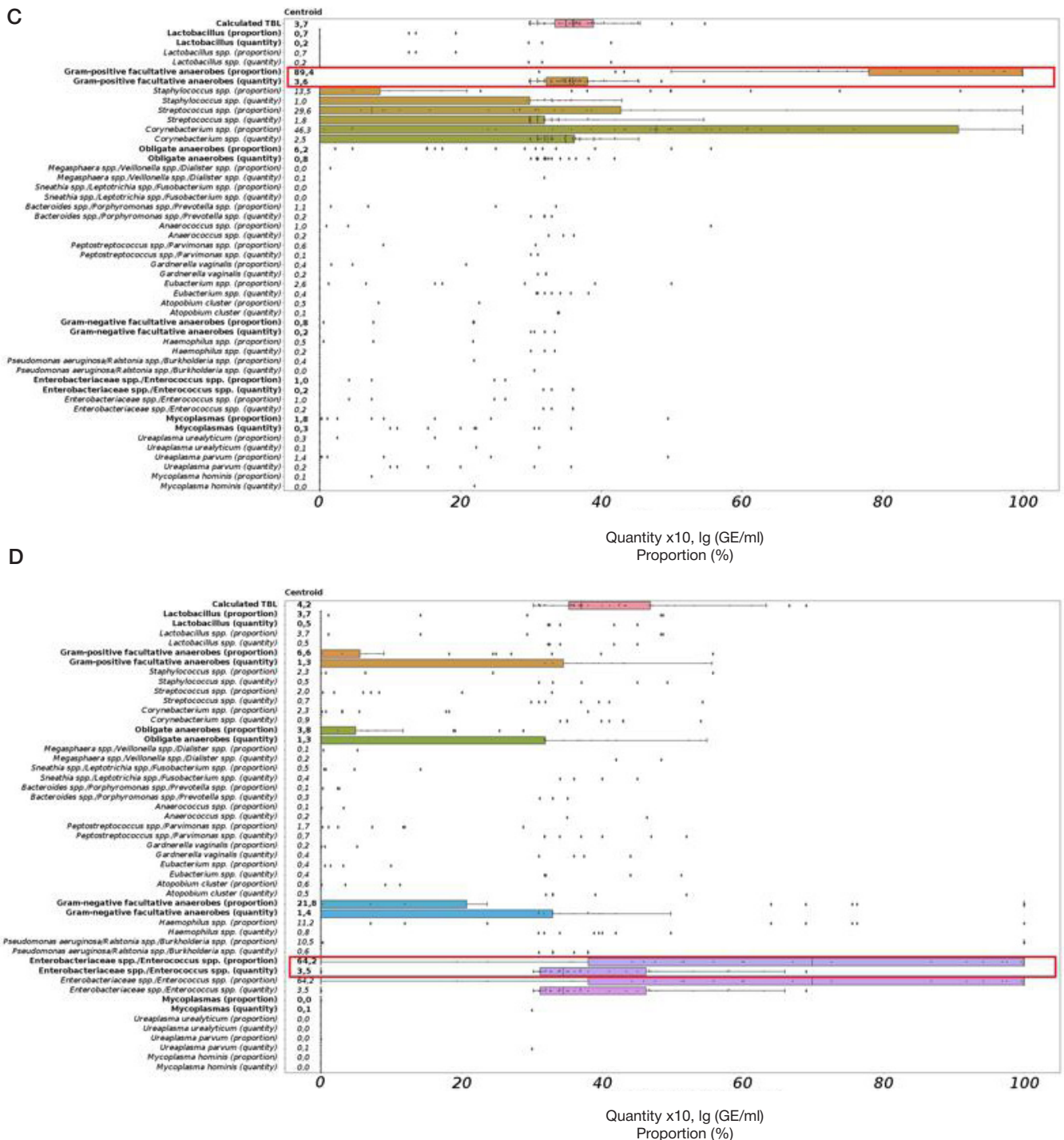


Fig. 1. Results of cluster analysis of semen microbiota analyzed by means of qPCR ($n = 350$). The ordinate shows the values of the features in the centroid. Diagrams of the predominant cluster of microorganisms are highlighted using red rectangles. Cluster 1 ($n = 172$; Fig. A) is characterized by the predominance of obligate anaerobes, cluster 2 ($n = 78$; Fig. B) is characterized by the predominance of lactobacilli, cluster 3 ($n = 62$; Fig. C) is characterized by the predominance of gram-positive facultative anaerobes, cluster 4 ($n = 38$; Fig. D) is characterized by the predominance of enterobacteria / enterococci

Cluster 1 (with the predominance of obligate anaerobes) was less stable. This may be due to the greater species diversity of the microbiota in these semen samples.

The results of this study confirm observations of other authors on the heterogeneous composition of the semen microbiota which can be grouped into a number of clusters. Our approach has confirmed the stability of the 4 clusters selected on randomly generated samples of different sizes.

Further research is necessary to determine the detection rate of the described bacterial clusters in semen with normospermia and various types of pathospermia. We need

to establish the relationship between the characteristics of the semen microbiota and infertility in men. This will allow the development of new algorithms for treating patients with reproductive disorders, depending on the composition of the semen microbiota.

Conclusion

1. Bacterial DNA was detected in the quantity of at least 10^3 GE/ml in 72.5% of the semen samples by means of qPCR; in 55.2% semen samples, from 1 to 14 MO groups were detected in

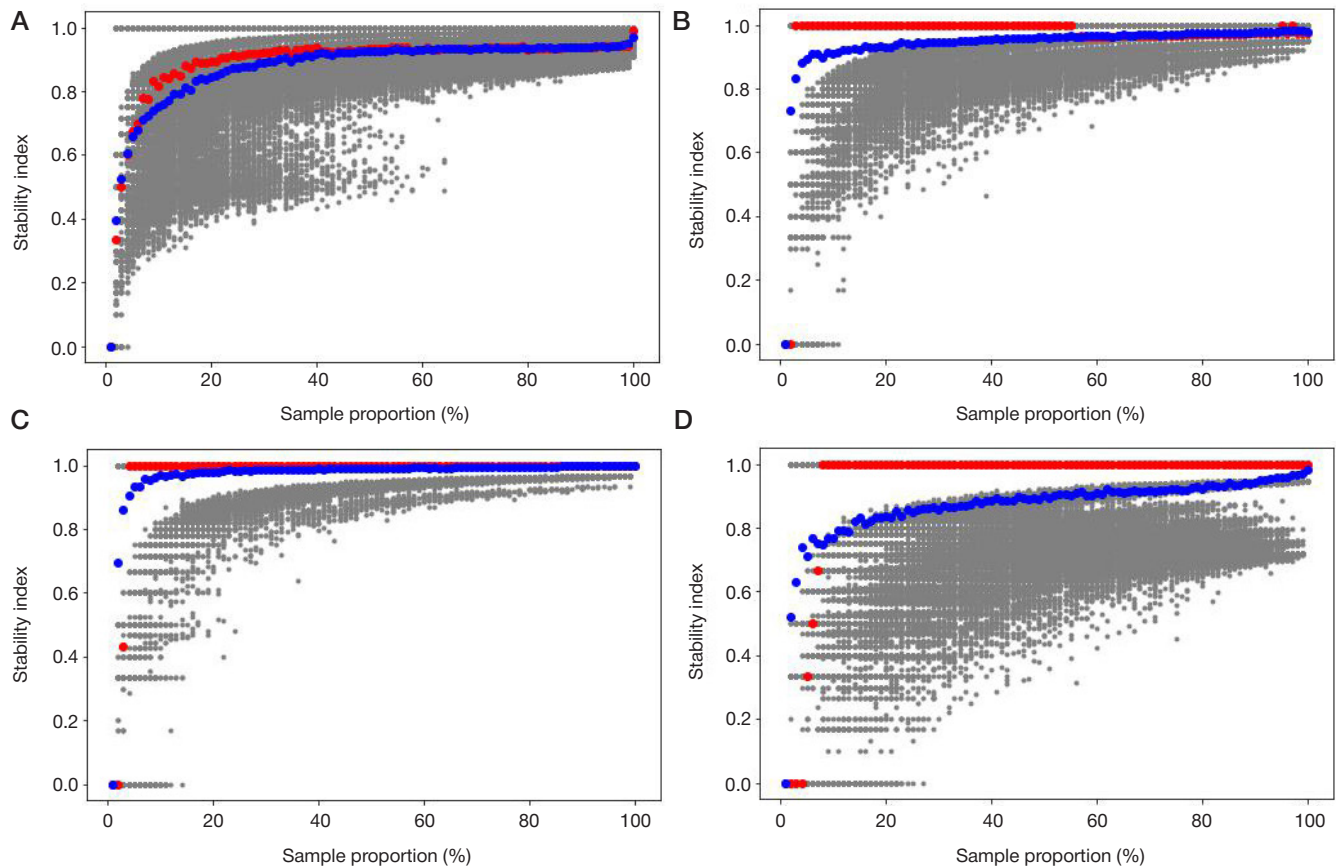


Fig. 2. Results of the cluster stability analysis 1 (A), 2 (B), 3 (C), 4 (D). The grey marker on the graphs shows cluster stability index on a random subsample, the red marker shows the median of the stability indices, calculated for 1000 random subsamples of the f volume, the blue marker shows the cluster stability index on a set of the f volume

quantities exceeding the threshold value. 2. We identified 4 stable clusters of semen microbiota. A certain consolidated MO group was predominant in each of these clusters: obligate anaerobes, lactobacilli, gram-positive facultative anaerobes,

Enterobacteriaceae / *Enterococcus* group. 3. In half of the samples microbiota was represented by cluster 1 (with obligate anaerobes being the predominant group), which was the least stable one and was characterized by the greatest species diversity.

References

- Baud D, Pattaroni C, Vulliamoz N, Castella V, Marsland BJ, Stojanov M. Sperm Microbiota and Its Impact on Semen Parameters. *Front Microbiol.* 2019; 10: 234. DOI: 10.3389/fmicb.2019.00234.
- Hou D, Zhou X, Zhong X, Settles ML, Herring J, Wang L, et al. Microbiota of the seminal fluid from healthy and infertile men. *Fertil Steril.* 2013; 100 (5): 1261–9. DOI: 10.1016/j.fertnstert.2013.07.1991.
- Liu CM, Osborne BJ, Hungate BA, Liu CM, Osborne BJ, Hungate BA, et al. The semen microbiome and its relationship with local immunology and viral load in HIV infection. *PLoS Pathog.* 2014; 10 (7): e1004262. DOI: 10.1371/journal.ppat.1004262.
- Mändar R, Punab M, Korrovits P, Türk S, Ausmees K, Lapp E, et al. Seminal microbiome in men with and without prostatitis. *Int J Urol.* 2017; 24 (3): 211–216. DOI: 10.1111/iju.13286.
- Weng SL, Chiu CM, Lin FM, Huang WC, Liang C, Yang T, et al. Bacterial communities in semen from men of infertile couples: metagenomic sequencing reveals relationships of seminal microbiota to semen quality. *PLoS One.* 2014; 9 (10): e110152. DOI: 10.1371/journal.pone.0110152.
- Zozaya M, Ferris MJ, Siren JD, Lillis R, Myers L, Nsuami MJ, et al. Bacterial communities in penile skin, male urethra, and vaginas of heterosexual couples with and without bacterial vaginosis. *Microbiome.* 2016; 4: 16. DOI: 10.1186/s40168-016-0161-6.
- Štšepetova J, Baranova J, Simm J, Parm Ü, Rööp T, Sokmann S, et al. The complex microbiome from native semen to embryo culture environment in human in vitro fertilization procedure. *Reprod Biol Endocrinol.* 2020; 18 (1): 3. DOI: 10.1186/s12958-019-0562-z.
- Kiessling AA, Desmarais BM, Yin HZ, Loverde J, Eyre RC. Detection and identification of bacterial DNA in semen. *Fertil Steril.* 2008; 90 (5): 1744–56. DOI: 10.1016/j.fertnstert.2007.08.083.
- Pochernikov DG, Galkina IS, Postovoytenko NT, Gerasimov AM. A comparative analysis of seminal and vaginal microbiota of married couples by real-time PCR with Androflor and Femoflor reagent kits. *Bulletin of Russian State Medical University.* 2017; 2: 34–39.
- Voroshilina ES, Zornikov DL, Panacheva EA. Evaluation of the ejaculate microbiota by real-time PCR and culture-based technique. *Bulletin of Russian State Medical University.* 2019; 1: 41–5.
- Pochernikov DG, Vitvickaja JuG, Boldyreva MN, Galkina IS. Informativnost' biomateriala dlja issledovaniya mikrobioty urogenital'nogo trakta muzhchin metodom PCR-RV (pilotnoe issledovanie). *Jeksperimental'naja i klinicheskaja urologija.* 2019; 2: 128–33. Russian.
- Schuppe HC, Pilatz A, Hossain H, Diemer T, Wagenlehner F, Weidner W. Urogenital Infection as a Risk Factor for Male Infertility. *Dtsch Arztebl Int.* 2017; 114 (19): 339–46.
- Jain AK, Murty MN, Flynn PJ. Data clustering: a review. *ACM computing surveys (CSUR).* 1999; 31 (3): 264–323.
- Arthur D, Vassilvitskii S. K-means++: the advantages of careful seeding. In: Hal Gabow, editor. *Proceedings of the Eighteenth Annual ACM-SIAM Symposium on Discrete Algorithms*

- (Proceedings in Applied Mathematics) 18th ed. Society for Industrial and Applied Mathematics (3 January 2007). P. 1027–1035.
15. Rousseeuw PJ. Silhouettes: A graphical aid to the interpretation and validation of cluster analysis. *J Comput Appl Math.* 1987; 20: 53–65.
 16. Davies DL, Bouldin DW. A Cluster Separation Measure. *IEEE Transactions on Pattern Analysis and Machine Intelligence.* PAMI-1. 1979; (2): 224–27.
 17. de Goffau MC, Lager S, Salter SJ, Wagner J, Kronbichler A, Charnock-Jones DS, et al. Recognizing the reagent microbiome. *Nat Microbiol.* 2018 Aug; 3 (8): 851–3.
 18. Yang H, Zhang J, Xue Z, Zhao C, Lei L, Wen Y, et al. Potential Pathogenic Bacteria in Seminal Microbiota of Patients with Different Types of Dysspermatism. *Sci Rep.* 2020; 10: 6876.

Литература

1. Baud D, Pattaroni C, Vulliamoz N, Castella V, Marsland BJ, Stojanov M. Sperm Microbiota and Its Impact on Semen Parameters. *Front Microbiol.* 2019; 10: 234. DOI: 10.3389/fmicb.2019.00234.
2. Hou D, Zhou X, Zhong X, Settles ML, Herring J, Wang L, et al. Microbiota of the seminal fluid from healthy and infertile men. *Fertil Steril.* 2013; 100 (5): 1261–9. DOI: 10.1016/j.fertnstert.2013.07.1991.
3. Liu CM, Osborne BJ, Hungate BA, Liu CM, Osborne BJ, Hungate BA, et al. The semen microbiome and its relationship with local immunology and viral load in HIV infection. *PLoS Pathog.* 2014; 10 (7): e1004262. DOI: 10.1371/journal.ppat.1004262.
4. Mändar R, Punab M, Korrovits P, Türk S, Ausmees K, Lapp E, et al. Seminal microbiome in men with and without prostatitis. *Int J Urol.* 2017; 24 (3): 211–216. DOI: 10.1111/iju.13286.
5. Weng SL, Chiu CM, Lin FM, Huang WC, Liang C, Yang T, et al. Bacterial communities in semen from men of infertile couples: metagenomic sequencing reveals relationships of seminal microbiota to semen quality. *PLoS One.* 2014; 9 (10): e110152. DOI: 10.1371/journal.pone.0110152.
6. Zozaya M, Ferris MJ, Siren JD, Lillis R, Myers L, Nsuami MJ, et al. Bacterial communities in penile skin, male urethra, and vaginas of heterosexual couples with and without bacterial vaginosis. *Microbiome.* 2016; 4: 16. DOI: 10.1186/s40168-016-0161-6.
7. Štšepetova J, Baranova J, Simm J, Parm Ü, Rööp T, Sokmann S, et al. The complex microbiome from native semen to embryo culture environment in human in vitro fertilization procedure. *Reprod Biol Endocrinol.* 2020; 18 (1): 3. DOI: 10.1186/s12958-019-0562-z.
8. Kiessling AA, Desmarais BM, Yin HZ, Loverde J, Eyre RC. Detection and identification of bacterial DNA in semen. *Fertil Steril.* 2008; 90 (5): 1744–56. DOI: 10.1016/j.fertnstert.2007.08.083.
9. Почерников Д. Г., Галкина И. С., Постовойтенко Н. Т., Герасимов А. М. Сравнительный анализ биотопа эякулята и цервикального канала методом ПЦР-РВ с тестами «Андрофлор» и «Фемофлор» в супружеских парах. *Вестник Российского государственного медицинского университета.* 2017; 2: 37–41.
10. Ворошилина Е. С., Зорников Д. Л., Паначева Е. А. Сравнительное исследование микробиоты эякулята методом количественной ПЦР и культуральным методом. *Вестник Российского государственного медицинского университета.* 2019; 1: 44–9.
11. Почерников Д. Г., Витвицкая Ю. Г., Болдырева М. Н., Галкина И. С. Информативность биоматериала для исследования микробиоты урогенитального тракта мужчин методом ПЦР-РВ (пилотное исследование). *Экспериментальная и клиническая урология.* 2019; 2: 128–33.
12. Schuppe HC, Pilatz A, Hossain H, Diemer T, Wagenlehner F, Weidner W. Urogenital Infection as a Risk Factor for Male Infertility. *Dtsch Arztebl Int.* 2017; 114 (19): 339–46.
13. Jain AK, Murty MN, Flynn PJ. Data clustering: a review. *ACM computing surveys (CSUR).* 1999; 31 (3): 264–323.
14. Arthur D, Vassilvitskii S. K-means++: the advantages of careful seeding. In: Hal Gabow, editor. *Proceedings of the Eighteenth Annual ACM-SIAM Symposium on Discrete Algorithms (Proceedings in Applied Mathematics) 18th ed.* Society for Industrial and Applied Mathematics (3 January 2007). P. 1027–1035.
15. Rousseeuw PJ. Silhouettes: A graphical aid to the interpretation and validation of cluster analysis. *J Comput Appl Math.* 1987; 20: 53–65.
16. Davies DL, Bouldin DW. A Cluster Separation Measure. *IEEE Transactions on Pattern Analysis and Machine Intelligence.* PAMI-1. 1979; (2): 224–27.
17. de Goffau MC, Lager S, Salter SJ, Wagner J, Kronbichler A, Charnock-Jones DS, et al. Recognizing the reagent microbiome. *Nat Microbiol.* 2018 Aug; 3 (8): 851–3.
18. Yang H, Zhang J, Xue Z, Zhao C, Lei L, Wen Y, et al. Potential Pathogenic Bacteria in Seminal Microbiota of Patients with Different Types of Dysspermatism. *Sci Rep.* 2020; 10: 6876.

EEG SENSORIMOTOR RHYTHMS IN CHILDREN WITH AUTISM SPECTRUM DISORDERS

Kaida AI [✉], Eismont EV, Mikhailova AA, Pavlenko VB

Vernadsky Crimean Federal University, Simferopol, Russia

One of the currently assumed causes of impaired social interaction exhibited by children with autism spectrum disorders (ASD) is dysfunction of the mirror neuron system (MNS), which is responsible for imitation, understanding the intentions and emotions of other people. Desynchronization of sensorimotor rhythms is considered to be the indicator of MNS activation. This study aimed to analyze the specific patterns of reactivity of the μ -rhythm in an individually determined frequency range and β -rhythm on the EEG in children with ASD during independent movements, observation, imitation and auditory perception of similar movements performed by another person. The data collected were compared to those describing normally developing children. The study involved right-handed children with ASD aged 5–10 ($n = 10$) and normally developing children ($n = 10$). In the independent movements exercise, β -rhythm desynchronization was more pronounced in children with ASD, with difference becoming significant in the P4 locus ($p = 0.03$). In the movements imitation exercise, the groups showed significant differences in the EEG μ -rhythm in the locus C3 ($p = 0.03$). Auditory perception of movements revealed significant differences in the ranges of both μ -rhythm (loci F3 and Fz ($p = 0.02$), F4 ($p = 0.04$), Cz ($p = 0.009$)) and β -rhythm (loci Fz ($p = 0.01$), F4 ($p = 0.02$)). In these situations, children with ASD exhibited synchronization of sensorimotor rhythms, while normally developing children showed desynchronization. The assumption is that the specific patterns revealed are the consequences of disruption of functions of MNS and anti-mirror system. The data obtained can be used in development of EEG biofeedback training protocols for children with ASD.

Keywords: children, autism, EEG, mu-rhythm, beta-rhythm, mirror neuron system

Funding: the study received a grant #VG08/2020 supported by Vernadsky Crimean Federal University.

Author contribution: Kaida AI — data collection and processing, article authoring; Eismont EV — research planning, data collection, article authoring; Mikhailova AA — data processing, article authoring; Pavlenko VB — research planning, article authoring.

Compliance with ethical standards: the study was approved by the Vernadsky Crimean Federal University ethics committee (Minutes #6 of June 04, 2020). Parents of the children submitted the informed consent forms allowing their children to participate in the experiment.

✉ **Correspondence should be addressed:** Anna I. Kaida
Angarskaya, 38, Simferopol, 295001; kaydaanna@gmail.com

Received: 19.08.2020 **Accepted:** 11.09.2020 **Published online:** 22.09.2020

DOI: 10.24075/brsmu.2020.055

СЕНСОМОТОРНЫЕ РИТМЫ ЭЭГ У ДЕТЕЙ С РАССТРОЙСТВАМИ АУТИСТИЧЕСКОГО СПЕКТРА

А. И. Кайда [✉], Е. В. Эйсмонт, А. А. Михайлова, В. Б. Павленко

Крымский федеральный университет имени В. И. Вернадского, Симферополь, Россия

В настоящее время одной из причин нарушения социального взаимодействия у детей с расстройствами аутистического спектра (РАС) считают дисфункцию системы зеркальных нейронов (СЗН), ответственной за подражание, понимание намерений и эмоций других людей. Индикаторами активации СЗН принято считать десинхронизацию сенсомоторных ритмов. Целью работы было проанализировать особенности реактивности μ -ритма в индивидуально определенном частотном диапазоне и β -ритма ЭЭГ у детей с РАС, по сравнению с нормально развивающимися детьми, при осуществлении самостоятельных движений, наблюдении, имитации и слуховом восприятии аналогичных движений, выполняемых другим человеком. В исследовании приняли участие дети-правши 5–10 лет с РАС ($n = 10$) и нормально развивающиеся ($n = 10$). При наблюдении движений у детей с РАС десинхронизация β -ритма была более выражена, различия достигали уровня статистической значимости в локусе P4 ($p = 0,03$). В ситуации имитации движений значимые различия в индексах реактивности μ -ритма ЭЭГ выявлены в отведении C3 ($p = 0,03$). При слуховом восприятии движений значимые различия зарегистрированы в диапазоне как μ -ритма (локусы F3 и Fz ($p = 0,02$), F4 ($p = 0,04$), Cz ($p = 0,009$)), так и β -ритма (локусы Fz ($p = 0,01$), F4 ($p = 0,02$)). В данных ситуациях у детей с РАС происходила синхронизация сенсомоторных ритмов, в отличие от нормально развивающихся детей, демонстрировавших десинхронизацию. Предполагается, что обнаруженные особенности являются следствием нарушения функционирования СЗН и антизеркальной системы мозга. Полученные данные могут быть использованы при разработке протоколов тренингов биологической обратной связи по ЭЭГ для детей с РАС.

Ключевые слова: дети, аутизм, ЭЭГ, μ -ритм, β -ритм, система зеркальных нейронов

Финансирование: исследование выполнено в рамках поддержанного федеральным государственным автономным образовательным учреждением высшего образования «Крымский федеральный университет имени В. И. Вернадского» гранта № ВГ08/2020.

Вклад авторов: А. И. Кайда — набор и обработка данных, написание статьи; Е. В. Эйсмонт — планирование исследования, набор данных, написание статьи; А. А. Михайлова — обработка данных, написание статьи; В. Б. Павленко — планирование исследования, написание статьи.

Соблюдение этических стандартов: исследование одобрено этическим комитетом Крымского федерального университета имени В. И. Вернадского (протокол № 6 от 04 июня 2020 г.). Получено добровольное информированное согласие родителей на участие детей в эксперименте.

✉ **Для корреспонденции:** Анна Ивановна Кайда
ул. Ангарская, д. 38, г. Симферополь, 295001; kaydaanna@gmail.com

Статья получена: 19.08.2020 **Статья принята к печати:** 11.09.2020 **Опубликована онлайн:** 22.09.2020

DOI: 10.24075/vrgmu.2020.055

Autism spectrum disorders (ASD) are a group of complex developmental disorders heterogeneous in their symptoms and signs. The distinctive manifestations of such disorders are hampered social interactions, difficulties with language learning, limited repetitive behavior. ASD also manifest in increased nervousness, embarrassment, eye contact avoidance [1]. The

prevalence of autism in the world varies depending on the diagnostic criteria, country, region [2]. On average, according to the World Health Organization, 1 in 160 children worldwide has ASD.

It should be noted that deficient social skills is one of the main and lifelong signs of this disorder. Numerous research

efforts report connection between social interaction difficulties experienced by autistic children and dysfunction of brain regions that are part of the mirror neuron system (MNS) [3]. Mirror neurons were originally thought to be involved in perception and understanding of actions, but they also play an important role in higher-order cognitive processes such as imitation, empathy, language and speech acquisition. This system also determines understanding of someone else's consciousness (theory of mind), that is, a person's ability to draw conclusions about intentions, desires and emotions that direct actions of another person [4]. It was established that impairment of this ability in children with ASD leads to difficulties in social interaction [5].

EEG study of MNS makes use of such parameters as reactivity of sensorimotor μ - and β -rhythms [6]. It was established that the amplitude of sensorimotor rhythms (SMR) decreases during performance, observation, imitation, mental representation and auditory perception of movements [7].

It is known that children with ASD exhibit μ -rhythm suppression when performing independent movements, but it is absent or weak when they observe similar actions performed by another person [8, 9]. Adult volunteers with high scores on the Autism Spectrum Quotient (AQ) scale also showed weaker μ -rhythm desynchronization when observing actions, compared to people scoring low on this scale [10]. In another study, adults with high scores on the Autism Spectrum Quotient scale did not show desynchronization in either μ - or β -ranges when observing actions [11]. Thus, low level of MNS activation indicated by the weak desynchronization of SMR can be the main reason behind the observed deficiency of empathy and imitation in people with ASD [8], which is further confirmed by a research effort that revealed a connection between impairment of the main MNS regions in the left hemisphere and imitation disorders [12]. However, a number of studies reported no significant differences in the μ -rhythm reactivity in children and adults with ASD compared to their healthy peers [13]. The results of a recent study indicate that, although μ -rhythm suppression in children with ASD differs from that shown by the control group children when observing specific types of actions, the difference was not significant overall. Nevertheless, authors note that children with ASD spent more time recognizing actions, i.e. their reaction was slower [14]. Thus, current experimental evidence of μ -rhythm reactivity specificity in children with ASD is mixed, and only a few researchers have studied sensorimotor β -rhythm in such children. Besides, SMR reactivity in children with ASD is mostly studied with the focus on movement observation and execution. Therefore, it is of particular interest to study such rhythms in connection with other activities, such as imitation and auditory recognition of actions.

EEG biofeedback training for children with ASD focuses on developing the μ -rhythm modulation capability [15]. Biofeedback therapy yielded better μ -rhythm desynchronization in autistic children when observing and executing actions. Moreover, this therapy improved social behavior of such children: they were able to better recognize emotions and actions of other people [16, 17].

However, previous research efforts did not consider individual ranges of μ -rhythm reactivity in the context of examining EEG of children with ASD and giving them biofeedback therapy. It is known that the degree of desynchronization of μ -rhythm can be assessed incorrectly because of the overlapping occipital α -rhythm, which has a close frequency range [13]. In this connection, the recommendation is to determine the individual μ -rhythm band when the child makes independent movements.

In view of the aforesaid, this study aimed to analyze the specific patterns of μ -rhythm reactivity in an individually

determined frequency range and β -rhythm on the EEG in children with ASD during independent movements (of computer mouse), observation, imitation and auditory perception of similar movements performed by another person.

METHODS

Sample characteristics

The study was carried out at the Scientific Equipment Shared Use Center "Experimental Physiology and Biophysics" of Vernadsky Crimean Federal University.

The study involved 20 right-handed children aged 5 to 10 (mean age 7.4 ± 0.5 years), of which 10 children have ASD (9 boys and 1 girl) and 10 are normally developing children of matching age and gender (control group). The ASD group included children diagnosed with "childhood autism" (F84.0 in ICD-10) or "autism spectrum disorder with intellectual disability and functional language impairment" (6A02.3 in ICD-11). The criteria for inclusion in control group were a sufficient level of cognitive development (IQ 90 to 120 scored in WPPSI and WISC variants of the Wechsler scale) and absence of chronic diseases of the nervous system. Inclusion criteria for both groups: normal (or corrected to normal) levels of vision and hearing; preference for the right hand in computer mouse operation.

EEG registration

We used a Neuron-Spectrum-3 (Neurosoft; Russia) 19 channel electroencephalograph to register EEG. EEG potentials were leaded monopolarly, following the 10–20 system. The areas of interest in this study were the frontal, central and parietal regions of the neocortex (loci F3, F4, Fz, C3, C4, Cz, P3, P4, Pz). Joint contacts fixed to the earlobes served as a reference electrode. The cutoff frequencies of the high- and low-frequency filters were 1.5 and 35 Hz, respectively, and the frequency of EEG signals digitization was 250 Hz.

We recorded EEG when children were performing a series of tasks lasting 30 seconds each. All children participating in the study understood the instructions and performed the tasks correctly. The sequence of tasks was as follows:

- 1) gaze fixation on the image of a computer mouse situated on the table in front of the experimenter (BACKGROUND 1);
- 2) independent movements with computer mouse at arbitrary speed (MOV.1);
- 3) gaze fixation on the image of a computer mouse situated on the table in front of the experimenter (BACKGROUND 2);
- 4) observation of movement of the experimenter's hand with a computer mouse (OBS);
- 5) gaze fixation on the image of a computer mouse situated on the table in front of the experimenter (BACKGROUND 3);
- 6) independent movements with computer mouse at arbitrary speed (MOV.2);
- 7) imitation of movements experimenter performs with computer mouse (IMIT);
- 8) the participant sits motionless with eyes closed (EC);
- 9) the participant hears (without prior instruction) characteristic sounds of a mouse rubbing against table surface when the experimenter moves the mouse (HEARING).

The data were processed using WinEEG software (Mitsar; Russia). The independent components method built into the application (with additional visual recording quality control interface) enabled removal of artifacts. EEG segments were subjected to fast Fourier transformation with 4 second epochs and 50% epoch overlap.

Table 1. Results of analysis of variance of differences in the μ -rhythm reactivity, children developing normally children with ASD

Reactivity indices	GROUP		LOCUS		GROUP \times LOCUS	
	$F_{1,18}$	p	$F_{8,144}$	p	$F_{8,144}$	p
RI MOV.1	0.04	0.84	4.64	< 0.001	1.85	0.07
RI OBS	0.1	0.75	0.28	0.97	0.59	0.79
RI IMIT	3.37	0.08	1.1	0.37	0.58	0.80
RI HEARING	5.35	0.03	1.48	0.17	0.74	0.66

For each stage, we calculated the mean EEG amplitude value in the range of μ - and β -rhythms (15–25 Hz). The μ -rhythm range for each participant was determined individually, in lead C3, during independent movements of the right hand. The full frequency range of the μ -rhythm (6–13 Hz) was divided into segments of 1 Hz. Two adjacent segments with maximum desynchronization relative to the background were further considered as an individual frequency range [18]. We selected the β -rhythm range within the 15–25 Hz span, since this is where the sensorimotor areas' amplitude is suppressed during actions [19]. To normalize the distribution, the amplitude values were log transformed.

We used the generally accepted approach to sensorimotor rhythm reactivity index (RI) calculation. The formula is as follows: $RI = \ln(B/A)$, where B is the amplitude of the sensorimotor rhythm in the main situation and A is the amplitude of the sensorimotor rhythm in the initial situation of comparison. For independent movement (MOV.1) and observation (OBS) situations, the sensorimotor rhythm RI calculation factored in the gaze fixation situation (BACKGROUND 1 and BACKGROUND 2, respectively). For the movements imitation situation (IMIT), RI was calculated against the preceding independent movements (MOV.2). HEARING situation had the RI determined against EC, calm wakefulness with closed eyes (GL). Positive RI corresponded to synchronization of the sensorimotor rhythm, while its negative values corresponded to desynchronization.

Statistical data processing

We used STATISTICA 12.0 software (StatSoft Inc.; USA) to perform statistical analysis of the data obtained. The inter-group differences in frequency of the individually defined μ -rhythm were assessed using the Mann–Whitney U test. Repeated measures ANOVA enabled assessment of differences in the amplitude and reactivity indices of sensorimotor rhythms. We

also assessed the influence of GROUP, an external participant-related factor (two levels: children with ASD and the control group) and LOCUS, and internal participant-related factor (nine EEG leads) relying on the 2×9 pattern. F-distribution estimation, or the method of a priori contrasts, was used to calculate significance of differences in the analyzed parameters of sensorimotor rhythms relative to each of the nine EEG leads. Median and interquartile range allowed preparing description of distributions differing from the norm (extreme values of the individual μ -rhythm range). For the normal data distribution cases (logarithmic values of amplitudes and reactivity indices), we used mean and standard error of the mean. The differences were considered statistically significant at $p < 0.05$, but because of the small sample size we also included "unshaped" differences, i.e. those already visible but not yet fully formed ($p < 0.10$).

RESULTS

Amplitude-frequency indicators of sensorimotor rhythms

In the group of normally developing children, the lower limit median values for the individual μ -rhythm range were 9.3 Hz (8.5; 10). In the group of children with ASD, the lower limit median values for the individual μ -rhythm range were 8.6 Hz (7; 9.5). Despite the fact that the lower and upper limit medians of the individual μ -rhythm in children with ASD are reduced, these differences between the groups, assessed with the Mann–Whitney U test, did not reach the level of statistical significance ($p = 0.57$).

Analysis of variance of the sensorimotor rhythms amplitude peculiar to the independent movements situation did not reveal significant influences of the studied factors: μ -rhythm — GROUP ($F_{1,18} = 0.15$; $p = 0.7$) and LOCUS \times GROUP ($F_{8,144} = 0.75$; $p = 0.7$), β -rhythm — GROUP ($F_{1,18} = 0.35$; $p = 0.6$) and LOCUS

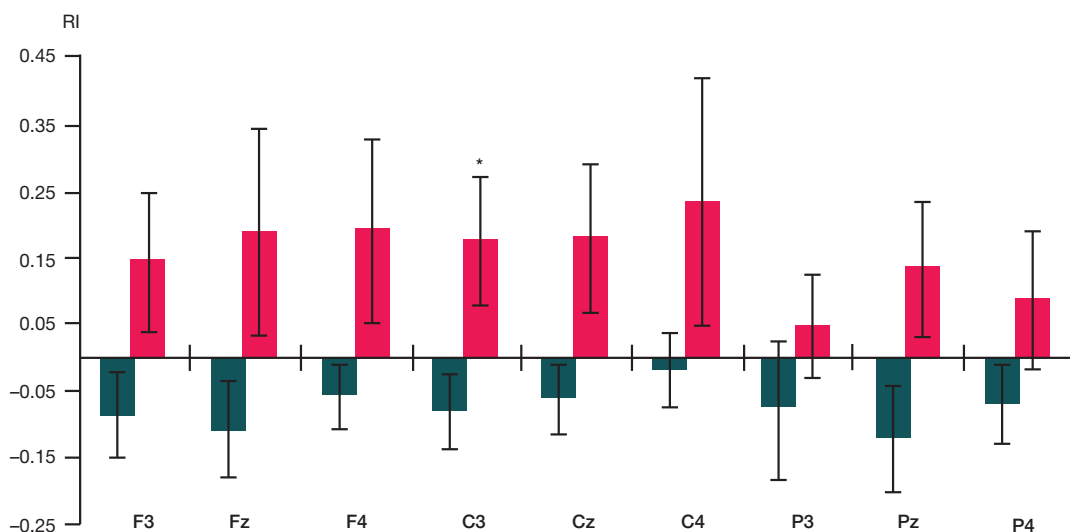


Fig. 1. EEG μ -rhythm reactivity indices (RI), children with ASD (red bars) and normally developing children (green bars), imitation of the experimenter's movements. * — $p < 0.05$ (significant differences in the μ -rhythm reactivity indices)

Table 2. Results of analysis of variance of differences in the β -rhythm reactivity, children developing normally children with ASD

Reactivity indices	GROUP		LOCUS		GROUP \times LOCUS	
	$F_{1,18}$	p	$F_{8,144}$	p	$F_{8,144}$	p
RI MOV.1	0.39	0.54	1.79	0.08	1.92	0.06
RI OBS	1.81	0.2	0.68	0.71	2.73	0.01
RI IMIT	2.93	0.1	1.01	0.43	0.4	0.92
RI HEARING	4.09	0.06	0.77	0.63	0.73	0.66

\times GROUP ($F_{8,144} = 0.72$; $p = 0.7$). In this experimental situation, only the LOCUS factor was found to have a significant effect on μ -rhythms ($F_{8,144} = 6.11$; $p < 0.001$) and β -rhythms ($F_{8,144} = 14.09$; $p < 0.001$). Thus, the sensorimotor rhythms amplitude did not differ significantly in children of the two groups when they performed independent movements.

Specific patterns of EEG μ -rhythm reactivity

Table 1 shows the results of analysis of variance applied to the differences in the μ -rhythm reactivity in children with and without ASD. For independent movements, we discovered a tendency of influence of the LOCUS \times GROUP factors interaction. Further analysis by the method of a priori contrasts yielded no significant differences. No significant differences were found in the μ -rhythm RI in the movements observation situation, too.

In the experimenter movements imitation situation we have discovered influence exerted by the GROUP factor, although this influence was just a tendency. The method of a priori contrasts, applied, showed that the differences in EEG μ -rhythm reactivity indices in two groups of children reached statistical significance in the central locus of the left hemisphere (C3: $p = 0.03$; mean value and standard error of the mean for the control group: -0.08 ± 0.06 ; for the RAS group: 0.18 ± 0.1) (Fig. 1). According to the diagrams presented below, μ -rhythm synchronizes in all leads in children with ASD when they imitate movements of the experimenter, whereas their normally developing peers show μ -rhythm desynchronization exclusively.

GROUP factor was also found to significantly influence auditory perception of familiar movements of a computer mouse. The EEG μ -rhythm RI differences between the two groups of children reached statistical significance at the frontal loci and the central median lead (loci F3 ($p = 0.02$; control group: -0.06 ± 0.06 ; ASD: 0.19 ± 0.08) and Fz ($p = 0.02$; control group: -0.1 ± 0.06 ; ASD: 0.16 ± 0.08), F4 ($p = 0.04$; control group:

-0.11 ± 0.04 ; ASD: 0.16 ± 0.11), Cz ($p = 0.009$; control group: -0.02 ± 0.05 ; ASD: 0.23 ± 0.06) (Fig. 2). In this experimental situation, we have registered growth of the μ -rhythm amplitude in all leads in children with ASD, whereas in the control group children it was mostly going down.

Specific patterns of EEG β -rhythm reactivity

Table 2 shows the results of analysis of variance applied to the differences in the β -rhythm reactivity in children of the two groups. Jointly, the LOCUS \times GROUP factors tended to exert influence in the independent movements situation. The sensorimotor β -rhythm RI in children with and without ASD did not differ significantly in this situation.

The GROUP \times LOCUS factors were found to exert significant influence in the observation situation, when the experimenter moved the mouse. The differences in β -rhythm reactivity between the groups of reached the statistical significance in the parietal locus of the right hemisphere (P4: $p = 0.03$; control group: 0.03 ± 0.03 ; ASD: 0.16 ± 0.08) (Fig. 3). Children with ASD showed β -rhythm desynchronization, while most of the normally developing children exhibited synchronization, with the exception of the frontal regions where we registered a decrease in the amplitude of the studied rhythm.

The experimenter movements imitation situation did not reveal any significant β -rhythm RI differences between the studied groups.

GROUP factor was discovered to have influence (tendency level) in the HEARING situation, with the participants perceiving sounds of movements of a computer mouse. The differences in EEG β -rhythm RI between the groups reached statistical significance in the median frontal lead and in the frontal locus of the right hemisphere (Fz loci ($p = 0.01$; control group: -0.05 ± 0.03 ; RAS: 0.08 ± 0.04), F4 ($p = 0.02$; control group: -0.09 ± 0.03 ; RAS: 0.08 ± 0.06) (Fig. 4). In the HEARING

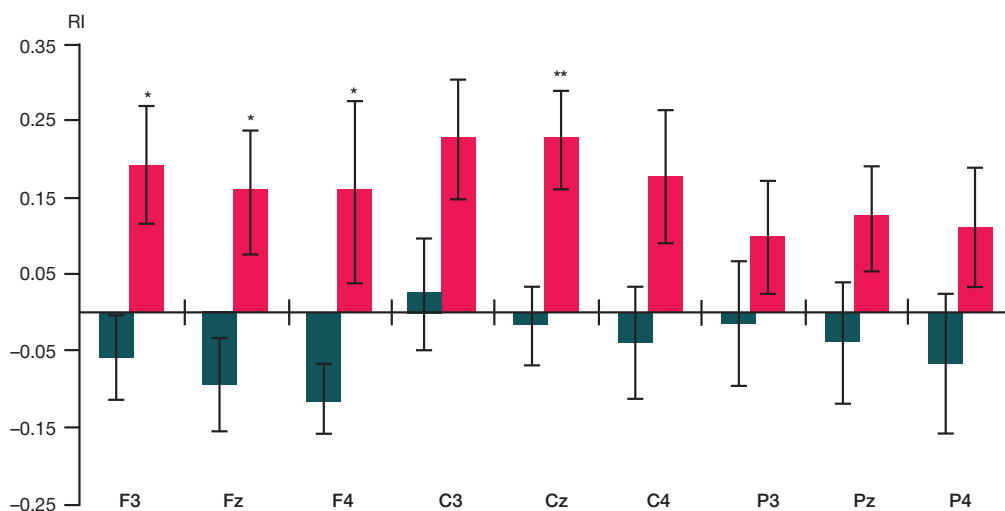


Fig. 2. EEG μ -rhythm reactivity indices (RI), children with ASD (red bars) and normally developing children (green bars), auditory perception of movements. — $p < 0.05$; ** — $p \leq 0.01$ (significant differences in the μ -rhythm reactivity indices)

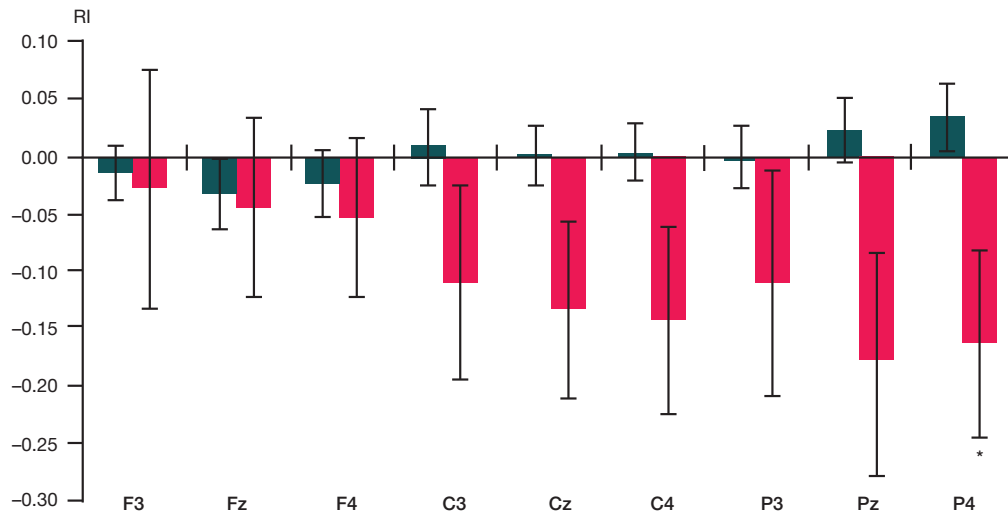


Fig. 3. EEG μ -rhythm reactivity indices (RI), children with ASD (red bars) and normally developing children (green bars), observation of movements. Other symbols are same as those on Fig. 1

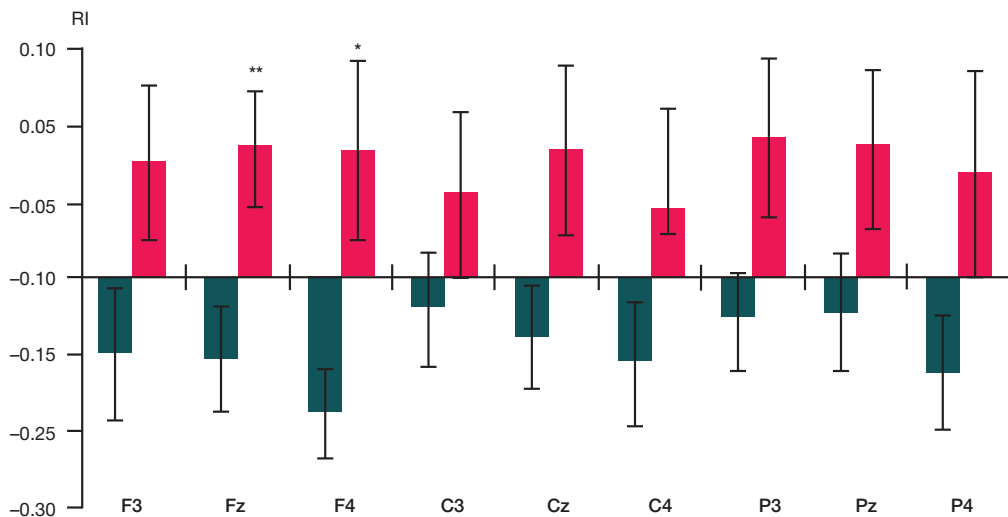


Fig. 4. EEG β -rhythm reactivity indices (RI), children with ASD (red bars) and normally developing children (green bars), auditory perception of movements. Other symbols are same as those on Fig. 2

situation children, with ASD exhibited synchronization of the β -rhythm in all leads, while the normally developing children had desynchronization of the studied rhythm.

DISCUSSION

The results of the present study indicate that the frequency of the μ -rhythm in an individually determined range does not differ significantly in children with and without ASD. Previously, we have shown that the individually determined frequency of the μ -rhythm does not depend on the age of children [21] on a sample of healthy 4–15 year-olds. However, both in the previous and in the present study, we revealed a wide variability of the lower and upper limits of the μ -rhythm individual frequency range. In this connection, we recommend determining the child's individual frequency range before investigating specific patterns of his/her μ -rhythm.

The independent movements exercise has shown that children with ASD have the same μ - and β -rhythm sensorimotor amplitudes as children that develop normally. Moreover, the analysis of SMR reactivity registered during performance of movements against motor rest condition has also uncovered no significant differences between the children of the studied groups. The data obtained confirm the results reported by

other authors that revealed a normal reaction of μ -rhythm desynchronization in children with ASD in the independent movements situation [8]. Thus, we can say that in children with this disorder, the somatosensory areas of the cortex that enable independent movements function normally.

Comparison of the SMR reactivity in children with ASD and the control group revealed differences in situations of observation, imitation and auditory perception of movements. In the movements imitation situation, children with autism had the μ -rhythm synchronizing, while their normally developing peers have shown desynchronization. Earlier, it was established that people with autism have impaired imitative abilities [22]. A connection was also found between impairment of MNS of the left hemisphere and impairment of a person's ability to imitate actions [12]. Thus, the lack of desynchronization of the μ -rhythm in children with ASD when imitating movements of another person may be associated with impaired MNS. Auditory perception with closed eyes (familiar movements of a computer mouse) was also not accompanied by desynchronization of sensorimotor μ - and β -rhythms in children with ASD. MNS is known to activate to sounds of familiar actions, which is accompanied with the SMR amplitude drop [23]. The results obtained once again confirm that children with ASD have MNS functions impaired.

In the movements observation situation, children with ASD exhibited greater desynchronization of the β -rhythm in parietal EEG leads than the control group children. Studies have shown that autistic people lack desynchronization when observing actions per se [8, 9]. However, these research efforts focused on μ -rhythm. The greater β -rhythm amplitude drop we have discovered in the movements observation situation may result from impaired functioning of the brain's anti-mirror system. It has been established that anti-mirror neurons detected during microelectrode examination of brain of epilepsy patients are triggered with movements and inhibited when such a patient observes movements of other people [24]. EEG shows inhibition of cortical neurons as β -rhythm synchronization [25]. A study involving adults registered β -rhythm synchronization when the participants observed emotionally neutral movements in a group of people with a low score on the Autism Coefficient scale, which the authors associate with the suppression of automatic copying of actions [10]. It was suggested that the anti-mirror system of the brain plays an important role in distinguishing between self and others' actions, as well as in preventing involuntary imitation [26]. Children with ASD have these functions impaired, which was reflected in our study as desynchronization of the β -rhythm registered when such children were observing actions. It can also be assumed that children with ASD spent more cognitive resources on incoming information processing, which was accompanied by a greater decrease in the β -range amplitude.

The results of the present study indicate that in children with ASD, there is no desynchronization of SMR during imitation and auditory recognition of actions, and there is also no greater decrease in the amplitude of the β -rhythm when observing movements. The specific patterns revealed may point to disruptions in the functioning of the nervous system, MNS and the anti-mirror system of the brain in particular. The research results can be used to improve the effectiveness of EEG-BFB trainings with children with ASD.

CONCLUSIONS

The study revealed specific patterns of SMR reactivity in children with ASD. Compared to the control group, children with ASD had EEG μ - and β -rhythms synchronizing when in the imitation and auditory recognition situations, which may indicate a dysfunction of the MNS that enables imitation and normal social interaction. When observing movements of children with ASD, we registered a greater decrease in the amplitude of the sensorimotor β -rhythm, which may be associated with a dysfunction of the activity of the anti-mirror system of the brain. The results obtained highlight the need to study reactivity of both the sensorimotor μ -rhythm and β -rhythm in children with ASD. The revealed patterns can be used to help children with ASD, for example, using biofeedback trainings to improve EEG sensorimotor rhythms characteristics.

References

- Lai MC, Lombardo MV, Baron-Cohen S. Autism. *Lancet*. 2014; 383 (9920): 896–910.
- Makushkin EV, Makarov IV, Pashkovskiy VE. The prevalence of autism: genuine and imaginary. *S.S. Korsakov Journal of Neurology and Psychiatry*. 2019; 119 (2): 80–86. Russian.
- Saffin JM, Tohid H. Walk like me, talk like me. The connection between mirror neurons and autism spectrum disorder. *Neurosciences (Riyadh)*. 2016; 21 (2): 108–19.
- Lebedeva NN, Zufman AI, Malcev VYu. Mirror neuron system as a key to learning, personality formation and understanding of another's mind. *Uspehi fiziologicheskikh nauk*. 2017; 48 (4): 16–28. Russian.
- Andreou M, Skrimpa V. Theory of mind deficits and neurophysiological operations in autism spectrum disorders: A review. *Brain Sci*. 2020; 10 (6): 393.
- Fox NA, Bakermans-Kranenburg MJ, Yoo KH, Bowman LC, Cannon EN, Vanderwert RE, et al. Assessing human mirror activity with EEG mu rhythm: A meta-analysis. *Psychol Bull*. 2016; 142 (3): 291–313.
- Ferrari PF, Rizzolatti G. *New frontiers in mirror neurons research*. NY: Oxford University Press, 2015; 408 p.
- Oberman LM, Hubbard EM, McCleery JP, Altschuler EL, Ramachandran VS, Pineda JA. EEG evidence for mirror neuron dysfunction in autism spectrum disorders. *Cognitive Brain Research*. 2005; 24 (2): 190–98.
- Martineau J, Cochin S, Magne R, Barthelemy C. Impaired cortical activation in autistic children: Is the mirror neuron system involved? *International Journal of Psychophysiology*. 2008; 68 (1): 35–40.
- Siqi-Liu A, Harris AM, Atkinson AP, Reed CL. Dissociable processing of emotional and neutral body movements revealed by μ -alpha and beta rhythms. *Soc Cogn Affect Neurosci*. 2018; 13 (12): 1269–79.
- de Vega M, Padron I, Moreno IZ, García-Marco E, Domínguez A, Marrero H, et al. Both the mirror and the affordance systems might be impaired in adults with high autistic traits. Evidence from EEG mu and beta rhythms. *Autism Res*. 2019; 12: 1032–42.
- Binder E, Dovern A, Hesse MD, Ebke M, Karbe H, Saliger J, et al. Lesion evidence for a human mirror neuron system. *Cortex*. 2017; 90: 125–37.
- Hobson HM, Bishop DVM. The interpretation of mu suppression as an index of mirror neuron activity: past, present and future. *Review R Soc Open Sci*. 2017; 4 (3): 160662.
- Sotoodeh MS, Taheri-Torbati H, Sohrabi M, Ghoshuni M. Perception of biological motions is preserved in people with autism spectrum disorder: electrophysiological and behavioural evidences. *J Intellect Disabil Res*. 2019; 63 (1): 72–84.
- Pineda JA, Carrasco K, Datko M, Pillen S, Schalles M. Neurofeedback training produces normalization in behavioural and electrophysiological measures of high-functioning autism. *Philos Trans R Soc Lond B Biol Sci*. 2014; 369 (1644): 20130183.
- Friedrich EVC, Sivanathan A, Lim T, Suttie N, Louchart S, Pillen S, et al. An effective neurofeedback intervention to improve social interactions in children with autism spectrum disorder. *J Autism Dev Disord*. 2015; 45: 4084–100.
- Datko M, Pineda JA, Muller RA. Positive effects of neurofeedback on autism symptoms correlate with brain activation during imitation and observation. *Eur J Neurosci*. 2018; 47 (6): 579–91.
- Mahin SA, Kaida AI, Eismont EV, Mikhailova AA, Pavlenko VB; FGAOU VO "Krymskij federal'nyj universitet imeni V.I. Vernadskogo", patentoobladatel'. Sposob opredelenija individual'nogo chastotnogo diapazona mju-ritma JeJeG. Patent RF # 2702728. 09.10.2019. Russian.
- Simon S, Mukamel R. Power modulation of electroencephalogram mu and beta frequency depends on perceived level of observed actions. *Brain Behav*. 2016; 6 (8): e00494.
- Raymaekers R, Wiersma JR, Roeyers H. EEG study of the mirror neuron system in children with high functioning autism. *Brain research*. 2009; 1304: 113–21.
- Kaida AI, Mikhailova AA, Eismont EV, Dzhapparova LL, Pavlenko VB. EEG μ -rhythm reactivity in children during imitation of biological and non-biological motion. [published online ahead of print, 2020.04.16]. *Bulletin of RSMU*. 2020. DOI: 10.24075/brsmu.2020.019.
- Bernier R, Dawson G, Webb S, Murias M. EEG mu rhythm and imitation impairments in individuals with autism spectrum disorder.

- Brain and Cognition. 2007; 64 (3): 228–37.
23. Pineda JA, Grichanik M, Williams V, Trieu M, Chang H, Keyzers C. EEG sensorimotor correlates of translating sounds into actions. *Front Neurosci*. 2013; 7: 203.
 24. Mukamel R, Ekstrom AD, Kaplan J, Iacoboni M, Fried I. Single-neuron responses in humans during execution and observation of actions. *Current Biology*. 2010; 20 (8): 750–56.
 25. Kropotov YuD. *Kolichestvennaja JeJeG, kognitivnye vyzvannye potencialy mozga cheloveka i nejroterapija*. Doneck: Izdatel' Zaslavkij Ju.A., 2010; 506 s. Russian.
 26. Rizzolatti G, Sinigaglia C. *Mirrors in the brain: how our minds share actions and emotions*. Oxford University Press, 2008; 242 p.

Литература

1. Lai MC, Lombardo MV, Baron-Cohen S. Autism. *Lancet*. 2014; 383 (9920): 896–910.
2. Макушкин Е. В., Макаров И. В., Пашковский В. Э. Распространенность аутизма: подлинная и мнимая. *Журнал неврологии и психиатрии им. С. С. Корсакова*. 2019; 119 (2): 80–86.
3. Saffin JM, Tohid H. Walk like me, talk like me. The connection between mirror neurons and autism spectrum disorder. *Neurosciences (Riyadh)*. 2016; 21 (2): 108–19.
4. Лебедева Н. Н., Зуфман А. И., Мальцев В. Ю. Система зеркальных нейронов мозга: ключ к обучению, формированию личности и пониманию чужого сознания. *Успехи физиологических наук*. 2017; 48 (4): 16–28.
5. Andreou M, Skrimpa V. Theory of mind deficits and neurophysiological operations in autism spectrum disorders: A review. *Brain Sci*. 2020; 10 (6): 393.
6. Fox NA, Bakermans-Kranenburg MJ, Yoo KH, Bowman LC, Cannon EN, Vanderwert RE, et al. Assessing human mirror activity with EEG mu rhythm: A meta-analysis. *Psychol Bull*. 2016; 142 (3): 291–313.
7. Ferrari PF, Rizzolatti G. *New frontiers in mirror neurons research*. NY: Oxford University Press, 2015; 408 p.
8. Oberman LM, Hubbard EM, McCleery JP, Altschuler EL, Ramachandran VS, Pineda JA. EEG evidence for mirror neuron dysfunction in autism spectrum disorders. *Cognitive Brain Research*. 2005; 24 (2): 190–98.
9. Martineau J, Cochin S, Magne R, Barthelemy C. Impaired cortical activation in autistic children: Is the mirror neuron system involved? *International Journal of Psychophysiology*. 2008; 68 (1): 35–40.
10. Siqi-Liu A, Harris AM, Atkinson AP, Reed CL. Dissociable processing of emotional and neutral body movements revealed by μ -alpha and beta rhythms. *Soc Cogn Affect Neurosci*. 2018; 13 (12): 1269–79.
11. de Vega M, Padron I, Moreno IZ, García-Marco E, Domínguez A, Marrero H, et al. Both the mirror and the affordance systems might be impaired in adults with high autistic traits. Evidence from EEG mu and beta rhythms. *Autism Res*. 2019; 12: 1032–42.
12. Binder E, Dovern A, Hesse MD, Ebke M, Karbe H, Saliger J, et al. Lesion evidence for a human mirror neuron system. *Cortex*. 2017; 90: 125–37.
13. Hobson HM, Bishop DVM. The interpretation of mu suppression as an index of mirror neuron activity: past, present and future. *Review R Soc Open Sci*. 2017; 4 (3): 160662.
14. Sotoodeh MS, Taheri-Torbati H, Sohrabi M, Ghoshuni M. Perception of biological motions is preserved in people with autism spectrum disorder: electrophysiological and behavioural evidences. *J Intellect Disabil Res*. 2019; 63 (1): 72–84.
15. Pineda JA, Carrasco K, Datko M, Pillen S, Schalles M. Neurofeedback training produces normalization in behavioural and electrophysiological measures of high-functioning autism. *Philos Trans R Soc Lond B Biol Sci*. 2014; 369 (1644): 20130183.
16. Friedrich EVC, Sivanathan A, Lim T, Suttie N, Louchart S, Pillen S, et al. An effective neurofeedback intervention to improve social interactions in children with autism spectrum disorder. *J Autism Dev Disord*. 2015; 45: 4084–100.
17. Datko M, Pineda JA, Muller RA. Positive effects of neurofeedback on autism symptoms correlate with brain activation during imitation and observation. *Eur J Neurosci*. 2018; 47 (6): 579–91.
18. Махин С. А., Кайда А. И., Эйсмонт Е. В., Михайлова А. А., Павленко В. Б.; ФГАОУ ВО «Крымский федеральный университет имени В.И. Вернадского», патентообладатель. Способ определения индивидуального частотного диапазона мю-ритма ЭЭГ. Патент РФ № 2702728. 09.10.2019.
19. Simon S, Mukamel R. Power modulation of electroencephalogram mu and beta frequency depends on perceived level of observed actions. *Brain Behav*. 2016; 6 (8): e00494.
20. Raymaekers R, Wiersema JR, Roeyers H. EEG study of the mirror neuron system in children with high functioning autism. *Brain research*. 2009; 1304: 113–21.
21. Kaica AI, Mikhailova AA, Eismont EV, Dzhabbarova LL, Pavlenko VB. EEG μ -rhythm reactivity in children during imitation of biological and non-biological motion. [published online ahead of print, 2020.04.16]. *Bulletin of RSMU*. 2020. DOI: 10.24075/brsmu.2020.019.
22. Bernier R, Dawson G, Webb S, Murias M. EEG mu rhythm and imitation impairments in individuals with autism spectrum disorder. *Brain and Cognition*. 2007; 64 (3): 228–37.
23. Pineda JA, Grichanik M, Williams V, Trieu M, Chang H, Keyzers C. EEG sensorimotor correlates of translating sounds into actions. *Front Neurosci*. 2013; 7: 203.
24. Mukamel R, Ekstrom AD, Kaplan J, Iacoboni M, Fried I. Single-neuron responses in humans during execution and observation of actions. *Current Biology*. 2010; 20 (8): 750–56.
25. Кротов Ю. Д. Количественная ЭЭГ, когнитивные вызванные потенциалы мозга человека и нейротерапия. *Донецк: Издатель Заславский Ю. А.*, 2010; 506 с.
26. Rizzolatti G, Sinigaglia C. *Mirrors in the brain: how our minds share actions and emotions*. Oxford University Press, 2008; 242 p.

TELOMERIZED FIBROBLASTS AS A CANDIDATE 3D *IN VITRO* MODEL OF PATHOLOGICAL HYPERTROPHIC SCARS

Shadrin VS ✉, Kozhin PM, Shoshina OO, Luzgina NG, Rusanov AL

Orekhovich Research Institute of Biomedical Chemistry, Moscow, Russia

The search for the optimal cell model for studying the pathogenesis of pathological scars is a pressing challenge. This study aimed at evaluating the feasibility of using telomerized fibroblasts for the *in vitro* 3D modeling of pathological hypertrophic scars. NF and Fb-hTERT cells were cultured as monolayers and spheroids in the absence and in the presence of TGFβ1. The metabolic activity of the cultured cells was assessed using the MTT assay. Cell migration was estimated using the scratch assay. The expression of genes associated with fibrous scar tissue growth was measured by qRT-PCR. Fb-hTERT cells were more metabolically active than NF cells in the presence of TGFβ1 (for 1 ng/ml: 179 ± 12% vs. 135 ± 13% respectively; $p < 0.05$). Spheroids grown from Fb-hTERT cells were significantly larger than those derived from NF cells. In the presence of TGFβ1, the expression of proteins associated with extracellular matrix production (*COL1A1*, *COL3A1*, *FN1*) was lower in Fb-hTERT cells than in NF cells (more than 25, 20 and 2-fold, respectively; $p < 0.05$). Intact NF cells were more active in closing the scratch than Fb-hTERT cells: on day 2, the gap closure rate was 2.28 times higher in NF cells ($p < 0.05$). Exposure to TGFβ1 stimulated Fb-hTERT, unlike NF cells, to close the gap 2 times faster on day 2 ($p < 0.05$). Thus, telomerized fibroblasts have a few phenotypic traits observed in keloid fibroblasts; still there are some limitations that should be accounted for when using Fb-hTERT cells for the modeling of pathological hypertrophic scars.

Keywords: *in vitro* model, fibroblasts, hTERT, hypertrophic scar, keloid scar, TGFβ1

Funding: this research was supported by the Russian Ministry of Science and Higher Education and was conducted under the Federal Targeted Program on Research and Development in Priority Fields of Science and Technology for 2014–2020 (Agreement 05.604.21.0219, Project ID RFMEF160419X0219).

Author contribution: Luzgina NG, Rusanov AL conceived the study and proposed its design; Shadrin VS, Kozhin PM, Shoshina OO, Luzgina NG, Rusanov AL analyzed the literature, analyzed and interpreted the experimental data and wrote the manuscript; Shadrin VS, Kozhin PM planned and conducted the experiment; Shadrin VS wrote the manuscript.

✉ **Correspondence should be addressed:** Valerian S. Shadrin
Pogodinskaya, 10, str. 8, Moscow, 119121; valerianshadrin@gmail.com

Received: 28.08.2020 **Accepted:** 02.09.2020 **Published online:** 27.09.2020

DOI: 10.24075/brsmu.2020.057

ТЕЛОМЕРИЗОВАННЫЕ ФИБРОБЛАСТЫ КАК ПОТЕНЦИАЛЬНЫЙ ОБЪЕКТ ДЛЯ 3D-МОДЕЛИРОВАНИЯ ПАТОЛОГИЧЕСКИХ ГИПЕРТРОФИЧЕСКИХ РУБЦОВ *IN VITRO*

В. С. Шадрин ✉, П. М. Кожин, О. О. Шошина, Н. Г. Лузгина, А. Л. Русанов

Научно-исследовательский институт биомедицинской химии имени В. Н. Ореховича, Москва, Россия

Поиск оптимальных клеточных моделей для изучения патогенеза гиперпластических рубцов является актуальной задачей. Целью исследования было оценить перспективу использования теломеризованных фибробластов в качестве объекта при 3D-моделировании патологических гипертрофических рубцов *in vitro*. Клетки НФ и Фб-hTERT культивировали в виде монослоя и сфероидов, в интактном состоянии и при воздействии TGFβ1. Метаболическую активность клеток оценивали методом МТТ. Скорость заращения дефекта монослоя клеток вычисляли с помощью scratch-теста. Уровень экспрессии генов, ассоциированных с гиперпластическими процессами, определяли методом qRT-PCR. Для Фб-hTERT характерно более выраженное по сравнению с НФ усиление метаболической активности клеток при воздействии TGFβ1 (для 1 нг/мл 179 ± 12% и 135 ± 13% соответственно; $p < 0,05$). Сфероиды, сформированные из Фб-hTERT, были значительно крупнее сфероидов, полученных из НФ. Продукция основных специфических для фибробластов белков, ассоциированных с продукцией внеклеточного матрикса (*COL1A1*, *COL3A1*, *FN1*), при стимуляции TGFβ1 была ниже в Фб-hTERT по сравнению с НФ (более чем в 25, 20 и 2 раза соответственно; $p < 0,05$). Интактные НФ более активно, по сравнению с Фб-hTERT, восстанавливали дефект монослоя (в 2,28 раза на вторые сутки; $p < 0,05$). При этом воздействие TGFβ1 приводило к увеличению скорости заполнения дефекта клетками Фб-hTERT (в 2 раза на вторые сутки; $p < 0,05$), но не НФ. Таким образом, теломеризованные фибробласты имеют ряд фенотипических признаков, характерных для келоидных фибробластов, но в то же время есть ограничения, которые следует учитывать при использовании Фб-hTERT для моделирования патологических гипертрофических рубцов.

Ключевые слова: *in vitro* модель, фибробласты, hTERT, гипертрофический рубец, келоидный рубец, TGFβ1

Финансирование: работа выполнена при финансовой поддержке Министерства науки и высшего образования Российской Федерации в рамках ФЦП «Исследования и разработки по приоритетным направлениям развития научно-технологического комплекса России на 2014–2020 годы» (соглашение № 05.604.21.0219, Уникальный идентификатор проекта RFMEF160419X0219).

Вклад авторов: Н. Г. Лузгина, А. Л. Русанов — концепция и дизайн исследования; В. С. Шадрин, П. М. Кожин, О. О. Шошина, Н. Г. Лузгина, А. Л. Русанов — анализ литературы, анализ и интерпретация полученных данных, редактирование рукописи; В. С. Шадрин, П. М. Кожин — планирование и проведение исследования; В. С. Шадрин — написание статьи.

✉ **Для корреспонденции:** Валериан Сергеевич Шадрин
ул. Погодинская, д. 10, стр. 8, г. Москва, 119121; valerianshadrin@gmail.com

Статья получена: 28.08.2020 **Статья принята к печати:** 02.09.2020 **Опубликована онлайн:** 27.09.2020

DOI: 10.24075/vrgmu.2020.057

Every year, over 100 million people worldwide develop skin scars after surgical interventions, injuries or burns. Wounds heal differently depending on their location, depth, healing conditions, and clinical characteristics of the affected patients; wound repair can culminate in the formation of a normal (normotrophic) or pathological scar. Stimulated by a variety of factors, abnormal

fibrous tissue growth leads to hypertrophic and keloid scarring. Both types of scarring are a cutaneous fibroproliferative disorder characterized by the hyperactivation of fibroblasts in the wound and excessive proliferation of extracellular matrix [1].

The absence of simple and cost-effective *in vitro* cell models replicating profibrogenic pathways makes it difficult to explore

the pathogenesis of hypertrophic and keloid scarring and to develop effective preventive and curative treatments. Fibroblasts isolated from keloid tissue vary in phenotype between donors; besides obtaining the sufficient amount of clinical keloid tissue specimens is a real challenge. Therefore, the search for the optimal cell model for reproducing the phenotype of keloid fibroblasts is a pressing concern. It seems promising to use immortalized cell lines that can proliferate indefinitely and retain a stable phenotype at high passage numbers.

It is known that keloid fibroblasts are characterized by high proliferative activity, rapid growth, increased expression of collagen I, fibronectin, elastin, periostin (regulates production of collagen I), and tenascin (participates in cell adhesion) [2, 3], resulting in extensive connective tissue growth beyond the borders of the injury. Some aspects of keloid fibroblast metabolism are similar to those of tumor cells [4, 5].

It is hypothesized that the fibroblast phenotype observed in pathological scars is determined by high telomerase activity [6]. A research team was able to suppress proliferation and growth of keloid fibroblasts and normalize some of their phenotypic traits by decreasing telomerase activity in these cells; the authors concluded that telomerase inhibition might be a promising strategy for keloid therapy [5]. Therefore, it would be interesting to evaluate the potential of telomerized fibroblasts for the *in vitro* modeling of pathological scarring.

Optimization of cell culture techniques is crucial for designing an adequate scarring model. It is known that the center of keloid tissue is often hypoxic due to capillary occlusion resulting from excess collagen and endothelial cells [7]. Fibroblasts at the margins are more metabolically active, invasive, and capable of activating angiogenesis, presumably for maintaining their invasiveness [8]. Therefore, models utilizing spheroid cell culture systems look very attractive.

Transforming growth factor $\beta 1$ (TGF $\beta 1$) is often used to induce the profibrogenic fibroblast phenotype *in vitro* [9]. This multifunctional protein regulates cellular growth, differentiation, motility, and production of extracellular matrix during normal tissue healing; importantly, increased expression of TGF $\beta 1$ can trigger fibrotic skin disorders [10]. TGF $\beta 1$ stimulates collagen growth and secretion and induces fibronectin synthesis in keloid fibroblasts [11]. It would be interesting to evaluate the functional response of model cell candidates to TGF $\beta 1$.

The aim of this study was to evaluate the feasibility of using telomerized fibroblasts for the *in vitro* 3D modeling of hypertrophic scars.

METHODS

Cell lines

The study was carried out using normal (NF) and telomerized (Fb-hTERT) human skin fibroblasts. Primary third-passage NF isolated from the foreskin of 35–38-year-old donors were purchased from a cryobank (Perspective; Russia). In order to account for different phenotypic traits of cells obtained from different donors, three cell lines were used.

Fb-hTERT cells were a gift from Prof. Egorov EE. (Engelhardt Institute of Molecular Biology, RAS). They are a HAF-1608 cell culture with the telomerase catalytic subunit gene. Fb-hTERT cells maintain a stable phenotype over up to 200 passages [12].

Culture

The cells were cultured in a complete DMEM/F-12 (Gibco; USA) medium supplemented with 10% FBS (Dia-M; Russia),

1% antibiotic-antimycotic solution by Gibco, USA (final concentrations: 100 un/ml penicillin, 0.25 μ g/ml amphotericin B, 100 un/ml streptomycin) and 1% GlutaMAX solution by Gibco, USA (the final concentration of L-alanyl-L-glutamine was 2 mM).

MMT-based analysis of TGF $\beta 1$ effect on cells

For the MTT assay [13], 2,500 NF cells at passage 4 and Fb-hTERT cells harvested at 70% confluency from the culture flask were plated in each well of a flat-bottom 96-well plate and incubated for 24 h in a complete DMEM/F-12 medium at 37 °C and 5% CO₂. Then, the medium was replaced with a fresh medium containing TGF $\beta 1$ (ProSpec; Israel), and the cells were incubated for another 48 h, the medium being changed every 24 h. After that, the medium was collected and the wells were washed in DPBS (Gibco; USA); 100 μ l of 1 mg/ml MTT solution (Dia-M; Russia) was added to each well, and the cells were incubated for 2.5 h at 37 °C and 5% CO₂. After 2.5 h of incubation, the MTT solution was replaced with DMSO (Biolot; Russia) and the mixture was further incubated at room temperature until formazan crystals were completely solubilized. Absorbance was measured in each well at 490 nm; background absorbance at 655 nm was subtracted. The MTT assay was run in 3 replicates (5 wells per replicate) using the following TGF $\beta 1$ concentrations: 0 ng/ml; 0.1 ng/ml; 1 ng/ml; 5 ng/ml; 10 ng/ml.

Cell metabolic activity was calculated using the formula: $100\% * (AB_{490}(\text{experimental wells}) - AB_{490}(\text{medium})) / (AB_{655}(\text{control wells}) - AB_{655}(\text{medium}))$. AB stands for absorbance.

Spheroid cell culture

Spheroids were grown in ultra-low attachment 96-well plates (Corning; USA); 5, 10 or 20 thousand NF or Fb-hTERT cells at 70% confluency were dispensed into the wells and incubated for 9 days in a complete DMEM/F-12 medium at 37 °C and 5% CO₂. The medium was replaced every 24 h.

To study the effect exerted by TGF $\beta 1$ on spheroids, 20,000 NF cells and 10,000 Fb-hTERT cells (sufficient for growing spheroids of comparable sizes) harvested at 70% confluency from culture flasks were dispensed into each well and incubated for 3 days in a complete DMEM/F-12 medium supplemented with 1 ng/ml TGF $\beta 1$ at 37 °C and 5% CO₂. The medium was replaced every 24 h to maintain stable concentrations of the growth factor.

Spheroids were photographed every day using a Primovert microscope (Carl Zeiss; Germany). Their diameters were measured using ImageJ software and a Fiji extension (National Institutes of Health; USA) [14].

Estimating wound closure rate in cell monolayer using scratch assay

Harvested at 70% confluency from a culture flask, 50,000 NF or Fb-hTERT cells were added to each well of a 24-well plate and incubated for 24 h in a complete DMEM/F-12 medium at 37 °C and 5% CO₂ until the monolayer was formed. Then the medium was replaced, and a scratch was made on the cell monolayer with a 1 ml-pipet tip. The cells were washed in DPBS; then, DMEM/F-12 (control) or DMEM/F-12 containing 1 ng/ml TGF $\beta 1$ (experiment) was added to the cells. The cells were incubated for 2 days. In each well, the entire length of the scratch was photographed daily. The photos were processed in CellProfiler (Broad Institute of Harvard and MIT; USA) [15]. The closed area of the gap was calculated at 24 and 48 h;

the ratio of the closing gap area to the initial scratch area was calculated. The experiment was conducted in 3 replicates in 3 wells per replicate.

Measuring expression of genes associated with abnormal fibrous growth using qRT-PCR

After analyzing the literature, we chose the *PAI-1* gene and the genes encoding synthesis of collagen I, collagen III and fibronectin as target genes. Obviously, this list is not exhaustive but the increased expression of these genes suggests modulation of profibrogenic cell potential.

Briefly, qRT-PCR was performed as described below. The suspension of 200,000 cells in 5 ml of the culture medium was transferred to a flask and preincubated for 48 h in a complete DMEM/F-12 medium at 37 °C and 5% CO₂. Then, the medium was replaced with a fresh medium containing 1 ng/ml TGFβ1 and the cells were incubated for another 48. The medium was replaced every 24 h. After that, RNA was isolated from the cells using an RNeasy Mini Kit (Qiagen; Germany) according to the standard protocol. The obtained RNA was quantified on a NanoDrop 2000c spectrophotometer (Thermo Scientific; USA). Reverse transcription was performed following the standard protocol using an MMLV RT kit (Evrogen; Russia) and 1 µg of RNA. qPCR was performed using a qPCRMix-HS SYBR+LowROX reaction mix (Evrogen; Russia). For each gene and each sample, the reaction was run in 3 replicates. GAPDH was chosen as a reference gene.

Primers are listed below:

GAPDH Forward Primer F: 5'-TCGACAGTCAGCCGCATCTTC TTT-3' Reverse Primer R: 5'-ACCAAATCCGTTGACTCCGACCTT-3';
COL1A1 F: 5'-CCAAGAGGAAGGCCAAGTC-3' R: 5'-ACAC GTCTCGGTCATGGTA-3'; *COL3A1* F: 5'-CTGGTGCTAAG GGTGAAGTT-3' R: 5'-GTCCAGGTTCTCCTCTTTGTC-3';
FN1 F: 5'-GAATAAGCTGTACCATCGCAAAC-3' R: 5'-ACCAAG ACACACACTCTAAC-3'; *PAI-1* F: 5'-GGCTGACTTC ACGAGTCTTT-3' R: 5'-CGTTCACCTCGATCTTCACTT-3';

Measuring collagen I production by spheroid culture

Spheroids were grown as described above. After 3 days of incubation, spheroids grown from 10,000 cells were fixed in 4% formalin and embedded in paraffin following the standard

protocol. Paraffin sections were stained with goat anti-human collagen I primary antibodies (IMTEK; Russia) and donkey anti-goat IgG FITC secondary antibodies (ab6881, Abcam; USA). Three spheroid samples per each cell line were chosen for the analysis; for further staining, we used 5 paraffin sections per sample. All sections were stained simultaneously using the same reagent kit (antibody solutions and buffers).

The stained paraffin sections were examined under a laser confocal LSM 710 microscope (Carl Zeiss; Germany); in all cases, the settings were identical. Photographs were processed in CellProfiler [15]. For each sample, the mean fluorescence intensity was calculated as the total fluorescence intensity divided by the spheroid area. Mean fluorescence intensity values were normalized to the mean fluorescence intensity of NF cells that had not been exposed to TGFβ1.

Statistical analysis

The obtained data were processed using the programming language R. Differences between the groups were tested using Student's *t* test with the Benjamini–Hochberg procedure for multiple comparisons. Differences were considered significant at $p < 0.05$. Statistical data are presented below as $M \pm m$ unless specified otherwise.

RESULTS

Normal and immortalized skin fibroblasts differed in their size and proliferative activity. The surface area of NF cells cultured at low density (> 50% confluency) was $723 \pm 54 \mu\text{m}^2$ (Fig. 1A).

Doubling time was calculated by the formula $DT = T * \ln 2 / \ln (X_t/X_0)$, where *T* is incubation time, *X_t* is the number of cells after culture, *X₀* is the initial number of cells. For NF cells, doubling time was 3.1 ± 0.6 days. Cultured as a monolayer, NF cells reached 100% confluence at a density of $16.5 \pm 3.1 * 10^3$ cells/cm².

The surface area of Fb-hTERT cells was smaller: $675 \pm 29 \mu\text{m}^2$ (Fig. 1A). Doubling time was 1.8 ± 0.4 days. Fb-hTERT cells reached 100% confluence at $41.9 \pm 7.2 * 10^3$ cells/cm².

The MTT assay revealed a dose-dependent effect of TGFβ1 on NF and Fb-hTERT cultures (Fig. 1B). The metabolic activity of Fb-hTERT and NF increased significantly after the cells were treated with 0.1 ng/ml and 1 ng/ml of TGFβ1, respectively. For both cell lines, a peak in the metabolic activity

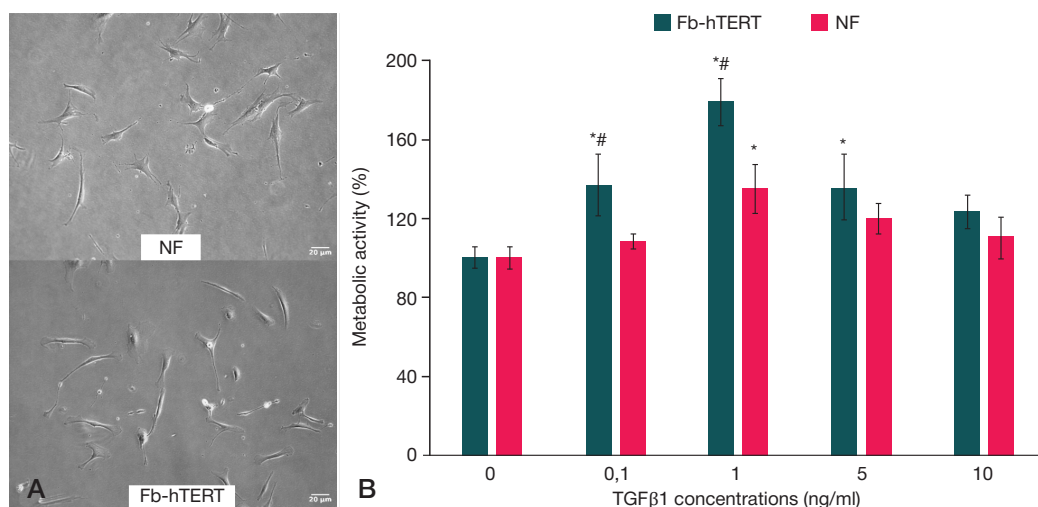


Fig. 1. Characteristics of NF and Fb-hTERT cells in a 2D-culture. **A.** The appearance of NF and Fb-hTERT cells. Light microscopy, $\times 100$ magnification. **B.** The metabolic activity of NF and Fb-hTERT cells at different concentrations of TGFβ1 (the MTT-assay). * — differences are significant relative to the previous TGFβ1 concentration ($p < 0.05$); # — differences are significant relative to NF cells at the same TGFβ1 concentration ($p < 0.05$). Note: hereinafter, NF stands for normal human foreskin fibroblast cells, Fb-hTERT stands for human skin telomerized postnatal fibroblasts

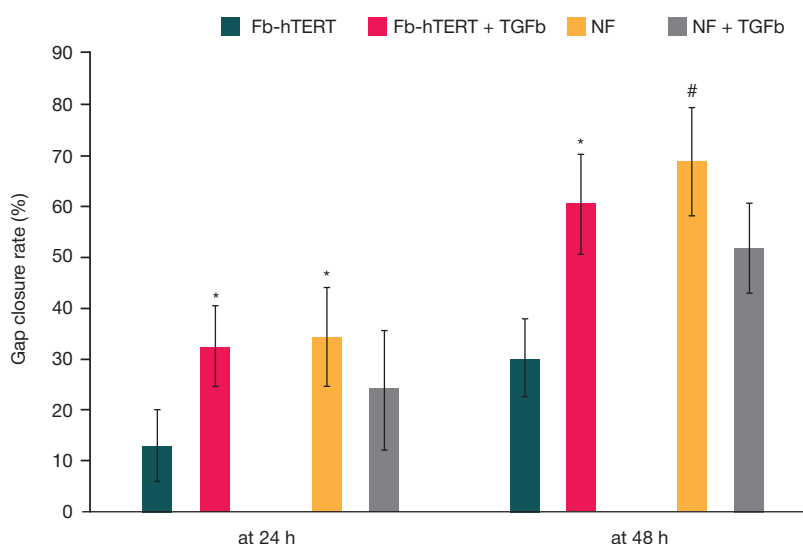


Fig. 2. Basal (control) and TGFβ1-stimulated gap closure rate in the monolayer of NF and Fb-hTERT cells (the scratch assay, TGFβ1 concentration in the culture medium is 1 ng/ml). * — differences are significant relative to the basal gap closure rate ($p < 0.05$); # — differences are significant relative to Fb-hTERT cells under the same culture conditions ($p < 0.05$)

was observed following exposure to 1 ng/ml of TGFβ1 and was significantly higher for Fb-hTERT cells ($179 \pm 12\%$ vs. $135 \pm 13\%$, respectively; $p < 0.05$). A further increase in TGFβ1 concentrations added to the culture medium caused a decline in the metabolic activity of the cells relative to the effect exerted by 1 ng/ml TGFβ1. Therefore, we decided to use 1 ng/ml TGFβ1 to boost cell profibrogenic activity in the subsequent experiments.

The scratch assay demonstrated that the gap closure rate was different for the NF and Fb-hTERT cells and in the presence of TGFβ1 (Fig. 2).

The gap closure rate at 24 h and 48 h after creating the scratch was significantly higher in the monolayer of the control NF cells (in the absence of TGFβ1) than in the control Fb-hTERT cells. At the same time, the gap closure rate did not differ significantly between the NF cells cultured in the presence of TGFβ1 and the control cells. Stimulated by TGFβ1, the Fb-hTERT monolayer closed the scratch two times faster than the control cells at both time checkpoints: 24 h ($33 \pm 8\%$ and $13 \pm 7\%$ respectively) and 48 h ($61 \pm 10\%$ and $30 \pm 7\%$, respectively). Thus, in the absence of TGFβ1, NF cells closed the scratch in the monolayer faster than Fb-hTERT cells, whereas in the

presence of TGFβ1, the Fb-hTERT monolayer recovered faster than the NF monolayer.

Spheroids were grown from 5, 10 and 20 thousand fibroblast cells. In all cases, spheroids were shrinking in size during the first 5 days of culture. After that, their size remained relatively stable (Fig. 3A). The more cells were used to grow a spheroid, the more pronounced was the rate of shrinking, for both NF and Fb-hTERT cells.

Fb-hTERT spheroids were approximately two times larger than NF spheroids although Fb-hTERT cells themselves were smaller than NF.

TGFβ1 effects on NF and Fb-hTERT spheroids were studied using cellular aggregates formed by 20,000 (NF) and 10,000 cells (Fb-hTERT) (Fig. 3B). The sizes of the grown spheroids were comparable. The size is a crucial parameter for cell aggregates since it determines nutrient availability at the margin and in the center and affects the intensity of hypoxia in the center of the spheroid.

Spheroids grown from NF significantly increased in size 24 h after the culture medium was supplemented with 1 ng/ml TGFβ1, as compared with the control NF spheroids (Fig. 4).

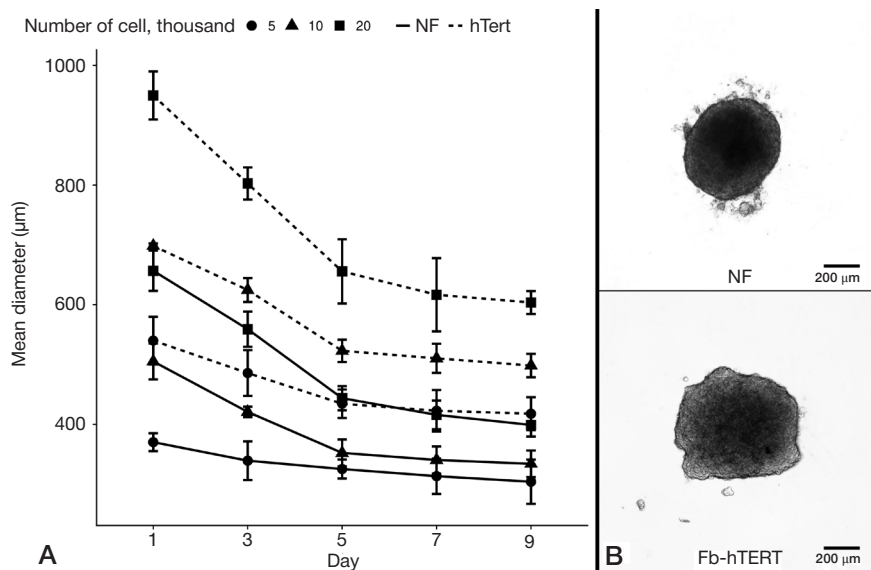


Fig. 3. Growing spheroids from NF and Fb-hTERT cells. **A.** Changes in the mean spheroid diameter grown from initially different numbers of NF and Fb-hTERT cells ($M \pm \sigma$). **B.** The appearance of an NF spheroid (20,000 cells) and an Fb-hTERT spheroid (10,000 cells). Light microscopy, $\times 40$ magnification

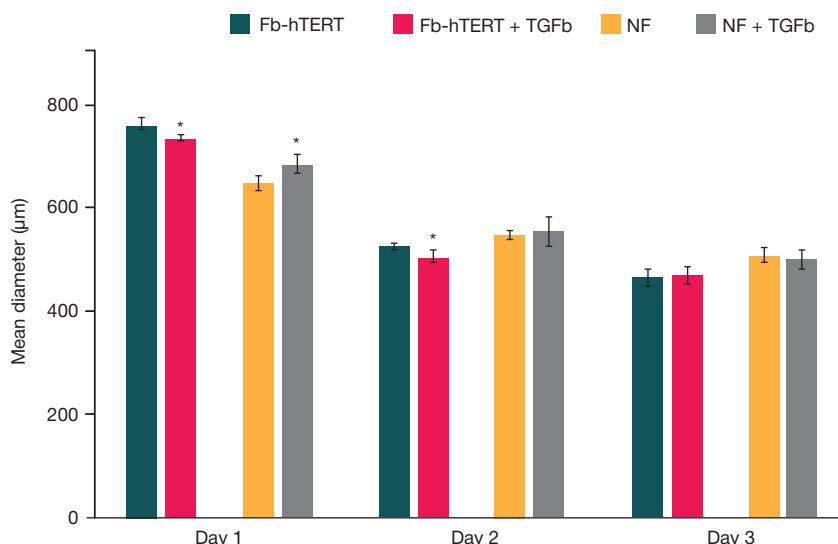


Fig. 4. The mean diameter of spheroids grown from NF and Fb-hTERT at different incubation times in the presence of 1 ng/ml TGFβ1 in the culture medium and in the absence of this growth factor (control). In order to obtain spheroids comparable in their size, we used 20,000 NF and 10,000 Fb-hTERT cells, respectively. * — differences are significant relative to the control group at the same time point ($p < 0.05$)

After that, the differences started to level out and disappeared by day 3 of culture.

Spheroids grown from Fb-hTERT cells displayed a different behavior. In the presence of TGFβ1, they significantly diminished in size on days 1 and 2 of culture, in comparison with the control. By day 3, these differences smoothed out.

Slight differences in the size dynamics of spheroids formed from NF and Fb-hTERT cells at the early stages of the culture exposed to TGFβ1 might be explained by the phenotypic traits of the used cell lines and differences in their initial number. However, by day 3, as the spheroids grew and the cell density increased, there were almost no differences.

NF and Fb-hTERT cells differed in the expression of genes associated with fibrous tissue growth both in the absence or presence of TGFβ1 (Fig. 5).

In the absence of TGFβ1, NF cells tended to increasingly express the genes coding for collagen I and III, unlike Fb-hTERT cells, which expressed PAI-1 slightly more actively. The expression of the gene coding for fibronectin synthesis was comparable between NF and Fb-hTERT.

NF cells incubated for 2 days in the presence of 1 ng/ml TGFβ1 exhibited a tendency for increased expression of all studied

genes, in comparison with the control. Significant differences were observed for the gene coding for fibronectin synthesis.

At the same time, no significant changes were observed in the expression of *COL1A1*, *COL3A1*, *FN1*, and *PAI-1* in Fb-hTERT cells incubated with TGFβ1.

Those differences between the basal and TGFβ1-stimulated expression of collagen I by NF and Fb-hTERT cells were also present in spheroid cultures (Fig. 6A). According to microscopy findings, the level of collagen expression in the spheroids derived from NF was significantly higher than in the spheroids formed from Fb-hTERT cells (Fig. 6B). When NF-spheroids were incubated with TGFβ1, there was a 1.7-fold increase in collagen I production, whereas for Fb-hTERT-derived spheroids cultured under the same conditions the increase in the production of collagen I was moderate (1.4-fold).

DISCUSSION

We have been exploring the possibility of stimulating the profibrogenic potential of normal and telomerized human skin fibroblasts (NF and Fb-hTERT, respectively) *in vitro*. It is known that telomerase is active in fibroblasts isolated from keloid scars

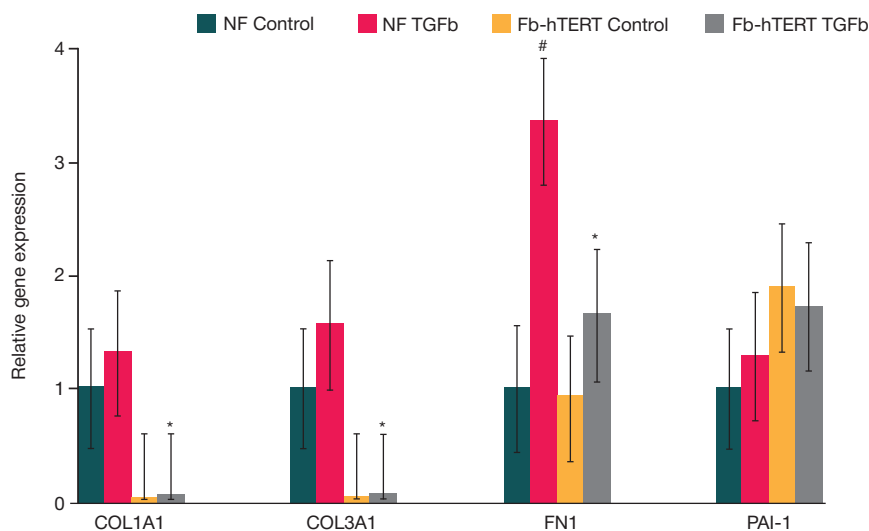


Fig. 5. Expression of genes associated with fibrous tissue growth in NF and Fb-hTERT cells in the absence and presence of TGFβ1 (1 ng/ml). * — differences are significant between Fb-hTERT and NF cells in the presence of TGFβ1 ($p < 0.05$); # — differences are significant between the 2 cell lines in the absence and in the presence of TGFβ1 ($p < 0.05$)

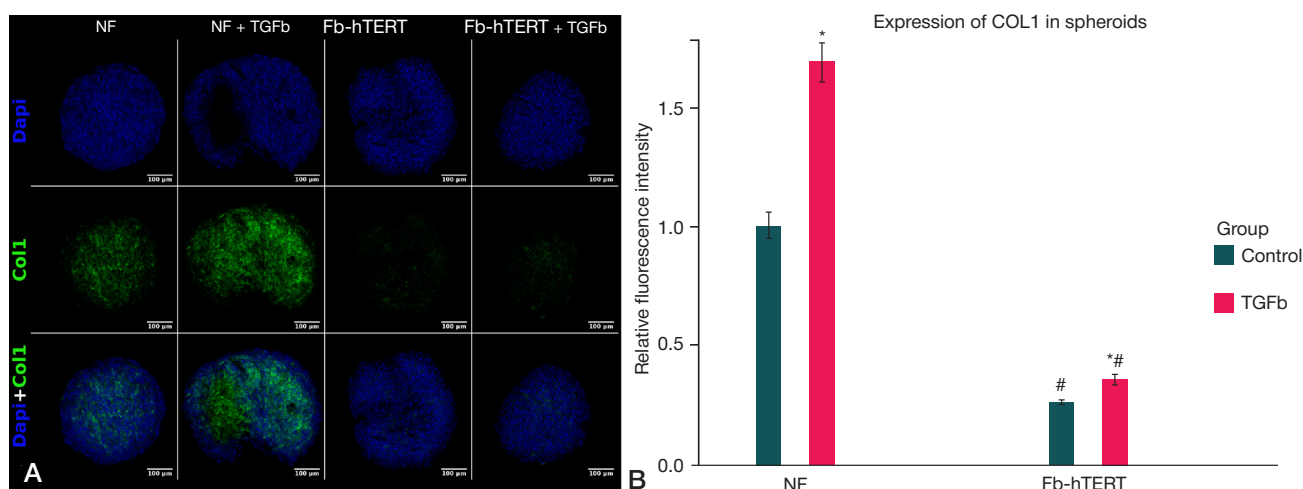


Fig. 6. Collagen I production in the spheroids grown from NF and Fb-hTERT cells in the presence of 1 ng/ml TGFβ1. **A.** Immunofluorescence assay, laser confocal microscopy, ×100 magnification; cell nuclei are stained blue (Dapi), collagen I is stained green. **B.** Relative fluorescence intensity of collagen I in the spheroids formed by NF and Fb-hTERT cells in the presence of 1 ng/ml TGFβ1. * — indicates statistically significant differences in collagen I fluorescence intensity in spheroids cultured in the presence or absence of TGFβ1 ($p < 0.05$); # — indicates statistically significant differences in collagen I fluorescence intensity between Fb-hTERT spheroids and NF spheroids in the presence of TGFβ1 ($p < 0.05$)

[6]. In terms of telomerase activity, keloid fibroblasts resemble immortalized cells; therefore, Fb-hTERT make a promising *in vitro* candidate model for pathological keloid and hypertrophic scars. At the same time, according to the literature, the phenotype of normal fibroblasts can be modified to approximate the phenotype of cells isolated from pathological scars by using growth factors that play a key role in the pathogenesis of pathologic fibrous growth; one of such growth factors is TGFβ1 [16]. TGFβ1 activates a variety of signal cascades triggering increased cell proliferation, adhesion and migration, as well as extracellular matrix production [17].

Importantly, *in vitro* models of any tissue type, including normal and fibrous connective tissue of scars, must reproduce its 3D structure ensuring natural cell-cell interactions and mutual influences. Therefore, the phenotypic traits of NF and Fb-hTERT cells were investigated in spheroid cultures. This model is actively used in carcinogenesis research and in the studies evaluating the efficacy of anticancer therapies as tumor microenvironments, nutrient supply, gas exchange and physiology is best reproduced in cellular spheroids [18]. However, prior to our experiment, spheroids had not been used for creating a cell model of a pathologic hypertrophic or keloid scar, which indicates the novelty of our findings.

On the whole, intact Fb-hTERT cells, as compared with NF, had a number of phenotypic traits typical to immortalized cells: a smaller size, a higher doubling rate and a higher rate of confluent monolayer formation, which was, perhaps, determined by their high proliferative activity. This feature of Fb-hTERT cells might underlie their higher (as compared to NF cells) metabolic activity both in the absence or presence of TGFβ1 (according to the MTT assay results).

An MTT assay allows assessing the metabolic and — arguably — proliferative activity of cells [19]. In this study, we have demonstrated a dose-dependent effect exerted by TGFβ1 on the metabolic activity of NF and Fb-hTERT, which was more pronounced for Fb-hTERT cells. This finding is consistent with other reports of TGFβ1 effects on the proliferative and metabolic activity of fibroblasts [20, 21]. In our study, the peak increase of cell metabolic activity was observed following exposure to 1 ng/ml TGFβ1 and was more pronounced in Fb-hTERT cells.

The size dynamics of growing spheroids was consistent with other reports [22, 23] of spheroids shrinking in size on the first day of culture and then plateauing gradually (spheroid maturation). Unsurprisingly, our spheroids derived from the

initially greater number of cells (especially those grown from 20,000 cells) showed a sharper reduction in size, because the optimal diameter of a cellular spheroid is determined by nutrient supply and adequate gas exchange and ranges from 200 to 500 μm [24].

Spheroids formed from Fb-hTERT cells were significantly larger than NF-derived spheroids, although NF cells are bigger than Fb-hTERT cells. This was probably the result of higher proliferative activity normally observed in telomerized cells. At the same time, we cannot rule out that Fb-hTERT spheroids were less capable of retraction due to weak cell-cell contacts.

Exposure to TGFβ1 decreased the size of Fb-hTERT spheroids and also increased the rate of gap closure (in the scratch test), which was lower in intact Fb-hTERT cells than in NF. Perhaps, TGFβ1 not only stimulated Fb-hTERT proliferation but also promoted their adhesion capacity and facilitated cell cooperation. However, this question requires further investigation.

Importantly, Fb-hTERT cells had other phenotypic traits distinguishing them from normally differentiated fibroblasts. For example, production of basic proteins specific to fibroblasts that are building blocks for connective tissue fibers (collagen I and III, fibronectin) was lower in Fb-hTERT cells than in NF (both intact or exposed to TGFβ1); this was also true for spheroid cultures, as demonstrated by PCR-based assays and fluorescent staining. Because Fb-hTERT are an immortalized cell line, their proliferation programs seem to be far more active than differentiation programs. Consequently, the expression of collagen genes (characteristic of differentiated connective tissue cells) was low in both intact and TGFβ1-stimulated cells. At the same time, when exposed to TGFβ1, NF cells demonstrated the phenotype of differentiated cells with increased expression of extracellular matrix-related genes.

It is known that the expression of genes involved in the synthesis of connective tissue components is increased in keloid scars. There are reports of increased transcription and translation of collagens I and III and fibronectin in fibrous growths [2]. The abundance of collagen in keloid tissue is explained by the increased expression of PAI-1 not typically seen in normal fibroblasts [25]. Of note, PAI-1 expression in intact Fb-hTERT cells observed in our experiment was higher than in NF.

Besides, the scratch in the monolayer of intact NF cells closed faster than in Fb-hTERT cells. The scratch test is used for the indirect assessment of cell regeneration potential (the ability

to close a wound). The gap closure rate depends on the levels of cell proliferation and/or migration. It is known that TGF β 1 promotes wound healing [17]. In our experiments, exposure to TGF β 1 allowed the Fb-hTERT monolayer (but not the NF monolayer) to recover more rapidly. This finding needs to be further analyzed in Fb-hTERT and NF cultures by evaluating the effects of TGF β 1 on cell adhesion and cooperation programs involved in the implementation of cell capacity to migrate.

CONCLUSION

Telomerized fibroblasts have a few phenotypic traits observed in keloid fibroblasts: high proliferative and metabolic activity; the ability to close a gap in the monolayer (the scratch assay)

in the presence of TGF β 1; increased, as compared to NF, levels of *PAI-1* expression (trending, statistically insignificant). Other important features include their ability to divide infinitely, maintain phenotypic homogeneity at high passage numbers and form cell spheroids. This makes telomerized fibroblasts a promising candidate for the 3D modeling of pathologic scars. However, the expression of proteins associated with extracellular matrix production (*COL1A1*, *COL3A1*, *FN1*) is low in telomerized fibroblasts, including in the presence of TGF β 1, whereas keloid fibroblasts are characterized by overproduction of these proteins. This fact should be accounted for when exploiting Fb-hTERT cells for modeling hypertrophic scars. Further research is needed to study the possibility of activating the expression of extracellular matrix proteins in these cells.

References

- Jumper N, Paus R, Bayat A. Functional histopathology of keloid disease. *Histology and histopathology*. 2015; 30 (9): 1033–57.
- Sidgwick GP, Bayat A. Extracellular matrix molecules implicated in hypertrophic and keloid scarring. *Journal of the European Academy of Dermatology and Venereology*. 2012; 26 (2): 141–152.
- Liang CJ, Yen YH, Hung LY, Wang SH, Pu CM, Chien HF, et al. Thalidomide inhibits fibronectin production in TGF- β 1-treated normal and keloid fibroblasts via inhibition of the p38/Smad3 pathway. *Biochemical pharmacology*. 2013; 85 (11): 1594–02.
- De Felice B, Wilson RR, Nacca M. Telomere shortening may be associated with human keloids. *BMC medical genetics*. 2009; 10 (1): 110.
- Huang Y, Lin LX, Bi QX, Wang P, Wang XM, Liu J, et al. Effects of hTERT antisense oligodeoxynucleotide on cell apoptosis and expression of hTERT and bcl-2 mRNA in keloid fibroblasts. *European Review for Medical and Pharmacological Sciences*. 2017; 21 (8): 1944–51.
- Yu D, Shang Y, Yuan J, Ding S, Luo S, Hao L. Wnt/ β -catenin signaling exacerbates keloid cell proliferation by regulating telomerase. *Cellular Physiology and Biochemistry*. 2016; 39 (5): 2001–13.
- Kischer CW, Thies AC, Chvapil M. Perivascular myofibroblasts and microvascular occlusion in hypertrophic scars and keloids. *Human pathology*. 1982; 13 (9): 819–24.
- Bran GM, Goessler UR, Hormann K, Riedel F, Sadick H. Keloids: current concepts of pathogenesis. *International journal of molecular medicine*. 2009; 24 (3): 283–93
- Chin D, Boyle GM, Parsons PG, Coman WB. What is transforming growth factor-beta (TGF- β)?. *British journal of plastic surgery*. 2004; 57 (3): 215–21.
- Yang GP, Lim IJ, Phan TT, Lorenz HP, Longaker MT. From scarless fetal wounds to keloids: molecular studies in wound healing. *Wound repair and regeneration*. 2003; 11 (6): 411–8.
- Jagadeesan J, Bayat A. Transforming growth factor beta (TGF β) and keloid disease. *International journal of surgery*. 2007; 5 (4): 278–85.
- Egorov EE, Terekhov SM, Vishniakova K, Karachentsev DN, Kazimirchuk EV, Tsvetkova TG, et al. Telomerization as a method of obtaining immortal human cells preserving normal properties. *Ontogenez*. 2003; 34 (3): 183.
- Kupcsik L. Estimation of cell number based on metabolic activity: the MTT reduction assay. In *Mammalian cell viability*. Humana Press. 2011: 13–19.
- Schindelin J, Arganda-Carreras I, Frise E, Kaynig V, Longair M, Pietzsch T, et al. Fiji: an open-source platform for biological-image analysis. *Nature methods*. 2012; 9 (7): 676–82.
- Carpenter AE, Jones TR., Lamprecht MR, Clarke C, Kang IH, Friman O, et al. CellProfiler: image analysis software for identifying and quantifying cell phenotypes. *Genome biology*. 2006; 7 (10): R100.
- Lee TY, Chin GS, Kim W, Chau D, Gittes GK, Longaker MT. Expression of transforming growth factor beta 1, 2, and 3 proteins in keloids. *Annals of plastic surgery*. 1999; 43 (2): 179–84.
- Klass BR, Grobbelaar AO, Rolfe KJ. Transforming growth factor β 1 signalling, wound healing and repair: a multifunctional cytokine with clinical implications for wound repair, a delicate balance. *Postgraduate Medical Journal*. 2009; 85 (999): 9–14.
- Friedrich J, Ebner R, Kunz-Schughart LA. Experimental anti-tumor therapy in 3-D: spheroids—old hat or new challenge? *International journal of radiation biology*. 2007; 83 (11–12): 849–71.
- Ohno M, Abe T. Rapid colorimetric assay for the quantification of leukemia inhibitory factor (LIF) and interleukin-6 (IL-6). *Journal of immunological methods*. 1991; 145 (1–2): 199–203.
- Meran S, Thomas DW, Stephens P, Enoch S, Martin J, Steadman R, et al. Hyaluronan facilitates transforming growth factor- β 1-mediated fibroblast proliferation. *Journal of Biological Chemistry*. 2008; 283 (10): 6530–45.
- Negreros M, Hagood JS, Espinoza CR, Balderas-Martínez YI, Selman M, Pardo A. Transforming growth factor beta 1 induces methylation changes in lung fibroblasts. *PLoS one*. 2019; 14 (10): e0223512.
- Takezawa T, Mori Y, Yonaha T, Yoshizato K. Characterization of morphology and cellular metabolism during the spheroid formation by fibroblasts. *Experimental cell research*. 1993; 208 (2): 430–41.
- Frandsen SK, Gibot L, Madi M, Gehl J, Rols MP. Calcium electroporation: evidence for differential effects in normal and malignant cell lines, evaluated in a 3D spheroid model. *PLoS One*. 2015; 10 (12): e0144028.
- Mittler F, Obeid P, Rulina AV, Haguët V, Gidrol X, Balakirev MY. High-content monitoring of drug effects in a 3D spheroid model. *Frontiers in oncology*. 2017; 7: 293.
- Tuan TL, Wu H, Huang EY, Chong SS, Laug W, Messadi D, et al. Increased plasminogen activator inhibitor-1 in keloid fibroblasts may account for their elevated collagen accumulation in fibrin gel cultures. *The American journal of pathology*. 2003; 162 (5): 1579–89.

Литература

- Jumper N, Paus R, Bayat A. Functional histopathology of keloid disease. *Histology and histopathology*. 2015; 30 (9): 1033–57.
- Sidgwick GP, Bayat A. Extracellular matrix molecules implicated in hypertrophic and keloid scarring. *Journal of the European Academy of Dermatology and Venereology*. 2012; 26 (2): 141–152.
- Liang CJ, Yen YH, Hung LY, Wang SH, Pu CM, Chien HF, et al. Thalidomide inhibits fibronectin production in TGF- β 1-treated normal and keloid fibroblasts via inhibition of the p38/Smad3 pathway. *Biochemical pharmacology*. 2013; 85 (11): 1594–02.
- De Felice B, Wilson RR, Nacca M. Telomere shortening may be

- associated with human keloids. *BMC medical genetics*. 2009; 10 (1): 110.
5. Huang Y, Lin LX, Bi QX, Wang P, Wang XM, Liu J, et al. Effects of hTERT antisense oligodeoxynucleotide on cell apoptosis and expression of hTERT and bcl-2 mRNA in keloid fibroblasts. *European Review for Medical and Pharmacological Sciences*. 2017; 21 (8): 1944–51.
 6. Yu D, Shang Y, Yuan J, Ding S, Luo S, Hao L. Wnt/ β -catenin signaling exacerbates keloid cell proliferation by regulating telomerase. *Cellular Physiology and Biochemistry*. 2016; 39 (5): 2001–13.
 7. Kischer CW, Thies AC, Chvapil M. Perivascular myofibroblasts and microvascular occlusion in hypertrophic scars and keloids. *Human pathology*. 1982; 13 (9): 819–24.
 8. Bran GM, Goessler UR, Hormann K, Riedel F, Sadick H. Keloids: current concepts of pathogenesis. *International journal of molecular medicine*. 2009; 24 (3): 283–93.
 9. Chin D, Boyle GM, Parsons PG, Coman WB. What is transforming growth factor-beta (TGF- β)?. *British journal of plastic surgery*. 2004; 57 (3): 215–21.
 10. Yang GP, Lim IJ, Phan TT, Lorenz HP, Longaker MT. From scarless fetal wounds to keloids: molecular studies in wound healing. *Wound repair and regeneration*. 2003; 11 (6): 411–8.
 11. Jagadeesan J, Bayat A. Transforming growth factor beta (TGF β) and keloid disease. *International journal of surgery*. 2007; 5 (4): 278–85.
 12. Egorov EE, Terekhov SM, Vishniakova K, Karachentsev DN, Kazimirchuk EV, Tsvetkova TG, et al. Telomerization as a method of obtaining immortal human cells preserving normal properties. *Ontogenez*. 2003; 34 (3): 183.
 13. Kupcsik L. Estimation of cell number based on metabolic activity: the MTT reduction assay. In *Mammalian cell viability*. Humana Press. 2011: 13–19.
 14. Schindelin J, Arganda-Carreras I, Frise E, Kaynig V, Longair M, Pietzsch T, et al. Fiji: an open-source platform for biological-image analysis. *Nature methods*. 2012; 9 (7): 676–82.
 15. Carpenter AE, Jones TR., Lamprecht MR, Clarke C, Kang IH, Friman O, et al. CellProfiler: image analysis software for identifying and quantifying cell phenotypes. *Genome biology*. 2006; 7 (10): R100.
 16. Lee TY, Chin GS, Kim W, Chau D, Gittes GK, Longaker MT. Expression of transforming growth factor beta 1, 2, and 3 proteins in keloids. *Annals of plastic surgery*. 1999; 43 (2): 179–84.
 17. Klass BR, Grobbelaar AO, Rolfe KJ. Transforming growth factor β 1 signalling, wound healing and repair: a multifunctional cytokine with clinical implications for wound repair, a delicate balance. *Postgraduate Medical Journal*. 2009; 85 (999): 9–14.
 18. Friedrich J, Ebner R, Kunz-Schughart LA. Experimental anti-tumor therapy in 3-D: spheroids—old hat or new challenge? *International journal of radiation biology*. 2007; 83 (11–12): 849–71.
 19. Ohno M, Abe T. Rapid colorimetric assay for the quantification of leukemia inhibitory factor (LIF) and interleukin-6 (IL-6). *Journal of immunological methods*. 1991; 145 (1–2): 199–203.
 20. Meran S, Thomas DW, Stephens P, Enoch S, Martin J, Steadman R, et al. Hyaluronan facilitates transforming growth factor- β 1-mediated fibroblast proliferation. *Journal of Biological Chemistry*. 2008; 283 (10): 6530–45.
 21. Negreros M, Hagoood JS, Espinoza CR, Balderas-Martínez YI, Selman M, Pardo A. Transforming growth factor beta 1 induces methylation changes in lung fibroblasts. *PLoS one*. 2019; 14 (10): e0223512.
 22. Takezawa T, Mori Y, Yonaha T, Yoshizato K. Characterization of morphology and cellular metabolism during the spheroid formation by fibroblasts. *Experimental cell research*. 1993; 208 (2): 430–41.
 23. Frandsen SK, Gibot L, Madi M, Gehl J, Rols MP. Calcium electroporation: evidence for differential effects in normal and malignant cell lines, evaluated in a 3D spheroid model. *PLoS One*. 2015; 10 (12): e0144028.
 24. Mittler F, Obeid P, Rulina AV, Haguët V, Gidrol X, Balakirev MY. High-content monitoring of drug effects in a 3D spheroid model. *Frontiers in oncology*. 2017; 7: 293.
 25. Tuan TL, Wu H, Huang EY, Chong SS, Laug W, Messadi D, et al. Increased plasminogen activator inhibitor-1 in keloid fibroblasts may account for their elevated collagen accumulation in fibrin gel cultures. *The American journal of pathology*. 2003; 162 (5): 1579–89.

CLINICAL SIGNIFICANCE OF THE MUSCULUS GLUTEUS MINIMUS IN TOTAL HIP ARTHROPLASTY

Yegiazaryan KA¹, Sirotin IV¹✉, Chizhikova IO², Lazishvili GD¹, Ratiev AP¹, But-Gusaim AB¹¹ Pirogov Russian National Research Medical University, Moscow, Russia² Bureau of Forensic Medical Expertise, Moscow Department of Health, Moscow, Russia

Dislocation of the acetabular component is one of the most frequent complications of total hip arthroplasty. It is commonly attributed to implant malpositioning. However, not all dislocations can be explained by this hypothesis. The aim of our study was to elucidate the role of intraoperative injury to hip abductors (*m. gluteus minimus*) in the first place, since it is reportedly an important hip stabilizer in the development of postoperative hip dislocation. The experiment was conducted in 4 male and 3 female cadavers. A total of 12 THA were performed. The Hardinge and Watson-Jones approaches were used in equal proportion. On plain radiography, acetabular inclination was 40–47°, anteversion was 10–22°; technically and biomechanically, these values were within the normal range and did not depend on the type of surgical approach (for inclination, $p = 0.94$; for anteversion, $p = 0.63$), ruling out implant malpositioning as a risk factor for hip dislocation. Nevertheless, implant stability was significantly disrupted following transection of the anterior or posterior fascicle of *m. gluteus minimus*, leading to the dislocation of the acetabular component in standard rotation and flexion tests. Thus, our study shows the significant role of *m. gluteus minimus* in stabilizing the hip joint. Preservation or adequate repair of this muscle during surgery will reduce the risk of dislocation and help to restore the anatomy and biomechanics of the operated joint.

Keywords: hip dislocation after arthroplasty, *m. gluteus minimus*, hip abductor, hip arthroplasty, hip approach

Author contribution: Yegiazaryan KA supervised the study, analyzed the literature and contributed to writing the manuscript; Sirotin IV, Chizhikova IO analyzed the literature, conducted the experimental part of the study and contributed to writing the manuscript; Lazishvili GD, Ratiev AP, But-Gusaim AB analyzed the literature and contributed to writing the manuscript.

Compliance with ethical standards: the study followed the principles of the Declaration of Helsinki by the World Medical Association.

✉ **Correspondence should be addressed:** Ivan V. Sirotin
Ostrovityanova, 1, 117997, Moscow; ivsir@mail.ru

Received: 04.09.2020 **Accepted:** 18.09.2020 **Published online:** 04.10.2020

DOI: 10.24075/brsmu.2020.058

КЛИНИЧЕСКОЕ ЗНАЧЕНИЕ МАЛОЙ ЯГОДИЧНОЙ МЫШЦЫ ПРИ ЭНДОПРОТЕЗИРОВАНИИ ТАЗОБЕДРЕННОГО СУСТАВА

К. А. Егизарян¹, И. В. Сиротин¹✉, И. О. Чижикова², Г. Д. Лазишвили¹, А. П. Ратьев¹, А. Б. Бут-Гусаим¹¹ Российский национальный исследовательский медицинский университет имени Н. И. Пирогова, Москва, Россия² Бюро судебно-медицинской экспертизы Департамента здравоохранения города Москвы, Москва, Россия

Возникновение вывихов бедренного компонента эндопротеза — одно из частых осложнений эндопротезирования тазобедренного сустава. Наиболее популярным объяснением возникновения данного осложнения является мальпозиция компонентов эндопротеза. Однако не все вывихи удается объяснить исходя из данной гипотезы. Целью работы было уточнить значение в генезе данного осложнения повреждения мышц абдукторов бедра и в первую очередь *m. gluteus minimus*, описываемой в ряде источников как важный стабилизатор тазобедренного сустава. Для изучения данного тезиса был поставлен эксперимент с использованием четырех мужских и трех женских биоманекенов. Было произведено 12 установок эндопротеза тазобедренного сустава. В равных долях применяли доступы по Hardinge и Watson-Jones. По данным рентгенконтроля, наклон вертлужного компонента составил 40–47°, антеверсия — 10–22°, что технически и биомеханически соответствует допустимым значениям, зависимость данных показателей от типа доступа статистически не значима (для наклона вертлужного компонента $p = 0,94$; для антеверсии вертлужного компонента $p = 0,63$), что исключало мальпозицию компонентов как фактор риска вывиха. Тем не менее при пересечении переднего или заднего пучка *m. gluteus minimus* стабильность эндопротеза существенно нарушалась, что приводило к вывиху бедренного компонента при выполнении стандартных тестов ротации и сгибания. Таким образом, показана значимость *m. gluteus minimus* в стабилизации тазобедренного сустава. Сохранение или тщательное восстановление ее структуры в ходе выполнения операции позволит не только провести профилактику возникновения вывиха, но и восстановить более правильную анатомию и биомеханику оперированного сустава.

Ключевые слова: вывих эндопротеза тазобедренного сустава, малая ягодичная мышца, абдукторы бедра, артропластика тазобедренного сустава, доступ к тазобедренному суставу

Вклад авторов: К. А. Егизарян — общее руководство работой, анализ литературы, написание статьи; И. В. Сиротин, И. О. Чижикова — анализ литературы, проведение экспериментального исследования, написание статьи; Г. Д. Лазишвили, А. П. Ратьев, А. Б. Бут-Гусаим — анализ литературы, написание статьи.

Соблюдение этических стандартов: исследование проведено с соблюдением этических принципов медицинских исследований Хельсинской декларации Всемирной медицинской ассоциации.

✉ **Для корреспонденции:** Иван Владимирович Сиротин
ул. Островитянова, д. 1, г. Москва, 117997; ivsir@mail.ru

Статья получена: 04.09.2020 **Статья принята к печати:** 18.09.2020 **Опубликована онлайн:** 04.10.2020

DOI: 10.24075/vrgmu.2020.058

Total hip arthroplasty (THA) is a surgical treatment of choice for a damaged hip joint. According to most estimates, its success rate ranges from 92 to 95%. However, low as it is, the rate of THA complications remains stable over the years, showing no significant improvement [1].

Postoperative dislocation of the acetabular hip component is a serious complication of THA and is largely

associated with the use of a posterior approach to the hip. However, dislocation is also reported for patients who had the lateral or anterolateral Hardinge or Watson-Jones approach traditionally viewed as safer. In some cases, the underlying cause of dislocation is implant malposition and a movement beyond the recommended range that forces the joint out of the socket [2–4].

Deficiency of hip abductors, including *m. gluteus medius* and *m. gluteus minimus*, is another factor predisposing to dislocation after THA. Abductor deficiency can be very pronounced following a fracture of trochanter major, the main attachment site for these muscles. In some cases, the true cause of postoperative dislocation remains unknown. Some authors point out that apart from abduction itself, hip abductors (*m. gluteus minimus* in particular) are responsible for stabilizing or “centering” the femoral head in the socket and rotating the hip externally and internally [5, 6]. *M. gluteus medius* and *m. gluteus minimus* are broad, thick, short muscles with a broad tendon that originate proximally on the outer surface of the ilium and insert distally into trochanter major et fossa piriformis. Some studies of human anatomy and abductor tendinopathy refer to this group of muscles as the hip rotator cuff, similar to the rotator cuff of the shoulder joint.

Magnetic resonance imaging made it possible to more precisely identify the sites of *m. gluteus medius* and *m. gluteus minimus* insertion on the greater trochanter and to describe their functions. *M. gluteus medius* attaches to the posterosuperior and lateral facets of the greater trochanter; 3 fascicles of this muscle stabilize the pelvis during gait initiation and are also involved in pelvic rotation. The fibers of *m. gluteus minimus* course toward the internal surface of the anterosuperior facet of the greater trochanter; its fibers are oriented horizontally and play the role of key stabilizers in the mid and terminal gait phases [7].

In-depth studies of muscle anatomy provide an insight into how functions are distributed among separate bundles of fibers constituting these muscles. The anterior and posterior fascicles can be clearly distinguished in the structure of *m. gluteus medius*; they are responsible for external and internal hip rotation, respectively [8]. Although there is only a limited number of studies addressing the anatomy of *m. gluteus minimus*, some of them report the functional division of its fascicles, similarly to *m. gluteus medius* [8].

Previously, it was hypothesized that *m. gluteus minimus* might promote stabilization of both the native hip joint and the implant [5]. Due to intimate bonding with the fibers of the joint capsule, this muscle might not only “drive” hip movements but also stabilize the joint, similarly to pes anserinus in the knee joint. This hypothesis, however, did not take off.

The aim of this work was to test the hypothesis that *m. gluteus minimus* can play a significant role in hip dislocation following THA.

METHODS

The experiment was conducted in cadavers after the resolution of rigor mortis; the cadavers did not have visible signs of damage to the gluteal and hip regions. For hip replacement, we used instrumentation by DePuy, USA, and a CORAIL-PINNACLE hip construct by the same manufacturer. At our disposal, we had 28-mm trial femoral heads with +1.5 to +12 mm offset. The Hardinge and Watson-Jones approaches to the hip were used in all cases. All surgeries were performed by an experienced surgeon who had done over 500 hip replacements over the past 3 years using these traditional approaches.

For the experiment, 4 male and 3 female cadavers (78–86 years) were selected, comparable in terms of their anthropometric characteristics; THA was performed on 3 male (mean age 82.33 years) and 3 female (mean age 84.33 years) cadavers with the normosthenic body type and no visible damage to the pelvis and lower limbs (see Table).

The remaining cadaver was exploited for primary visualization of *m. gluteus minimus*; THA was not performed on this cadaver.

In total, 12 hip replacements were performed, one on each body side. The Hardinge and Watson-Jones approaches were used in equal proportion. Implant positioning was assessed on plain radiographs using the Lewinnek method [9] (Fig. 1).

Differences in inclination and anteversion of the acetabular hip component between the applied surgical approaches were compared using the Mann–Whitney *U* test. Statistical analysis was carried out using open Python libraries.

RESULTS

Firstly, we indirectly assessed the role of *m. gluteus minimus* in hip rotation. For better muscle visualization, the portion of *m. gluteus medius* overlying *m. gluteus minimus* was removed. The anterior and posterior sections of the muscle belly were clearly distinguishable, meaning that there were 2 fiber bundles sharing a broad tendonous part (Fig. 2).

We found that fibers and tendons constituting the anterior fascicle of *m. gluteus minimus* stretched during external hip rotation, whereas the posterior fascicle stretched on hip flexion and internal rotation, limiting the possible range of motion. This observation inspired a hypothesis that *m. gluteus minimus* might have a significant role in the stabilization of a native hip joint.

Table. Characteristics of surgeries, including age and sex of the cadavers, the operated body side, surgical approaches, acetabular inclination and anteversion

Sex	Age	Side	Access	Acetabular inclination	Acetabular anteversion
f	82	left	Hardinge	40	12
f	82	right	Watson-Jones	42	18
f	84	left	Watson-Jones	45	20
f	84	right	Hardinge	46	22
f	87	left	Hardinge	47	15
f	87	right	Watson-Jones	45	17
m	78	left	Watson-Jones	42	20
m	78	right	Hardinge	43	15
m	83	left	Hardinge	41	21
m	83	right	Watson-Jones	45	20
m	86	left	Watson-Jones	46	12
m	86	right	Hardinge	45	10

Note: m — male; f — female.

In the second step, we performed THA using the traditional Hardinge and Watson-Jones approaches. After the implant was installed, a section of *m. gluteus medius* just above *m. gluteus minimus* was removed for better visualization. Both surgical approaches resulted in the injury to the anterior portion of *m. gluteus minimus*; the damage was slightly more pronounced for the Hardinge approach. The joint capsule was not dissected but closed with sutures. Measured on plain radiographs, acetabular inclination was 40–47°, anteversion was 10–22°; technically and biomechanically, these values were within the normal range. Then, the hip was rotated inward and outward with the maximum amplitude possible for the cadaver under examination and flexed to 90°. These movements did not provoke dislocation of the acetabular component. However, with the Hardinge approach, a femoral head with a bigger offset was used to ensure joint stability. Traction of the acetabular component with a surgical instrument along the axis of the prosthetic neck (after the joint capsule was dissected) did not cause the escape of the prosthetic femoral head from the cup.

After the implant was installed and the joint capsule was repaired, the anterior fascicle of *m. gluteus minimus* was transversely transected and the posterior fascicle was left intact. Then, the hip was rotated outward with the maximum possible amplitude. This resulted in the dislocation of the initially stable implant but did not damage the joint capsule. Attempts to compensate for the instability of the implant by using femoral heads with more offset were unsuccessful. Traction of the acetabular component with a surgical instrument along the axis of the prosthetic neck (after the joint capsule was dissected) caused the escape of the prosthetic femoral head from the cup during hip flexion.

In the fourth step, we transversely transected the posterior fascicle of *m. gluteus minimus*, leaving its anterior fascicle intact. Then, the hip was rotated inward and flexed or just flexed without rotation, using the maximum possible amplitude. The combination of hip flexion and inward rotation resulted in the dislocation of the initially stable implant but did not damage the joint capsule. Attempts to compensate for the instability of the implant by using femoral heads with more offset were unsuccessful. Traction of the acetabular component with a surgical instrument along the axis of the prosthetic neck (with the opened joint capsule) caused the escape of the prosthetic femoral head during hip flexion.

On plain radiography, inclination of the acetabular component was 40–47°, anteversion was 10–22°; technically and biomechanically, these values were within the normal range (see Table). No statistical differences were detected in mean acetabular inclination and anteversion values for the Watson-Jones and Hardinge approaches (for inclination, $p = 0.94$; for anteversion, $p = 0.63$), suggesting that implant malposition was not the case in our study and could not be a risk factor for postoperative hip dislocation.

DISCUSSION

The modern literature looks at hip abductors from 2 different perspectives. Firstly, degenerative or traumatic injury of hip abductors causes pronounced pain and gait disturbance [10]. Secondly, abductor rupture (due to trochanter major fracture) or weakness (caused by an injury to nervus gluteus superior) precipitates the instability of the artificial joint [11].

It was shown that the physiological cross-sectional area of *m. gluteus minimus* is smaller than that of *m. gluteus medius*, suggesting that the force of *m. gluteus minimus* contraction is proportionally weaker [12]. Perhaps, the architecture of separate

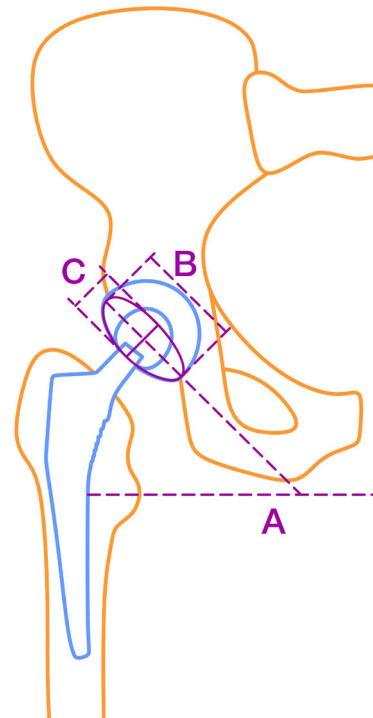


Fig. 1. Measuring acetabular inclination and anteversion (cup inclination is calculated as the angle between the horizontal line **A** and the continuation of the long axis **B** of the ellipsis; anteversion is calculated as $\arcsin(\text{short axis } C / \text{long axis } B)$)

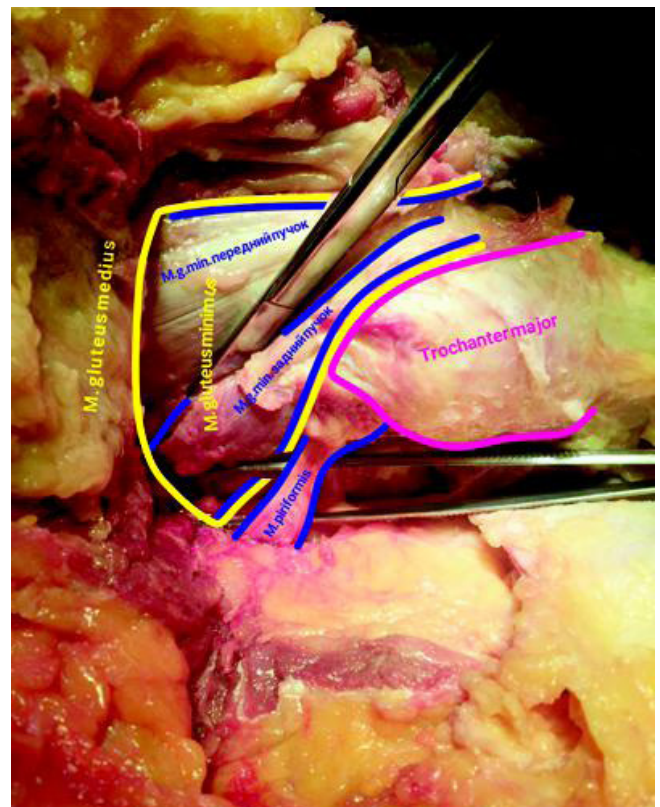


Fig. 2. The region of the greater trochanter featuring the site of *m. gluteus minimus* attachment and parts of external hip rotators (see the article)

bundles of *m. gluteus minimus* determines the stabilizing function of this muscle. In a series of dissections, some of *m. gluteus minimus* fascicles were found to be attached to the joint capsule, but the functional role of such bonding, its prevalence and force are still a matter of debate [6, 13].

Ultrasonography and functional tests conducted *in vivo* revealed that the thickness of hip abductors does not correlate with their strength or function; the authors of the study hypothesized that this was due to the inability of applying the tests to separate muscle bundles *in vivo* [14].

There is a paucity of studies exploring the functions of hip abductors in general and *m. gluteus minimus* in particular. This can be partially explained by the fact that hip abductor pathology unrelated to conditions requiring hip replacement is relatively rare and usually responds well to traditional therapy; in such cases, no detailed investigation of abductor anatomy is needed.

Being an effective orthopedic surgery, THA is not free of complications, although their rate is low. Better understanding of causes underlying THA complications will help to reduce their risks, contribute to the knowledge of biomechanics of both native and artificial hip joints, improve the quality of treatment, and develop effective regimens for such complications.

Our study looked at the possibility of injuring *m. gluteus minimus* during hip replacement with lateral approaches to the hip. Our findings and results of some other studies [15] also

suggest a significant role of intraoperative injury to the posterior fascicle of *m. gluteus minimus* in postoperative complications following the use of posterior approaches to the hip. Although repair of the tendinous section of *m. piriformis* is crucial for maintaining stability of the hip joint in hip replacement with posterior approaches, injury to this region remains a probable cause of posterior acetabular dislocations in patients with repaired *m. piriformis*.

CONCLUSION

We have demonstrated a significant role of *m. gluteus minimus* in stabilizing the hip joint, especially in artificial hips following THA. Preservation or adequate repair of *m. gluteus minimus* when performing surgical access or closing soft tissue is a good prophylaxis for postoperative dislocation and helps to restore the anatomy and biomechanics of the hip joint. Further research is needed to better understand the functions of *m. gluteus minimus* and other muscles and ligaments surrounding the hip joint in the context of their contribution to implant stability and the range of motion, similarly to the knee joint.

References

1. Learmonth ID, Young C, Rorabeck C. The operation of the century: total hip replacement. *Lancet*. 2007; 370: 1508–19.
2. De Martino I, Triantafyllopoulos GK, Sculco PK, Sculco TP. Dual mobility cups in total hip arthroplasty. *World J Orthop*. 2014; 5: 180–7.
3. De Martino I, D'Apolito R, Soranoglou VG, Poultsides LA, Sculco PK, Sculco TP. Dislocation following total hip arthroplasty using dual mobility acetabular components: a systematic review. *Bone Joint J*. 2017 Jan; 99-B (ASuppl1): 18–24.
4. Tsikandylakis G, Kärrholm JN, Hallan G, Furnes O, Eskelinen A, Mäkelä K, Pedersen AB, Overgaard S, Mohaddes M. Is there a reduction in risk of revision when 36-mm heads instead of 32 mm are used in total hip arthroplasty for patients with proximal femur fractures? *Acta Orthop*. 2020 Apr 14: 1–7.
5. Beck M, Sledge JB, Gautier E, Dora CF, Ganz R.J The anatomy and function of the gluteus minimus muscle. *Bone Joint Surg Br*. 2000 Apr; 82 (3): 358–63.
6. Flack NA, Nicholson HD, Woodley SJ. The anatomy of the hip abductor muscles. *Clin Anat*. 2014; 27 (2): 241–53.
7. Pfirrmann CW, Chung CB, Theumann NH, Trudell DJ, Resnick D. Greater Trochanter of the Hip: Attachment of the Abductor Mechanism and a Complex of three bursae — MR Imaging and MR Bursography in Cadavers and MR Imaging in Asymptomatic Volunteers. *Radiology*. 2001; 221 (2): 469–77.
8. Conneely M, O'Sullivan K, Edmondston S. Dissection of gluteus maximus and medius with respect to their suggested roles in pelvic and hip stability: Implications for rehabilitation? *Phys Therapy Sport Conf Proc*. 2006; 7: 176–8.
9. Park YS, Shin WC, Lee SM, et al. The Best Method for Evaluating Anteversion of the Acetabular Component After Total Hip Arthroplasty on Plain Radiographs. *J Orthop Surg Res*. 2018 Apr 2; 13 (1): 66.
10. Gullledge CM, Makhni EC. Open Gluteus Medius and Minimus Repair With Double-Row Technique and Bioinductive Implant Augmentation. *Arthrosc Tech*. 2019 May 17; 8 (6): e585–e589.
11. Kung PL, Ries MD. Effect of Femoral Head Size and Abductors on Dislocation after revision THA. *Clin Orthop Relat Res*. 2007; 465: 170–4.
12. Parvaresh KC, Chang C, Patel A, Lieber RL, Ball ST, Ward SR. Architecture of the Short External Rotator Muscles of the Hip. *BMC Musculoskelet Disord*. 2019; 20 (1): 611.
13. Walters J, Solomons M, Davies J. Gluteus minimus: observations on its insertion. *J Anat*. 2001; 198 (Pt 2): 239–42.
14. Whiler L, Fong M, Kim S, et al. Gluteus Medius and Minimus Muscle Structure, Strength, and Function in Healthy Adults: Brief Report. *Physiother Can*. 2017; 69 (3): 212–16.
15. Whiteside LA, Roy ME. Incidence and Treatment of Abductor Deficiency During Total Hip Arthroplasty Using the Posterior Approach: Repair With Direct Suture Technique and Gluteus Maximus Flap Transfer. *Bone Joint J*. 2019 Jun; 101-B (6_Supple_B): 116–22.

Литература

1. Learmonth ID, Young C, Rorabeck C. The operation of the century: total hip replacement. *Lancet*. 2007; 370: 1508–19.
2. De Martino I, Triantafyllopoulos GK, Sculco PK, Sculco TP. Dual mobility cups in total hip arthroplasty. *World J Orthop*. 2014; 5: 180–7.
3. De Martino I, D'Apolito R, Soranoglou VG, Poultsides LA, Sculco PK, Sculco TP. Dislocation following total hip arthroplasty using dual mobility acetabular components: a systematic review. *Bone Joint J*. 2017 Jan; 99-B (ASuppl1): 18–24.
4. Tsikandylakis G, Kärrholm JN, Hallan G, Furnes O, Eskelinen A, Mäkelä K, Pedersen AB, Overgaard S, Mohaddes M. Is there a reduction in risk of revision when 36-mm heads instead of 32 mm are used in total hip arthroplasty for patients with proximal femur fractures? *Acta Orthop*. 2020 Apr 14: 1–7.
5. Beck M, Sledge JB, Gautier E, Dora CF, Ganz R.J The anatomy and function of the gluteus minimus muscle. *Bone Joint Surg Br*. 2000 Apr; 82 (3): 358–63.
6. Flack NA, Nicholson HD, Woodley SJ. The anatomy of the hip abductor muscles. *Clin Anat*. 2014; 27 (2): 241–53.
7. Pfirrmann CW, Chung CB, Theumann NH, Trudell DJ, Resnick D. Greater Trochanter of the Hip: Attachment of the Abductor Mechanism and a Complex of three bursae — MR Imaging and MR Bursography in Cadavers and MR Imaging in Asymptomatic Volunteers. *Radiology*. 2001; 221 (2): 469–77.
8. Conneely M, O'Sullivan K, Edmondston S. Dissection of gluteus maximus and medius with respect to their suggested roles in pelvic and hip stability: Implications for rehabilitation? *Phys Therapy Sport Conf Proc*. 2006; 7: 176–8.
9. Park YS, Shin WC, Lee SM, et al. The Best Method for Evaluating

- Anteversion of the Acetabular Component After Total Hip Arthroplasty on Plain Radiographs. *J Orthop Surg Res.* 2018 Apr 2; 13 (1): 66.
10. Gullidge CM, Makhni EC. Open Gluteus Medius and Minimus Repair With Double-Row Technique and Bioinductive Implant Augmentation. *Arthrosc Tech.* 2019 May 17; 8 (6): e585–e589.
 11. Kung PL, Ries MD. Effect of Femoral Head Size and Abductors on Dislocation after revision THA. *Clin Orthop Relat Res.* 2007; 465: 170–4.
 12. Parvaresh KC, Chang C, Patel A, Lieber RL, Ball ST, Ward SR. Architecture of the Short External Rotator Muscles of the Hip. *BMC Musculoskelet Disord.* 2019; 20 (1): 611.
 13. Walters J, Solomons M, Davies J. Gluteus minimus: observations on its insertion. *J Anat.* 2001; 198 (Pt 2): 239–42.
 14. Whiler L, Fong M, Kim S, et al. Gluteus Medius and Minimus Muscle Structure, Strength, and Function in Healthy Adults: Brief Report. *Physiother Can.* 2017; 69 (3): 212–16.
 15. Whiteside LA, Roy ME. Incidence and Treatment of Abductor Deficiency During Total Hip Arthroplasty Using the Posterior Approach: Repair With Direct Suture Technique and Gluteus Maximus Flap Transfer. *Bone Joint J.* 2019 Jun; 101-B (6_Supple_B): 116–22.

RETINAL LASER PHOTOCOAGULATION IN MANAGEMENT OF EALES' DISEASE

Takhchidi KhP, Takhchidi EK, Kasminina TA, Tebina EP ✉, Mokrunova MV

Pirogov Russian National Medical Research University, Moscow, Russia

Eales' disease is an idiopathic occlusive inflammatory vasculopathy resulting in peripheral retinal ischemia, neovascularization, recurrent hemophthalmos, and proliferative tissue formation. It is often complicated by tractional retinal detachment, secondary glaucoma, and central retinal vein occlusion. The management of patients with Eales' disease includes mainly glucocorticosteroid therapy, the use of angiogenesis inhibitors, vitreoretinal surgery and laser photocoagulation. The clinical case reported demonstrates the potential of retinal laser photocoagulation for treatment of the Eales' disease in the ischemic and proliferative stages. The results of retinal laser photocoagulation used as monotherapy demonstrate the clinical and functional indices improvement: enhanced visual acuity, stabilized central retinal sensitivity value, restored clarity to the ocular media, regression of neovascularization and macular edema in the patient's eye being in the proliferative (3b) stage, and the process stabilization in the eye being in the ischemic (2a) stage of the disease.

Keywords: Eales' disease, laser photocoagulation, optical coherence tomography, fluorescein angiography

Author contribution: Takhchidi KhP — study concept and design, manuscript editing; Takhchidi EK — literature analysis; Tebina EP — manuscript writing; Kasminina TA — laser treatment; Mokrunova MV — data acquisition and processing.

Compliance with ethical standards: the patient submitted informed consent to laser treatment and personal data processing.

✉ **Correspondence should be addressed:** Ekaterina P. Tebina
Volokolamskoe shosse, 30, str. 2, Moscow, 123182; ekaterinatebina@mail.ru

Received: 20.09.2020 **Accepted:** 12.10.2020 **Published online:** 23.10.2020

DOI: 10.24075/brsmu.2020.063

ПРИМЕНЕНИЕ ЛАЗЕРНОЙ КООГУЛЯЦИИ СЕТЧАТКИ ПРИ БОЛЕЗНИ ИЛЗА

X. П. Тахчиди, Е. X. Тахчиди, Т. А. Касмынина, Е. П. Тебина ✉, М. В. Мокрунова

Российский национальный исследовательский медицинский университет имени Н. И. Пирогова, Москва, Россия

Болезнь Илза — идиопатическая окклюзионная воспалительная васкулопатия, которая приводит к периферической ишемии сетчатки, неоваскуляризации, рецидивирующим гемофтальмам, развитию пролиферативной ткани и нередко осложняется тракционной отслойкой сетчатки, вторичной глаукомой, окклюзией центральной вены сетчатки. В основном при ведении пациентов с данной патологией используют глюкокортикостероидную терапию, ингибиторы ангиогенеза, витреоретинальную хирургию и лазерную коагуляцию. Представленный клинический случай демонстрирует возможность использования лазерной коагуляции сетчатки при лечении болезни Илза на ишемической и пролиферативной стадиях. Полученные результаты применения лазерной коагуляции сетчатки в качестве монотерапии свидетельствуют об улучшении клинико-функциональных показателей: увеличении остроты зрения, стабилизации показателя центральной светочувствительности сетчатки, восстановлении прозрачности оптических сред, регрессе неоваскуляризации и макулярного отека на глазу с пролиферативной стадией (3b), а также стабилизации процесса на глазу в стадии ишемии (2a).

Ключевые слова: болезнь Илза, лазерная коагуляция, оптическая когерентная томография, флюоресцентная ангиография

Вклад авторов: X. П. Тахчиди — концепция и дизайн исследования, редактирование текста; Е. X. Тахчиди — анализ литературных данных; Е. П. Тебина — написание текста; Т. А. Касмынина — лазерное лечение пациента; М. В. Мокрунова — сбор и обработка материала.

Соблюдение этических стандартов: от пациента получено согласие на лазерное лечение и обработку персональных данных.

✉ **Для корреспонденции:** Екатерина Павловна Тебина
Волоколамское шоссе, д. 30, корп. 2, г. Москва, 123182; ekaterinatebina@mail.ru

Статья получена: 20.09.2020 **Статья принята к печати:** 12.10.2020 **Опубликована онлайн:** 23.10.2020

DOI: 10.24075/vrgmu.2020.063

Eales' disease is an idiopathic occlusive inflammatory vasculopathy, which results in peripheral retinal ischemia, neovascularization, recurrent hemophthalmos and proliferative tissue formation [1, 2].

The literature indicates that the disorder is most common in healthy young males in their second decade of life, and in 90% of patients both eyes are affected [3].

The disorder was first described by British ophthalmologist Henry Eales in 1880 [4]. Etiopathogenesis of the Eales' disease is not completely understood. In recent years, as a result of immunological, molecular biological and biochemical studies, the role of human leukocyte antigen, autoimmune mechanisms, *Mycobacterium tuberculosis* and free radicals in the disease pathogenesis has been shown [5, 6]. The natural course of the disease is quite variable, with alternating periods of remission and exacerbation [7, 3].

According to the literary sources, the disorder usually presents with involvement of peripheral retina and is

characterized by a number of manifestations of varying intensity: inflamed veins, ischemia and retinal neovascularization. The listed above manifestations often result in the following complications: recurrent retinal and vitreous hemorrhages, traction/rhegmatogenous retinal detachment, rubeosis iridis and secondary glaucoma [8]. In some cases, central retina is affected, which results in macular edema [9].

The "gold standard" in the Eales' disease detection is fluorescein angiography (FA) allowing one to assess blood flow and damage to retinal blood vessels: dye transudation, retinal vascular tortuosity and telangiectasia, vascular shunt, venous stasis, ischemia, retinal neovascularization [10–12].

In 2007, the new Eales' disease classification was proposed based on the ophthalmoscopy and FA data [13].

Stage 1

(1a) Periphlebitis of small caliber vessels

(1b) Periphlebitis of large caliber vessels with superficial retinal hemorrhages

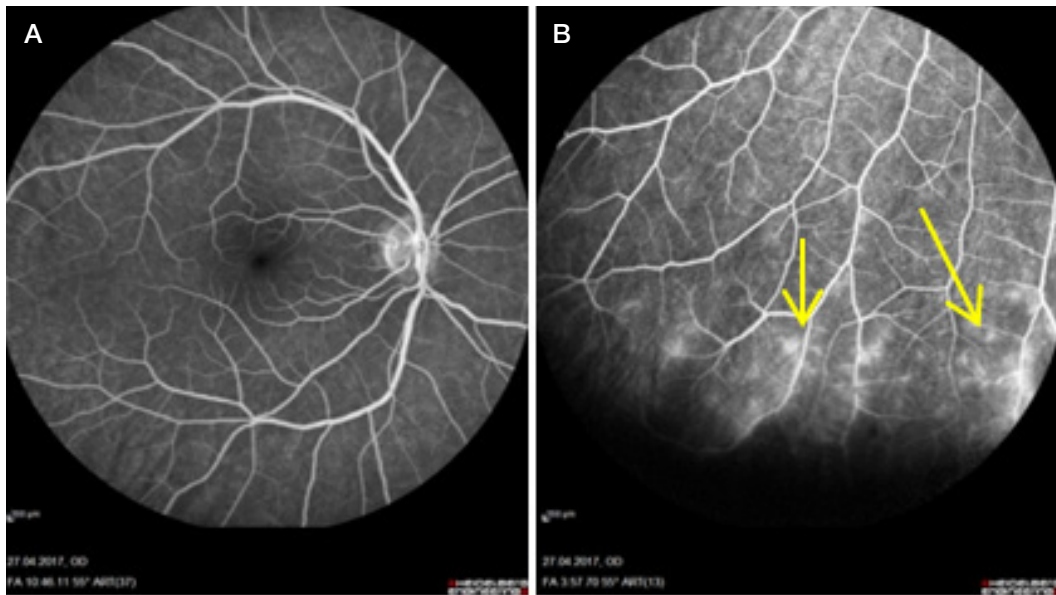


Fig. 1. FA, right eye. **A.** Optic disc with sharp margins, vascular calibers not altered, AV ratio 2/3, normal macular area. **B.** Dye extravasation and aneurysms are visualized in the area of altered blood vessels in the peripheral fundus (yellow arrow)

Stage 2

(2a): Capillary nonperfusion

(2b): Neovascularization of the disc and/or retina

Stage 3

(3a): Fibrovascular proliferation

(3b): Hemophthalmos

Stage 4

(4a): Traction and/or rhegmatogenous retinal detachment

(4b): Rubeosis iridis, neovascular glaucoma, complicated cataract, optic atrophy

The current diagnosis procedures together with wide range of treatment options significantly improve the Eales' disease prognosis and outcome [3, 7]. The management tactics depends on the stage of the disease [14–20] and includes the following: taking glucocorticosteroids (systemic and/or periorbital) in the stage of inflammation [7]; intravitreal injection of angiogenesis inhibitor [16]; vitreoretinal surgery (in patients with recurrent hemophthalmos, vitreoretinal traction and/or retinal detachment) [21].

Laser photocoagulation is one of the first-line therapeutic options for Eales' disease in the ischemic and proliferative stages [3, 15, 16, 19–22]. According to the foreign authors,

regression of retinal neovascularization and vitreoretinal traction after laser photocoagulation is detected in 80–90% of patients [16, 23–25]. Moreover, bilateral photocoagulation in the ischemic areas of asymptomatic eyes is an effective measure for prevention of the Eales' disease complications [16, 26]. In this case study we attempted to assess the effectiveness and safety of retinal laser photocoagulation for management of Eales' disease in the ischemic (2a) and proliferative (3b) stages.

Clinical case

Patient A., aged 20, complaining of floaters and decreased visual acuity in his left eye contacted the Scientific Research Center for Ophthalmology of Pirogov Russian National Medical Research University. It was also known from his case history that the described manifestations emerged spontaneously and persisted for six months. The patient sought medical assistance from ophthalmologist at his place of residence, and was diagnosed with uveitis of unknown etiology in both eyes. He received conservative management, which included administration of glucocorticosteroids. No response to treatment was observed.

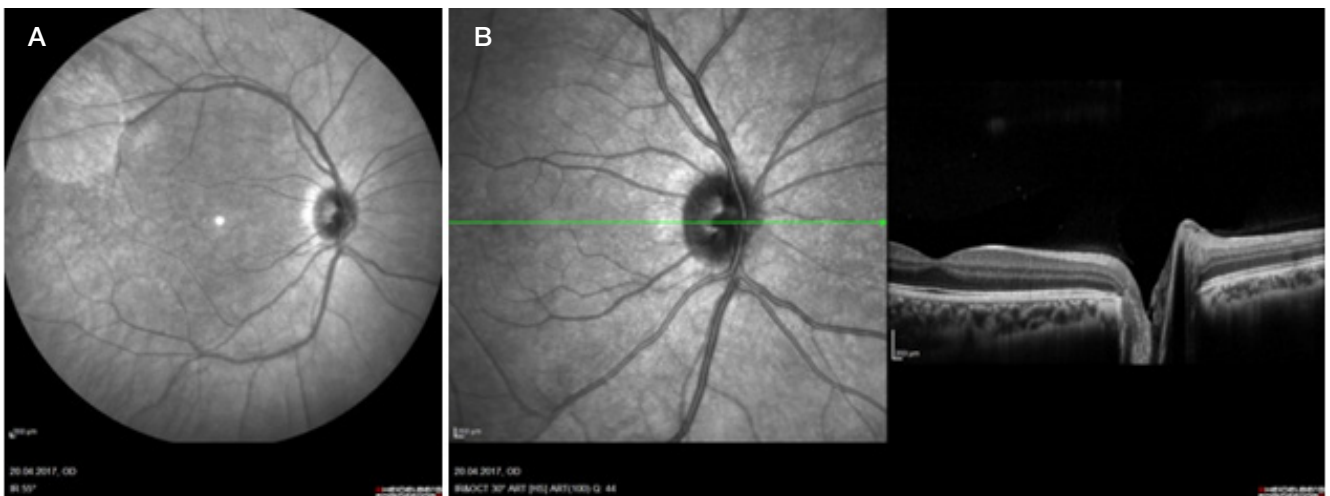


Fig. 2. **A.** IR reflectance image of fundus, right eye. Optic disc with sharp margins, normal macular area. **B.** OCT scan of the right eye. Cross-section image with normal optic disc and macular area

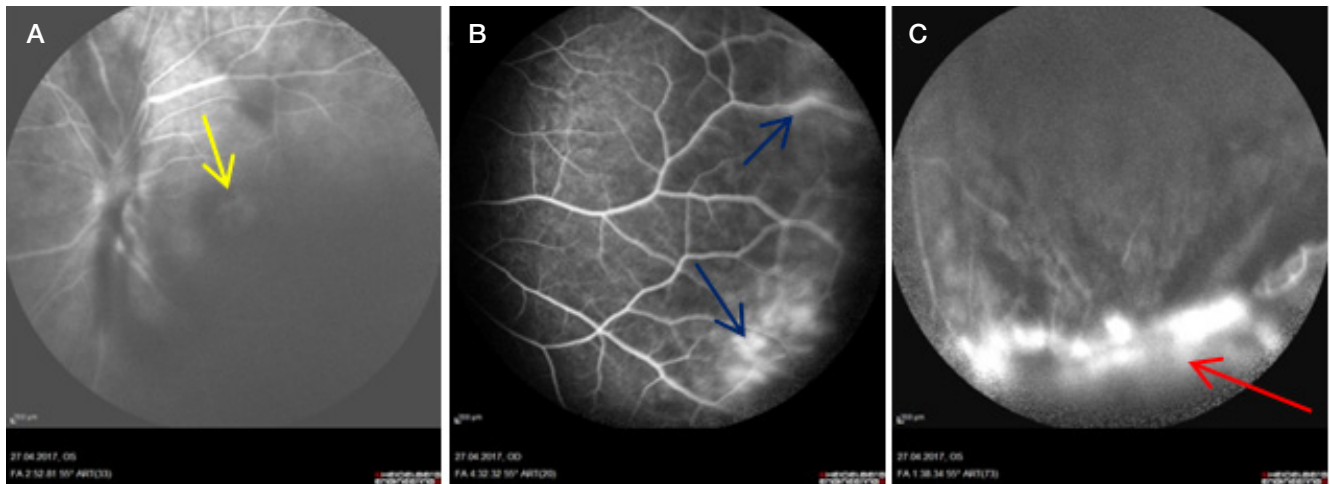


Fig. 3. FA, left eye. **A.** Optic disc with blurry margins; altered vascular caliber, petaloid (flower-like) pattern of hyperfluorescence is visible through hemophthalmos in central retina (*yellow arrow*). **B.** Periphlebitis with dye extravasation across the visible periphery (*blue arrows*). **C.** Protruding proliferative lesion with blurry margins visualized as a dense hyperfluorescent focus in the clock hour sector 5 (*red arrow*); hypofluorescent areas corresponding to hemorrhagic foci

The patient underwent complex assessment by the following methods: visometry aimed at determining the best corrected visual acuity (BCVA), ophthalmoscopy using the MaxField 78D lens (Ocular Inc.; USA), fluorescein angiography (FA) and spectral domain optical coherence tomography (SDOCT) imaging using the Spectralis HRA+OCT, OCT2 platform with a scanning speed of 85,000 Hz (Heidelberg Engineering; Germany), computer perimetry using the Humphrey Field Analyzer II (Carl Zeiss Meditec Inc.; USA) and the 30-2 SITA-Standard test, computer microperimetry and assessment of central light sensitivity using the MAIA system (CenterVue Inc.; Italy). The patient had normal chest x-ray and negative Mantoux test. Serology testing revealed no changes. The patient did not associate the onset of the disease with anything, and he had no hereditary taint. Laser photocoagulation was performed using the VISULAS Trion laser workstation working in the 532 nm mode (Carl Zeiss; Germany).

At initial examination, the BCVA in the right eye (OD) was 1.0, and in the left eye (OS) it was 0.1. Biomicroscopy OU revealed no pathological changes in the anterior segment of both eyes.

Ophthalmoscopy OD revealed pale-pink optic disc with sharp margins, normal macular reflex. Pathological reflex was

detected in the paravasal area, the artery to vein (A/V) ratio was 2/3. Aneurysmal dilations and ischemic lesions were observed in peripheral retina. The venous phase FA detected contrast media extravasation and ischemic lesions in the area of altered vasculature involving the full circumference of the peripheral retina (Fig. 1). SDOCT revealed normal macular profile, structured retinal layers, and retinal thickness of 310 μm (Fig. 2).

Visualization during ophthalmoscopic examination OS was hampered by partial hemophthalmos. The optic disc was hyperemic, blurry, and protruded into the vitreous chamber. There was a fibrous cord over the optic disc extending to the inferior outer quadrant of the retina, the macular area was blurry. The veins were dilated and tortuous. In peripheral retina, there was a protruding lesion with blurry margins, retinal and preretinal hemorrhages in the clock hour sector 5. The venous phase FA detected the hyperfluorescent optic disc. The petaloid (flower-like) pattern of hyperfluorescence (macular edema) was observed in the central retina. Hyperfluorescent focus with hypofluorescent areas was detected on the periphery in the lower sector (Fig. 3). SDOCT revealed the retinal thickness increase up to 600 μm in the macular area, and cystic cavities in the outer and inner nuclear layers (Fig. 4).

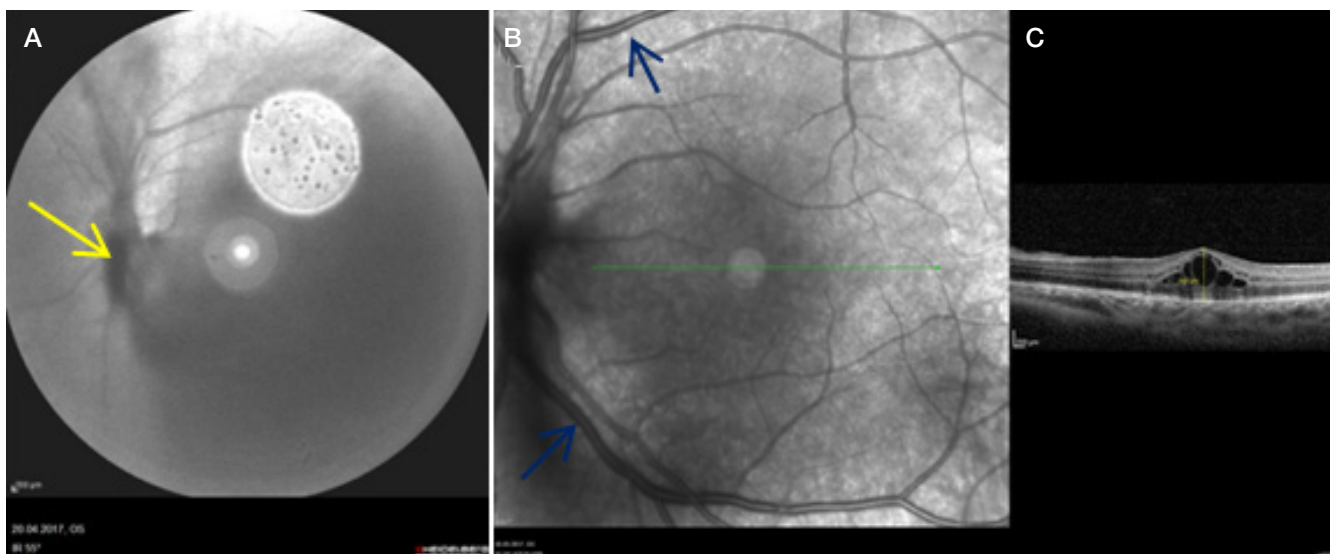


Fig. 4. **A.** IR reflectance image of fundus, left eye: partial hemophthalmos, fibrous cord over the optic disc extending to the inferior outer quadrant of the retina (*yellow arrow*). **B.** IR reflectance image of fundus, left eye: retinal veins dilated and tortuous (*blue arrows*). **C.** Macula OCT scan, left eye: cystoid edema 600 μm



Fig. 5. Macula OCT scan, right eye: normal macular profile, structured retinal layers; no signs of clinical worsening have been revealed within the one month follow-up period

Taking into account the complaints, medical history and complex ophthalmological assessment data, the patient was diagnosed with Eales' disease, stage 2a (ischemic areas detected by FA), OD, and stage 3b (proliferation and hemophthalmos), OS.

We agreed to perform laser photocoagulation. The extent of coagulation was determined by the amount of damage to retina. In OD (stage 2a) the extensive laser photocoagulation of the peripheral retina was performed (single session), in OS (stage 3b) the panretinal photocoagulation (four sessions at monthly intervals) was carried out. The following energy parameters were used in OD: the power was 100 mW, the exposure time was 0.1 s, the spot size was 200 μm , the distance between the spots was 300 μm , and the total number of burns was 500. The following energy parameters were used in OS: the power was 100–120 mW, the exposure time was 0.1 s, the spot size was 200 μm , the distance between the spots was 300 μm , and the total number of burns was 3,000. The following energy

parameters were used for central retina in OS: the power was 50–100 mW, the exposure time was 0.05–0.1 s, the spot size was 100 μm , and the distance between the spots was 150 μm .

After a month of treatment BCVA OD was 1.0, and BCVA OS had increased to 0.7. Ophthalmoscopy OD revealed pale-pink optic disc with sharp margins. The retinal A/V ratio was 2/3. The macular anatomy was intact. Pigmented coagula were observed across the peripheral retina, aneurysms and ischemic lesions were sealed (Fig. 5). Examination OS revealed declined hemophthalmos; the optic disc was pale-pink with sharp margins; the fibrous cord became smaller. The A/V ratio was 2/3. Partial regression of macular edema and lightly pigmented coagula were detected in the central retina (except the avascular zone). Pigmented coagula were revealed in the peripheral retina, the protruding lesion was sealed (Fig. 6).

After two years BCVA OU was 1.0. Biomicroscopy OU revealed no pathological changes in the anterior segment, the ocular media were clear.

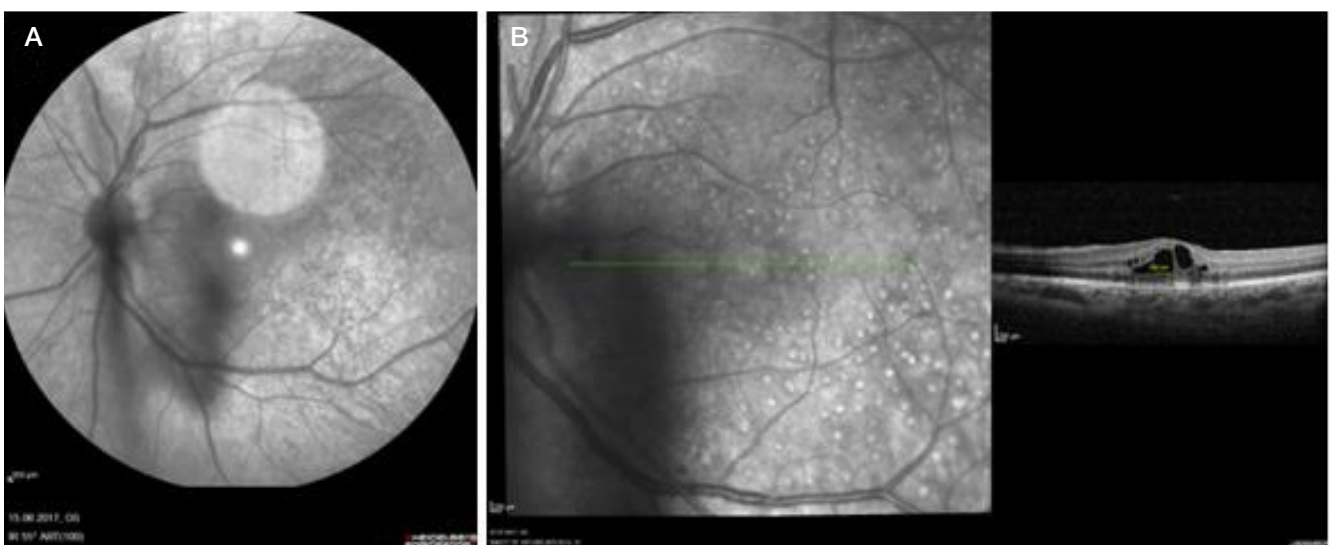


Fig. 6. A. IR reflectance image of fundus, left eye: declined hemophthalmos detected during a one month follow-up visit. **B.** Macula OCT scan, left eye: macular edema reduced from 600 to 500 μm



Fig. 7. Macula OCT scan, right eye: normal macular profile, structured retinal layers; no signs of clinical worsening have been revealed during the 2-year follow-up period

SDOCT detected no signs of clinical worsening in OD (Fig. 7). Ophthalmoscopy revealed pigmented coagula with sharp margins in the peripheral retina, no new lesions were observed. The central retinal sensitivity was 25.7 dB.

Ophthalmoscopy OS revealed pale-pink optic disc with sharp margins, the fibrous cord over the optic disc became smaller. The retinal A/V ratio was 2/3. There were lightly pigmented coagula in the macular area (except the avascular zone). SDOCT detected restored macular profile, and regression of edema (Fig. 8). The fibrotic neovascularization focus with sharp margins was observed in the peripheral retina (Fig. 9). Pigmented coagula were detected in the paravascular area and across the peripheral retina. The central retinal sensitivity value was 25.4 dB.

Computer perimetry OU revealed no visual field deficits.

Discussion

Successful implementation of laser photocoagulation as monotherapy for patients not responsive to glucocorticosteroids

was reported by many foreign [14, 27] and national authors [28, 29]. However, the energy parameters of laser treatment play a vital part in the prognosis of the disease. The use of “rigid” retinal laser photocoagulation may result in complications, such as exudative retinal detachment, iatrogenic choroidal neovascularization, cystoid macular edema, epiretinal fibrosis, visual field deficits, deterioration in color vision and decline in contrast sensitivity [30–32]. According to literary sources, the most commonly used spot size is 400–500 μm, and the proposed pulse duration is 0.15–0.2 s with an interpulse interval of 0.15–0.3 s [3]. Similar energy parameters have been used in other studies: spot size of 400 μm, pulse duration of 0.15 s, and the individually adopted average power value of 160–200 mW [28, 29].

In this study, in contrast to the international experience, we performed laser photocoagulation using the smaller spot size (200 μm), lower power (100–120 mW) and exposure time of 0.1 s in order to improve the clinical and functional treatment results in patient with Eales’ disease. The retinal laser photocoagulation safety in patient with stage 2a (ischemic) and

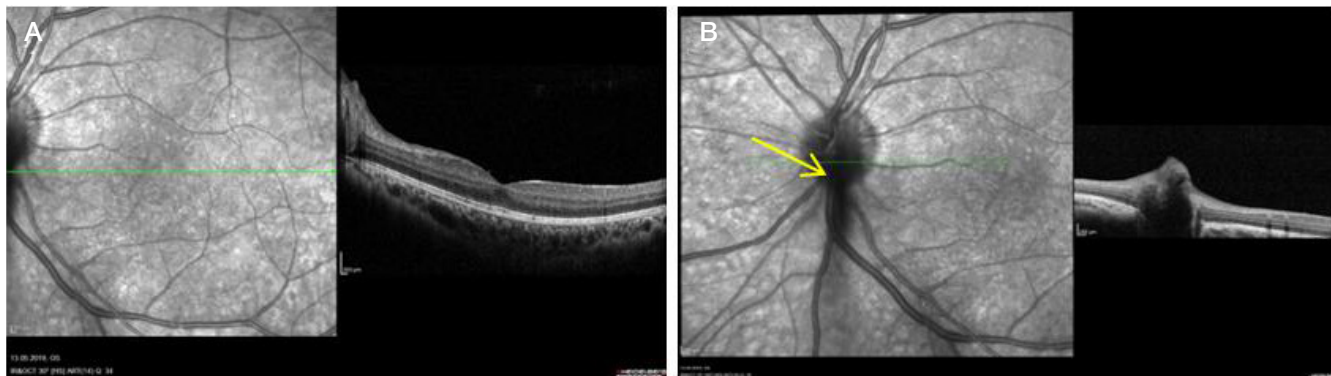


Fig. 8. A. Macula OCT scan, left eye: regression of cystoid macular edema, restored anatomic structure of retinal layers. **B.** Optic disc OCT, left eye: persisting fibrous cord over the optic disc (yellow arrow)

3b (proliferative) Eales' disease and preserved retinal function were confirmed by advanced diagnosis methods: computer perimetry (no visual field deficits), computer microperimetry (preserved central retinal sensitivity), and optical coherence tomography imaging (regression of cystoid macular edema).

The proposed energy parameters made it possible to obtain good clinical and functional results within the long-term postoperative period, including the improved BCVA, stabilized central retinal sensitivity value, restored clarity to the ocular media, regression of neovascularization and macular edema in the eye being in the proliferative (3b) stage, and the process stabilization in the eye being in the ischemic (2a) stage of the disease.

CONCLUSION

The results obtained suggest that the use of retinal laser photocoagulation as monotherapy for patients with Eales' disease in the ischemic (2a) and proliferative (3b) stages contributes to the improvement of clinical and functional treatment results, and the late fate of laser treatment shows long-term remission.



Fig. 9. IR — reflectance image of fundus, left eye: fibrotic neovascularization focus with sharp margins visualized in the clock hour sector 5 of peripheral retina (yellow arrow)

References

1. Therese KL, Deepa P, Therese J, Bagyalakshmi R, Biswas J, Madhavan HN. Association of mycobacteria with Eales' disease. *Indian J Med Res.* 2007; 126: 56–62.
2. Yannuzzi LA. The Retinal Atlas. Retinal Vascular Diseases, Eales' Disease. Elsevier. 2010: 433–8.
3. Das T, Pathengay A, Hussain N, Biswas J. Eales' disease: diagnosis and management. *Eye.* 2010; 24 (3): 472–82.
4. Eales H. Retinal haemorrhages associated with epistaxis and constipation. *Brim Med.* 1880; 9: 262.
5. Madhavan HN, Therese KL, Doraiswamy K. Further investigations on the association of Mycobacterium tuberculosis with Eales' disease. *Indian J Ophthalmol.* 2002; 50: 35–39.
6. Patwardhan SD, Azad E, Shah BM, Sharma Y. Role of intravitreal bevacizumab in Eales disease with dense vitreous haemorrhage: a prospective randomized control study. *Retina.* 2011; 31 (5): 866–70.
7. Biswas J, K R R, Pal B, Gondhale HP, Kharel Sitaula R. Long-Term Outcomes of a Large Cohort of Patients with Eales' Disease. *Ocul Immunol Inflamm.* 2018; 26 (6): 870–6.
8. Sen A, Paine SK, Chowdhury IH, Mukherjee A, Choudhury S, Mandal LK, Bhattacharya B. Assessment of gelatinase and tumor necrosis factor-alpha level in the vitreous and serum of patients with Eales disease; role of inflammation-mediated angiogenesis in the pathogenesis of Eales disease. *Retina.* 2011; 31 (7): 1412–20.
9. Saxena S, Kumar D. Macular involvement in Eales disease. *Ann Ophthalmol.* 2000; 32 (2): 98–100.
10. Gupta V, Al-Dhibi HA, Arevalo JF. Retinal imaging in uveitis. *Saudi J Ophthalmol.* 2014; 28: 95–103.
11. Kumar V, Chandra P, Kumar A. Ultra-wide field angiography in the management of Eales disease. *Indian J Ophthalmol.* 2016; 64: 504–7.
12. Mwndoza KA, Lauer A. Eales Disease. *American Academy of Ophthalmology.* 2015. Available from: http://eyewiki.org/Eales_Disease.
13. Saxena S, Kumar D. New classification system-based visual outcome in Eales' disease. *Indian J Ophthalmol.* 2007; 55 (4): 267–9.
14. Biswas J, Ravi RK, Naryanasamy A, Kulandai LT, Madhavan HN. Eales' disease — current concepts in diagnosis and management. *J Ophthalmic Inflamm Infect.* 2013; 3: 11.
15. Das TP, Namperumalsamy P. Photocoagulation in Eales' disease. Results of pro-spective randomised clinical study. Presented in XXVI Int Cong Ophthalmol – Singapore, 1990.
16. Ishaq M, Niazi MK. Usefulness of laser photocoagulation in managing asymptomatic eyes of Eales disease. *J Ayub Med Coll Abbottabad.* 2002; 14 (4): 22–25.
17. Ishaq M, Feroze AH, Shahid M, Baig MA, Ameen SS, Feroze SH, Chishti RA. Intravitreal steroids may facilitate treatment of Eales' disease (idiopathic retinal vasculitis): an interventional case series. *Eye (Lond).* 2007; 21: 1403–5.
18. Kumar A, Sinha S. Rapid regression of disc and retinal neovascularization in a case of Eales disease after intravitreal bevacizumab. *Can J Ophthalmol.* 2007; 42 (2): 335–6.
19. Magargal LE, Walsh AW, Magargal HO, et al. Treatment of Eales' disease with scatter laser photocoagulation. *Ann Ophthalmol.* 1989; 21: 300–2.
20. Talat L, Lightman S, Tomkins-netzer O. Ischemic retinal vasculitis and its management. *J Ophthalmol.* 2014; 2014: 197675.
21. Li J, Liu SM, Dong WT, Li F, Zhou CH, Xu XD, Zhong J. Outcomes of transconjunctival sutureless 27-gauge vitrectomy for vitreoretinal diseases. *Int J Ophthalmol.* 2018; 11 (3): 408–15.
22. El-Asrar AM, Al-Kharashi SA. Full panretinal photocoagulation and early vitrectomy improve prognosis of retinal vasculitis associated with tuberculo-protein hypersensitivity (Eales' disease). *Br J Ophthalmol.* 2002; 86 (11): 1248–51.
23. Dehghan MH, Ahmadi H, Soheilian M, Azarmina M, Mashayekhi A, Naghibozakerin J. Therapeutic effects of laser photocoagulation and/or vitrectomy in Eales' disease. *Eur J Ophthalmol.* 2005; 15 (3): 379–83.
24. Gopal L, Abraham C. Efficacy of photocoagulation in Eales' disease. *Trans Asia-Pacific Acad.* 1985; 10: 689.
25. Nada M, Qanoongo S, Singh SV, Khurana AK. A rare presentation of exudative macroaneurysms in unilateral Eales' disease. *Nepal J Ophthalmol.* 2017; 9 (18): 95–98.
26. Murphy RP, Gieser SC, Fine SL, et al. Retinal and vitreous findings in Eales disease. *Invest Ophthalmol Vis Sci.* 1986; 27: 121.
27. Nicolcescu A, Mocanu C, Dinu L, Olaru A, Ionete M, Stefanescu DA. Unilateral Eales' disease a case report. *Rom J Ophthalmol.* 2017; 61 (2): 144–9.
28. Pedanova EK, Burjakov DA. Jeffektivnost' lazerkoaguljacii pri bolezni Ilza v svete sovremennyh predstavlenij ob jetiopatogeneze zabojevanija. *Sovremennye tehnologii lechenija vitreoretinal'noj patologii — 2013.* 2013: 136. Available from: <https://eyepress.ru/article.aspx?12646>. Russian.

29. Tolstuhina EA, Magaramov DA, Volodin PL, Timohov VL, Fomin AV. Lazer-inducirovannyj regress perifericheskoj retinal'noj neovaskuljarizacii pri bolezni Ilza (klinicheskij sluchaj). *Sovremennye tehnologii v oftal'mologii*. 2019; 1 (26): 381–3. Russian.
30. Mainster MA. Decreasing retinal photocoagulation damage: principles and techniques. *Semin Ophthalmol*. 1999; 14 (4): 200–9.
31. Moutray T, Evans JR, Lois N, Armstrong DJ, Peto T, Azuara-Blanco A. Different lasers and techniques for proliferative diabetic retinopathy. *Cochrane Database Syst Rev*. 2018; 3 (3): CD012314.
32. Reddy SV, Husain D. Panretinal Photocoagulation: A Review of Complications. *Semin Ophthalmol*. 2018; 33 (1): 83–88.

Литература

1. Therese KL, Deepa P, Therese J, Bagyalakshmi R, Biswas J, Madhavan HN. Association of mycobacteria with Eales' disease. *Indian J Med Res*. 2007; 126: 56–62.
2. Yannuzzi LA. *The Retinal Atlas. Retinal Vascular Diseases, Eales' Disease*. Elsevier. 2010: 433–8.
3. Das T, Pathengay A, Hussain N, Biswas J. Eales' disease: diagnosis and management. *Eye*. 2010; 24 (3): 472–82.
4. Eales H. Retinal haemorrhages associated with epistaxis and constipation. *Brim Med*. 1880; 9: 262.
5. Madhavan HN, Therese KL, Doraiswamy K. Further investigations on the association of Mycobacterium tuberculosis with Eales' disease. *Indian J Ophthalmol*. 2002; 50: 35–39.
6. Patwardhan SD, Azad E, Shah BM, Sharma Y. Role of intravitreal bevacizumab in Eales disease with dense vitreous haemorrhage: a prospective randomized control study. *Retina*. 2011; 31 (5): 866–70.
7. Biswas J, K R R, Pal B, Gondhale HP, Kharel Sitaula R. Long-Term Outcomes of a Large Cohort of Patients with Eales' Disease. *Ocul Immunol Inflamm*. 2018; 26 (6): 870–6.
8. Sen A, Paine SK, Chowdhury IH, Mukherjee A, Choudhury S, Mandal LK, Bhattacharya B. Assessment of gelatinase and tumor necrosis factor-alpha level in the vitreous and serum of patients with Eales disease; role of inflammation-mediated angiogenesis in the pathogenesis of Eales disease. *Retina*. 2011; 31 (7): 1412–20.
9. Saxena S, Kumar D. Macular involvement in Eales disease. *Ann Ophthalmol*. 2000; 32 (2): 98–100.
10. Gupta V, Al-Dhibi HA, Arevalo JF. Retinal imaging in uveitis. *Saudi J Ophthalmol*. 2014; 28: 95–103.
11. Kumar V, Chandra P, Kumar A. Ultra-wide field angiography in the management of Eales disease. *Indian J Ophthalmol*. 2016; 64: 504–7.
12. Mwendoza KA, Lauer A. Eales Disease. *American Academy of Ophthalmology*. 2015. Available from: http://eyewiki.org/Eales_Disease.
13. Saxena S, Kumar D. New classification system-based visual outcome in Eales' disease. *Indian J Ophthalmol*. 2007; 55 (4): 267–9.
14. Biswas J, Ravi RK, Naryanasamy A, Kulandai LT, Madhavan HN. Eales' disease — current concepts in diagnosis and management. *J Ophthalmic Inflamm Infect*. 2013; 3: 11.
15. Das TP, Namperumalsamy P. Photocoagulation in Eales' disease. Results of pro-spective randomised clinical study. Presented in XXVI Int Cong Ophthalmol – Singapore, 1990.
16. Ishaq M, Niazi MK. Usefulness of laser photocoagulation in managing asymptomatic eyes of Eales disease. *J Ayub Med Coll Abbottabad*. 2002; 14 (4): 22–25.
17. Ishaq M, Feroze AH, Shahid M, Baig MA, Ameen SS, Feroze SH, Chishti RA. Intravitreal steroids may facilitate treatment of Eales' disease (idiopathic retinal vasculitis): an interventional case series. *Eye (Lond)*. 2007; 21: 1403–5.
18. Kumar A, Sinha S. Rapid regression of disc and retinal neovascularization in a case of Eales disease after intravitreal bevacizumab. *Can J Ophthalmol*. 2007; 42 (2): 335–6.
19. Magargal LE, Walsh AW, Magargal HO, et al. Treatment of Eales' disease with scatter laser photocoagulation. *Ann Ophthalmol*. 1989; 21: 300–2.
20. Talat L, Lightman S, Tomkins-netzer O. Ischemic retinal vasculitis and its management. *J Ophthalmol*. 2014; 2014: 197675.
21. Li J, Liu SM, Dong WT, Li F, Zhou CH, Xu XD, Zhong J. Outcomes of transconjunctival sutureless 27-gauge vitrectomy for vitreoretinal diseases. *Int J Ophthalmol*. 2018; 11 (3): 408–15.
22. El-Asrar AM, Al-Kharashi SA. Full panretinal photocoagulation and early vitrectomy improve prognosis of retinal vasculitis associated with tuberculo-protein hypersensitivity (Eales' disease). *Br J Ophthalmol*. 2002; 86 (11): 1248–51.
23. Dehghan MH, Ahmadieh H, Soheilian M, Azarmina M, Mashayekhi A, Naghibozakerin J. Therapeutic effects of laser photocoagulation and/or vitrectomy in Eales' disease. *Eur J Ophthalmol*. 2005; 15 (3): 379–83.
24. Gopal L, Abraham C. Efficacy of photocoagulation in Eales' disease. *Trans Asia-Pacific Acad*. 1985; 10: 689.
25. Nada M, Qanoongo S, Singh SV, Khurana AK. A rare presentation of exudative macroaneurysms in unilateral Eales' disease. *Nepal J Ophthalmol*. 2017; 9 (18): 95–98.
26. Murphy RP, Gieser SC, Fine SL, et al. Retinal and vitreous findings in Eales disease. *Invest Ophthalmol Vis Sci*. 1986; 27: 121.
27. Nicolcescu A, Mocanu C, Dinu L, Olaru A, Ionete M, Stefanescu DA. Unilateral Eales' disease a case report. *Rom J Ophthalmol*. 2017; 61 (2): 144–9.
28. Педанова Е. К., Буряков Д. А. Эффективность лазеркоагуляции при болезни Илза в свете современных представлений об этиопатогенезе заболевания. *Современные технологии лечения витреоретинальной патологии — 2013*. 2013: 136. Доступно по ссылке: <https://eyeexpress.ru/article.aspx?12646>.
29. Толстухина Е. А., Магарамов Д. А., Володин П. Л., Тимохов В. Л., Фомин А. В. Лазер-индуцированный регресс периферической ретиальной неоваскуляризации при болезни Илза (клинический случай). *Современные технологии в офтальмологии*. 2019; 1 (26): 381–3.
30. Mainster MA. Decreasing retinal photocoagulation damage: principles and techniques. *Semin Ophthalmol*. 1999; 14 (4): 200–9.
31. Moutray T, Evans JR, Lois N, Armstrong DJ, Peto T, Azuara-Blanco A. Different lasers and techniques for proliferative diabetic retinopathy. *Cochrane Database Syst Rev*. 2018; 3 (3): CD012314.
32. Reddy SV, Husain D. Panretinal Photocoagulation: A Review of Complications. *Semin Ophthalmol*. 2018; 33 (1): 83–88.

STAGED APPROACH TO TREATMENT OF COMBINED HAMARTOMA OF THE RETINA AND RETINAL PIGMENT EPITHELIUM

Takhchidi KhP, Takhchidi NKh, Kasminina TA, Tebina EP ✉

Pirogov Russian National Medical Research University, Moscow, Russia

Combined hamartoma of the retina and retinal pigment epithelium (RPE) is a rare congenital benign lesion. It is most often detected in young adults and adolescents. The disorder is mostly asymptomatic, however, in 24% of patients the loss of visual function results from complications, such as epiretinal fibrosis associated with tractional distortion of the fovea, hemophthalmos, choroidal neovascularization, exudative retinal detachment, macular edema, and combined tractional/rhegmatogenous retinal detachment. Currently, there is no consensus on the combined hamartoma complications management. The reported clinical case demonstrates the feasibility of staged approach to treatment of combined hamartoma of the retina and RPE complicated by epiretinal fibrosis and partial hemophthalmos using the advanced diagnosis (optical coherence tomography) and treatment methods.

Keywords: hamartoma, retinal pigment epithelium, retina, laser photocoagulation, angiogenesis inhibitor

Author contribution: Takhchidi KhP — study concept and design, manuscript editing; Takhchidi NKh — literature analysis; Tebina EP — data acquisition and processing, manuscript writing; Kasminina TA — laser treatment.

Compliance with ethical standards: the patient submitted informed consent to staged surgery and personal data processing.

✉ **Correspondence should be addressed:** Ekaterina P. Tebina
Volokolamskoe shosse, 30, str. 2, Moscow, 123182; ekaterinatebina@mail.ru

Received: 07.09.2020 **Accepted:** 03.10.2020 **Published online:** 12.10.2020

DOI: 10.24075/brsmu.2020.060

ПОЭТАПНЫЙ ПОДХОД В ЛЕЧЕНИИ КОМБИНИРОВАННОЙ ГАМАРТОМЫ СЕТЧАТКИ И РЕТИНАЛЬНОГО ПИГМЕНТНОГО ЭПИТЕЛИЯ

Х. П. Тахчиди, Н. Х. Тахчиди, Т. А. Касмынина, Е. П. Тебина ✉

Российский национальный исследовательский медицинский университет имени Н. И. Пирогова, Москва, Россия

Комбинированная гамартома пигментного эпителия и сетчатки — редкое врожденное доброкачественное новообразование. Наиболее часто ее выявляют у молодых людей и подростков. В большинстве случаев заболевание протекает бессимптомно, однако в 24% снижение зрительных функций обусловлено развитием осложнений: эпиретинального фиброза, сопровождающегося тракционным искажением фovea, гемофтальмом, хориоидальной неоваскуляризацией, экссудативной отслойкой сетчатки, макулярным отеком, тракционной/регматогенной отслойкой сетчатки. В настоящее время не существует единого мнения в лечении осложнений, вызванных комбинированной гамартомой. Данный клинический случай демонстрирует возможность поэтапного лечения комбинированной гамартоты сетчатки и ретинального пигментного эпителия, осложненного эпиретинальным фиброзом и частичным гемофтальмом, с использованием современных методов диагностики (оптическая когерентная томография) и лечения.

Ключевые слова: гамартома, ретинальный пигментный эпителий, сетчатка, лазерная коагуляция, ингибитор неоангиогенеза

Вклад авторов: Х. П. Тахчиди — концепция и дизайн исследования, редактирование текста; Н. Х. Тахчиди — анализ литературных данных; Е. П. Тебина — сбор и обработка материала, написание текста; Т. А. Касмынина — лазерное лечение пациента.

Соблюдение этических стандартов: от пациента получено добровольное информированное согласие на поэтапное оперативное лечение и обработку персональных данных.

✉ **Для корреспонденции:** Екатерина Павловна Тебина
Волоколамское шоссе, д. 30, корп. 2, г. Москва, 123182; ekaterinatebina@mail.ru

Статья получена: 07.09.2020 **Статья принята к печати:** 03.10.2020 **Опубликована онлайн:** 12.10.2020

DOI: 10.24075/vrgmu.2020.060

Combined hamartoma of the retina and retinal pigment epithelium (RPE) is an uncommon benign lesion. This congenital lesion is most often found at an early age. The tumor was first described by Gass in 1973 [1].

Hamartoma is usually associated with tuberous sclerosis (Bourneville disease), and is less frequently detected in patients with neurofibromatosis type II (to a lesser extent in patients with neurofibromatosis type I), Gorlin syndrome, juvenile nasopharyngeal angiofibroma. However, solitary tumors of the described type may occur sporadically in healthy people [2–4].

The total disorganization of the inner retinal layers associated with glial cell and pigment epithelial cell proliferation is observed in histological sections [2]. Gass distinguished the following four types of combined hamartoma based on the tumor location and clinical manifestations: papillary and juxta-papillary (56–76%), macular (17–38%) and peripheral (5–7%) [1, 4].

Lesion is usually detected through routine fundus examination or when handling patients complaining of decreased visual

acuity, strabismus, leukocoria. The loss of visual function directly depends on the degree of macular and optic nerve involvement. Combined hamartomas are usually unilateral, however, there are several documented cases of bilateral lesions [4].

Juxta-papillary, papillary or macular hamartomas are visualized by ophthalmoscopy as protruding lesions with blurred margins. The tumor with nonuniform pigmentation is light or dark grey, and covered with semi-translucent shiny membrane. The abnormally tortuous retinal blood vessels are frequently noted, and in a number of patients, exudative retinal detachment, microhemorrhages and hard exudates are detected [4]. Peripheral combined hamartomas are associated with significant preretinal blood vessels malformations and retinal thickening, and the tumor margins are poorly distinguishable.

Currently, optical coherence tomography (OCT) makes it possible to image the morphometric features of combined hamartoma: epiretinal membrane, minor vertical vitreoretinal

traction (mini peaks), major vertical vitreoretinal traction with folding of inner retinal layers (maxi peaks), distortion of the outer plexiform layer (saw tooth appearance or “omega” sign) [5–8].

In 24% of patients, the loss of visual function results from complications of the disease: epiretinal fibrosis associated with vitreomacular traction syndrome, hemophthalmos, choroidal neovascularization, exudative retinal detachment, macular edema, combined tractional and rhegmatogenous retinal detachment [2].

To date, there is no consensus on the combined hamartoma complications treatment. However, a number of authors reported cases of *pars plana* vitrectomy aimed at relieving vitreoretinal traction (epiretinal fibrosis removal) and improving visual acuity to 60% [9, 10]. Extravasation may be reduced by intravitreal injection of angiogenesis inhibitor or retinal laser photocoagulation [11, 12]. The aim of our study was to prove the effectiveness of staged treatment in patients with combined hamartoma of the retina and RPE.

Clinical case

The female patient, aged 38, complaining of decreased visual acuity in her left eye during the last six months, was admitted to the Scientific Research Center for Ophthalmology of Pirogov Russian National Medical Research University in September 2019. Facts from medical history: in January 2019 the patient sought medical assistance from ophthalmologist at her place of residence because of the complaints described above; she was diagnosed with thrombosis of superior-temporal branch of the central retinal vein OS and received conservative management; no response to treatment was observed. The systemic disease was ruled out.

On admission, the patient underwent complex assessment by standard methods, such as visometry aimed at determining the best corrected visual acuity (BCVA), indirect ophthalmoscopy using the MaxField non-contact lens (OcularInc.; USA), and specific examination methods, such as OCT imaging using the Spectralis HRA+OCT, Module OCT2 platform with a scanning speed of 85,000 Hz (Heidelberg Engineering Inc.; Germany).

At initial examination of the patient’s left eye, the BCVA was 0.6. Biomicroscopy demonstrated no pathological

changes in the anterior segment. Partial hemophthalmos was identified. Ophthalmoscopy revealed pale-pink optic disk with sharp margins, cellophane macular reflex. Retinal vasculature: superior temporal arcade — arteries with narrowed lumen, veins greatly dilated and tortuous, artery to vein (A/V) ratio 1/3; inferior temporal arcade — uniform meshwork of blood vessels; no changes in vessel calibre, A/V ratio 2/3. The protruding grey lesion with multiple sites of vitreoretinal traction was identified in the area of the central retinal vein superior temporal branch, the lesion margins were undistinguishable. No peripheral retinal changes were detected. Disorganization of the inner retinal layers (maxi peaks) in the protruding lesion area was observed on spectral-domain OCT scans (Fig. 1A, B). Epiretinal fibrosis was identified on the surface of macular area (Fig. 2).

The patient was diagnosed with combined hamartoma of the retina and RPE complicated by epiretinal fibrosis and partial hemophthalmos in her left eye based on the clinical and instrumental assessment results.

Staged treatment was recommended:

stage 1 — laser photocoagulation aimed at reducing extravasation;

stage 2 — intravitreal administration of angiogenesis inhibitor aimed at reducing vascular permeability in the areas that cannot be subjected to laser photocoagulation, as well as at reducing the risk of intra- and postoperative vitreous haemorrhage;

stage 3 — microinvasive subtotal vitrectomy + schvartectomy + endolaser photocoagulation aimed at restoring of clarity to the ocular media and traction relieving.

Laser photocoagulation (first stage of treatment) was performed using the VISULAS Trion laser workstation (532, 561, 659 nm) (Carl Zeiss; Germany). The following energy parameters were used: power was 80 mW, exposure time was 0.1 s, and wavelength was 532 nm. Paravasal irradiation was applied to restricted protruding lesion. One month after laser photocoagulation the BCVA was 0.6. Biomicroscopy detected no pathological changes in the anterior segment. Partial hemophthalmos was identified. Ophthalmoscopy revealed pale-pink optic disk with sharp margins, cellophane macular reflex. Retinal vasculature: superior temporal arcade — arteries with narrowed lumen, veins greatly dilated and tortuous, A/V

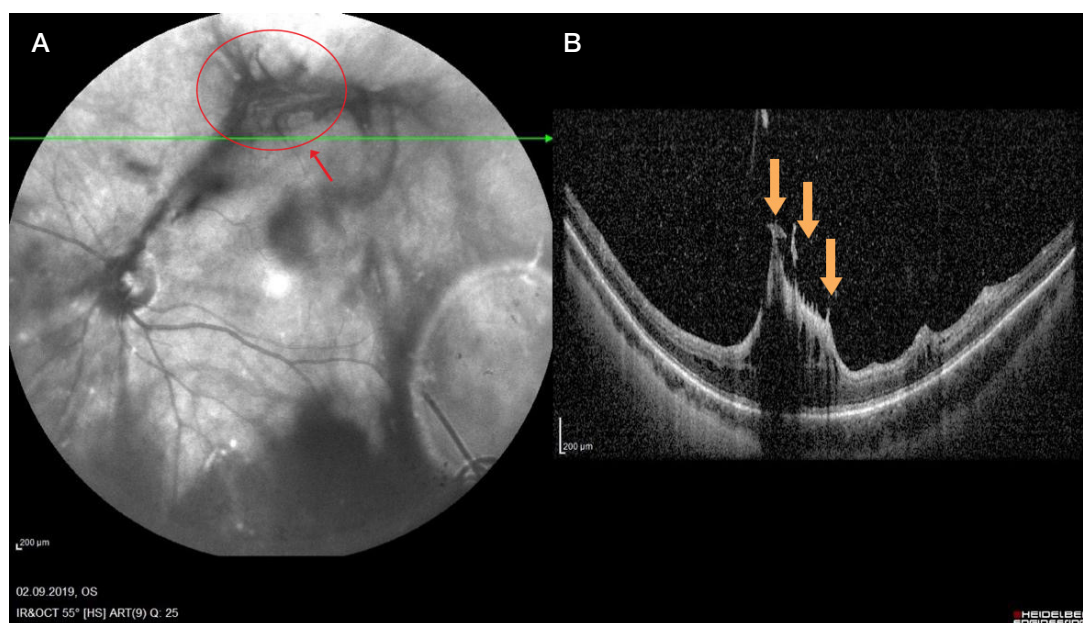


Fig. 1. A. IR reflectance image of fundus: protruding grey lesion with multiple sites of vitreoretinal traction in the area of the central retinal vein superior temporal branch. Partial hemophthalmos. B. OCT scan of retina: disorganization of the inner retinal layers in the protruding lesion area (maxi peaks, yellow arrow)

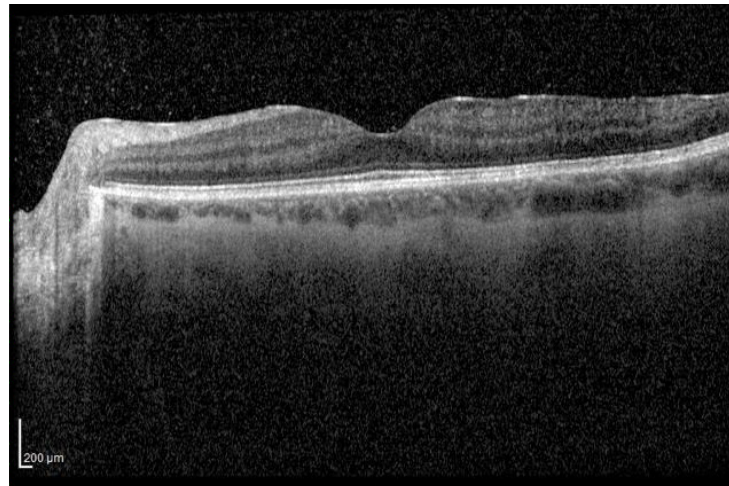


Fig. 2. OCT scan of retina: hyperreflective band in the central area of retinal surface, which is tightly attached to the internal limiting membrane, normal macular profile

ratio 1/3; inferior temporal arcade — uniform meshwork of blood vessels; no changes in vessel calibre, A/V ratio 2/3. The protruding grey lesion with multiple sites of vitreoretinal traction was identified in the area of the central retinal vein superior temporal branch, the lesion margins were undistinguishable. Pigmented coagula were visualized in the paravasal area, and the focal area was surrounded by pigmented coagula. OCT revealed no signs of clinical worsening.

One month after laser photocoagulation, during the second stage, the patient's left eye received the intravitreal injection of angiogenesis inhibitor (Aflibercept, 0.1 mg/0.04 mL). During the check-up performed two weeks later the BCVA was 0.7. Biomicroscopy demonstrated no pathological changes in the anterior segment. Partial regression of hemophthalmos was detected. Ophthalmoscopy revealed no clinical worsening. No changes were observed on OCT scan.

Three weeks after the intravitreal injection of angiogenesis inhibitor, during the third stage, the patient underwent microinvasive subtotal vitrectomy + schvartectomy + endolaser photocoagulation. One week after surgery the BCVA became 1.0. Biomicroscopy demonstrated no pathological changes in the anterior segment. Avitria was detected. Ophthalmoscopy revealed pale-pink optic disk with sharp margins. Persisting cellophane macular reflex was observed. Retinal vasculature:

superior temporal arcade — restored uniformity of blood vessels meshwork, A/V ratio 2/3, pigmented coagula visualized in the paravasal area; inferior temporal arcade — uniform meshwork of blood vessels; no changes in vessel calibre, A/V ratio 2/3. The vitreoretinal traction along the superior temporal branch of central retinal vein was relieved, the shrunk protruding lesion (optic disk $d = 0.5$) was surrounded by pigmented coagula (Fig. 3A). Fig. 3B presents the OCT scan.

During the check-up performed three months later no clinical worsening was detected.

Discussion

To date, there is no generally accepted approach to management of patients with combined hamartoma of the retina and RPE. Literature analysis shows that the disorder may remain asymptomatic for a long period of time, and that the loss of visual function results from complications.

Several treatment options for the disorder and its complications are reported in literature: the effectiveness of radiation therapy in combined hamartoma of the retina and RPE has not yet been proven since the tumor is benign and not radiosensitive [13]; photodynamic therapy, focal laser photocoagulation and intravitreal angiogenesis inhibitor injections are widely

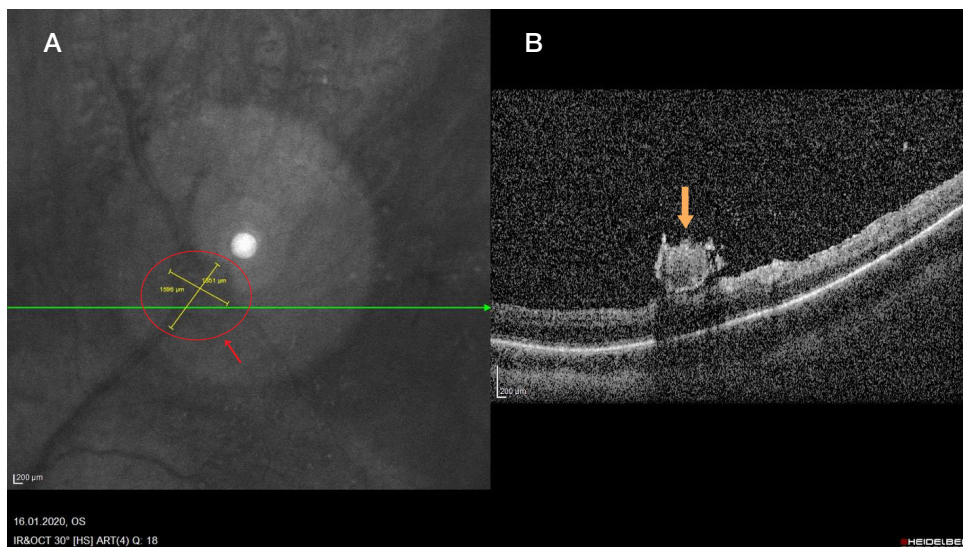


Fig. 3. A. IR reflectance image of fundus a week after the subtotal vitrectomy: restored blood vessels calibre in the superior temporal branch, relieved vitreoretinal traction, shrunk protruding lesion (optic disk $d = 0.5$; red arrow) **B.** OCT scan of retina: single protruding lesion on the retinal surface (yellow arrow) with no vitreoretinal traction, restored anatomic structure of retinal layers

used in patients with choroidal neovascularization [11, 14]. Angiogenesis inhibitors are also used to reduce the vascular permeability and decrease the risk of vitreous haemorrhage [14]. Subtotal vitrectomy with internal limiting membrane (ILM) and epiretinal membrane (ERM) peeling remains the gold standard for treatment of patients with epiretinal fibrosis. However, this method has a number of limitations: first, the ILM peeling results in damage to Muller glial cells, leading to biomechanical dysfunction of the retina and incomplete recovery of visual function during the postoperative period [15–17]; second, the technical complexity of ILM peeling may result in complications, such as retina injured with instruments for endovitreous intervention, intraretinal hemorrhages in the areas of ILM gripping, high risk of intra- and postoperative vitreous haemorrhage; third, the visual function improvement during the postoperative period correlates with the degree of the retinal layers disorganization [18].

Unlike the international experience, in this study we used staged approach to improve the clinical and functional treatment outcome in patient with combined hamartoma of the retina and RPE, which included paravasal retinal

photocoagulation aimed at reducing extravasation at the first stage, intravitreal angiogenesis inhibitor injection aimed at reducing the vascular permeability and the risk of intra- and postoperative haemorrhage at the second stage, and subtotal vitrectomy aimed at restoring of clarity to the ocular media and traction relieving in the area of lesion at the third stage.

Our proposed staged approach to treatment of combined hamartoma of the retina and RPE complicated by partial hemophthalmos and epiretinal fibrosis made it possible to achieve good clinical and functional results: improved BCVA, restored clarity to the ocular media, relieved traction and decreased risk of eventual vitreous haemorrhage.

CONCLUSION

Personalized staged approach to treatment of combined hamartoma of the retina and retinal pigment epithelium based on the use of advanced diagnosis and treatment methods allowed us to achieve good functional results in the long-term follow-up.

References

- Gass JDM. An unusual hamartoma of the pigment epithelium and retina simulating choroidal melanoma and retinoblastoma. *Trans Am Ophthalmol Soc.* 1973; 71: 171–83.
- Gupta R, Fung AT, Lupidi M, et al. Peripapillary Versus Macular Combined Hamartoma of the Retina and Retinal Pigment Epithelium: Imaging Characteristics. *Am J Ophthalmol.* 2019; 200: 263–9.
- Fonseca RA, Dantas MA, Kaga T, et al. Combined hamartoma of the retina and retinal pigment epithelium associated with juvenile nasopharyngeal angiofibroma. *Am J Ophthalmol.* 2001; 132 (1): 131–32.
- Kojen SI, Kvintel G. Flyuorescentnaja angiografija v diagnostike patologii glaznogo dna. M.: Rejtar, 2005; 311 s. Russian.
- Shields CL, Mashayekhi A, Dai VV, et al. Optical Coherence Tomographic Findings of Combined Hamartoma of the Retina and Retinal Pigment Epithelium in 11 Patients. *Arch Ophthalmol.* 2005; 123 (12): 1746–50.
- Arepalli S, Pellegrini M, Ferenczy SR, et al. Combined hamartoma of the retina and retinal pigment epithelium: findings on enhanced depth imaging optical coherence tomography in eight eyes. *Retina.* 2014; 34 (11): 2202–7.
- Schachat AP, Shields JA, Fine SL, et al. Combined hamartomas of the retina and retinal pigment epithelium. *Ophthalmology.* 1984; 91 (12): 1609–15.
- Kumar V, Chawla R, Tripathy K. Omega Sign: A Distinct Optical Coherence Tomography Finding in Macular Combined Hamartoma of Retina and Retinal Pigment Epithelium. *Ophthalmic Surg Lasers Imaging Retina.* 2017; 48 (2): 122–5.
- Cohn AD, Quiram PA, Drenser KA, et al. Surgical outcomes of epiretinal membranes associated with combined hamartoma of the retina and retinal pigment epithelium. *Retina.* 2009; 29: 825–30.
- Zhang X, Dong F, Dai R, et al. Surgical management of epiretinal membrane in combined hamartomas of the retina and retinal pigment epithelium. *Retina.* 2010; 30: 305–09.
- Nam DH, Shin KH, Lee DY, et al. Vitrectomy, laser photocoagulation, and intravitreal triamcinolone for combined hamartoma of the retina and retinal pigment epithelium. *Ophthalmic Surg Lasers Imaging.* 2010; 9: 1–4.
- Xue K, Mellington F, Gout I, et al. Combined hamartoma of the retina and retinal pigment epithelium. *BMJ. Case Reports.* 2012.
- Dave T, Dave V, Pappuru R. Combined hamartoma of the retina and retinal pigment epithelium with hypo-autofluorescence and cystic degeneration at the macula. *Clin Exp Optom.* 2014; 97: 475–6.
- Cormos D, Ocusan C. Complication of combined retinal and retinal pigment epithelium hamartoma involving optic disc in a child, treated with Avastin — a review of the literature and case presentation. *Romanian Journal of Ophthalmology.* 2015; 59 (4): 255–62.
- Tari SR, Vidne-Hay O, Greenstein VC, et al. Functional and structural measurements for the assessment of internal limiting membrane peeling in idiopathic macular pucker. *Retina.* 2007; 27 (5): 567–72.
- Kumagai K, Ogino N, Furukawa M. Retinal thickness after vitrectomy and internal limiting membrane peeling for macular hole and epiretinal membrane. *Clin Ophthalmol.* 2012; 6: 679–88.
- Wolf S, Schnurbusch U, Wiedemann P. Peeling of the basal membrane in the human retina: ultrastructural effects. *Ophthalmology.* 2004; 111: 238–43.
- Karimov AI, Lyskin PV, Zgoba MI, Makarenko IR. Hirurgicheskoe lechenie makuljarnyh otverstij bez pilinga vnutrennej pograničnoj membrany. *Sovremennye tehnologii v oftal'mologii.* 2018; 4: 137–9. Russian.

Литература

- Gass JDM. An unusual hamartoma of the pigment epithelium and retina simulating choroidal melanoma and retinoblastoma. *Trans Am Ophthalmol Soc.* 1973; 71: 171–83.
- Gupta R, Fung AT, Lupidi M, et al. Peripapillary Versus Macular Combined Hamartoma of the Retina and Retinal Pigment Epithelium: Imaging Characteristics. *Am J Ophthalmol.* 2019; 200: 263–9.
- Fonseca RA, Dantas MA, Kaga T, et al. Combined hamartoma of the retina and retinal pigment epithelium associated with juvenile nasopharyngeal angiofibroma. *Am J Ophthalmol.* 2001; 132 (1): 131–32.
- Коэн С. И., Квинтель Г. Флюоресцентная ангиография в диагностике патологии глазного дна. М.: Рейтар, 2005; 311 с.
- Shields CL, Mashayekhi A, Dai VV, et al. Optical Coherence Tomographic Findings of Combined Hamartoma of the Retina and Retinal Pigment Epithelium in 11 Patients. *Arch Ophthalmol.* 2005; 123 (12): 1746–50.
- Arepalli S, Pellegrini M, Ferenczy SR, et al. Combined hamartoma

- of the retina and retinal pigment epithelium: findings on enhanced depth imaging optical coherence tomography in eight eyes. *Retina*. 2014; 34 (11): 2202–7.
7. Schachat AP, Shields JA, Fine SL, et al. Combined hamartomas of the retina and retinal pigment epithelium. *Ophthalmology*. 1984; 91 (12): 1609–15.
 8. Kumar V, Chawla R, Tripathy K. Omega Sign: A Distinct Optical Coherence Tomography Finding in Macular Combined Hamartoma of Retina and Retinal Pigment Epithelium. *Ophthalmic Surg Lasers Imaging Retina*. 2017; 48 (2): 122–5.
 9. Cohn AD, Quiram PA, Drenser KA, et al. Surgical outcomes of epiretinal membranes associated with combined hamartoma of the retina and retinal pigment epithelium. *Retina*. 2009; 29: 825–30.
 10. Zhang X, Dong F, Dai R, et al. Surgical management of epiretinal membrane in combined hamartomas of the retina and retinal pigment epithelium. *Retina*. 2010; 30: 305–09.
 11. Nam DH, Shin KH, Lee DY, et al. Vitrectomy, laser photocoagulation, and intravitreal triamcinolone for combined hamartoma of the retina and retinal pigment epithelium. *Ophthalmic Surg Lasers Imaging*. 2010; 9: 1–4.
 12. Xue K, Mellington F, Gout I, et al. Combined hamartoma of the retina and retinal pigment epithelium. *BMJ. Case Reports*. 2012.
 13. Dave T, Dave V, Pappuru R. Combined hamartoma of the retina and retinal pigment epithelium with hypo-autofluorescence and cystic degeneration at the macula. *Clin Exp Optom*. 2014; 97: 475–6.
 14. Cormos D, Ocusan C. Complication of combined retinal and retinal pigment epithelium hamartoma involving optic disc in a child, treated with Avastin — a review of the literature and case presentation. *Romanian Journal of Ophthalmology*. 2015; 59 (4): 255–62.
 15. Tari SR, Vidne-Hay O, Greenstein VC, et al. Functional and structural measurements for the assessment of internal limiting membrane peeling in idiopathic macular pucker. *Retina*. 2007; 27 (5): 567–72.
 16. Kumagai K, Ogino N, Furukawa M. Retinal thickness after vitrectomy and internal limiting membrane peeling for macular hole and epiretinal membrane. *Clin Ophthalmol*. 2012; 6: 679–88.
 17. Wolf S, Schnurbusch U, Wiedemann P. Peeling of the basal membrane in the human retina: ultrastructural effects. *Ophthalmology*. 2004; 111: 238–43.
 18. Каримов А. И., Лыскин П. В., Згоба М. И., Макаренко И. Р. Хирургическое лечение макулярных отверстий без пилинга внутренней пограничной мембраны. *Современные технологии в офтальмологии*. 2018; 4: 137–9.

DIFFICULTIES IN DIFFERENTIAL DIAGNOSIS OF CUTANEOUS MANIFESTATIONS IN PATIENTS WITH CORONAVIRUS INFECTION

Tairova RT^{1,2}, Gaydina TA^{1,2}✉, Dvornikov AS², Tazartukova AD¹, Lyang OV¹

¹ Federal Center for Brain Research and Neurotechnology of FMBA, Moscow, Russia

² Pirogov Russian National Research Medical University, Moscow, Russia

Patients with severe SARS-CoV-2 infection (COVID-19) and multiple comorbidities should be monitored for possible adverse reactions to prescribed drugs, including drug eruptions (DE) at any stage of treatment. Below, we describe a clinical case of a 92-year-old female patient with severe PCR-confirmed COVID-19. The patient was treated with amoxicillin/clavulanic acid, moxifloxacin, acetylcysteine, and sodium enoxaparin. On day 9 into treatment, the patient developed moderately itching macular rashes showing a tendency to coalesce, but overall showed no signs of deterioration. On day 15, the rashes regressed, following a short course of dexamethasone and chloropyramine. This kind of skin reaction might have been provoked by β -lactams and fluoroquinolones included in the treatment regimen, a secondary bacterial infection, compromised immunity due to advanced age, and high viral load associated with dermatological symptoms. Delayed onset of skin symptoms might be regarded as a marker of COVID-19 severity.

Keywords: coronavirus infection, skin manifestations, toxidermia, drug eruptions

Author contribution: Tairova RT, Gaydina TA: interpretation of the obtained data, manuscript draft; Dvornikov AS: literature analysis; Tazartukova AD: interpretation of the obtained data; Lyang OV: manuscript draft.

Compliance with ethical standards: the patient gave informed consent to medical treatment and publication of this case report.

✉ **Correspondence should be addressed:** Tatiana A. Gaydina
Ostrovityanova, 1, Moscow, 117997; doc429@yandex.ru

Received: 23.09.2020 **Accepted:** 08.10.2020 **Published online:** 20.10.2020

DOI: 10.24075/brsmu.2020.062

СЛОЖНОСТИ ДИФФЕРЕНЦИАЛЬНОЙ ДИАГНОСТИКИ КОЖНЫХ ПРОЯВЛЕНИЙ ПРИ КОРОНАВИРУСНОЙ ИНФЕКЦИИ

Р. Т. Таирова^{1,2}, Т. А. Гайдина^{1,2}✉, А. С. Дворников², А. Д. Тазартукова¹, О. В. Лянг¹

¹ Федеральный центр мозга и нейротехнологий Федерального медико-биологического агентства, Москва, Россия

² Российский национальный исследовательский медицинский университет имени Н. И. Пирогова, Москва, Россия

При лечении мультиморбидных пациентов с тяжелым течением новой коронавирусной инфекции, вызванной вирусом SARS-CoV-2 (COVID-19), необходимо проявлять внимание к возможному развитию лекарственной экзантемы (ЛЭ) в любой период времени лечения. Представлено клиническое наблюдение больной 92 лет с тяжелым течением подтвержденного ПЦР COVID-19. На фоне лечения амоксициллином/клавулановой кислотой, моксифлоксацином, ацетилцистеином, омега-3, эноксапарином натрия на 9-й день лечения появились умеренно зудящие макулезные высыпания с тенденцией к слиянию без отрицательной динамики соматического статуса. На 15-й день лечения на фоне приема дексаметазона и хлоропирамина кожные высыпания регрессировали. Появление сыпи может быть обусловлено применением β -лактамов антибактериальных препаратов и фторхинолонов, присоединением бактериальной инфекции и иммуносупрессивным статусом пациентки старческого возраста, а также высокой вирусной нагрузкой, ассоциированной с появлением дерматологических симптомов. Отсроченное появление кожных изменений на фоне COVID-19 возможно рассматривать как «маркер» тяжести заболевания.

Ключевые слова: коронавирусная инфекция, кожные проявления, токсидермия, лекарственная экзантема

Вклад авторов: Р. Т. Таирова, Т. А. Гайдина — интерпретация данных, подготовка черновика рукописи; А. С. Дворников — анализ литературы; А. Д. Тазартукова — интерпретация данных; О. В. Лянг — подготовка черновика рукописи.

Соблюдение этических стандартов: пациентка подписала добровольное информированное согласие на лечение и публикацию данных.

✉ **Для корреспонденции:** Татьяна Анатольевна Гайдина
ул. Островитянова, д. 1, г. Москва, 117997; doc429@yandex.ru

Статья получена: 23.09.2020 **Статья принята к печати:** 08.10.2020 **Опубликована онлайн:** 20.10.2020

DOI: 10.24075/vrgmu.2020.062

The etiology of exanthems afflicting patients with the coronavirus infection (CVI) caused by SARS-CoV-2 (COVID-19) can pose a diagnostic challenge [1–3], especially during the ongoing epidemic, when clinicians are required to follow physical distance guidelines and wear personal protective equipment while examining the skin and the oral mucosa of patients with COVID-19 [2, 4].

It is vital that comorbid patients with severe CVI undergoing systemic combination therapy for the viral infection should continue receiving their usual medicines for preexisting conditions [5]. Effective pharmacotherapeutic strategies for CVI must account for such comorbidities and possible adverse reactions to anti-CVI therapy, the most common being cutaneous drug eruptions (DE). The diagnosis of DE can be difficult, especially at onset. Establishing a causal link between

DE and a specific drug is even more challenging if the treatment regimen includes more than one medication [6–8].

Since the beginning of the pandemic, a variety of skin manifestations have been reported in patients with COVID-19; however, specific skin symptoms that would help in verifying the diagnosis of COVID-19 are yet to be identified [1, 9–11]. Skin manifestations observed in patients with CVI should be thoroughly studied, systematized and analyzed for the possible association with the severity of the infection.

Clinical case

A female patient C. aged 92 years had acute-onset symptoms, including cough, weakness and increased body temperature

(37.8 °C), followed by sudden deterioration, shortness of breath and febrile chills two days later. The patient was taken to hospital by an EMS team. She denied any contact with individuals showing symptoms of acute respiratory infection suggestive of COVID-19 in the preceding 14 days. The patient shares a flat with her niece, who had no health complaints at the time of her aunt's illness. The history of preexisting conditions included elevated blood pressure, coronary artery disease, long-standing persistent atrial fibrillation, and gallstone disease. The patient denied any allergies or drug intolerance.

On admission, the patient's condition was assessed as severe. Her skin color was normal, and visible mucous membranes showed no signs of dryness. No discoloration of the sclera was observed. Peripheral lymph nodes were unremarkable. The patient was not edematous. Her chest was symmetrical and cylinder-shaped. SpO₂ was 70%, increasing to 95% after oxygen insufflation at 10 L/min. Cardiac and lung auscultation was not performed due to the risk of SARS-CoV-2 spread. BP was 160/80 mmHg; heart rate was 80 beats/min. The abdomen was soft without tenderness. The liver was not enlarged. There were no signs of peritoneal irritation. The patient described her bowel movement as regular. The kidney percussion test was negative on both sides. The patient denied dysuria. Neurological examination was unremarkable.

The subsequent CT scan was suggestive of community-acquired polysegmental viral pneumonia and interstitial pulmonary edema, indicating the onset of hemodynamic compromise. Blood count: white blood cells $9.7 \times 10^9/L$; absolute and relative lymphocyte counts $0.7 \times 10^9/L$ and 7.2%, respectively, indicating lymphopenia; relative monocyte count 1.3% (relative monocytopenia); absolute and relative granulocyte counts $8.9 \times 10^9/L$ and 91.5%, respectively (granulocytosis). Blood biochemistry: elevated C-reactive protein (67 mg/L), AST 56 u/L, ALT 41 u/L, D-dimer 1817 ng/ml.

The patient's nasopharyngeal swab tested positive for SARS-CoV-2 RNA. The test was conducted using a reagent kit

for RT-PCR-based detection of SARS-CoV-2/SARS-CoV RNA in human specimens (DNA-Technology TS; Russia).

Biological specimens for PCR analysis were collected from the patient's nasopharynx.

Viral RNA was manually extracted from 400 µl of the biological specimens using a Proba-NK reagent kit (DNA-Technology; Russia) and eluted in 50 µL of an RNA buffer.

The SARS-CoV-2/SARS-CoV RT-PCR reagent kit (DNA-Technology TS; Russia) is designed to target 3 viral genome regions: those specific to SARS-CoV-2 (the Cy5/Red detection channel), the E gene regions (the Rox/Orange detection channel), and the conserved region of the E gene (the Fam/Green detection channel) common to the group of SARS-CoV-like coronaviruses, including SARS-CoV and SARS-CoV-2.

The kit contains a heterologous amplification system (Internal Control, or IC, detectable in the Hex/Yellow channel) for monitoring RT-PCR inhibition and checking the integrity of the reagents. The kit includes a positive control. The assay was run in a DPrime thermocycler (DNA-Technology; Russia).

In total, 4 specimens were studied; the specimens were collected on May 28, 2020, June 3, June 9, and June 16.

For the sample collected on May 28, an early exponential increase in fluorescence was detected in the Fam/Green channels (the conserved region of the E gene; Fig. 1), with Ct = 24.6, indicating the presence of SARS-CoV RNA.

In the Rox/Orange detection channel (the E gene of SARS-CoV-2; Fig. 2), the Ct value was 24.5.

In the Cy5/Red detection channel (the N gene of SARS-CoV-2; Fig. 3), the Ct value was 23.9, indicating the presence of SARS-CoV-2 RNA.

Given that valid negative and positive controls were used in the assay, the absence of fluorescence in the Hex/Yellow channel (Fig. 4) indirectly suggested high SARS-CoV-2 RNA levels in the studied sample. For the sample collected on June 3 (day 7), an increase in fluorescence intensity was observed in the Fam/Green channel (SARS-CoV RNA), with Ct = 37.4; the Hex/Yellow (IC) channel, with Ct = 31.0; the Rox/Orange

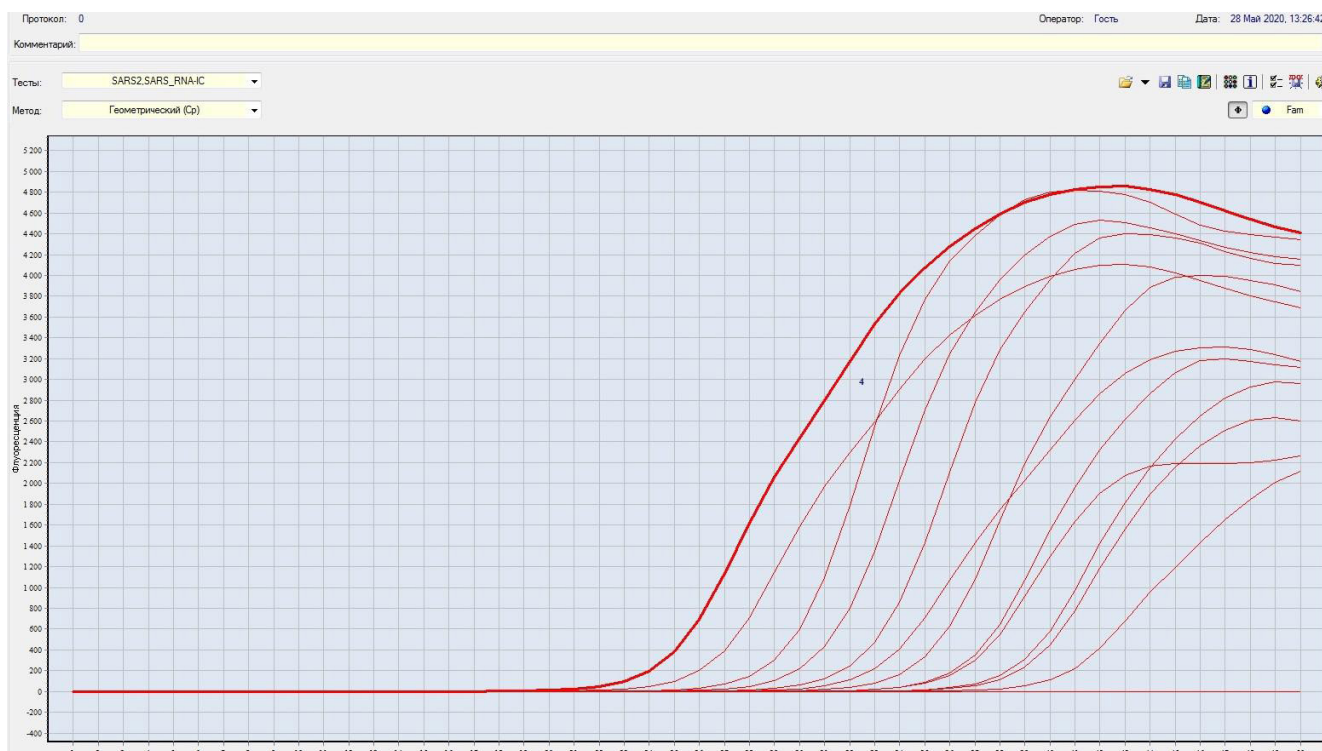


Fig. 1. Early exponential increase in fluorescence intensity in the Fam/Green channels (conserved region of the E gene) in the sample collected on May 28, 2020 (day 1)



Fig. 2. Early exponential increase in fluorescence intensity in the Rox/Orange channel in the sample collected on May 28, 2020 (day 1)

channel (the E gene of SARS-CoV-2), with Ct = 37.5, and the Cy5/Red channel (the N gene SARS-CoV-2), with Ct = 38.1, indicating the presence of SARS-CoV-2 RNA.

In the sample collected on June 9 (day 13), an increase in fluorescence intensity was detected in the Fam/Green channel (SARS-CoV RNA), with Ct = 31.9; the Hex/Yellow channel (IC),

with Ct = 30.0; the Rox/Orange channel (the E gene of SARS-CoV-2), with Ct = 32.1; the Cy5/Red channel (the N gene of SARS-CoV-2), with Ct = 31.8, indicating the presence of SARS-CoV-2 RNA.

In the sample collected on June 20 (day 20), an increase in fluorescence intensity was detected in the Fam/Green channel



Fig. 3. Early exponential increase in fluorescence intensity in the Cy5/Red channel in the sample collected on May 28, 2020 (day 1)

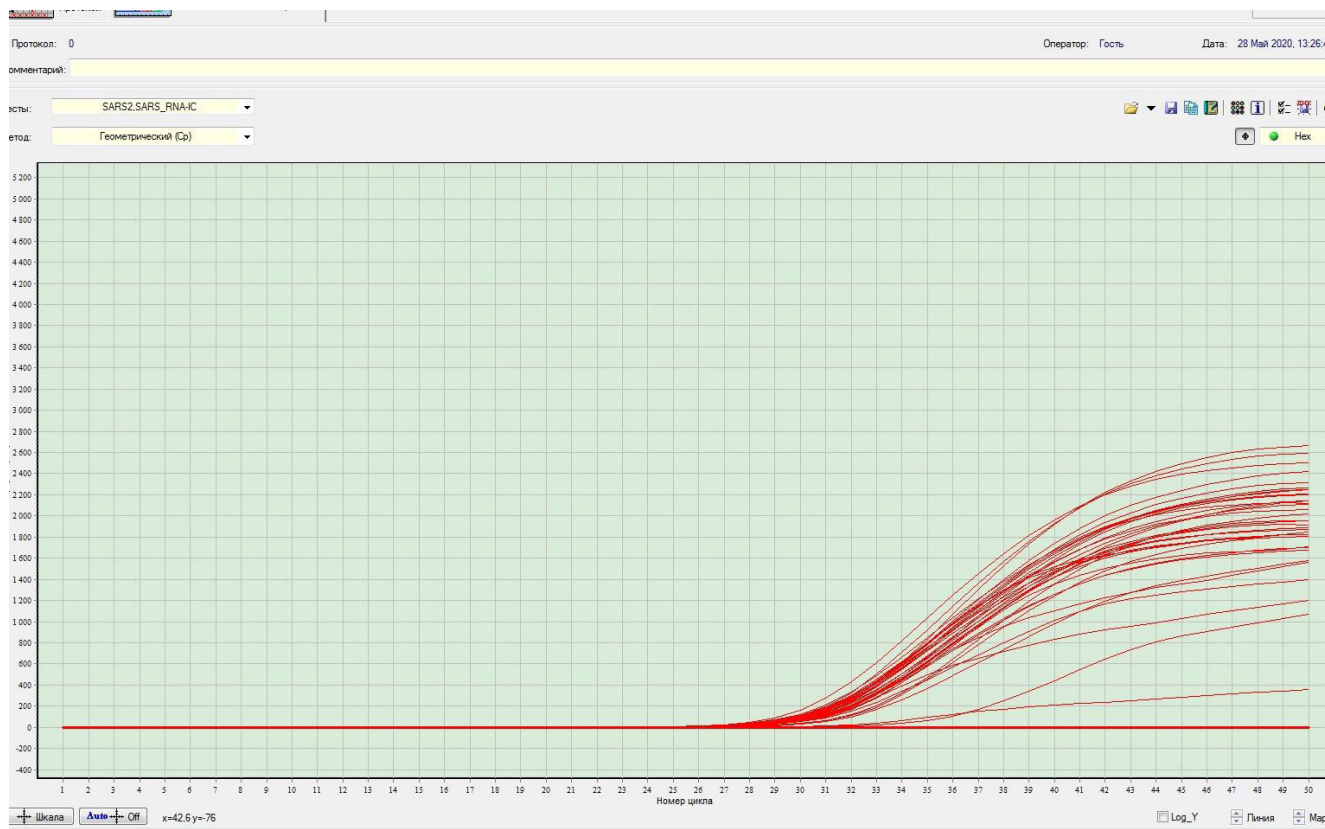


Fig. 4. The absence of the fluorescent signal in the Hex/Yellow channel (the assay included valid positive and negative controls)

(SARS-CoV RNA), with Ct = 34.6; the Hex/Yellow (IC) channel, with Ct = 31.0; the Rox/Orange channel (the E gene of SARS-CoV-2), with Ct = 34.5; the Cy5/Red channel (the N gene of SARS-CoV-2), with Ct = 34.7, indicating the presence of SARS-CoV-2 RNA.

The E and N genes of SARS-CoV-2 were detected in each of the 4 studied samples.

Considering the patient's medical history, clinical presentations and the results of laboratory and instrumental tests, the final diagnosis was *COVID-19, severe course; community-acquired bilateral polysegmental pneumonia*. Given the severity of the patient's condition, she was admitted to the intensive care unit, where she received infusions of sodium chloride 0.9%, amoxicillin, clavulanic acid, moxifloxacin, paracetamol, ascorbic acid, acetylcysteine, omeprazole, bisoprolol, and sodium enoxaparin. After two days, her condition stabilized and she was transferred to the floor. On day 9, the patient developed moderately itching macular rashes, which tended to coalesce (Fig. 5–7). The patient's overall condition was stable, without deterioration. After completing the full course of the prescribed antibiotics, the patient received intramuscular injections of dexamethasone (16 mg per day) and intramuscular injections of chloropyramine (20 mg twice a day). On day 15, the rashes regressed. A chest CT scan showed improvement. On day 20 the patient was discharged home in satisfactory condition.

Discussion

So far, there have been a variety of clinical case reports and propositions on the management of patients with CVI [12, 13].

Cutaneous manifestations differing in morphology and duration pose a particular interest for a clinician. At the moment, their underlying causes are being investigated. Establishing an

accurate etiological diagnosis is essential for working out the right treatment strategy [4].

A study conducted in 88 patients hospitalized for severe CVI reported cutaneous involvement in 18 (20.4%) participants. Skin manifestations were described by the authors as erythematous rash, widespread urticaria, and chickenpox-like vesicles; 8 patients had rashes prior to hospitalization, 10 developed them at hospital [14].

There are reports of petechial and purpuric rashes, transient livedo reticularis livedo and acroischemic lesions [15]. A question remains whether these manifestations should be associated with COVID-19 as exanthems are often caused by viral infections or are the adverse reaction to a prescribed drug.

Our female patient was old and had severe CVI and preexisting conditions. On day 9, she developed itchy macular skin eruptions showing a tendency to coalesce. It is difficult to establish an association between cutaneous manifestations, which can be caused by infection or allergy, and COVID-19. According to the literature, cutaneous involvement is observed in patients with COVID-19 starting from day 2 and into the second week of the infection.

Exanthems are an important criterion for differentiating a viral infection from an adverse drug reaction. Because of COVID-19 safety precautions, the physical examination of patients with CVI symptoms does not follow the standard protocol which includes oral cavity examination. For example, of 21 patients with PCR-confirmed COVID-19 and skin rashes, 6 (29%) had exanthems [15], 4 of 6 (66%) were women, and none had an erythematovesicular exanthem. The mean time from the onset of COVID-19 symptoms to cutaneous/mucosal manifestations was 12.3 days (2 to 24 days). The authors of that study emphasized that rash morphology, other clinical symptoms and the presence of exanthems can help in differentiating between viral and drug-induced skin conditions. The presence



Fig. 5. Macular rashes on the patient's trunk, with a tendency to coalesce. Day 9 into treatment



Fig. 6. Macular rashes on the patient's back, with a tendency to coalesce. Day 9 into treatment

of pustules and macular spots on the skin suggests an adverse reaction to a prescribed drug, whereas petechias and vesicles localized to the buttocks or the acral parts of the extremities in combination with exanthems are indicative of infection, including viral infection [15]. Some histopathological features of the lesions like parakeratosis, spongiosis, or extravasated erythrocytes, may suggest the viral nature of the condition [16].

The treatment regimen for our patient had to include a number of different drugs, which increased the risk of drug cross-reactivity. Another factor supporting the hypothesis of drug eruptions is that the patient developed rashes after she was put on the regimen that included β -lactams and fluoroquinolones.

It is possible that cutaneous manifestations may have been associated with a secondary bacterial infection and the compromised immune status of the patient. This hypothesis is supported by the fact that the antigen was detected in the blood samples of the patient through day 20 of the disease, suggesting a weak immune response to the infection. In an aging individual, immunocompetent cells become less active due to involutional changes.

Since high viral load may also be associated with dermatological symptoms, delayed cutaneous manifestations (on day 9) could be regarded as markers of CVI severity, regressing as the patient improved.

CONCLUSIONS

This clinical case demonstrates the difficulty in the differential diagnosis of cutaneous manifestations in patients with CVI.

References

1. Casas C, Catala A, Hernandez G, Rodríguez-Jimenez P, Nieto D, Rodríguez-Villa A, et al. Classification of the cutaneous manifestations of COVID-19: a rapid prospective nationwide consensus study in Spain with 375 cases. *British Journal of Dermatology*. 2020; 183 (1): 71–77. DOI: 10.1111/bjd.19163.
2. Almutairi N, Schwartz RA. COVID-2019 with dermatologic manifestations and implications: an unfolding conundrum. *Dermatol Therapy*. 2020; e13544. Available from: <https://doi.org/10.1111/dth.13544>.
3. Recalcati S, Barbagallo T, Frasin LA, Prestinari F, Cogliardi A, Provero MC, et al. Acral cutaneous lesions in the time of COVID-19. *J Eur Acad Dermatol Venereol*. 2020; 34 (8): e346–e347. DOI: 10.1111/jdv.16533.
4. Criado PR, Abdalla BMZ, Assis IC, Blarcum de Graaff Mello C, Caputo GC, Vieira IC. Are the cutaneous manifestations during or due to SARS-CoV-2 infection/COVID-19 frequent or not? Revision of possible pathophysiologic mechanisms. *Inflamm Res*. 2020; 69 (8): 745–56. DOI: 10.1007/s00011-020-01370-w.



Fig. 7. Macular rashes on the patient's thighs, with a tendency to coalesce. Day 9 into treatment

Their etiology is especially hard to identify in patients with multiple comorbidities requiring complex treatment regimens, which can provoke skin eruptions. Involutional changes accompanied by a decline in the immune function should also be taken into account. Delayed onset of skin symptoms might be regarded as a marker of CVI severity.

5. Wang C, Horby PW, Hayden FG, Gao GF. A novel coronavirus outbreak of global health concern. *Lancet*. 2020; 395 (10223): 470–73. DOI: 10.1016/S0140-6736(20)30185-9.
6. Formica D, Sultana J, Cutroneo P, et al. The economic burden of preventable adverse drug reactions: a systematic review of observational studies. *Expert Opin Drug Saf*. 2018; 17 (7): 681–95. DOI: 10.1080/14740338.2018.1491547
7. Aung A, Tang M, Adler N, et al. Adverse Drug Reactions Reported by Healthcare Professionals: Reaction Characteristics and Time to Reporting. *The Journal of Clinical Pharmacology*. 2018; 58 (10): 1332–9. DOI: 10.1002/jcph.1148.
8. Gelincik A, Brockow K, Celik GE, Dona I, Mayorga C, Romano A, et al. Diagnosis and management of the drug hypersensitivity reactions in Coronavirus disease 19. *Allergy*. 2020; 10.1111/all.14439. DOI: 10.1111/all.14439.
9. Marzano AV, Cassano N, Genovese G, Moltrasio C, Vena GA. Cutaneous manifestations in patients with COVID-19: a preliminary review of an emerging issue. *British Journal of Dermatology*. 2020; 183 (3): 431–42. DOI: 10.1111/bjd.19264.
10. Su CJ, Lee CH. Viral exanthem in COVID-19, a clinical enigma with biological significance. *J Eur Acad Dermatol Venereol*. 2020; 34 (6): e251–e252. DOI: 10.1111/jdv.16469.
11. Henry D, Ackerman M, Sancelme E, Finon A, Esteve E. Urticarial eruption in COVID-19 infection. *J Eur Acad Dermatol Venereol*. 2020; 34 (6): e244–e245. DOI: 10.1111/jdv.16472.
12. Tang K, Wang Y, Zhang H, Zheng Q, Fang R, Sun Q. Cutaneous manifestations of the Coronavirus Disease 2019 (COVID-19): A brief review. *Dermatol Ther*. 2020; e13528. DOI: 10.1111/dth.13528.
13. Vremennye metodicheskie rekomendacii 'Profilaktika, diagnostika i lechenie novej koronavirusnoj infekcii (COVID-19)'. Versija 8.1 (01.10.2020), utverzhdennye Ministerstvom zdravoohraneniya RF. Available from: https://static-0.minzdrav.gov.ru/system/attachments/attaches/000/052/219/original/%D0%92%D1%80%D0%B5%D0%BC%D0%B5%D0%BD%D0%BD%D1%8B%D0%B5_%D0%9C%D0%A0_COVID-19_%28v.8.1%29.pdf?1601561462. Russian.
14. Recalcati S. Cutaneous manifestations in COVID-19: a first perspective. *J Eur Acad Dermatol Venereol*. 2020; 34 (5): e212–e213. DOI: 10.1111/jdv.16387.
15. Jimenez-Cauhe J, Ortega-Quijano D, Prieto-Barrios M, Moreno-Arrones OM, Fernandez-Nieto D. Reply to "COVID-19 can present with a rash and be mistaken for dengue": Petechial rash in a patient with COVID-19 infection. *J Am Acad Dermatol*. 2020; 83 (2): e141–e142. DOI: 10.1016/j.jaad.2020.04.016.
16. Diaz-Guimaraens B, Dominguez-Santas M, Suarez-Valle A, Pindado-Ortega C, Selda-Enriquez G, Bea-Ardebol S, et al. Petechial Skin Rash Associated With Severe Acute Respiratory Syndrome Coronavirus 2 Infection. *JAMA Dermatol*. 2020; 156 (7): 820–22. DOI: 10.1001/jamadermatol.2020.1741.

Литература

1. Casas C, Catala A, Hernandez G, Rodríguez-Jimenez P, Nieto D, Rodríguez-Villa A, et al. Classification of the cutaneous manifestations of COVID-19: a rapid prospective nationwide consensus study in Spain with 375 cases. *British Journal of Dermatology*. 2020; 183 (1): 71–77. DOI: 10.1111/bjd.19163.
2. Almutairi N, Schwartz RA. COVID-2019 with dermatologic manifestations and implications: an unfolding conundrum. *Dermatol Therapy*. 2020; e13544. Available from: <https://doi.org/10.1111/dth.13544>.
3. Recalcati S, Barbagallo T, Frasin LA, Prestinari F, Cogliardi A, Provero MC, et al. Acral cutaneous lesions in the time of COVID-19. *J Eur Acad Dermatol Venereol*. 2020; 34 (8): e346–e347. DOI: 10.1111/jdv.16533.
4. Criado PR, Abdalla BMZ, Assis IC, Blarcum de Graaff Mello C, Caputo GC, Vieira IC. Are the cutaneous manifestations during or due to SARS-CoV-2 infection/COVID-19 frequent or not? Revision of possible pathophysiologic mechanisms. *Inflamm Res*. 2020; 69 (8): 745–56. DOI: 10.1007/s00011-020-01370-w.
5. Wang C, Horby PW, Hayden FG, Gao GF. A novel coronavirus outbreak of global health concern. *Lancet*. 2020; 395 (10223): 470–73. DOI: 10.1016/S0140-6736(20)30185-9.
6. Formica D, Sultana J, Cutroneo P, et al. The economic burden of preventable adverse drug reactions: a systematic review of observational studies. *Expert Opin Drug Saf*. 2018; 17 (7): 681–95. DOI: 10.1080/14740338.2018.1491547
7. Aung A, Tang M, Adler N, et al. Adverse Drug Reactions Reported by Healthcare Professionals: Reaction Characteristics and Time to Reporting. *The Journal of Clinical Pharmacology*. 2018; 58 (10): 1332–9. DOI: 10.1002/jcph.1148.
8. Gelincik A, Brockow K, Celik GE, Dona I, Mayorga C, Romano A, et al. Diagnosis and management of the drug hypersensitivity reactions in Coronavirus disease 19. *Allergy*. 2020; 10.1111/all.14439. DOI: 10.1111/all.14439.
9. Marzano AV, Cassano N, Genovese G, Moltrasio C, Vena GA. Cutaneous manifestations in patients with COVID-19: a preliminary review of an emerging issue. *British Journal of Dermatology*. 2020; 183 (3): 431–42. DOI: 10.1111/bjd.19264.
10. Su CJ, Lee CH. Viral exanthem in COVID-19, a clinical enigma with biological significance. *J Eur Acad Dermatol Venereol*. 2020; 34 (6): e251–e252. DOI: 10.1111/jdv.16469.
11. Henry D, Ackerman M, Sancelme E, Finon A, Esteve E. Urticarial eruption in COVID-19 infection. *J Eur Acad Dermatol Venereol*. 2020; 34 (6): e244–e245. DOI: 10.1111/jdv.16472.
12. Tang K, Wang Y, Zhang H, Zheng Q, Fang R, Sun Q. Cutaneous manifestations of the Coronavirus Disease 2019 (COVID-19): A brief review. *Dermatol Ther*. 2020; e13528. DOI: 10.1111/dth.13528.
13. Временные методические рекомендации «Профилактика, диагностика и лечение новой коронавирусной инфекции (COVID-19)». Версия 8.1 (01.10.2020), утвержденные Министерством здравоохранения РФ. Доступно по ссылке: https://static-0.minzdrav.gov.ru/system/attachments/attaches/000/052/219/original/%D0%92%D1%80%D0%B5%D0%BC%D0%B5%D0%BD%D0%BD%D1%8B%D0%B5_%D0%9C%D0%A0_COVID-19_%28v.8.1%29.pdf?1601561462.
14. Recalcati S. Cutaneous manifestations in COVID-19: a first perspective. *J Eur Acad Dermatol Venereol*. 2020; 34 (5): e212–e213. DOI: 10.1111/jdv.16387.
15. Jimenez-Cauhe J, Ortega-Quijano D, Prieto-Barrios M, Moreno-Arrones OM, Fernandez-Nieto D. Reply to "COVID-19 can present with a rash and be mistaken for dengue": Petechial rash in a patient with COVID-19 infection. *J Am Acad Dermatol*. 2020; 83 (2): e141–e142. DOI: 10.1016/j.jaad.2020.04.016.
16. Diaz-Guimaraens B, Dominguez-Santas M, Suarez-Valle A, Pindado-Ortega C, Selda-Enriquez G, Bea-Ardebol S, et al. Petechial Skin Rash Associated With Severe Acute Respiratory Syndrome Coronavirus 2 Infection. *JAMA Dermatol*. 2020; 156 (7): 820–22. DOI: 10.1001/jamadermatol.2020.1741.

EFFICACY OF SMARTPHONE-COMPATIBLE OPTICAL INSTRUMENT FOR ASSESSING MELANOCYTIC NEVI FOR MALIGNANCY

Gaydina TA ✉, Dvornikova EG

Pirogov Russian National Research Medical University, Moscow, Russia

Early detection of melanocytic nevus progression to malignant melanoma is a pressing concern. Traditionally, patients with multiple melanocytic nevi (MMN) are monitored for extended periods of time and excisional biopsies are performed on individual suspicious melanocytic nevi (MN). This approach is costly and tremendously time-consuming for both doctors and patients. The aim of this study was to evaluate the efficacy of a smartphone-compatible optical instrument in the assessment of MN for malignancy. Seven patients aged 43 to 65 years with MMN on the trunk and upper/lower extremities were followed-up for 4 years. Dermoscopy images of MN were taken and analyzed using a Handyscope smartphone-compatible optical system operated at 20x magnification and a Handyscope3 application. A total of 74 MN were surgically removed during the follow-up period. None of the patients had melanoma. The results of dermoscopy image analysis generated by the convolutional neural network coincided with histopathology findings in all cases. The optical Handyscope system demonstrated its efficacy in assessing MN for malignancy. AI can be used for primary screening of MMN dermoscopy images. However, histopathological verification of the diagnosis is still needed.

Keywords: melanocytic nevus, artificial intelligence, mobile application, skin biopsy, early melanoma detection

Author contribution: both authors equally contributed to this manuscript.

Compliance with ethical standards: the study was approved by the Ethics Committee of Pirogov Russian National Research Medical University (Protocol № 201 dated October 21, 2020); all patients gave voluntary consent to surgery.

✉ **Correspondence should be addressed:** Tatiana A. Gaydina
Ostrovityanova, 1, Moscow, 117997; doc429@yandex.ru

Received: 11.09.2020 **Accepted:** 25.09.2020 **Published online:** 27.10.2020

DOI: 10.24075/brsmu.2020.065

ЭФФЕКТИВНОСТЬ ИСПОЛЬЗОВАНИЯ ОПТИЧЕСКОЙ СИСТЕМЫ СМАРТФОНА ДЛЯ ОЦЕНКИ ЗЛОКАЧЕСТВЕННОСТИ МЕЛАНОЦИТАРНЫХ НЕВУСОВ

Т. А. Гайдина ✉, Е. Г. Дворникова

Российский национальный исследовательский медицинский университет имени Н. И. Пирогова, Москва, Россия

Ранняя диагностика злокачественной трансформации меланоцитарных невусов в меланому кожи (МК) является актуальной проблемой современной медицины. Общепризнанная тактика ведения пациентов с множественными меланоцитарными невусами кожи (ММНК) представляет собой динамическое наблюдение с проведением эксцизионной биопсии отдельных онкологически подозрительных или меланомоопасных меланоцитарных невусов кожи (МНК). Данная тактика требует дорогостоящего оборудования и огромных временных затрат врача и пациента. Целью работы было оценить эффективность использования оптической системы смартфона для определения злокачественности меланоцитарных невусов. Семь пациентов в возрасте 43–65 лет с ММНК на коже туловища и конечностей находились под наблюдением в течение четырех лет. Получение дерматоскопических микроснимков и оценку злокачественности МНК проводили при помощи оптического устройства Handyscope с 20-кратным увеличением, сопряженного со смартфоном под управлением мобильного приложения Handyscope3. За период наблюдения пациентам было удалено 74 МНК, МК не было обнаружено ни в одном случае. Оценка злокачественности всех удаленных 74 МНК, проведенная сверточной нейронной сетью, совпала с результатами гистологических исследований. Оптический адаптер к смартфону показал эффективность в диагностике злокачественности МНК. Для скрининговой первичной диагностики дерматоскопических изображений ММНК возможно использовать искусственный интеллект (ИИ), однако необходимо гистологическое исследование для верификации диагноза.

Ключевые слова: меланоцитарный невус кожи, искусственный интеллект, мобильные приложения, биопсия кожи, ранняя диагностика меланомы

Вклад авторов: авторы внесли равнозначный вклад в работу.

Соблюдение этических стандартов: исследование одобрено этическим комитетом РНИМУ имени Н. И. Пирогова (протокол № 201 от 21 октября 2020 г.); все пациенты подписали добровольное информированное согласие на проведение оперативного лечения.

✉ **Для корреспонденции:** Татьяна Анатольевна Гайдина
ул. Островитянова, д. 1, г. Москва, 117997; doc429@yandex.ru

Статья получена: 11.09.2020 **Статья принята к печати:** 25.09.2020 **Опубликована онлайн:** 27.10.2020

DOI: 10.24075/vrgmu.2020.065

Skin neoplasms can be evaluated using portable smartphone-compatible instruments and artificial intelligence (AI) algorithms. Such systems are a real time-saver for both the physician and the patient. They are also a good aid in monitoring melanocytic nevi (MN). To this day, progression of benign MN to malignant melanoma (MM) remains understudied; therefore, with most MN health professionals should be watchful for any worrying signs. Statistically, in 2018 skin cancer was the most incident type of malignancy in the Russian population, amounting to 12.6 or 14.4% of cancers depending on whether malignant melanoma was excluded or included in the analysis. In Russia,

MM-associated mortality increased by 11.19% between 2008 and 2018 [1]. At the same time, according to the American Cancer Society, the number of deaths from MM in the USA was decreasing by 6.1% in men and 6.3% in women every year from 2013 to 2017, whereas the annual incidence of MM was growing by 2.2% in men and 1.9% in women [2]. Life expectancy of patients with MM largely depends on how advanced the disease is at the time of treatment initiation; grim figures suggest that early detection strategies existing in Russia need improving: in 2017, only one in 3 MM diagnoses was the result of active screening. In 2016–2017, stage IV

MM was initially diagnosed in 19.0% of melanoma patients. This is a disturbing figure given that such tumors are visible to the naked eye [3]. Early detection of skin neoplasms (SN) can be significantly improved by optical instruments that are compatible with a smartphone and can be operated using a mobile application.

Risk factors for MM include excessive exposure to UV radiation, sunburns during childhood, Fitzpatrick skin types I and II, DKN2A gene mutations, the presence of 10 or more dysplastic nevi or over 100 multiple melanocytic nevi (MMN), a past history of skin cancer, and familial melanoma [4–6]. A combination of these factors increases the risk for MM. Patients with increased risk for MM are advised to undergo total body photography and digital dermoscopy once every 3–6 months; the obtained MN images should be analyzed with AI, and excisional biopsies should be performed on suspicious lesions [7–9]. Patients with MNS (one of risk factors for MM) are recommended to have regular skin checkups once or twice; examination should be performed using noninvasive diagnostic techniques. With digital dermoscopy, a dermatologist can track changes occurring in MN over time and analyze them using AI, thereby improving the quality of diagnosis [10–12]. All noninvasive methods for early MM detection can be arbitrarily classified into the following groups:

Group 1, total body photography for preliminary diagnosis that can be performed at a non-specialist clinic;

Group 2, evaluation of suspicious MN that can potentially progress to melanoma;

Group 3, evaluation of suspicious MN that can potentially progress to melanoma at a specialist clinic, including the extent of surgery for their removal [13].

Smartphone-compatible optical systems for dermoscopy imaging are a novel promising method of noninvasive MN diagnostics. Total body photography requires costly space-consuming equipment, whereas smartphone optical adapters are portable and convenient. Smartphones are affordable gadgets that can be used for taking, storing and sharing dermoscopy images or other medical data in case a second opinion is needed [14].

Patients with MMN should be carefully examined for possible changes in the existing nevi and closely monitored for the development of de novo lesions. However, it may still be difficult to spot the first signs of malignization even when more than one noninvasive diagnostic technique is applied. Unexperienced dermatologists are not always able to accurately interpret dermoscopy findings. This might result in overdiagnosis and unnecessary surgical interventions, on the one hand, and delayed melanoma diagnosis, on the other. Telediagnosics can help with difficult cases and save time for both patients and doctors. The rapid evolution of high technology and the digitalization of the medical field create a new, efficient environment for public health workers and improve the quality of medical care. The vigorous development of portable diagnostic devices makes it possible to monitor the broad range of clinically significant parameters of the human body. The aim of this study was to evaluate the efficacy of a smartphone-compatible optical system in diagnosing malignant melanocytic nevi.

METHODS

We followed up 4 male and 3 female patients aged 43–65 years (mean age being 51.14 years) over the course of 4 years. The following inclusion criteria were applied: male/female sex; age of 18 years or older; MMN on the trunk and/or extremities.

Exclusion criteria: age under 18 years; decompensated chronic conditions. MN were defined as multiple if a patient had over 100 MN. A total of 875 MN were detected and examined during the entire follow-up period. Of them, 74 MN were surgically removed. To take dermoscopy images and evaluate MN for malignancy, a smartphone-compatible Handyscope optical instrument with 20x magnification (FotoFinder; Germany) and a mobile Handyscope3 application were used. Handyscope3 is essentially a convolutional neuronal network trained on a large dataset of images of histologically confirmed malignancies.

Conveniently, high-quality dermoscopy images can be obtained with a digital smartphone camera, which is a great aid in practical clinical work. However, without an additional lens and adequate lighting, a smartphone camera cannot ensure the uniformity of shooting conditions and the sufficient amount of detail at high resolution. From a large selection of optical systems available on the market, we chose a Handyscope. The manufacturer has developed an AI-based application for evaluating and storing dermoscopy images. In difficult cases, the image can be uploaded to a second opinion service, where it can be evaluated by experienced dermoscopy experts.

RESULTS

In all patients, MMN were localized predominantly to the trunk ($n = 699$; 79.89%), upper ($n = 117$; 13.37%) and lower ($n = 59$; 6.74%) extremities. The highest number of MN ($n = 183$, including 3 dysplastic nevi) was observed in a 65-year-old female patient; this woman received the maximum number of surgical excisions for her MN ($n = 25$) over the course of 4 years. The smallest number of MN ($n = 126$) was observed in a 45-year-old man; in total, he had 5 MN removed. The highest number of suspicious nevi was detected during primary examinations in the first year of observation (47 MN; 63.5%). In the follow-up period, the patients visited a dermatologist twice a year; during each visit, the patients underwent digital dermoscopy with a smartphone and an optical attachment. The obtained images were analyzed by AI in the Handyscope3 application; AI assessed the photographed moles for malignancy on the scale from 0 to 1. Values from 0.5 and 1 were interpreted as suspicious for malignancy, whereas values from 0 to 0.2 suggested a benign lesion. The risk of developing MM was explained to the patients; they were also strongly advised to have a checkup with a dermatologist twice a year. All patients were recommended to avoid direct sunlight, always use a maximum protection sunscreen and to give up on tanning at tanning salons. Patients with suspicious lesions were referred to an oncologist for deciding on the treatment strategy and evaluating the need for biopsy. According to the protocol proposed by the International Agency for Research on Cancer (IARC), the following clinical features of dysplastic nevi suggest the risk of melanoma: diameter over 5 mm, irregular pigmentation patterns, asymmetry, irregular borders, peripheral hyperemia. According to the classic ABCD criteria, none of our patients had MM. However, 5 patients had dysplastic nevi (totaling to 10), and in another 2 patients an equivocal diagnosis could not be established based on dermoscopy findings. All MN were analyzed by the mobile application, and all patients were referred to an oncologist.

Surgical excision of MN was performed by an oncologist at a specialist facility. In some cases, it was the patients who insisted on surgery because their nevi caused esthetic problems or were constantly subjected to mechanical irritation. Prior to surgery, the patients underwent dermoscopy, and the nevi were photographed. Either excisional or shave biopsies

were performed under infiltration anesthesia; the biopsied specimens were subjected to a histopathological examination. Fig. 1 shows stages of the diagnostic procedure and the AI-based assessment for malignancy.

In total, 74 MN were removed. None of the patients was found to have MM. Results of the AI-based malignancy assessment coincided with histopathology findings in all cases. Ten (13.5%) nevi excised from 5 patients were histologically confirmed to be dysplastic. In 35 cases (47.3%) histopathology findings were suggestive of intradermal melanocytic nevi. Nine (12.2%) melanocytic nevi were found to be of combined type. Two lesions (2.7%) were Sutton's nevi. One lesion (1.6%) was a simple lentigo. In 17 cases (22.97%) of benign nevi, patients insisted on their surgical removal. Most of the excised nevi were localized to the trunk (60 MN; 81.1%), followed by upper (8 MN; 10.8%) and lower (6 MN; 8.1%) extremities (Fig. 2).

Postoperatively, the patients complained of occasional itching and tenderness in the area of hypertrophic scar formation and some found scarring esthetically distressing. Such patients were prescribed topical medications for scar management.

DISCUSSION

There are no robust data on the epidemiology of MN. The terminology used to define MN is conflicting, and only malignant SN are covered by statistical analysis. Retrospective studies of digitized biopsies can improve our understanding of MN prevalence but so far this type of analysis is limited to a few regions [15]. There are a lot of different terms to describe MN at risk for progressing to melanoma [16]. In 1978, Clark described 2 families with MMN and high frequency of MN malignization. This condition was referred to as the B-K mole syndrome, where B and K are the initials of the affected families.

According to some estimates, MN progress to melanoma in 4 to 54.2% cases [17, 18]. There are MN with unknown potential for malignancy [19]. Patients with MMN are at risk for melanoma; the risk is the higher, the more lesions the patient has. It increases 7-fold for patients who have 100 or more borderline nevi, as compared to those who have only 15 simple nevi [4]. The risk of melanoma also increases in patients with MMN and dysplastic nevi [5]. Nevertheless, some authors argue that preventive MN excision is not rational [4, 16] and propose that noninvasive screening should be actively promoted instead, including manual dermoscopy, sequential digital dermoscopy, computer -aided diagnosis, total body photography, high-frequency ultrasonography, reflectance confocal microscopy, multiphoton tomography, electrical impedance spectroscopy, Raman spectroscopy, and quantitative dynamic infrared imaging [13].

Zink et. al compared the results of the analysis of dermoscopy images with clinical data and histopathology findings. Dermoscopy images were taken in 26 patients using a mobile phone and a Handyscope optical instrument. Physical examinations and dermoscopy were performed by 5 dermatologists who worked independently of each other. The results were compared in terms of diagnostic accuracy, differential diagnosis and management strategies. The concordance of diagnoses was 92.3%, whereas the concordance of recommended management strategies was 76.9%. Of 6 histologically confirmed diagnoses, 66.7% were established based on dermoscopy images and a clinical examination. The authors concluded that digital dermoscopy microimages of individual lesions, including MN, combined with macrophotographs could be assessed qualitatively and

that mobile digital dermoscopy could be a good alternative to a traditional dermatologic examination [20]. In our study, the results of AI-based analysis of dermoscopy images coincided with histopathology findings in 74 (100%) cases. An optical adapter for a smartphone and an accompanying mobile application are very practical. AI can assess the mole for malignancy in a matter of seconds. Importantly, the system can be used in teleradiology, saving time for patients and doctors [21].

The existing noninvasive techniques for skin diagnostics cannot replace a histopathological examination. It takes a doctor two years to be properly trained and build up sufficient experience. In difficult cases, there is a risk of misinterpretation. AI is a good aid in the primary screening of SN and establishing an accurate diagnosis [22].

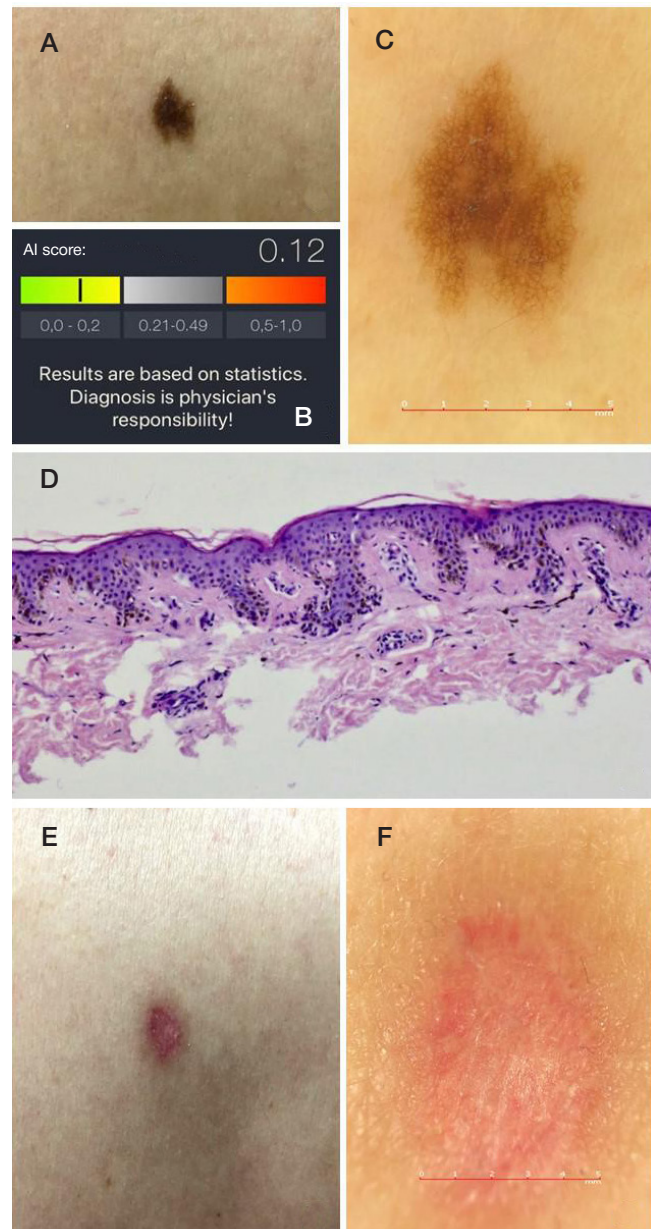


Fig. 1. AI in the assessment of MN for malignancy. **A.** A plain image of a melanocytic nevus. **B.** A malignancy score calculated by AI. **C.** A dermoscopy image at $\times 20$ magnification: a reticular dysplastic nevus with hyperpigmentation at the center. **D.** A histological slide (hematoxylin-eosin stain, $\times 100$ magnification) showing the stratified squamous keratinized epithelium with areas of mild acanthosis. Multiple nevus cells adjacent to the epithelium are organized in a nesting pattern. Impression: D22. Borderline melanocytic nevus. ICD-O code: 8740/0. No nevoid cells are found at the margin of excision. **D.** Formation of a normotrophic scar. **E.** A dermoscopy image of the normotrophic scar (at $\times 20$ magnification)

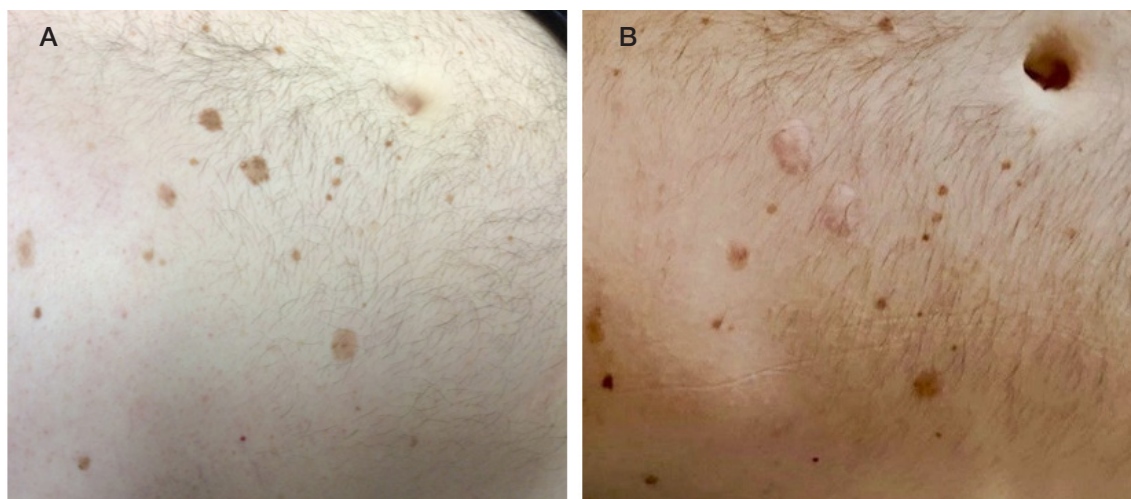


Fig. 2. **A** preoperative photo of MMN on the abdomen. **B**. Postoperative scars

In Russia, MN screening strategies, including telescreening, are currently in development [23].

CONCLUSION

Patients with MMN must be closely monitored for possible malignization, which dictates the need for novel accurate

noninvasive diagnostic techniques. In this study, malignant MN were reliably detected using a smartphone-compatible optical instrument with 20x magnification and an AI-based mobile application for the analysis of dermoscopy images. Digitalization of the medical field and development of portable diagnostic instruments opens up new opportunities for providing medical care at a new hi-tech level.

References

1. Kaprin AD, Starinskij VV, Petrova GV, redaktory. Zlokachestvennye novoobrazovaniya v Rossii v 2018 godu (zabolevaemost' i smertnost'). M.: MNIOL im. P.A. Gercena — filial FGBU «NMIC radiologii» Minzdrava Rossii, 2019; 250 s. Russian.
2. Henley SJ, Ward EM, Scott S, Ma JM, Anderson RN, Firth AU, et al. Annual report to the nation on the status of cancer, part I: National cancer statistics. *Cancer*. 2020; 126 (10): 2225–49.
3. Kaprin AD, Starinskij VV, Petrova GV, redaktory. Sostojanie onkologicheskoi pomoshhi naseleniju Rossii v 2017 godu. M.: MNIOL im. P.A. Gercena — filial FGBU «NMIC radiologii» Minzdrava Rossii, 2018; 236 s. Russian.
4. Kubanov AA, Sysoeva TA, Galljamova YuA, Bisharova AS, Mercalova IB. Algoritm obsledovaniya pacientov s novoobrazovaniyami kozhi. *Lechashhij vrach*. 2018; (3): 83–8. Russian.
5. Salamova IV, Mordovceva VV, Lamotkin IA. Problema profilaktiki melanomy kozhi u pacientov s mnozhestvennymi nevusami. *Klinicheskaja dermatologija i venerologija*. 2014; 12 (2): 110–115. Russian.
6. Klinicheskie rekomendacii: melanoma kozhi i slizistyh obolochek (utv. Minzdravom Rossii) (17 ijulja, 2020). Dostupno po ssylke: https://melanomapro.ru/page/clinical-guidelines-melanoma_2020. Russian.
7. Salerni G, Carrera C, Lovatto L, Puig-Butille JA, Badenas C, Plana E, et al. Benefits of total body photography and digital dermoscopy (“two-step method of digital follow-up”) in the early diagnosis of melanoma in patients at high risk for melanoma. *J Am Acad Dermatol*. 2012; 67 (1): e17–e27.
8. Romanova OA, Artemyeva NG, Yagubova EA, Rudakova IM, Marycheva VN, Veshchevailov AA. Principles of excisional biopsy of dysplastic nevus in outpatient settings. *Onkologiya Zhurnal imeni PA Gertsena*. 2016; 5 (1): 36–41.
9. Sergeev YuYu, Sergeev VYu, Mordovceva VV. Dinamicheskoe nabljudenie za melanocitarnymi obrazovaniyami pri pomoshhi dermoskopii (obzor literatury). *Medicinskij alfavit*. 2020; (6): 66–71. Russian.
10. Sondermann W, Utikal J, Enk A, Schadendorf D, Klode J, Hauschild A, et al. Prediction of melanoma evolution in melanocytic nevi via artificial intelligence: A call for prospective data. *Eur J Cancer*. 2019; 119: 30–4.
11. Hekler A, Utikal J, Enk A, Hauschild A, Weichenthal M, Maron RC, et al. Superior skin cancer classification by the combination of human and artificial intelligence. *Eur J Cancer*. 2019; 120: 114–121.
12. Glotsos D, Kostopoulos S, Lalissidou S, Sidiropoulos K, Asvestas P, Konstantinou C, et al. Design of a decision support system, trained on GPU, for assisting melanoma diagnosis in dermoscopy images. *Journal of Physics: Conference Series*. 2015; 633: 012079.
13. Grajdeanu I, Vata D, Statescu L, Popescu I, Porumb-Andrese E, Patrascu A, et al. Use of imaging techniques for melanocytic naevi and basal cell carcinoma in integrative analysis (Review). *Exp Ther Med*. 2020; 78–86.
14. Doukas C, Stagkopoulou P, Maglogiannis I. Skin lesions image analysis utilizing smartphones and cloud platforms. *Mobile Health Technologies*. 2015; 1256: 435–458.
15. Lott J, Boudreau D, Barnhill R, Weinstock MA, Knopp E, Piepkorn MW, et al. Population-Based Analysis of Histologically Confirmed Melanocytic Proliferations Using Natural Language Processing. *JAMA Dermatol*. 2018; 154 (1): 24–9.
16. Emiroglu N, Sallahoglu K, Cengiz F, Cemil B, Onsun N. Three years dermoscopic follow-up of atypical nevi. *Dermatol Ther*. 2020; 33 (1): e13205.
17. Haenssle H, Mograby N, Ngassa A, Buhl T, Emmert S, Schön MP, et al. Association of Patient Risk Factors and Frequency of Nevus-Associated Cutaneous Melanomas. *JAMA Dermatol*. 2016; 152 (3): 291–298.
18. Melamed R, Aydin I, Rajan G, Phelps R, Silvers DN, Emmett KJ, et al. Genomic Characterization of Dysplastic Nevi Unveils Implications for Diagnosis of Melanoma. *Journal of Investigative Dermatology*. 2017; 137 (4): 905–909.
19. Woltsche N, Schmid-Zalaudek K, Deinein T, Rammel K, Hofmann-Wellenhof R, Zalaudek I. Abundance of the benign melanocytic universe: Dermoscopic-histopathological correlation in nevi. *J Dermatol*. 2017; 44 (5): 499–506.
20. Zink A, Kolbinger A, Leibl M, Suarez I, Gloning J, Merkel C, et al.

- Teledermoscopy by mobile phones. Reliable help in the diagnosis of skin lesions? *Der Hautarzt*. 2017; 68 (11): 890–895.
21. Wu X, Oliveria S, Yagerman S, Chen L, Defazio J, Braun R, et al. Feasibility and Efficacy of Patient-Initiated Mobile Teledermoscopy for Short-term Monitoring of Clinically Atypical Nevi. *JAMA Dermatol*. 2015; 151 (5): 489–496.
 22. Gaydina TA, Dvornikov AS, Skripkina PA. Case report: removal of a proliferating pilomatricoma with a CO₂ laser. *Bulletin of Russian state medical university*. 2019; 6: 110–113. Russian.
 23. Demidov LV, Sinel'nikov IE, Baryshnikov KA, Utjashev IA, Nazarova VV. Perspektivy skrininga melanomy kozhi v Rossii. *Vestnik FGBU «RONC im. N.N. Blohina»*. 2017; 28 (1–2): 28–35.

Литература

1. Каприн А. Д., Старинский В. В., Петрова Г. В., редакторы. Злокачественные новообразования в России в 2018 году (заболеваемость и смертность). М.: МНИОИ им. П.А. Герцена — филиал ФГБУ «НМИЦ радиологии» Минздрава России, 2019; 250 с.
2. Henley SJ, Ward EM, Scott S, Ma JM, Anderson RN, Firth AU, et al. Annual report to the nation on the status of cancer, part I: National cancer statistics. *Cancer*. 2020; 126 (10): 2225–49.
3. Каприн А. Д., Старинский В. В., Петрова Г. В., редакторы. Состояние онкологической помощи населению России в 2017 году. М.: МНИОИ им. П.А. Герцена — филиал ФГБУ «НМИЦ радиологии» Минздрава России, 2018; 236 с.
4. Кубанов А. А., Сысоева Т. А., Галлямова Ю. А., Бишарова А. С., Мерцалова И. Б. Алгоритм обследования пациентов с новообразованиями кожи. *Лечащий врач*. 2018; (3): 83–88.
5. Саламова И. В., Мордовцева В. В., Ламоткин И. А. Проблема профилактики меланомы кожи у пациентов с множественными невусами. *Клиническая дерматология и венерология*. 2014; 12 (2): 110–115.
6. Клинические рекомендации: меланома кожи и слизистых оболочек (утв. Минздравом России) (17 июля, 2020). Доступно по ссылке: https://melanomapro.ru/page/clinical-guidelines-melanoma_2020.
7. Salerni G, Carrera C, Lovatto L, Puig-Butlle JA, Badenas C, Plana E, et al. Benefits of total body photography and digital dermatoscopy (“two-step method of digital follow-up”) in the early diagnosis of melanoma in patients at high risk for melanoma. *J Am Acad Dermatol*. 2012; 67 (1): e17–e27.
8. Романова О. А., Артемьева Н. Г., Ягубова Э. А., Рудакова И. М., Марычева В. Н., Вещевайлов А. А. Принципы эксцизионной биопсии диспластического невуса в амбулаторных условиях. *Онкология. Журнал им. П.А. Герцена*. 2016; 5 (1): 36–41.
9. Сергеев Ю. Ю., Сергеев В. Ю., Мордовцева В. В. Динамическое наблюдение за меланокитарными образованиями при помощи дерматоскопии (обзор литературы). *Медицинский алфавит*. 2020; (6): 66–71.
10. Sondermann W, Utikal J, Enk A, Schadendorf D, Klode J, Hauschild A, et al. Prediction of melanoma evolution in melanocytic nevi via artificial intelligence: A call for prospective data. *Eur J Cancer*. 2019; 119: 30–4.
11. Hekler A, Utikal J, Enk A, Hauschild A, Weichenthal M, Maron RC, et al. Superior skin cancer classification by the combination of human and artificial intelligence. *Eur J Cancer*. 2019; 120: 114–121.
12. Glotsos D, Kostopoulos S, Lalissidou S, Sidiropoulos K, Asvestas P, Konstandinou C, et al. Design of a decision support system, trained on GPU, for assisting melanoma diagnosis in dermatoscopy images. *Journal of Physics: Conference Series*. 2015; 633: 012079.
13. Grajdeanu I, Vata D, Statescu L, Popescu I, Porumb-Andrese E, Patrascu A, et al. Use of imaging techniques for melanocytic naevi and basal cell carcinoma in integrative analysis (Review). *Exp Ther Med*. 2020; 78–86.
14. Doukas C, Stagkopoulos P, Maglogiannis I. Skin lesions image analysis utilizing smartphones and cloud platforms. *Mobile Health Technologies*. 2015; 1256: 435–458.
15. Lott J, Boudreau D, Barnhill R, Weinstock MA, Knopp E, Piepkorn MW, et al. Population-Based Analysis of Histologically Confirmed Melanocytic Proliferations Using Natural Language Processing. *JAMA Dermatol*. 2018; 154 (1): 24–9.
16. Emiroglu N, Sallahoglu K, Cengiz F, Cemil B, Onsun N. Three years dermoscopic follow-up of atypical nevi. *Dermatol Ther*. 2020; 33 (1): e13205.
17. Haenssle H, Mograby N, Ngassa A, Buhl T, Emmert S, Schön MP, et al. Association of Patient Risk Factors and Frequency of Nevus-Associated Cutaneous Melanomas. *JAMA Dermatol*. 2016; 152 (3): 291–298.
18. Melamed R, Aydin I, Rajan G, Phelps R, Silvers DN, Emmett KJ, et al. Genomic Characterization of Dysplastic Nevi Unveils Implications for Diagnosis of Melanoma. *Journal of Investigative Dermatology*. 2017; 137 (4): 905–909.
19. Woltsche N, Schmid-Zalaudek K, Deinlein T, Rammel K, Hofmann-Wellenhof R, Zalaudek I. Abundance of the benign melanocytic universe: Dermoscopic-histopathological correlation in nevi. *J Dermatol*. 2017; 44 (5): 499–506.
20. Zink A, Kolbinger A, Leibl M, Suarez I, Gloning J, Merkel C, et al. Teledermoscopy by mobile phones. Reliable help in the diagnosis of skin lesions? *Der Hautarzt*. 2017; 68 (11): 890–895.
21. Wu X, Oliveria S, Yagerman S, Chen L, Defazio J, Braun R, et al. Feasibility and Efficacy of Patient-Initiated Mobile Teledermoscopy for Short-term Monitoring of Clinically Atypical Nevi. *JAMA Dermatol*. 2015; 151 (5): 489–496.
22. Гайдина Т. А., Дворников А. С., Скрипкина П. А. Клинический случай: удаление пролиферирующей пиломастрикомы CO₂-лазером. *Вестник Российского государственного медицинского университета*. 2019; 6: 110–113.
23. Демидов Л. В., Синельников И. Е., Барышников К. А., Утяшев И. А., Назарова В. В. Перспективы скрининга меланомы кожи в России. *Вестник ФГБУ «РОНЦ им. Н. Н. Блохина»*, 2017; 28 (1–2): 28–35.

In the journal Bulletin of the Russian State Medical University (July–August 2020/04, p. 60–66), mistakes were made in the article:

HYPOXIA ENHANCES TRANSCYTOSIS IN INTESTINAL ENTEROCYTES

Maltseva DV, Shkurnikov MYu, Nersisyan SA, Nikulin SV, Kurnosov AA, Raigorodskaya MP, Osipyants AI, Tonevitsky EA

✉ **Correspondence should be addressed:** Diana V. Maltseva
Vavilova, 7, Moscow, 117321; dmaltseva@gmail.com

Received: 08.08.2020 **Accepted:** 21.08.2020

DOI: 10.24075/brsmu.2020.049

The following corrections should be applied:

	Published text:	Correction:
p. 60, item «Funding»	The study received public financial support from the Ministry of Science and Higher Education of the Russian Federation (project ID RFMEFI60519X0184).	The study was supported by the Ministry of Science and Higher Education of the Russian Federation (Project ID RFMEFI61719X0056).
p. 60, item «Финансирование»	Работа выполнена при финансовой поддержке государства в лице Минобрнауки России (идентификатор соглашения: RFMEFI60519X0184).	Работа выполнена при финансовой поддержке государства в лице Минобрнауки России (идентификатор соглашения: RFMEFI61719X0056).